

COMPUTER SIMULATION OF SELF-ASSEMBLING AMPHIPHILIC SYSTEMS: BULK AND INTERFACIAL PROPERTIES

A Thesis Submitted

in Partial Fulfillment of the Requirements

for the Degree of

Doctor of Philosophy

by

PRABAL KUMAR MAITI

to the

DEPARTMENT OF PHYSICS

INDIAN INSTITUTE OF TECHNOLOGY KANPUR

JULY 1997

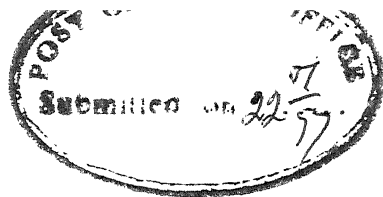
13 JUL 1998

CENTRAL LIBRARY
I. I. T., KANPUR

Acc. No. A 125700

PHY-1997-D-MAI-COM

CERTIFICATE



It is certified that the work contained in this thesis entitled "*Computer Simulation of Self-assembling Amphiphilic Systems: Bulk and Interfacial properties*", by *Prabal Kumar Maiti*, has been carried out under my supervision and that this work has not been submitted elsewhere for any degree.

A handwritten signature in cursive script, reading 'Debashish Chowdhury'.

Dr. Debashish Chowdhury

Professor

Department of Physics

Indian Institute of Technology

Kanpur

July 1997

I dedicate this thesis to
indigent children in straitened circumstances.

“A certain man had the power of grunting exactly like a pig, so much so that whenever he grunted where pigs were grazing, they would all turn to see if any new member had come into their fold. Slowly he became popular and started presenting a show of his art for a price. Once when he was showing his skills in a village pandal, a sage with his disciples chanced to pass through the village and was surprised to hear about the show. The sage immediately got another pandal erected and advertised that there was going to be a bigger grunting show and that too without any tickets. Naturally a big crowd assembled to watch the feat. But, to their, utter disappointment, the sage was just making an actual pig grunt loudly. The crowd left the pandal in sheer disgust claiming that they heard this everyday and that the sage was merely wasting their time. No amount advertising could get the crowd back, whereas, the show of the man imitating the pig's grunt was still pulling huge crowds. Now the sage addressed his disciples, “Here is a splendid lesson for us. Men seldom care for reality, but always go in for imitation. That is why this world exists, which is a mere imitation, a reflection in the distorting mirror of Maya of the great Atman. No external help is needed to see the self but very few want it and even if you eagerly advertise it, none will go to you except those who love Truth for Truth's sake. Reflect on this”.”

SYNOPSIS

Name of Student : PRABAL KUMAR MAITI *Roll No. :* 9210968

Degree for which submitted : Ph.D., Department of Physics

Thesis Title : **Computer simulation of self-assembling amphiphilic systems: bulk and interfacial properties.**

Thesis Supervisor : Prof. Debashish Chowdhury, Department of Physics,
Indian Institute of Technology, Kanpur 208016, India.

Month and Year of thesis submission : July, 1997

The "head" of amphiphilic molecules (also called surfactants) consist of a polar or ionic group. The "tail" of many amphiphiles consist of a single hydrocarbon chain whereas that of some other amphiphiles, e.g., phospholipids, are made of two hydrocarbon chains both of which are connected to the same head. Yet another class of surfactants, called *gemini* surfactants, consist of two single-chain amphiphiles whose heads are connected by a "spacer" chain and, hence, these "double-headed" surfactants are sometimes also referred to as "dimeric surfactants". When put into an aqueous medium, the "heads" of the amphiphiles like to get immersed in water and, hence, called "hydrophilic" while the tails tend to minimize contact with water and, hence, called "hydrophobic" . The spacer in gemini surfactants is usually hydrophobic but gemini surfactants with hydrophilic spacers have also been synthesized. In aqueous medium amphiphiles optimize their contact with water forming various types of *self-assemblies* (i.e., supramolecular aggregates), e.g., monolayer and bilayer membranes, micelles, vesicles, etc.

The aim of the thesis is to develop, generalize and/or extend realistic, but simple microscopic models of self assembling amphiphilic systems and to study their bulk and interfacial properties. We check the reliability of the models by comparing the results of computer simulation with known experimental results and, then, predict new phenomena by carrying out novel computer experiments. Since Monte Carlo (MC) simulation is more efficient than Molecular Dynamics (MD) method for the equilibration of such systems, we compute most of the quantities of interest by MC simulation.

In chapter 1 we give a brief overview of the physical properties of the amphiphilic systems, the nature of the self assemblies formed by the amphiphiles, and also describe the theoretical and computational techniques to model these systems. Chapters 2,3 and 4 deal with almost exclusively the interfacial properties, chapter 5 deals with both the interface and the bulk while chapters 6 and 7 deal with self-assemblies in bulk and chapter 8 deals with self-assemblies in porous media. Our conclusions are summarized in chapter 9.

It is known from continuum models of membranes/interfaces that when bending rigidity is low, thermal fluctuations govern the out-of-plane thermal fluctuations, amphiphilic membranes can crumple above a critical temperature. In the chapter 2 of the thesis we show that the oil-water interface is rough, but not crumpled, in the droplet phase of the Widom model which is the simplest microscopic lattice model of ternary microemulsions.

In chapter 3 we construct a class of discrete lattice models of membranes/interfaces where we can make a clear distinction between the interfacial tension and bending rigidity which can be "switched off" independently of each other. More specifically, in chapter 3, we propose a $d + 1$ -dimensional *restricted discrete solid-on-solid* (RDSOS) model as well as *un-*

restricted discrete solid-on-solid (UDSOS) model for d -dimensional amphiphilic membranes where the bending stiffness of the membrane is incorporated following the same prescription as in the Widom model. We also point out some analogies between the relaxation to rough equilibrium states of these SOS models and nonequilibrium growth of some kinetically roughened model surfaces.

In all the above models bending energy of the amphiphilic monolayer membranes is introduced as a parameter. In the remaining chapters we use the Larson prescription for modelling amphiphilic systems, as it explicitly takes into account the conformational degrees of freedom of the amphiphilic chain molecules. Jan, Stauffer and collaborators reformulated the Larson model in terms of Ising-like variables. We have used Jan and Stauffer's prescription for our models in chapters 4 - 8.

In chapter 4 we study the roughening of the oil-water interface in the presence of single-chain surfactants and investigate the physical origin of the lowering of the oil-water interfacial tension.

After studying the properties of the amphiphilic membrane at the oil-water interface in chapters 2,3 and 4, we investigate the air-water interface in the presence of single-chain amphiphiles in chapter 5. In this chapter we introduce a microscopic lattice model of a binary mixture of amphiphilic molecules, of two different lengths, in a system where water is separated from the air above it by a sharp well defined interface. We demonstrate an entropy-driven phase segregation in a direction perpendicular to the air-water interface when the initial total surface density of the amphiphiles is sufficiently high. We also investigate (a) the conformations of the amphiphiles, (b) the distribution of the sizes of the clusters

of monomers belonging to the long amphiphiles as well as of those belonging to the short amphiphiles in planes parallel to the interface, (c) the effects of varying the lengths, total concentration and the ratio of the numbers of the two types of the amphiphilic molecules, the strength of the inter-monomer interactions and temperature.

In the chapters 4 and 5 only single-chain amphiphiles have been considered although the general conclusions drawn from our MC studies are valid also for double-chain amphiphiles. In chapter 6 we compare and contrast the self-assemblies of single-chain and double-chain amphiphiles, respectively, in water. In this chapter we study the self-assemblies of binary mixtures of single-chain and double-chain amphiphiles and compare these with those formed by the corresponding single species of amphiphiles.

In chapter 7 we propose a microscopic lattice model of gemini surfactants. We show that these model gemini surfactants form long, thread-like and entangled micellar aggregates even at low concentrations where single-chain model surfactants form spherical micelles. We compare the morphologies of the micellar aggregates formed in our MC simulations with those observed in laboratory experiments and in earlier molecular dynamics simulations. We also study the variation of the critical micellar concentration of these model gemini surfactants with the variation of the (a) length of the hydrocarbon spacer connecting the two hydrophilic heads, (b) length of the hydrophobic tail and (c) the bending rigidity of the hydrocarbon chains forming the spacer and the tail. Some of the trends of variation are counter-intuitive but are in excellent agreement with the available experimental results.

In chapter 8 we propose a scheme for MC simulation of ternary microemulsions in porous media (such as vycor glass). Finally, in chapter 9 we summarize our conclusions and outline

directions of future work.

Acknowledgments

I am indebted to my supervisor Prof. Debashish Chowdhury for his help and guidance throughout the thesis work. I thank him for the encouragement and constant support during this period.

It is a pleasure to thank Prof. J. K. Bhattacharjee and Prof. B. K. Chakrabarti for all discussions and collaboration. I am grateful to Profs. Avinash Singh, Mahendra K. Mahto, K. P. Rajeev for useful suggestions and encouragement. I also thank Alexander Humboldt Foundation, Bonn, for donating a SPARCstation20 to Prof. D. Chowdhury. I thank Mr. P. V. K. Reddy for setting up the computer on which large amount of computer calculations were performed. I thank Prof. P. Guptabhaya for giving access to graphics package for generating some of the figures.

The best moments of my stay at IIT have been with my friends, and children from various schools that we have been organizing. I am greatly inspired by Shreesh and Vijaya Lakshmi, whose dedication and vision provided a great support for all of us in the social activities like Vivekananda Samiti and Jagriti Bal Vikas Samiti and Worker's Cooperative. I thank everyone who has been associated with these activities. The help rendered by Mr. H. K.

Panda, L. S. Rathour, A. K. Srivastava and other members of Physics office is gratefully acknowledged. Mr. Aftab Alam of Compter Center has been very helpful in computer related work.

I thank my father, my aunt, and other members of the family for encouraging me to pursue higher studies.

Contents

Synopsis	i
Acknowledgments	v
List of Figures	xii
List of Tables	xvii
1 Introduction	1
1.1 The Aim	1
1.2 The Amphiphilic Molecules and Their Supramolecular Aggregates	2
1.3 Phase Diagrams and Physical Properties	4
1.3.1 Interfacial properties	5
1.3.2 The Phase Diagram	5
1.4 Models describing Amphiphilic Systems	11
1.4.1 Microscopic models	12
1.4.2 Landau-Ginzburg models	21
1.4.3 Interface/Membrane models	23
1.5 Organization of the thesis:	27
2 Oil-Water Interface in the Widom model is it smooth, rough or crumpled?	31
2.1 Introduction	31
2.2 Simulation	34
2.3 Results	35
3 Restricted and unrestricted discrete SOS models of interface with bending rigidity: equilibrium and non-equilibrium properties	41
3.1 Introduction	41
3.2 The Model	43
3.3 UDSOS Model	46
3.4 RDSOS Model	60
3.5 Comparison with Other Models	66

6	Conclusion	68
oil	- Water Interface in the 2-dimensional Larson type of model	70
1	Introduction	70
2	The Model	74
3	Results	75
4	Conclusion	80
Out-of-plane phase segregation and in-plane clustering in a binary mixture of amphiphiles at air-water interface		81
1	Introduction	81
2	The Model	84
3	Definitions of characteristics quantities of interest	87
4	Concentration profiles for chemically identical amphiphiles of different lengths	89
5.4.1	Dependence on the lengths of the hydrophobic tails	94
5.4.2	Dependence on the ratio of the initial surface densities of the two components	97
5.4.3	Dependence on the temperature	97
5.4.4	Effect of bending stiffness of the amphiphiles	100
5	In-plane clustering of the amphiphiles	101
6	Conformation of amphiphiles	105
7	Chemically different amphiphiles	112
8	Physical mechanism, Comparison with experiments and similar phenomena in other systems	115
9	Summary and conclusion	116
Self assemblies of single chain and double chain amphiphiles		117
1	Introduction	117
2	Micelle formation	118
3	Vesicle formation	120
4	Conclusion	127
Microscopic Model of Gemini Surfactants: Self-assemblies in Water and at Air-Water Interface		128
1	Introduction	128
2	The Model and The Characteristic Quantities of Interest	131
7.2.1	General aspects	131
7.2.2	Model of Gemini Surfactants in Bulk Water	136
7.2.3	Model of Gemini Surfactants at Air-Water Interface	137
7.2.4	Characteristic Quantities of Interest	138
3	Micellar Aggregates of Gemini Surfactants	140
7.3.1	Aggregates of Gemini Surfactants: Results for Hydrophobic Spacers .	140
7.3.2	Aggregates of Gemini Surfactants; Results for Hydrophilic Spacers: .	148

7.4	Spatial Organization of Gemini Surfactants at Air-Water Interface: Results for Hydrophobic and Hydrophilic Spacers:	151
7.4.1	Dilute regime	151
7.4.2	High Surface density regime	155
7.5	Summary and Conclusion	158
8	Monte Carlo simulation of amphiphiles in complex fluids confined in porous medium	163
8.1	Introduction	163
8.2	The Model	164
8.3	Preparation of the Model porous medium	165
8.4	Results and Discussion	166
8.5	Summary and conclusion	171
9	Conclusion	173
9.1	Future direction of research	178
	References	180
	List of Publications	193

st of Figures

Different types of amphiphiles.	3
Different structures formed by amphiphiles in aqueous medium (after[6]).	4
Schematic diagram illustrating the phase behaviour of real surfactant-oil-water systems (after[43]).	6
Different structures formed by amphiphiles in a mixture of oil-water-amphiphile system. Figure (d) and (e) after[2] and figure (c) after[19].	8
Theoretical description of amphiphile molecules on different length scales (after[19]).	11
A typical configuration of Widom model.	13
Origin of bending and different neighbors in Widom model	14
(a) A model amphiphilic molecule, (b) Allowed moves for amphiphiles.	19
Phase Diagram of the Widom Model, (a) in space dimension 2 (after[100]) (b) in space dimension 3 (after[101]).	33
Two typical plots of $N_b(y)$ for $j = 1.0$, $m = 0.0$ are shown. $L_x = 2000$ in (a) and 20000 in (b). $L_y = 200$ in both (a) and (b). The data in (a) and (b) have been obtained by averaging over 20 and 6 configurations, respectively.	36
The width of the interface of the Ising model with only nearest-neighbour ferromagnetic interactions (i.e., $m = 0$) are plotted against $L_x^{1/2}$ for three different values of j	37
The width of the interface of the Widom model (i.e., $j \neq 0$, $m \neq 0$) are plotted against $L_x^{1/2}$ for two different values of j ; the corresponding plots for $m = 0$ are also given for comparison.	38
A discrete model SOS interface	43
The equilibrium width W of the interface plotted against $L^{1/2}$ for two different sets of values of the parameters J and K , namely, $J = 1.5, K = 0.0$ and $J = 1.5, K = 1.0$. The lines through the data points are the corresponding best fitted straight lines	47
The width W of the interface plotted against $L^{1/2}$ for the parameter values $J = 0.0$, $K = 3.0$ (full curves) and $J = 0.0$, $K = 1.0$ (dashed curves) at three different times, namely, $t = 1000$, $t = 2000$ and $t = 5000$ Monte Carlo steps. . .	49

3.4	The normal-normal correlation function $N(x)$ for (a) $K = 5.0$, (b) $K = 1.0$. . .	51
3.5	The height-height correlation function $C(x)$ for (a) $K = 5.0$, (b) $K = 1.0$	52
3.6	The correlation function $G(x)$ for (a) $K = 5.0$, (b) $K = 1.0$	53
3.7	The square of the interfacial width plotted against time t for $J = 0.0$, $K = 3.0$. The inset shows the same data plotted against $1/t$ to emphasize the fact that, when $J = 0$, $K \neq 0$, the interfacial width diverges in the limit $t \rightarrow \infty$	60
3.8	The time evolution of the width W of the interface in the RDSOS model in $d = 1$ for $N = 2$ (i.e., $ \Delta h_i = 0, 1$ and 2). The different symbols correspond to different system sizes L : $L = 100(\times)$, $L = 200(*)$, $L = 400(\square)$, $L = 800(\blacksquare)$ and $L = 10000(\circ)$. The dashed line has slope $\beta = 0.25$. The parameter values are $J = 0$, and $K = 1$	63
3.9	Height-height correlation function $c(l)$ for $J = 0$, $K = 1$, $N = 2$. The dashed line is the best fitted curve.	64
3.10	The data of figure 3.9 rescaled according to equation (3.16) The different symbols correspond to different system sizes L : $L = 100(\times)$, $L = 200(*)$, $L = 400(\square)$, $L = 800(\blacksquare)$ and $L = 10000(\circ)$. The slope of the dashed line is $\beta = 0.25$	65
4.1	New moves introduced in reformulated version of Larson model	73
4.2	The width of the interface of the two dimensional Ising model is plotted against $\sqrt{L_x}$ for two different values of J : $J = 1.5(*)$ and $J = 1.8(\square)$	76
4.3	The width of the interface of the Larson model for different concentration (ϕ_a) of amphiphiles for different values of J is plotted against $\sqrt{L_x}$: $J = 1.5$ and $\phi_a = 50\% (*)$, $J = 1.5$ and $\phi_a = 80\%(\square)$, $J = 1.8$ and $\phi_a = 50\%(\blacksquare)$ and $J = 1.8$ and $\phi_a = 80\%(\circ)$	77
4.4	(a) Picture of the interface when no amphiphiles are present. (b) interface after a single spin flip. a denotes water molecule and . denotes oil molecule.	78
4.5	(a) Picture of the interface when one single amphiphile is present. (b) interface after the amphiphile has made a reptation movement. a denotes water molecule and . denotes oil molecule. A and - are the head and tail of the amphiphile molecule respectively.	79
5.1	The equilibrium concentration profile of the hydrophilic heads perpendicular to the air-water interface. The system consists of $30 \times 30 \times 100$ lattice sites and contains a mixture of 405 long amphiphiles of length 17 and 405 short amphiphiles of length 7 equilibrated at temperature $T = 2.5$. The solid lines correspond to the long amphiphiles whereas the dashed lines correspond to the short amphiphiles.	90
5.2	Same as in fig.5.1 except that there are 45 amphiphiles of each type, instead of 405.	91
5.3	Same as in fig.5.2 except that the size of the lattice is $10 \times 10 \times 100$	93
5.4	Same as in fig.5.1 except that the lengths of the long and the short amphiphiles are 17 and 13, respectively.	94
5.5	Same as in fig.5.1 except that the lengths of the long and the short amphiphiles are 10 and 7, respectively.	95

The equilibrium concentration profile of the hydrophilic heads perpendicular to the air-water interface. The system consists of $30 \times 30 \times 100$ lattice sites and contains 810 amphiphiles each of length 17. The system has been equilibrated at temperature $T = 2.5$	96
The equilibrium concentration profile of the hydrophilic heads at $T = 2.5$ perpendicular to the air-water interface in a system consisting of $20 \times 20 \times 100$ lattice sites. The numbers of long and short amphiphiles are, respectively, 300 and 60 in (a), 60 and 300 in (b), 240 and 120 in (c), 120 and 240 in (d); the continuous line corresponds to the long amphiphiles and the dashed line corresponds to the short amphiphiles.	98
Same as in fig.5.7, except that the temperature of the system is $T = 1.0$	99
Same as in fig.4, except that the bending stiffness of each of the amphiphiles is $B = 2$ in contrast to $B = 0$ in fig.5.4.	100
1) The distribution of the sizes of the clusters formed by the monomers belonging to the long and the short amphiphiles in the layers (a) 20, (b) 21, (c) 22 and (d) 23, respectively. The values of all the parameters are identical to those in fig.5.1. The continuous and the dashed lines correspond to the long and short amphiphiles, respectively.	103
1 Same as in fig.5.10, except that the number of both the long and short amphiphiles is 90 and figures (a), (b), (c), (d) correspond to the layers 14, 15, 16 and 17, respectively.	104
2 The Z component of center of mass (Z_{cm}) of the amphiphiles averaged over all the amphiphiles is plotted against MC steps; (a) $N_\ell = N_s = 405$ and $T = 2.5$, (b) $N_\ell = N_s = 45$ and $T = 2.5$, (c) $N_\ell = N_s = 405$ and $T = 1.0$, (d) $N_\ell = N_s = 45$ and $T = 1.0$. The continuous line and white square correspond to the long amphiphiles and the dashed line and black square correspond to the short amphiphiles.	106
3 The averaged radius of gyration (R_g) of the amphiphiles plotted against MC steps; and the parameters and notations for figs.(a), (b), (c) and (d) correspond to those in fig. 5.12.	107
14 The average vertical extension $\langle \Delta Z \rangle$ plotted against MC steps and the parameters and notations for figs (a), (b), (c), (d) correspond to those in fig.5.12.	109
15 The probability distribution of the vertical extensions $P(\Delta Z)$ The parameter values and the notations for figs. (a), (b), (c), (d) are same as in fig.5.12.	110
16 Average orientational order parameter Ψ for different temperatures and surface densities of amphiphiles. The parameter values and notations for figures (a), (b), (c), (d) are same as in fig.5.12.	111
17 Average bond order parameter Φ as a function of bond number. The parameter values and the notations for figures (a), (b), (c), (d) are same as in fig.5.12.	113

5.18	The equilibrium concentration profile of the hydrophilic heads at $T = 2.5$ perpendicular to the air-water interface in a system consisting of $30 \times 30 \times 100$ lattice sites. The numbers of both long and short amphiphiles are 405; (a) $C_\ell = C_s = 10$, (b) $C_\ell = 10$ and $C_s = 1$, (c) $C_\ell = 1$ and $C_s = 10$. The continuous line corresponds to the long amphiphiles and the dashed line corresponds to the short amphiphiles.	114
6.1	Snapshots of micellar aggregates formed by single-chain (a) nonionic surfactants (b) ionic surfactants with $m = 14$ and the density 0.01. The symbols black spheres and grey spheres represent monomers belonging to head and tail, respectively.	121
6.2	Same as in figure 6.1(a) except that now $m = 9$	122
6.3	Snapshots of the micellar aggregates formed by the binary mixture of single chain amphiphiles. Black sphere represent head and grey sphere represent tail.	123
6.4	(a) Snapshots of the vesicles formed by the binary mixture of double chain amphiphiles. Black sphere represent head and grey sphere represent tail.	125
6.4	(b) Snapshots of the vesicles formed by the single component double chain amphiphiles. Black sphere represent head and grey sphere represent tail.	126
6.4	(c) A typical cross-section of the vesicle Black sphere represent head and grey sphere represent tail.	126
7.1	Larson-type models of single-chain, double-chain and gemini surfactants.	132
7.2	Schematic representation of the moves attempted by every surfactant at every MC step.	134
7.3	(a) Variation of CMC of ionic geminis with hydrophobic spacer length; $m = 15$, $T = 2.2$. The symbols \square and \times correspond to $K = 0$ and $K = 2$, respectively. (b) Same as (a), except that $m = 5$. The symbols \triangle and $*$ correspond to $K = 0$ and $K = 2$, respectively. The continuous curves are merely guides to the eye.	141
7.4	Variation of CMC of ionic geminis with tail length at $T = 2.2$ for three different lengths of the hydrophobic spacer, namely, $n = 6, 8, 16$. The straight lines connecting the successive data points are merely guides to the eye.	142
7.5	Variation of CMC of non-ionic geminis with the length of the hydrophobic spacer; $m = 15$ (\square) and $m = 5$ (\triangle) both with $K = 0$ and at $T = 2.2$. The continuous curves are merely guides to the eye.	142
7.6	Snapshots of the micellar aggregates formed by ionic geminis with hydrophobic spacer; $m = 15$, $n = 2$ and $K = 0$ at $T = 2.2$ when the surfactant density is 0.007. The symbols black spheres, dark grey spheres and light grey spheres represent monomers belonging to head, tail and spacer, respectively.	143
7.7	Same as in fig.6, except that $n = 16$ and the density is 0.005.	144
7.8	Snapshots of micellar aggregates formed by single-chain ionic surfactants with $m = 14$ and the density 0.01. The symbols black spheres and grey spheres represent monomers belonging to head and tail, respectively.	145
7.9	Same as in fig.7.6, except that the geminis are non-ionic.	146
7.10	Same as in fig.7.7, except that the geminis are non-ionic.	146

Snapshots of micellar aggregates formed by ionic gemini surfactants with hydrophobic spacer; $m = 5$, $n = 6$ and $K = 0$ at $T = 2.2$ when the surfactant density is 0.005.	147
1 (a) Variation of CMC of ionic geminis with hydrophilic spacer length; $m = 15$, $T = 2.2$. The symbols \square and \times correspond to $K = 0$ and $K = 2$, respectively. .	148
3 Same as fig. 7.6 except that the spacer is hydrophilic.	149
1 Same as fig. 7.7 except that the spacer is hydrophilic.	150
5 Variation of cross-sectional area of isolated individual gemini surfactant with spacer length. The solid line for hydrophobic spacer and broken line for hydrophilic spacer. To give an indication of the accuracy of the data points the error bar of only one point has been shown.	152
6 Variation of vertical extension of individual gemini surfactant with spacer length. The solid line for hydrophobic spacer and broken line for hydrophilic spacer. . . .	154
7 Concentration profiles for tail monomers for three different cases when the number of amphiphiles present in the systems are (i) 500 (solid line), (ii) 100 (broken line) and (iii) 10 (dashed line). (a) hydrophobic spacer (b) hydrophilic spacer.	156
8 Concentration profiles for heads when the number of amphiphiles is 500. Solid line is for hydrophobic spacer and broken line for hydrophilic spacer.	157
9 Snapshots of the gemini surfactants at the interface (a) with hydrophobic spacer and (b) with hydrophilic spacer. The black sphere represent monomers belonging to heads and grey sphere represent monomers belonging to spacers.	159
10 Same as in figure 7.19 except that now the black sphere represents monomers belonging to heads, grey sphere represent monomers belonging to tails and white sphere represent monomers belonging to liaisons.	160
1 (a) A model porous medium (b) A typical cross section Dark grey represent rocks and light grey represents pores.	167
2 Cluster size distribution amphiphiles inside (a) single pore (c) vycor glass. Cluster size distribution for oil inside (b) single pore and (d) vycor glass. The solid line is for temperature 1 and dashed line is for temperature 4.	168
3 (a) A cross section of bicontinuous microemulsion. w denotes water molecule, o denotes oil molecule and H and T denote head and tail of the amphiphile molecule. .	169
3 (b) Micellar aggregates (oil droplet) inside porous medium.	170
4 (a) A cross section of bicontinuous microemulsion. * denotes rocks.	171
4 (b) Micellar aggregates (oil droplet) inside porous medium.	172

List of Tables

3.1	Some of the possible transitions and the corresponding transition probabilities for UDSOS model in $d = 1$	57
3.1	Contd.	58

Chapter 1

Introduction

1.1 The Aim

Soap molecules are common examples of amphiphilic molecules; these not only find wide ranging applications in detergent and pharmaceutical industries, food technology, petroleum recovery, etc. but are also one of the most important constituents of cells in living systems. Therefore, physics, chemistry, biology and technology meet at the frontier area of interdisciplinary research on association colloids formed by surfactants [1–5]. The amphiphiles give rise to many interesting properties of complex (multi-component) fluids containing water and amphiphiles. For example, we know that at ordinary room temperature oil and water do not mix because of the high oil-water interfacial tension. However, the effective oil-water interfacial tension can be reduced to almost vanishingly small value by adding soap to the otherwise immiscible binary mixture of oil and water. That is why amphiphilic molecules are often referred to as **surfactants** (surface active agents).

Despite of decades of research efforts, a clear microscopic understanding of the behaviour of fluids containing amphiphilic molecules has not yet emerged. In most practical applications, these amphiphilic systems are so complex that it is difficult to calculate any physical property of the system analytically starting from a microscopic (molecular) description which includes all the details of these systems without making drastic approximations. Computer simulation of microscopic models can provide valuable insights into the bulk and interfacial properties of the amphiphilic systems, such as, the physics of the formation of supramolecular aggregates and their morphologies as well as the influence of these on the macroscopic physical properties. In order to gain insight into the physical origin of some of these bulk and interfacial properties, in this work we develop, generalize and/or extend realistic, but simple microscopic models of complex (multi-component) fluids containing amphiphilic molecules and water. We check the reliability of our models by comparing the results of computer simulation with known experimental results and, we predict new phenomena by carrying out novel computer experiments. Since Monte Carlo simulation is more efficient than Molecular Dynamics (MD) method for the equilibration of such systems, we compute most of the quantities of interest by MC simulation.

The Amphiphilic Molecules and Their Supramolecular Aggregates

The “head” part of amphiphilic molecules consist of a polar or ionic group. The “tail” of many amphiphiles consist of a single hydrocarbon chain whereas that of some other amphiphiles, phospholipids, are made of two hydrocarbon chains both of which are connected to the

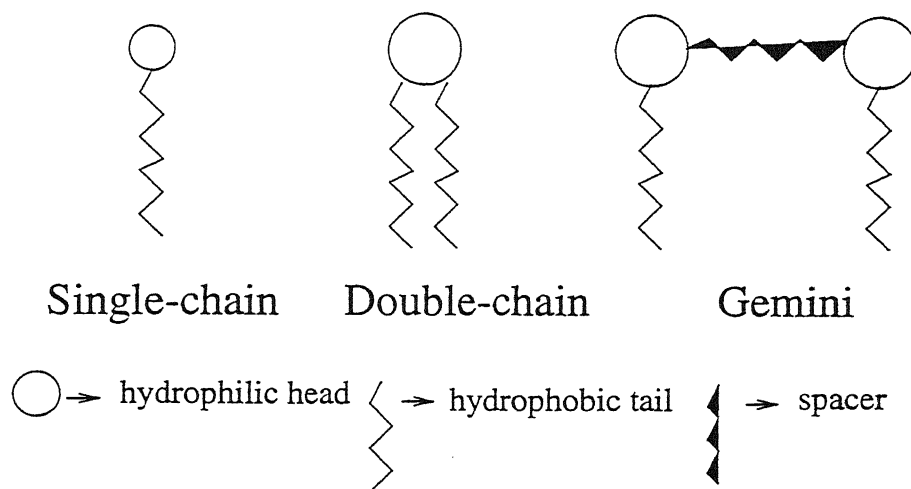


Figure 1.1: Different types of amphiphiles.

same head [6, 7, 9, 10]. Yet another class of amphiphiles, called *gemini* amphiphiles [11–14], consist of two single-chain amphiphiles whose heads are connected by a “spacer” chain and, hence, these “double-headed” amphiphiles are sometimes also referred to as “dimeric surfactants” [15, 16]. Some common example of the different amphiphiles are as follows: Single chain: Sodiumdodecylsulphate $\{Na^+SO_4^- \cdot (CH_2)_{11}CH_3\}$, Double chain: Dihexadecyl dimethylammonium bromide $\{C_{16}H_{33} \cdot N^+(CH_3)_2Br^- \cdot C_{16}H_{33}\}$, and Gemini surfactants: $\{Br^-, m - C_{16}H_{33} \cdot NMe_2^+ - (CH_2)_n - N^+Me_2 - m - C_{16}H_{33}, Br^-\}$ where n is the length of the spacer. Different types of model amphiphiles are shown in figure 1.1

When put into an aqueous medium, the “heads” of the amphiphiles like to get immersed in water and, hence, called “hydrophilic” while the tails tend to minimize contact with water and, hence, called “hydrophobic” [10]. The spacer in gemini amphiphiles is usually hydrophobic. However gemini amphiphiles with hydrophilic spacers have also been synthesized [17]. Therefore, in aqueous medium, amphiphiles form a variety of “*self assemblies*” (supramolecular aggregates),

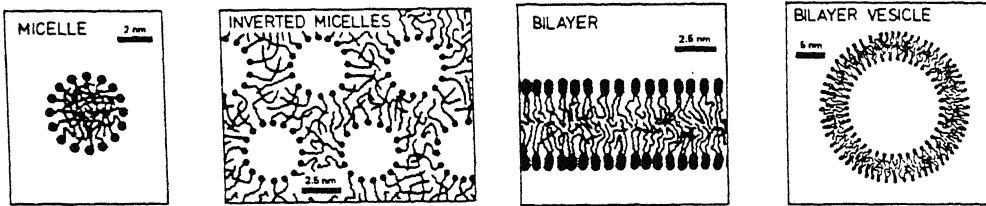


Figure 1.2: Different structures formed by amphiphiles in aqueous medium (after[6]).

monolayer and bilayer membranes, micelles, inverted-micelles, vesicles, etc. (figure 1.2). By varying the chemical structure, size, shape and flexibility of the amphiphiles, the relative concentration of water, surfactant (and other components in the fluid), temperature and external pressure the system moves from one region of the phase diagram to another. A brief overview of experimentally observed phase diagram and the associated physical properties of binary and ternary fluid mixtures, which contain amphiphiles, is given in the next section. Many attempts have been made to develop simple models to describe the *generic* behaviour of these systems. In section 1.4 a short summary of the theoretical and computational techniques used to model these systems is presented.

Phase Diagrams and Physical Properties

Various experimental techniques have been used to study these systems; these include freeze-fracture electron micrograph, X-ray, light scattering and neutron scattering experiments, nuclear magnetic resonance, transmission electron microscopy, measurement of conductivity and rheo-

logical measurements, e.g. measurement of viscosity.

1.3.1 Interfacial properties

One of the most spectacular effects of the amphiphiles on a mixture of oil and water is that a small amount of amphiphiles can reduce the effective interfacial tension between water and oil by several orders of magnitude. A particularly clear example is described below. Experiments were performed on a mixture of ionic amphiphile (Sodiumdodecylsulphate), water, salt and organic solvents [21]. The system was observed as the concentration of salt was increased and the system moved from (1) a mixture of organic phase and oil/water microemulsion to (2) a mixture of organic phase, a middle phase microemulsion and an aqueous phase and finally to (3) a mixture of water/oil microemulsion and an aqueous phase. It was observed that at the critical end-point at which the middle phase and the water-rich become identical, the interfacial tension between them goes to zero. The interfacial tension between the middle and the oil-rich phase also vanishes at another critical endpoint, where the middle and oil-rich phase are identical. Since the oil-water interfacial tension (which is only defined in the region of three phase coexistence) must always be less than the sum of the interfacial tensions between oil-rich and middle phases and the aqueous and middle phases, the oil-water tension was dramatically reduced, by 3 orders of magnitude in this case.

1.3.2 The Phase Diagram

- Phases of ternary systems:

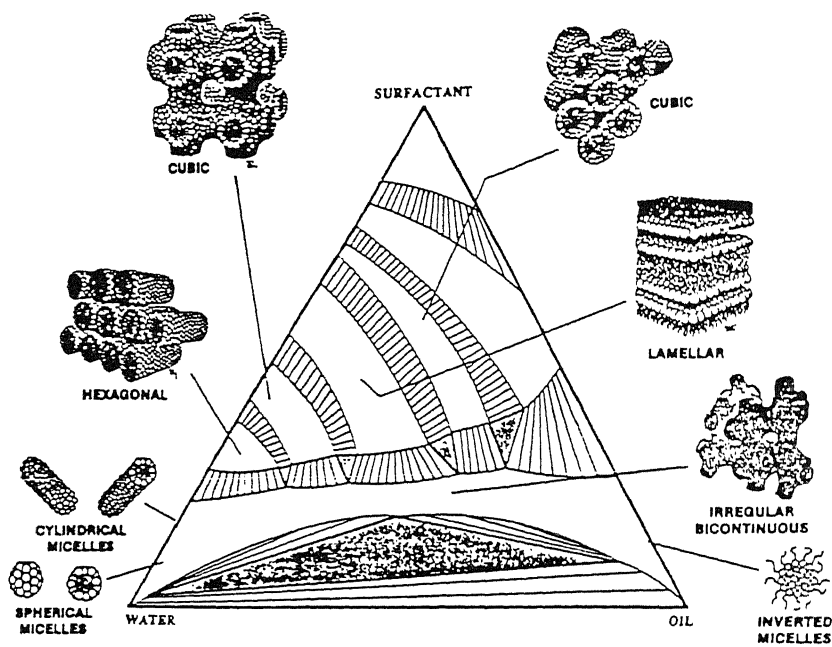


Figure 1.3: Schematic diagram illustrating the phase behaviour of real surfactant-oil-water systems (after [43]).

A schematic phase diagram of ternary system consisting of oil, water and surfactant has been shown in figure 1.3. Ternary mixtures of oil, water and surfactants, where the concentration of amphiphiles is low, are called **microemulsions** [9]. Suppose the volume fraction occupied by oil is very small compared to that occupied by water. Then at the microscopic level, droplets of oil are dispersed in water [10, 18] and the amphiphiles form a monolayer at the oil-water interface. The amphiphiles arrange themselves, at the oil-water interface in such a manner that the hydrophilic heads are in contact with water and the hydrophobic tails are in oil. Conversely, at low amphiphile and low water concentration, one observes 'droplets' of water dispersed in oil, coated by a monolayer of amphiphiles with the heads pointing into the centre (water) and the tails pointing outwards (oil) [10, 18]. These systems are often called **globular microemulsions** [18]. Schematic diagrams of both structures are shown in figures 1.4(a) and (b).

In contrast to emulsions, which are dispersions of particles of typical size 10\AA to 10000\AA in water globular microemulsions are dispersion of droplets of typical size 100\AA [26] in water. Consequently, at the macroscopic level microemulsions are transparent, in contrast to turbid emulsions, as light does not get scattered by the droplets whose size is much smaller than the wavelength of light.

When the concentrations of oil and water are comparable and much higher than that of the amphiphiles, an interconnected network of oil and water domains is formed with a monolayer of amphiphiles distributed at the oil-water interface [18]. This phase is usually called the **bicontinuous microemulsion** [25]. A bicontinuous microemulsion is shown schematically in Fig. 1.4(c); the monolayer at the interface between oil and water in such a phase is an example of amphiphilic monolayer *membranes*.

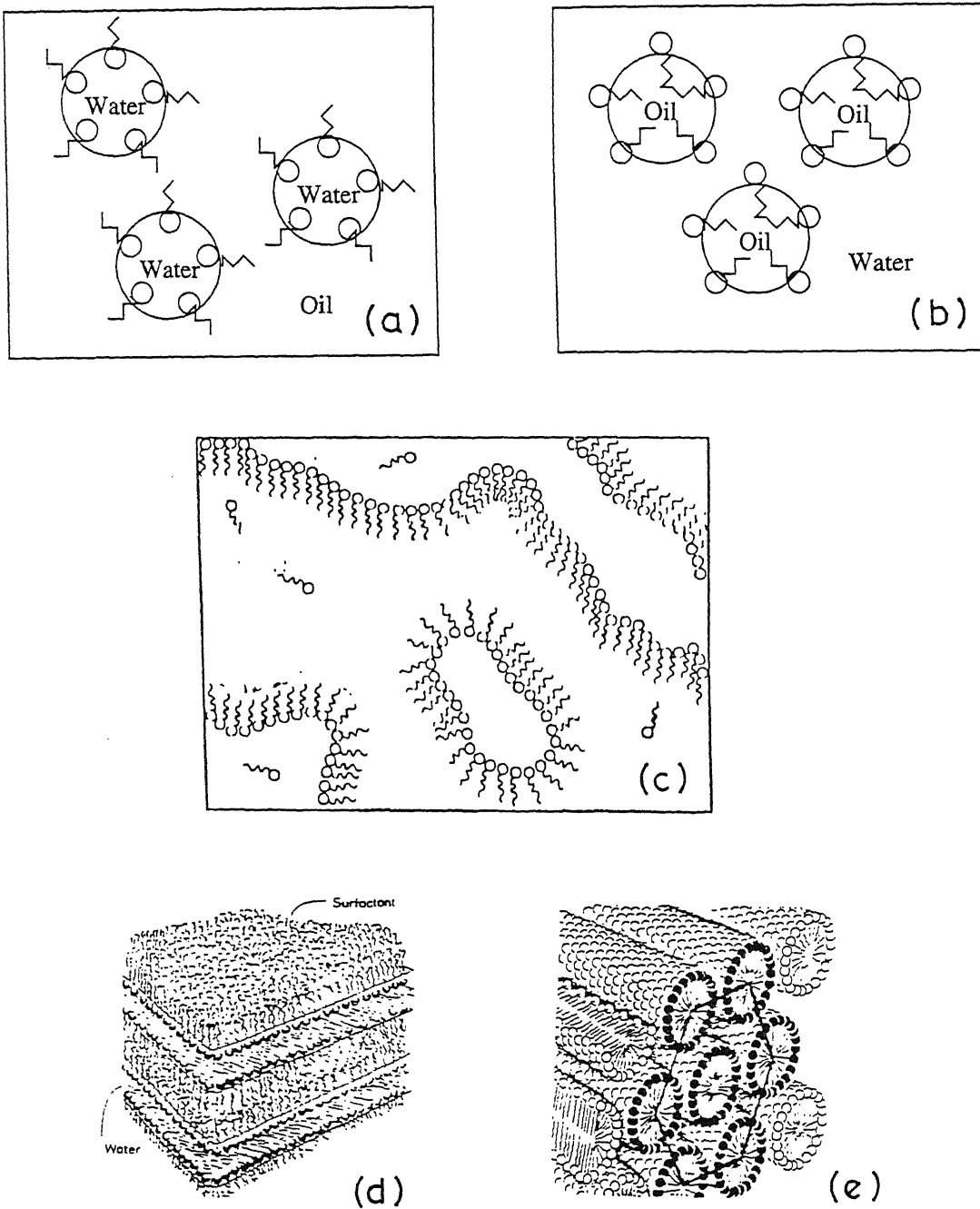


Figure 1.4: Different structures formed by amphiphiles in a mixture of oil-water-amphiphile system. Figure (d) and (e) after[2] and figure (c) after[19].

As the concentration of amphiphiles is increased, **liquid-crystalline phases** with long-range periodic order are observed [28, 29]. Similar phases have been observed in liquids [27] consisting of small non-spherical molecules and hence the name. The phases observed are the **lamellar phase** (Fig. 1.4(d)), the **hexagonal phase** (Fig. 1.4(e)), the **cubic phase** and the **inverted hexagonal phase** [28]. In the lamellar phase, flat or *rippled* layers of water and oil are separated by monolayers of amphiphiles. In the hexagonal phase, cylinders of oil domains, coated with amphiphiles, are so arranged that the centers of the circular cross sections of the cylinders form a (quasi-) two dimensional triangular lattice. The inverse hexagonal phase is obtained from the hexagonal phase by interchanging water and oil. Finally, in the cubic phase the centers of the spheres of amphiphile-coated oil droplets are arranged so as to form a three dimensional body-centered cubic lattice.

It is worth mentioning that the ternary mixture exhibits a disordered fluid phase at sufficiently high temperature.

•Phases of binary systems:

Binary mixtures of water and amphiphiles also have a rich and varied phase behaviour. At *very* low amphiphile concentrations, hardly any aggregation of the amphiphiles takes place; isolated single amphiphiles are uniformly distributed in the mixture. Above a particular concentration, called the **critical micelle concentration (CMC)** [10], the amphiphiles form supramolecular aggregates which are called *micelles*. (Actually CMC is not a single concentration but a very narrow range of concentration and, therefore, it may be more appropriate to call it the characteristic micellar concentration). Just above the CMC one finds micelles dispersed in water. There is also a 'transition' from a micellar to a condensed phase at a particular temperature called the

condensation transition temperature. Below this temperature, the amphiphiles are in a condensed phase where they form one large cluster and above this temperature, they form stable micelles of varying sizes [78].

Ordered liquid crystalline phases have also been observed [30, 31]. With the increase of amphiphile concentration, the progression is usually hexagonal, cubic, lamellar and inverted hexagonal in that order. It should be noted that *all* of these phases are *not* always present for particular amphiphilic systems. Disordered phases similar to the bicontinuous microemulsion have also been found. This disordered phase is often called the L_3 or **sponge phase** [32]. This L_3 phase is therefore made up of sheets of amphiphiles that are examples of amphiphilic **bilayer membranes**(see Fig.1.2).

Although the generic behaviour described above is common to most types of amphiphiles, the shape, size, flexibility, chemical structure, etc. of the amphiphiles are known to play a part in determining the details of the phase diagram as well as the morphology of the supramolecular aggregates. Surfactants can also have their behaviour affected by the addition of a fourth component: salt. Ionic amphiphiles have an electrostatic repulsion between the heads which becomes screened in the presence of counterions when salt dissolves in water. Therefore one finds that a quaternary system transforms from oil-in-water to bicontinuous and finally water-in-oil microemulsion as the concentration of salt is increased [20].

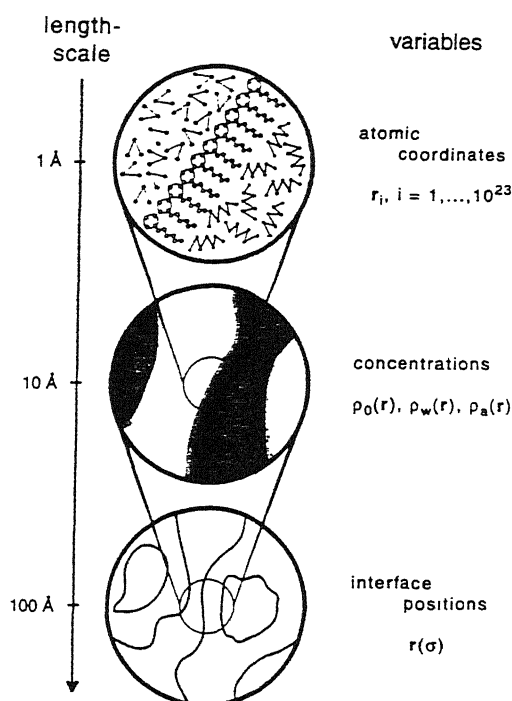


Figure 1.5: Theoretical description of amphiphile molecules on different length scales (after[19]).

1.4 Models describing Amphiphilic Systems

The theoretical description of amphiphilic systems depends on the length scale on which the phenomena are to be explained and predictions to be made, and on how much detail of information is expected to be extracted from the model. This has led to three different classes of models (see fig 1.5), which have been used in the last few years to study self-assembling amphiphilic systems [2].

1.4.1 Microscopic models

The natural starting point for a study of complex fluids is a microscopic model, in which the position of all the atoms of different molecules and their microscopic interactions are taken into account, as shown schematically in Fig 1.5. Such models have been used to study the structure of single micelles [95], but unfortunately they are too complex to calculate the macroscopic properties of microemulsions etc. Thus, the models have to be simplified considerably to make them tractable for both approximate analytical calculation and Monte Carlo simulations. These simplified models are most often formulated on a lattice in the spirit of lattice gas models. The models which have been studied range from the Ising model with next-nearest-neighbour and multispin interactions [35, 101, 104, 105], and the Blume-Emery-Griffiths (BEG) model [36] with three spin interaction [97, 37] to models in which the amphiphile is described by a vector [64, 38] or by a pair of charges, which are equal in magnitude but opposite in sign [48, 49] or by a short polymer chain [41–47, 60].

The Widom Model

The simplest lattice model is the Widom model [35] where the amphiphile, water and oil molecules all occupy bonds on a lattice, which is assumed to be square in two dimensions or a simple cubic in three dimensions. Each site of the lattice is occupied by classical Ising *spins* which can take one of two values, $S_i = \pm 1$. Without loss of generality, water molecules occupy a bond between two up spins, oil molecules occupy bonds between two down spins and amphiphile molecules occupy bonds between one up and one down spin, the head obviously corresponding to the up spin. The Widom Model is illustrated in Fig. 1.6.

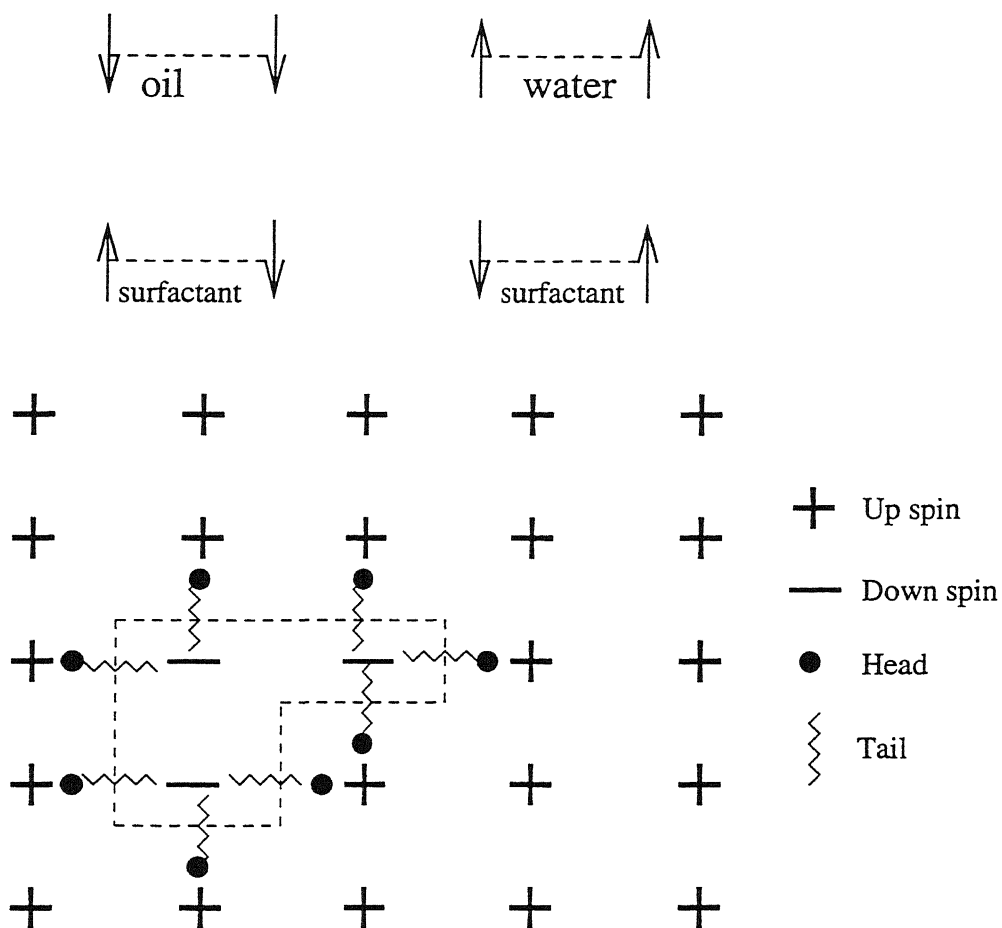


Figure 1.6: A typical configuration of Widom model.

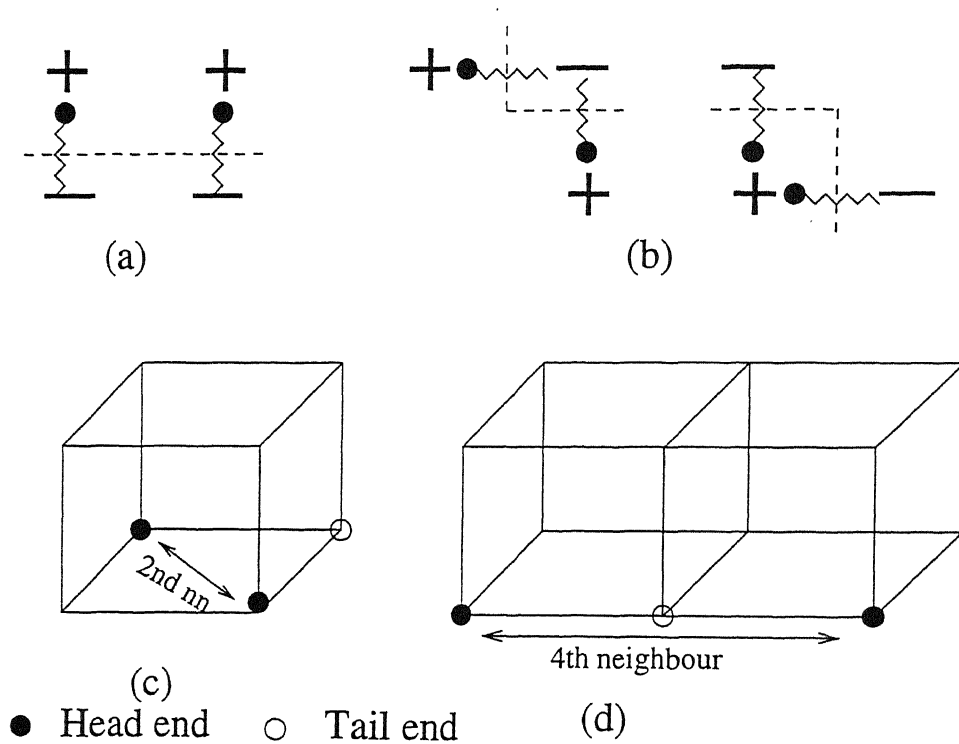


Figure 1.7: Origin of bending and different neighbors in Widom model

The effective Hamiltonian is,

$$H = -J \sum_{\langle ij \rangle}^{nn} S_i S_j - M \sum_{\langle ik \rangle}^{nnn} S_i S_k - 2M \sum_{\langle ik \rangle}^{nnnn} S_i S_k \quad (1.1)$$

where *nn* refers to nearest neighbours (i.e. 1st neighbour), *nnn* next nearest neighbours (i.e. 2nd neighbour, Fig. 1.7(c)) and *nnnn* is the next to next nearest neighbour (4th neighbour in case of simple cubic lattice, Fig. 1.7(d), and 3rd neighbour in case of square lattice). *J* is positive (ferromagnetic) and *M* is negative (antiferromagnetic). The farther neighbour interaction was included to take into account the bending of the amphiphilic molecule at the interface. Fig 1.7(a) represent a flat interface. On the other hand whenever heads or tails of two amphiphilic molecules meet at the same lattice point bending of the interface occurs (Fig. 1.7(b)).

The main advantage of this model is that it is simple; in fact it is essentially an Ising model with not only *nn* interactions but also farther-neighbour interactions of specific type. The Widom model can account for droplet and lamellar phases and a phase corresponding to bicontinuous microemulsion. More details of the model and results will be discussed in chapter 2.

The Three Component Model

Here oil, water and amphiphile all occupy *sites* on a lattice and are represented by the three states of a classical spin 1, where the spins can have a value $S_i = 0, \pm 1$. The tendency of amphiphiles to go to the oil-water interface can be included by the addition of a three-body interaction in the Blume, Emery and Griffiths (BEG) model [36], [39]. The effective Hamiltonian is

$$H = - \sum_{\langle ij \rangle} [JS_i S_j + KS_i^2 S_j^2 + M(S_i^2 S_j + S_i S_j^2)] - L \sum_{\langle ijk \rangle} S_i (1 - S_j^2) S_k, \quad (1.2)$$

where $\langle ij \rangle$ is a sum over nearest neighbours and $\langle ijk \rangle$ is a sum over all sets of three connected sites. The three body interaction is antiferromagnetic between sites i and k , and favours lamellar configuration. Lamellar and disordered phases are observed in this model.

The Alexander Model

In the Alexander model [40], which is a mixed site-bond model, oil and water occupy sites of a lattice. The “water-loving” head of each of the amphiphiles is assumed to be identical to a water molecule and the “oil-loving” tail of the amphiphiles is assumed to be identical to an oil molecule. Therefore, every lattice site is occupied by either water or oil molecule. Those pair of unlike nearest-neighbour sites (i.e., oil-water nearest-neighbour pairs) are identified as amphiphilic molecule which are connected by a rigid bond. Therefore this model is often referred to as the “decorated spin 1/2” model. The Hamiltonian of the system is taken to be [50, 51]

$$H = -h \sum_i S_i - J \sum_{\langle i,j \rangle} S_i S_j - \mu \sum_{\langle i,j \rangle} \tau_{ij} - V \sum_{\langle ij,ik \rangle} \tau_{ij} \tau_{ik} - V_1 \sum_{\langle\langle ij,ik \rangle\rangle} \tau_{ij} \tau_{ik} - J_1 \sum_{\langle i,j \rangle} S_i S_j \tau_{ij} \quad (1.3)$$

where $S_i = \pm 1$ occupy sites i of a d -dimensional, hypercubic lattice and $\tau_{ij} = 0, 1$ occupy links $\langle ij \rangle$; $\langle i, j \rangle$ are distinct, nearest-neighbor pairs of sites, and $\langle ij, ik \rangle$ and $\langle\langle ij, ik \rangle\rangle$ are, respectively, distinct pairs of links that meet at sites i at 90° and 180° . The field h is related directly to the difference between the chemical potentials of oil and water; the exchange interaction J is chosen to be positive so that it favours the phase separation of oil and water. $\tau_{ij} = 1(0)$ denotes presence (absence) of a surfactant molecule on link $\langle ij \rangle$, μ is the chemical potential of surfactant molecules, and V and V_1 parametrize the interactions of these molecules. J_1 is the strength of the surfactant-mediated interaction between nearest-neighbour spins. The phase diagram of this model has also been investigated exhaustively.

Vector Models

The microscopic models we have discussed so far do not include the orientational degrees of freedom of the amphiphile molecules and water and oil molecules are taken to be structureless. Without taking into account the orientational degrees of freedom of the amphiphile molecules and by treating water as structureless these models miss orientational bonding effects between water molecules and between water and amphiphile molecules. There are vector models where the amphiphile and/or water molecules are given orientations to more realistically simulate the directional nature of the interactions between the amphiphile and solution [64].

The Larson Model

The Larson model, which was introduced originally by Larson and co-workers [41–44] and subsequently reformulated by Jan, Stauffer and others [45, 46], is an attempt towards more realistic modelling by taking into account the conformations of amphiphiles as polymer chains rather than merely single units.

We first describe the original version of the model, as formulated by Larson and coworkers. The Larson model is simulated on a $L \times L$ square lattice (in $2d$) or $L \times L \times L$ cubic lattice (in $3d$). Each oil and water molecule can occupy one site of the lattice while the amphiphile, which is denoted [41] by $\mathcal{T}_m\mathcal{H}_q$, occupies $(m + q)$ neighbouring sites connected by rigid bonds with the head containing q sites and the tail m sites. All sites of the lattice are occupied. Amphiphilic chains can not break but bend and move in the solvent. Each head unit is effectively identical to a water molecule so far as its interactions with other molecules are concerned, and similarly, from the point of view of inter-molecular interactions, each tail unit is effectively identical to an oil molecule. Each site of the lattice interacts with nearest neighbours and next nearest neighbours.

The effective Hamiltonian can therefore be given by

$$H = - \sum_{ab} \sum_{ij} E_{ab} P_a^i P_b^j \quad (1.4)$$

where $\langle ij \rangle$ is over nearest and next (diagonally) nearest neighbours and the sum $\langle ab \rangle$ is over the pairs of sites, 'water' or 'oil', of monomers. The strength of the interactions with nearest and next nearest neighbours are equal. The occupation variable, $P_a^i = 1$ if a molecule of type a is on site i and is 0 otherwise. There are periodic boundary conditions in all directions. The energy parameters, E_{ww} , E_{wo} and E_{oo} , are between water-water, water-oil and oil-oil respectively. One can define $\beta = (2E_{wo} - E_{oo} - E_{ww})/2k_B T$ which is the only interaction parameter in the model. It may be considered a dimensionless inverse temperature.

A typical amphiphilic molecule with $q = 1$ and $m = 8$ is shown in Fig. 1.8(a). The system is allowed to change its configuration in three ways. First, a water and oil molecule can change position irrespective of how far apart they are, second, an amphiphile chain can move by *reptation* i.e. it slithers along its length like a reptile [63], and the chain can *twist* by forming a kink when one of its sites moves to a diagonal neighbour; these 'moves' are shown in Fig. 1.8(b). The chains are self-avoiding, i.e. an amphiphile is not allowed to intersect itself or other amphiphiles.

The system evolves using a Metropolis algorithm as follows: one of the allowed moves described above is 'attempted' and the corresponding change in energy, ΔE , that would be used by implementing the attempted move, is calculated using the Hamiltonian in equation (1.4). If $\Delta E \leq 0$, then the move is accepted with probability unity and if $\Delta E > 0$ then it is accepted with probability $p = \exp(-\Delta E/k_B T)$. This procedure was defined by Larson [41] as Monte Carlo Step. Larson performed simulations on lattices of size 40×40 and 100×100

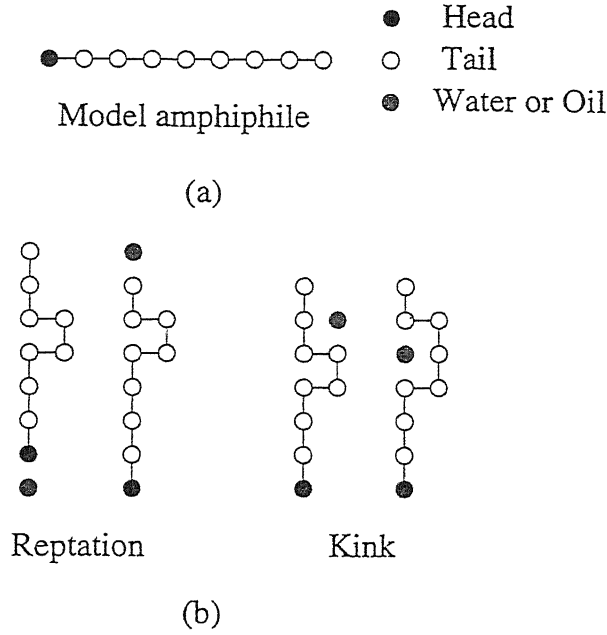


Figure 1.8: (a) A model amphiphilic molecule, (b) Allowed moves for amphiphiles.

lattices [41] in $2d$ and on $20 \times 20 \times 20$ lattices [42] in $3d$.

The model has been used extensively by Larson [41–44] to study the phase behaviour of ternary mixtures for different amphiphiles, $\mathcal{T}_1\mathcal{H}_1, \mathcal{T}_2\mathcal{H}_2, \dots, \mathcal{T}_4\mathcal{H}_4$. The simulations were performed at a temperature corresponding to $0.6T_c$ where T_c is the critical temperature below which oil and water, in the absence of amphiphile, phase separate on this lattice. This choice of temperature corresponds to $w = 0.5$ in $2d$ and $w = 0.1538$ in $3d$.

Three-phase coexistence was observed in all cases except for the amphiphiles $\mathcal{T}_1\mathcal{H}_1$. Lamellar phases, hexagonal phases and cubic phases were observed. For example, in the case $\mathcal{T}_4\mathcal{H}_4$, for amphiphile concentrations of $\phi_a = 30 - 40\%$, close-packed spherical structures are formed while for concentrations $\phi_a = 50 - 60\%$ hexagonally packed cylinders were formed and at concentration $\phi_a = 65 - 85\%$ co-existence of cylinders and lamellae and above $\phi_a = 85\%$ predominantly lamellar

ctures were observed. The microstructural transitions from less ordered to more ordered
ses as the temperature was lowered was also studied. It was also observed for the T_4H_4
cture that as the concentration of amphiphile was increased, the shape of micelles changed
n spherical to cigar-shaped to 'worm-like'. It was observed that head-tail asymmetry such as
 T_4H_3 increased the tendency to form cigar-shaped or 'worm-like' micelles.

Later Jan, Stauffer, and collaborators [45–47] reformulated the Larson model in terms of
g-like spin variables, in the same spirit in which a large number of simpler lattice model had
n formulated earlier for the convenience of calculation. This modified larson model will be
ussed in chapter 4 of the thesis.

Molecular models

The Shell Amsterdam group [60] has developed a molecular model of the amphiphiles in
tion in which water and oil molecules are represented by spherical monomers interacting via
ncated Lennard-Jones potentials in the *continuum*. An amphiphile is modelled as a linear
in of water and oil molecules. The forces are given by the gradient of the potentials and
numerically integrating Newton's second Law - the system evolves in real time towards its
ilibrium state. Equilibrium configurations are calculated using the molecular Dynamics (MD)
ulation technique. The advantage of this method is that the simulation results can be related
the measured parameters for the real physical system. The disadvantage of this approach
hat it is computationally very expensive, requiring long execution times. With present day
puters, one can normally only simulate nanoseconds making equilibrium configurations ex-
nely difficult to calculate. Using this model, Smit and co workers have studied some particular
sical realizations such as the clustering of amphiphiles at the oil-water interface. Because MD

is computationally expensive, they did not fully explore the phase diagram.

1.4.2 Landau-Ginzburg models

On a length scale somewhat longer than the microscopic one, a ternary amphiphilic system can be described by the local concentrations $\rho_o(r)$, $\rho_w(r)$ and $\rho_{amp}(r)$ of the three species of molecules, namely, oil, water, and amphiphile (see Fig. 1.5). The interaction between the molecules is now described by free energy functional $F[\rho_o, \rho_w, \rho_{amp}]$. This functional can either be obtained from a microscopic model by integrating out degrees of freedom on smaller length scales, or from symmetry considerations. The construction of Landau-Ginzburg model depends on the range of phenomena the model is expected to describe. If we want to study only ternary amphiphilic systems for which the water and oil concentration do not differ enormously, then a model with a single scalar order parameter is sufficient [65, 67]. On the other hand, if the whole range of concentrations between the binary and the ternary system is to be investigated, a model with two or three order parameter is required [68].

The Landau-Ginzburg free energy functional with a single scalar order parameter $\phi(r)$ is given by [65]

$$F(\Phi(r)) = \int d^3r [c(\nabla^2\Phi)^2 + g(\Phi)(\nabla\Phi)^2 + f(\Phi) - \mu\Phi] \quad (1.5)$$

with $g < 0$ and $c > 0$. The negative g tends to create the interface and positive c stabilize the system. Here the order parameter $\Phi(r)$ describes the difference between the local densities of oil and water and μ is the chemical potential difference between oil and water. The amphiphile concentration does not appear explicitly in the free energy functional and should be considered

have been integrated out [96]. In order to account for the three phase coexistence possible in this ternary system, Gompper and Shick imposed the condition that the function f must be chosen such a way as to have three minima. In the absence of amphiphile molecules $f(\Phi)$ has two minima at $\Phi = \Phi_o$ and $\Phi = \Phi_w$, which describe the oil rich and water rich phases, and $g(\Phi)$ is a positive constant. When amphiphile is added, a third minimum of f appears at $\Phi = 0$, which describes the disordered microemulsions phase.

The free energy functional with two order parameter can be written as [66]

$$F[\Phi(r), \rho(r)] = \int d^3r [c(\nabla\Phi)^2 - r_o\Phi^2 + u\Phi^4 + g\rho^2\Phi^2 + a\rho^2 - \mu\rho - (\Delta\mu)\Phi + F_s] \quad (1.6)$$

where $\rho(r)$ is the density of the surfactant molecules at the location r . c, r_o, u, g, a and μ are phenomenological coefficients. μ is the chemical potential of the amphiphilic molecules, whereas $\Delta\mu$ is the difference of the chemical potentials of water and oil. Cubic terms have been omitted from above equation; however in more general situations such terms may play some role. g is the strength of the coupling between two fields ρ and Φ . The surfactant property of the amphiphiles is taken into account through

$$F_s = s \int d^3r \rho (\nabla\Phi)^2 \quad (1.7)$$

A more detailed Landau-Ginzburg model with two order parameters was introduced by Chen et al. [69] for studying the equilibrium phase diagram.

Finally models can be constructed in which both the density and the orientational degrees of amphiphile are taken into account and in that case we have three order parameters in the Landau-Ginzburg free energy functional [68].

1.4.3 Interface/Membrane models

On a length scale which is even longer than that in the Landau-Ginzburg formulation, the detailed structure of the amphiphilic monolayer at the interface between oil and water (or that of a bilayer in water) can no longer be resolved. The interfaces (or “membranes”) are now described as two-dimensional mathematical surfaces. By studying the “out-of-plane” thermal fluctuations of these amphiphilic membranes, the membrane theories provide a universal description for ternary and binary mixtures. At this level of description, the effects of the amphiphilic molecules enter only through the surface tension and the other elastic constants, e.g., the bending rigidity, of these surfaces.

The nature of the out-of-plane thermal fluctuations of interfaces and amphiphilic membranes as well as their effects on the equilibrium conformations have been investigated extensively over the last ten years [106–108, 5, 109–111]. In the case of fluid-fluid interfaces in the absence of amphiphiles, these fluctuations are controlled by the interfacial tension. On the other hand, the effective interfacial tension of amphiphilic membranes can be vanishingly small and, therefore, their out-of-plane thermal fluctuations are controlled by the bending rigidity [111]. The interfaces can exhibit a transition from a “smooth” phase to a “rough” phase at a temperature known as the roughening temperature [112, 114]. Similarly, depending on the nature of the in-plane ordering, an amphiphilic membrane can exhibit a *crumpled* phase at sufficiently high temperatures. In the following we examine the different definitions of crumpling.

For a two dimensional fluid membrane embedded in a three dimensional space, bending deformation are expressed in terms of curvature. We define a unit normal $\hat{n}(x, y)$ to the membrane

a point (x, y) with height z . The x -component and y -component of the normal being given $n_x = -(\frac{\partial z}{\partial x})$ and $n_y = -(\frac{\partial z}{\partial y})$. The orientational correlation between the normals to the membrane at two different points decays exponentially and is given by

$$\langle n(0) \cdot n(r) \rangle \sim e^{-|r|/\zeta_p}, \quad (1.8)$$

where ζ_p is the persistence length and is given by [26]

$$\zeta_p \simeq a \exp(4\pi K/3k_B T). \quad (1.9)$$

If the length is smaller than ζ_p , the membrane is effectively flat, i.e. its normals at different points are well-correlated. Beyond the length ζ_p , the normals at different points become effectively uncorrelated, and the membrane is said to be crumpled.

A second alternative, but equivalent, definition of crumpling is due to Helfrich [108, 111] which we outline below. Having defined the normals one can define two principal curvatures at any point on the surface $c_1 = (\frac{\partial n_x}{\partial x})$ and $c_2 = (\frac{\partial n_y}{\partial y})$. The curvature elastic energy density can be expressed as a function of the two principal curvatures and is given by [108, 111]

$$H = K/2(c_1 + c_2)^2 - Kc_0(c_1 + c_2) + K_G c_1 c_2, \quad (1.10)$$

where c_0 is the spontaneous curvature, $K(> 0)$ is the modulus of bending rigidity, and K_G is the elastic modulus of Gaussian curvature $c_1 c_2$. This Hamiltonian is rotationally invariant in the $x-y$ plane. Let $A = L^2$ be the basal area of the membrane in the $x-y$ -plane. The instantaneous configuration of the membrane is defined by the local height variable $u(x, y)$ and $u(x, y)$ obey the periodic boundary condition. Fourier expansion of $u(x, y)$ leads to

$$u(\vec{r}) = \sum_{\vec{q}} [a_{\vec{q}} \cos(\vec{q} \cdot \vec{r}) + b_{\vec{q}} \sin(\vec{q} \cdot \vec{r})] \quad (1.11)$$

Because of the periodic boundary condition, allowed values of q are given by $(q_x, q_y) = (2\pi/L)(m, n)$ where the integers m and n cannot vanish simultaneously. Moreover, the sum is to be carried over only half the q - plane. For weakly deformed membrane ($|\nabla u|$) one has

$$c_1 + c_2 = \sum_{\vec{q}} q^2 [a_{\vec{q}} \cos(\vec{q} \cdot \vec{r}) + b_{\vec{q}} \sin(\vec{q} \cdot \vec{r})] \quad (1.12)$$

The total bending energy is given by

$$E_c = \frac{1}{4} K \sum_{\vec{q}} q^4 (a_{\vec{q}}^2 + b_{\vec{q}}^2) A \quad (1.13)$$

The absorbed membrane area per unit basal area is $1/2(\nabla u)^2$ to lowest order in ∇u . Integrating the local values gives the total absorbed area

$$\delta_q A = \frac{1}{4} \sum_{\vec{q}} q^2 (a_{\vec{q}}^2 + b_{\vec{q}}^2) A \quad (1.14)$$

In the presence of non-vanishing surface tension σ the total energy of thermal undulation is given by

$$E = \frac{1}{4} \sum_{\vec{q}} (\sigma q^2 + K q^4) (a_{\vec{q}}^2 + b_{\vec{q}}^2) A \quad (1.15)$$

From equipartition theorem of energy the mean square amplitude is given by

$$\langle a_{\vec{q}}^2 \rangle = \langle b_{\vec{q}}^2 \rangle = \frac{2k_B T}{(\sigma q^2 + K q^4) A} \quad (1.16)$$

The sum in the above equation (1.15) can be replaced by integration in the q plane to obtain the average mean square amplitude of undulation and is given by

$$\langle u^2 \rangle = \int \langle |u_{\vec{q}}|^2 \rangle d\vec{q} \quad (1.17)$$

$$= \int (1/2) \langle a_{\vec{q}}^2 \rangle d\vec{q} \quad (1.18)$$

$$= \frac{2k_B T}{4\pi} \int \frac{q dq}{(\sigma q^2 + K q^4)} \quad (1.19)$$

for $K = 0, \sigma \neq 0$ (only interfacial tension)

$$\begin{aligned} \langle u^2 \rangle &= \frac{k_B T}{2\pi\sigma} \int \frac{dq}{q} \\ &= \frac{k_B T}{2\pi\sigma} \ln(L/a) \end{aligned} \quad (1.20)$$

in this case the membrane is logarithmically rough. For $\sigma = 0, K \neq 0$ (only bending rigidity)

$$\begin{aligned} \langle u^2 \rangle &= \frac{k_B T}{2\pi K} \int \frac{dq}{q^3} \\ &= \frac{k_B T}{4\pi K} (L/a)^2 \end{aligned} \quad (1.21)$$

The crumpling of the membrane can be seen from the excess area δA per unit basal area A .

In the absence of interfacial tension ($\sigma = 0$) from the equations (1.14) and (1.16) we have

$$\frac{\delta A}{A} = \frac{k_B T}{4\pi K} \ln(L/a). \quad (1.22)$$

So in the thermodynamic limit $L \rightarrow \infty$, $\langle \delta A \rangle / A \rightarrow \infty$ i.e. (excess area/basal area)

diverges and the membrane is said to be crumpled. Roughly the length scale at which $\langle \delta A \rangle$

becomes of the order of A , the membrane loses its orientation and is said to be crumpled. This length can be

identified with the persistence length ζ_p and solving eq. (1.22) we find

$$\zeta_p = a \exp\left[\frac{4\pi K}{k_B T}\right] \quad (1.23)$$

where K is the bending rigidity. This formula differs from that given by eq. (1.9) by a numerical factor only.

Next, we mention a third alternative definition of crumpling. If the interfacial width W

scales as $W \sim L^\alpha$ with $\alpha > 0$, the membrane is rough. Moreover, if $\alpha > 1$ for $L \ll \zeta_p$, where ζ_p

is the persistence length [26], then the membrane is crumpled on length scales much longer than ξ_p ; thus, all crumpled membranes are rough but the converse is not necessarily true [109].

All the above definitions for crumpling are known to be equivalent when applied to continuum models of amphiphilic membranes.

1.5 Organization of the thesis:

In this thesis we study interface/membrane models and microscopic lattice models but do not consider any Landau-Ginzburg model. So far as the membrane models are concerned, we have studied only the out-of-plane thermal fluctuations of some model membranes and investigated its consequences on the conformational properties of the membrane. We have not studied the self-assemblies and bulk properties of the amphiphilic systems using membrane model approach. Different bulk properties and phase behaviours of the amphiphilic systems have been studied with microscopic lattice models. With microscopic models we have investigated the self-assemblies of three different classes of amphiphilic molecules with increasing complexity; we begin with single-chain amphiphiles and end with gemini surfactant and, in between, present a brief discussion on double-chain surfactants to maintain the logical sequence of development of our ideas and methodology of modelling.

The outline of the thesis is as follows:

In the chapter 2 of the thesis we show that the oil-water interface is rough, but not crumpled, in the droplet phase of the Widom model which is the simplest microscopic lattice model of ternary microemulsions.

In chapter 3 we construct a class of discrete lattice models of membranes/interfaces where we can make a clear distinction between the interfacial tension and bending rigidity which can be switched off independently of each other. More specifically, in chapter 3, we propose a $d + 1$ -dimensional *restricted discrete solid-on-solid* (RDSOS) model as well as *unrestricted discrete solid-on-solid* (UDSOS) model for d -dimensional amphiphilic membranes where the bending stiffness of the membrane is incorporated following the same prescription as in the Widom model. When the out-of-plane thermal fluctuations of the UDSOS model are controlled only by this bending stiffness we show that it is crumpled at all non-vanishing temperatures but the nature of the crumpling is very different from that observed in continuum models. We also point out some analogies between the relaxation to rough equilibrium states of these SOS models and nonequilibrium growth of some kinetically roughened model surfaces.

In chapter 4 we study the roughening of the oil-water interface in the presence of single-chain surfactants and investigate the physical origin of the lowering of the oil-water interfacial tension.

After studying the properties of the amphiphilic membrane at the oil-water interface in chapters 2,3 and 4, we investigate the air-water interface in the presence of single-chain amphiphiles in chapter 5. In this chapter we introduce a microscopic lattice model of a binary mixture of amphiphilic molecules, of two different lengths, in a system where water is separated from the air above it by a sharp well defined interface. We demonstrate an entropy-driven phase segregation in a direction perpendicular to the air-water interface when the initial total surface density of the amphiphiles is sufficiently high. We also investigate (a) the conformations of the amphiphiles, (b) the distribution of the sizes of the clusters of monomers belonging to the long amphiphiles as well as of those belonging to the short amphiphiles in planes parallel to the interface, (c) the

effects of varying the lengths, total concentration and the ratio of the numbers of the two types of the amphiphilic molecules, the strength of the inter-monomer interactions and temperature.

In the chapters 4 and 5 only single-chain amphiphiles have been considered although the general conclusions drawn from our MC studies are valid also for double-chain amphiphiles. In chapter 6 we compare and contrast the self-assemblies of single-chain and double-chain amphiphiles, respectively, in water. In this chapter we study the self-assemblies of binary mixtures of single-chain and double-chain amphiphiles and compare these with those formed by the corresponding single species of amphiphiles.

In chapter 7 we propose a microscopic lattice model of gemini surfactants. We show that these model gemini surfactants form long, thread-like and entangled micellar aggregates even at low concentrations where single-chain model surfactants form spherical micelles. We compare the morphologies of the micellar aggregates formed in our MC simulations with those observed in laboratory experiments and in earlier molecular dynamics simulations. We also study the variation of the critical micellar concentration of these model gemini surfactants with the variation of the (a) length of the hydrocarbon spacer (both hydrophobic and hydrophilic) connecting the two hydrophilic heads, (b) length of the hydrophobic tail and (c) the bending rigidity of the hydrocarbon chains forming the spacer and the tail. Some of the trends of variation are counter-intuitive but are in excellent agreement with the available experimental results. We also investigate the conformations and spatial organizations of the gemini surfactants at the air-water interface both in the dilute and semi-dilute regime.

In chapter 8 we propose a scheme for MC simulation of ternary microemulsions in porous media (such as vycor glass). Finally, in chapter 9 we summarize our conclusions and outline

rections of future work.

Chapter 2

Oil-Water Interface in the Widom model is it smooth, rough or crumpled?¹

2.1 Introduction

The Widom model (described in chapter 1) is, effectively, a spin-1/2 Ising model with not only nearest-neighbour ferromagnetic interactions but also with farther neighbour antiferromagnetic interactions. The Hamiltonian for the Widom model is given by equation (1.1). The interaction J is positive (ferromagnetic) whereas M is negative (antiferromagnetic); the latter arise from a particular prescription, suggested by Widom, for taking into account the bending energy of the

¹A paper based on this chapter has already been published by us (Prabal K. Maiti and Debashish Chowdhury, J. de Physique. I, 5, 671 (1995))

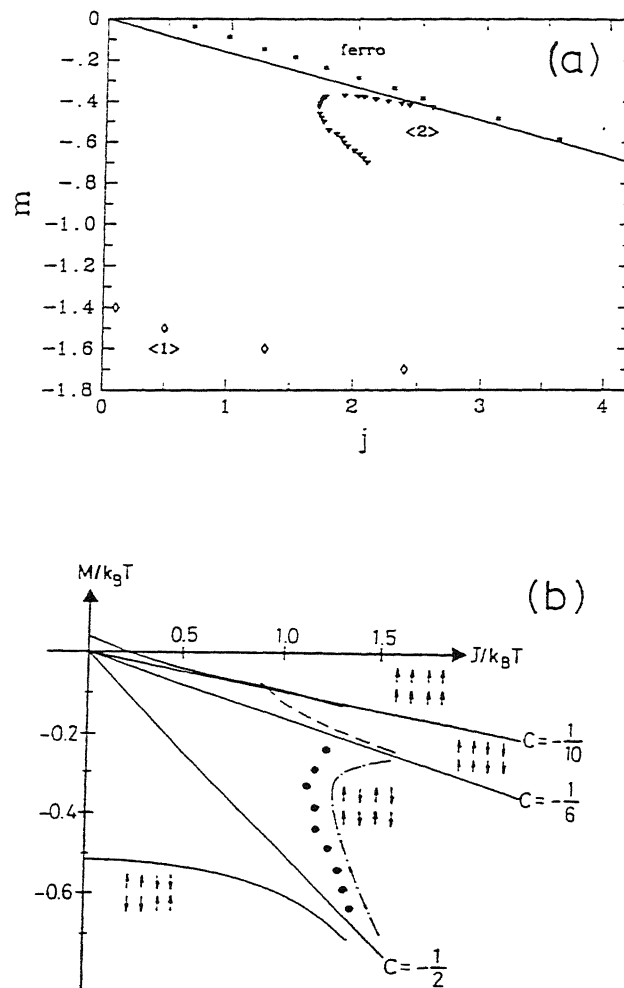


Figure 2.1: Phase Diagram of the Widom Model, (a) in space dimension 2 (after[100]) (b) in space dimension 3 (after[101]).

So far no attempt has been made to study the possibility of roughening/ crumpling of the amphiphilic membranes in the lattice models of complex fluids, e.g., monolayers at the oil-water interface in ternary microemulsions. In this chapter we study the nature of interface in the Widom model. The $M = 0$ limit of the Widom Hamiltonian (equation 1.1) is identical to the ordinary Ising Model with nearest neighbour interactions on a simple cubic lattice; the interface between domains of up and down spins in this case is known to be rough at all $T \neq 0$. Therefore, our investigation of the interface in the Widom model in this chapter will show the effects of the specific farther-neighbour antiferromagnetic interactions of the Widom model (non-vanishing M) on the roughened interface of the nearest-neighbour Ising model; we restrict our Monte Carlo (MC) study to square lattice ($d = 2$) only. We have focussed attention only on that part of the phase diagram on the $j - m$ -plane where the droplet phase (i.e., the ferromagnetic phase in the spin language) is thermodynamically stable.

2.2 Simulation

We have used the standard techniques of Monte Carlo (MC) simulation. The system consists of $L_x \times (L_y + 4)$ lattice where, by convention X and Y denote the horizontal and vertical directions, respectively. Each site of the lattice is occupied by a classical Ising spin ($S_i = \pm 1$). Periodic boundary condition is applied in the X -direction whereas a fixed boundary condition is applied in the Y -direction; the spins in the two uppermost layers remain "frozen" in the up (+) state while those in the two lowermost layers remain "frozen" in the down (−) state throughout the simulation. In some of our runs we used an alternative boundary condition where, instead of

fixed boundaries, anti-periodic boundary condition was applied in the Y -direction. However, within the accuracy of our computation, the data for these two sets of boundary conditions were indistinguishable. Therefore, almost all of our production runs were made with fixed boundary condition in the Y -direction. Application of these boundary conditions are used routinely in creating interfaces in the Ising model where majority of the spins in the upper half are in the up state whereas majority of the spins in the lower half are in the down state. For each set of values of j, m, L_x and L_y we began with an initial state in which all the spins in the upper half of the system were in the up state whereas those in the lower half were in the down state; this initial condition helps us in faster equilibration of the system.

2.3 Results

If the two nearest neighbour spins are antiparallel we call the bond connecting these two spins to be a "broken" one. After the equilibration of each configuration, we measured the number of broken bonds, $N_b(y)$, as a function of the row-index y ; in the droplet phase (ferromagnetic phase) one expects a maximum in $N_b(y)$ near $L_y/2$ provided accurate data have been generated by averaging over sufficiently large number of configurations. In fig.2.2 we plot $N_b(y)$ as a function of y for the parameter values $j = 1.0$ and $m = 0$; this corresponds to a two-dimensional Ising model with only nearest-neighbour interactions. The figures 2.2(a) and (b) correspond to $L_x = 2000$ and 20000 , respectively. Similar plots were also obtained for $j = 1.25, m = 0.0$ and $j = 1.6, m = 0.0$.

The full width at half maximum (FWHM) in the plot of $N_b(y)$ can be taken as a measure

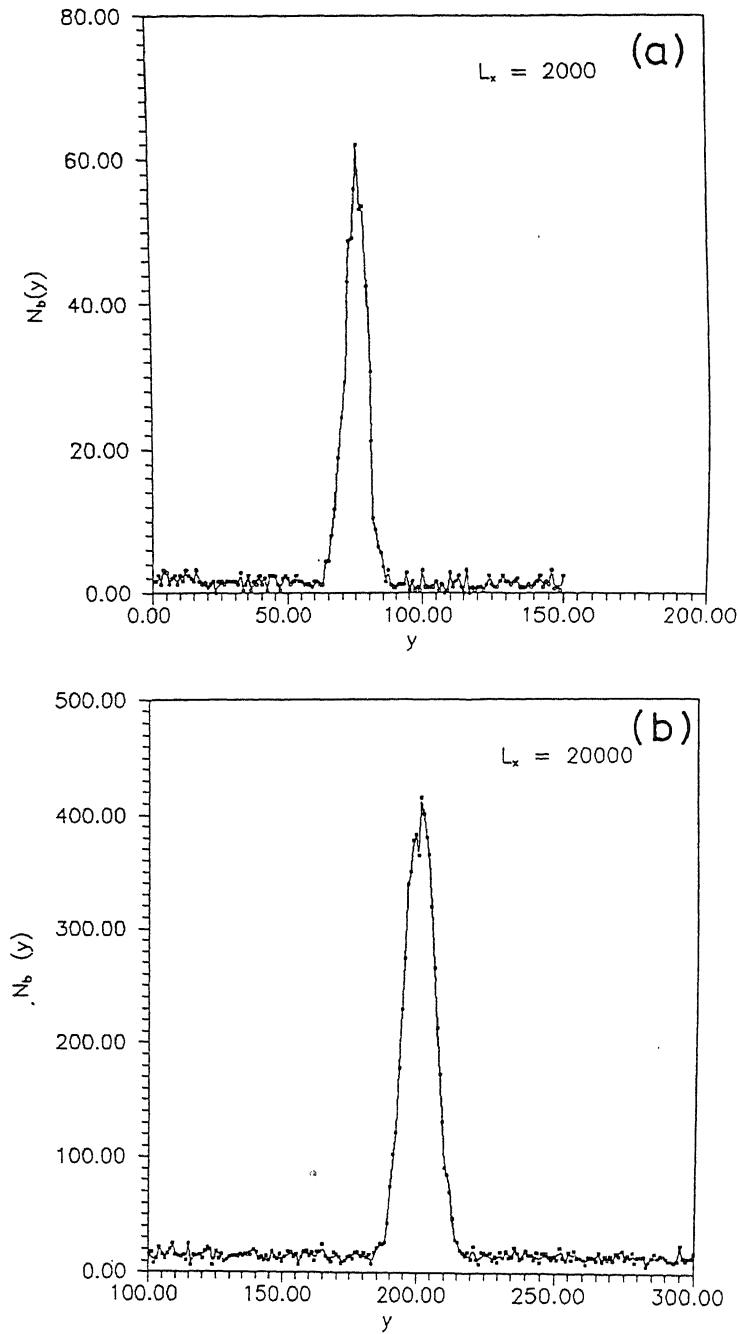


Figure 2.2: Two typical plots of $N_b(y)$ for $j = 1.0$, $m = 0.0$ are shown. $L_x = 2000$ in (a) and 20000 in (b). $L_y = 200$ in both (a) and (b). The data in (a) and (b) have been obtained by averaging over 20 and 6 configurations, respectively.

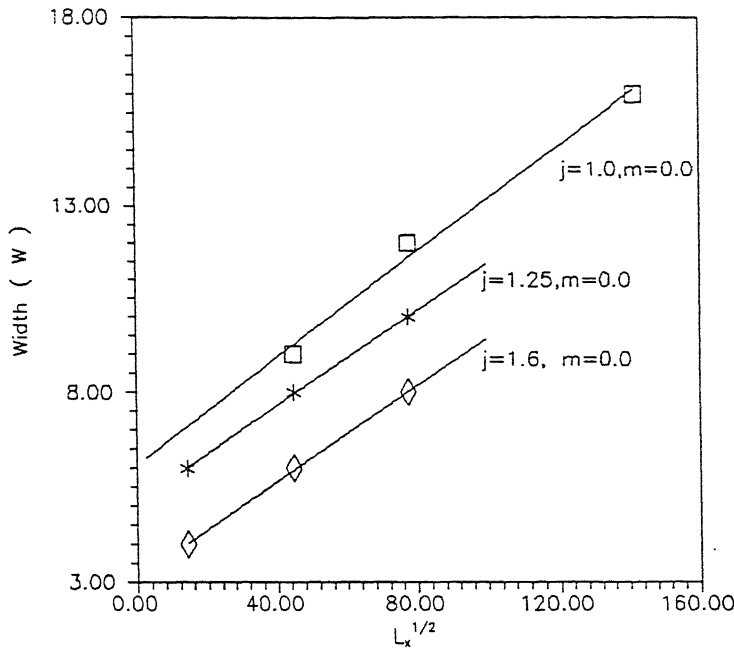


Figure 2.3: The width of the interface of the Ising model with only nearest-neighbour ferromagnetic interactions (i.e., $m = 0$) are plotted against $L_x^{1/2}$ for three different values of j .

of the *width* of the interface. Since the width W of the interface of two-dimensional Ising model with only nearest- neighbour interaction is known to vary as $\sqrt{L_x}$ with the length L_x we show in fig.2.3 that our corresponding data are, indeed, consistent with this behaviour. Moreover, note that for the same L , the smaller is the value of j the larger is the width of the interface, as it should be.

Next, in fig.2.4, we plot the width of the interface as a function of $\sqrt{L_x}$ for the same values of j as in fig.2.3, but now for non-zero values of m . Clearly, the interface is still rough in spite of the non-zero values of the farther-neighbour antiferromagnetic interactions. Moreover, note that, for given L and j , the interface is wider for non-zero values of m as compared to the Ising

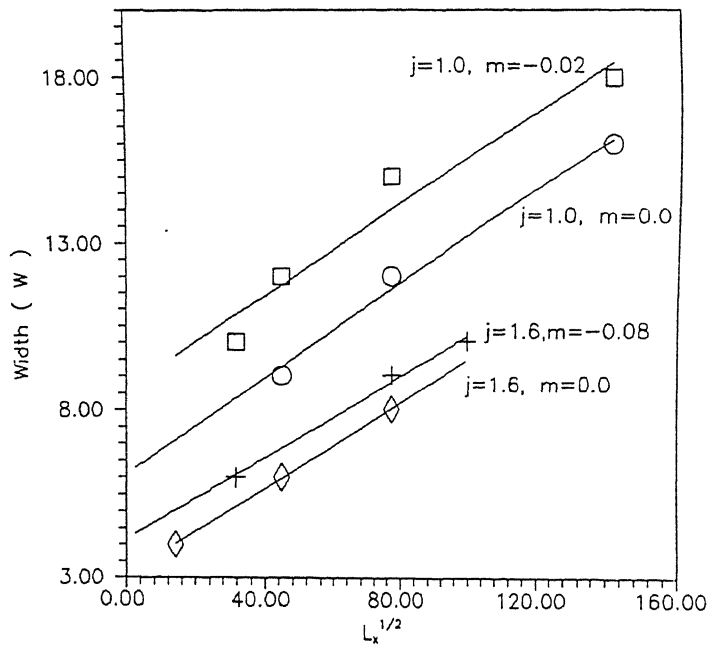


Figure 2.4: The width of the interface of the Widom model (i.e., $j \neq 0$, $m \neq 0$) are plotted against $L_x^{1/2}$ for two different values of j ; the corresponding plots for $m = 0$ are also given for comparison.

interface for which $m = 0$. This arises from the fact that, for given j , the system is closer to the critical point for larger value of m as long as the system remains in the ferromagnetic phase.

We conclude that although the farther-neighbour interactions in the Widom model give rise to a richer bulk phase diagram, as compared to that of the Ising model with nearest-neighbour interactions on the simple cubic lattice, these do not affect the interface roughening exponent, except for the fact that the interface becomes wider when these further-neighbour interactions are switched on.

In contrast to our Monte Carlo simulation in $2d$, Khang et. al [99] have studied the same Widom Hamiltonian (equation 1.1) by performing low-temperature series expansions in the three dimensional cubic lattice. In their study they used periodic boundary condition in the x and y directions and antiperiodic boundary conditions in the z direction. The interface at $T = 0$ was chosen to lie at $z = 0$ and in the zero temperature state, all spins are positive for $z < 0$ and negative for $z > 0$. Thus the ground state normalized layer density is $\rho(z) = 1$ for $z < 0$, associated with positive spins, and $\rho(z) = 0$ for $z > 0$, associated with negative spins. In their paper they also studied a solid-on-solid (SOS) model and a restricted solid-on-solid (RSOS) model (which will be discussed in next chapter) associated with the Widom Hamiltonian. To study the roughening transition they calculated moments of density gradient and the surface density. The moments of density gradient is defined as

$$\langle z^{2n} \rangle = \sum_{-\infty}^{\infty} [\rho(z - 1/2) - \rho(z + 1/2)] z^{2n} \quad (2.1)$$

which diverges as $T \rightarrow T_R$. The other order parameter is defined as

$$\mathcal{R} = \frac{1}{1 - \rho(1/2) - \rho(3/2)} \quad (2.2)$$

ahng et al obtained the low-temperature series of the the order parameters , $\langle z^2 \rangle$ and R in terms of the small parameters $x \equiv e^{-4M/k_B T}$ and $y \equiv e^{-4J/k_B T}$ for the Hamiltonian (1.1) as well for both the SOS and RSOS models. They observed that roughening transition curve passes through the region in which paramagnetic, ferromagnetic and modulated phases merge, and is parallel to the phase boundary of the ferromagnetic and modulated phases. It was also found that crossover behaviour occurs in the roughening transition from the surface tension dominant regime to the bending-energy dominant regime.

Chapter 3

Restricted and unrestricted discrete SOS models of interface with bending rigidity: equilibrium and non-equilibrium properties¹

3.1 Introduction

In the previous chapter we have studied the roughening properties of the oil-water interface in the Widom model in the droplet phase (ferromagnetic phase). Though the interface was found to be rough at all non-vanishing temperatures there was no evidence for crumpled phase

¹The following papers are based on this chapter:
P. K. Maiti, D. Chowdhury and J. K. Bhattacharjee, *Phy. Rev. E* **54**, 2670 (1996); P. K. Maiti and D. Chowdhury, IITK preprint (1997), submitted for publication

the interface. This might be due to fact that in the droplet phase of the Widom model the out-of-plane thermal fluctuations are controlled by surface tension as well as bending rigidity. When bending rigidity alone governs the out-of-plane thermal fluctuation, fluid like membranes are crumpled at all non-vanishing temperatures [108, 5, 109, 8]. One disadvantage of the Widom model is that we can not switch off the surface tension J since that would destroy the droplet phase itself. Now the question arises whether it is possible to construct a discrete model of an interface where we can make a clear distinction between the interfacial tension and bending rigidity and whether or not that model can exhibit a crumpled phase.

The roughening and crumpling of isolated planar interfaces have been studied extensively in the solid-on-solid (SOS) approximation [112, 114]. The results obtained from the discrete and continuum models of interfaces have been found to be qualitatively consistent with each other [115, 113].

In this chapter we propose a $d + 1$ -dimensional *unrestricted discrete SOS (UDSOS)* as well as *restricted discrete SOS (RDSOS)* model for d -dimensional amphiphilic membranes where the bending stiffness of the membrane is incorporated following a prescription suggested earlier by Widom [35] in order to account for the bending rigidity of the membrane at the oil-water interface in the lattice model of ternary microemulsions studied in chapter 2.

In the case of the RDSOS model the restrictions imposed on the step sizes are such that a clear distinction between the interfacial tension and bending stiffness can be made. The motivation for imposing this restriction will be clarified later in the appropriate context.

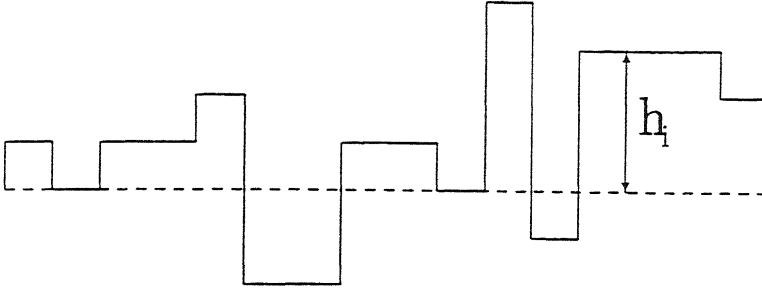


Figure 3.1: A discrete model SOS interface

3.2 The Model

For simplicity, we formulate the model as a d -dimensional membrane embedded in a $d + 1$ -dimensional space. For $d = 1$ we have a one dimensional membrane (curve) embedded in two-dimensional space and for $d = 2$ we have two-dimensional membrane embedded in three-dimensional space. Suppose the sites on a d -dimensional lattice are labelled by the integers i ($i = 1, 2, 3, \dots, L^d$) where L is the linear size of the lattice in each of the d -directions. The height of the membrane, measured from the reference line (in $d = 1$) or reference plane (in $d = 2$), is assumed to be given by a single-valued discrete height function; h_i , the height at the i -th site, can take only integer values. A model discrete SOS interface has been shown in figure 3.1. If h_i is constant and independent of i then the membrane is flat everywhere. On the other hand, unequal heights at neighbouring sites gives rise to bending of the interface; these bends are identical to the bendings of the amphiphilic monolayer at the oil-water interface in the Widom model.

The hamiltonian for the model membrane is given by [116]

$$H = \mathcal{J} \sum_{i>j} |h_i - h_j| + \mathcal{K} \sum_{i>j} (1 - \delta_{h_i, h_j}) \quad (3.1)$$

where δ_{h_i, h_j} is Kronecker δ -function and the constant \mathcal{K} is a measure of the bending stiffness of

the membrane whereas \mathcal{J} is a measure of the interfacial tension. The summations in both the terms are to be carried out only over pairs of nearest neighbour sites on the d -dimensional lattice. Note that an energy cost \mathcal{K} is associated here with every bending of the interface at right angle over a single lattice spacing. In the limit $\mathcal{K} = 0$, this model reduces to the standard SOS model for an interface with only interfacial tension.

We denote the absolute value of the difference in the height variables at two neighbouring sites i and j , i.e., $|h_i - h_j|$, by the symbol $|\Delta h_i|$ which, in general, can be any positive integer $1, 2, \dots, N$. If N is allowed to be *infinitely* large (i.e. the height variable at a particular lattice point i can take any value irrespective of its neighbouring height variables) we call the model unrestricted discrete solid-on-solid (UDSOS) model. On the other hand if N is allowed to take only a *finite* integer value we call the model as restricted discrete solid-on-solid (RDSOS) model.

If $|\Delta h_i|$ is allowed to take only the values 0 and 1 (i.e., $N = 1$), both \mathcal{J} term (surface tension term) and \mathcal{K} term (bending stiffness term) are identical and the model may be regarded as a standard restricted discrete SOS model with effective interfacial tension $\mathcal{J} + \mathcal{K}$. Therefore, in order to make clear distinction between *bending* rigidity and interfacial tension the minimum allowed value of N should be 2. In all our computer simulations of RDSOS model 0, 1 and 2 were the allowed values of $|\Delta h_i|$.

We have applied periodic boundary condition in all the d -directions of the d -dimensional lattice. We work with the parameters $J = \mathcal{J}/(k_B T)$ and $K = \mathcal{K}/(k_B T)$ where T is the temperature and k_B , the Boltzmann constant is chosen to be unity in our units. Note that if the magnitudes of J and K are increased (decreased) simultaneously keeping the ratio J/K constant, it effectively mimics a decrease (increase) of the temperature for fixed \mathcal{J} and \mathcal{K} .

In our MC simulation of the UDSOS model, the system is allowed to evolve, starting from a flat initial condition ($h_i = 0$ for all i), following the standard Metropolis algorithm [117] : a site on the d -dimensional lattice is selected randomly and the corresponding height of the interface h_i was allowed to change by letting $h_i \rightarrow h_i \pm 1$ certainly if $\Delta E < 0$ and with a probability proportional to $\exp(-\Delta E)$ if $\Delta E \geq 0$, where ΔE is the change in energy that would be caused by the change in height variable h_i . In the case of RDSOS model the algorithm for time evolution is identical to that for the UDSOS model except that none of those changes in the height variable which would violate the restriction $|\Delta h_i| = 0, 1, \dots, N$ is allowed at any step.

The width , W , of the interface is defined through the relation $W^2(L, t) = [\langle (h_i(t) - \langle h \rangle)^2 \rangle]_{av}$ where $h_i(t)$ ($i = 1, 2, \dots, L^d$) is the height at the i -th site at time t , the symbol $\langle X \rangle$ implies average of X over all the lattice sites, i.e. $\langle X \rangle = \frac{1}{L} \sum_i X_i$, whereas the symbol $[Y]_{av}$ implies average of Y over a large number of MC runs. The quantity $W(L, t)$ is monitored, for fixed L , as a function of time t ; $W(L, \infty)$ is the width of the system in equilibrium. We define the exponents α and β as follows: $W(L, t) \simeq t^\beta$ for fixed L and for *very early times* whereas $W(L, \infty) \simeq L^\alpha$ in equilibrium.

Another quantity that scales in the same way as the interface width is the height-height correlation function

$$C(l) = [\langle (h_{i+l} - h_i)^2 \rangle]^{1/2} \quad (l < L) \quad (3.2)$$

The roughness exponent can be determined from the relation

$$C(l) \simeq l^\alpha \quad (l \ll L). \quad (3.3)$$

We have also computed two other correlation functions in the case of UDSOS model in $d = 1$. The correlation function $G(x)$ is defined as

$$G(x) = [(h_0 - \langle h \rangle)(h_x - \langle h \rangle)]_{av} \quad (3.4)$$

In the continuum formulation, De Gennes and Taupin [26] studied the correlation between the normals to the membrane at two-spatially separated points. We have introduced a novel discrete counterpart of this normal-normal correlation appropriate for our discrete model. Only three directions are possible for the normal to our discrete interface- it can be directed either towards left ($-\hat{x}$) or right (\hat{x}) or can be vertical. Therefore, we can define the "normal" n_i as follows:

$$n_i = +1 \text{ if } h_i > h_{i+1}$$

$$n_i = 0 \text{ if } h_i = h_{i+1}$$

$$n_i = -1 \text{ if } h_i < h_{i+1}$$

In terms of these "normals" the *normal-normal* correlation function $N(x)$ for our discrete model is defined as

$$N(x) = [n_0 \bullet n_x]_{av} \quad (3.5)$$

3.3 UDSOS Model

In order to test our algorithm and computer program we have calculated $W(L, \infty)$ as a function of L first in special case $d = 1$, $K = 0$, $J = 1.5$, i.e. for the standard SOS model. From Fig 3.2 we find that in this special case of $J \neq 0$, $W(L, \infty) \propto \sqrt{L}$, in agreement with the known result for the standard SOS model.

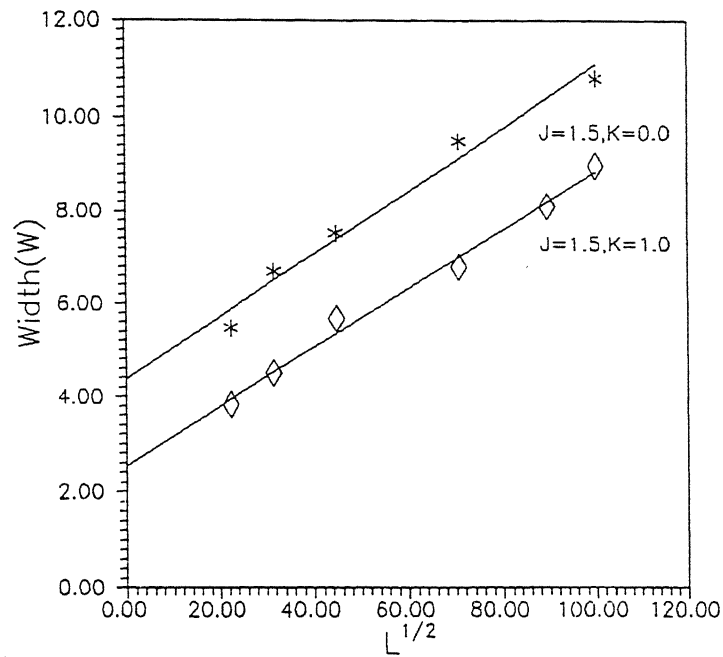


Figure 3.2: The equilibrium width W of the interface plotted against $L^{1/2}$ for two different sets of values of the parameters J and K , namely, $J = 1.5, K = 0.0$ and $J = 1.5, K = 1.0$. The lines through the data points are the corresponding best fitted straight lines .

The advantage of the SOS model (3.1) is that one can "switch off" \mathcal{J} and thus, choosing non-vanishing \mathcal{K} , can have a discrete model of interface with purely bending rigidity only. Therefore, we next computed $W(L, t)$ in the other special case $d = 1$, $J = 0$, $K \neq 0$. We found that $W(L, t)$ kept increasing for ever with the increasing time t . In fig.3.3 the solid curves represent $W(L, t)$, plotted against $L^{1/2}$ for three different values of t , when $K = 3.0$; the corresponding curves for $K = 1.0$ are shown by the dashed curves in the same figure. Note that smaller K corresponds to an effectively higher temperature T . From Fig.3.3 it is clear that (a) for a fixed time t the interface is wider at a higher temperature than at a lower temperature after the elapse of the same time interval beginning from the flat conformation at $t = 0$, and (b) at any given t , W is independent of L but $W(L, t) \rightarrow \infty$ as $t \rightarrow \infty$ for all L .

Thus the actual area A of the membrane in equilibrium is infinitely large, if $J = 0$ but $K \neq 0$, at all $T \neq 0$, even for all finite values of the basal area (length L in $d = 1$)! Does it necessarily imply that the membrane is crumpled at all non-vanishing temperatures?

In order to answer this central question we shall now summarize the three different definitions of crumpling. All these definitions yield identical results when applied to standard continuum models of membranes and, therefore, usually regarded as equivalent. But, our discrete lattice model, with $J = 0$ and $K \neq 0$, satisfies the criterion of crumpling set by one of these definitions. It appears to be smooth when examined against the two other definitions. (i) If the ratio of the excess area $\delta A = A - A_p$ created by thermal fluctuations and the original basal area A_p of the membrane diverges in the thermodynamic limit the membrane is crumpled. This criterion of crumpling is certainly satisfied by our lattice model (3.1) at all $T \neq 0$ if $J = 0$ but $K \neq 0$. (ii) If the interfacial width W scales as $W \sim L^\alpha$ with $\alpha > 0$, the membrane is rough. Moreover, if

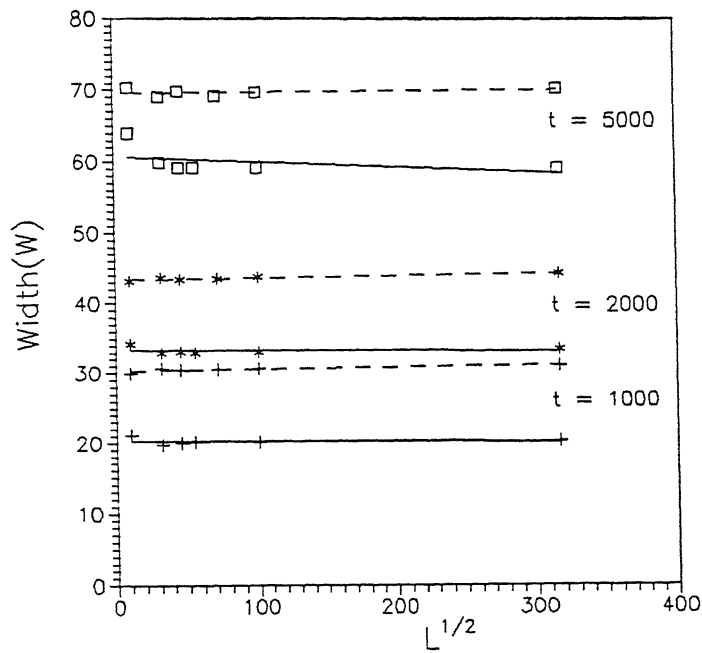


Figure 3.3: The width W of the interface plotted against $L^{1/2}$ for the parameter values $J = 0.0$, $K = 3.0$ (full curves) and $J = 0.0$, $K = 1.0$ (dashed curves) at three different times, namely, $t = 1000$, $t = 2000$ and $t = 5000$ Monte Carlo steps.

> 1 for $L \ll \zeta_p$, where ζ_p is the persistence length [26], then the membrane is crumpled on length scales much longer than ζ_p ; thus, all crumpled membranes are rough but the converse is not necessarily true [109]. From fig.2, we conclude that, after the very early times (when no clear trends emerge due to the presence of transients), one can extract an effective roughening exponent α_{eff} for all longer times and one finds that $\alpha_{eff} = 0$. This, however, would imply that at all times, except the very early stages, during its growth the membrane remains effectively smooth! (iii) If the correlation between the normals to the membrane at two spatially-separated points follows $\langle \vec{n}(\vec{r}) \bullet \vec{n}(0) \rangle \sim e^{-r/\zeta_p}$, then the membrane is defined as crumpled on length scales much larger than ζ_p [26]. But, we neither find any exponential decay in the "normal-normal correlation function" $N(x)$ nor observe any qualitative difference in $N(x)$ computed for $K = 1.0$ and $K = 5.0$ (see figs.3.4(a) and 3.4(b)), which correspond to an interface of fixed bending rigidity \mathcal{K} at two different effective temperatures.

In fig.3.5(a) and 3.5(b) we present the height-height correlation function $C(x)$ for $K = 5.0$ and $K = 1.0$, respectively. The corresponding correlation functions $G(x)$ are plotted in figs. 3.6(a) and 3.6(b), respectively. Noting that $K = 1.0$ corresponds to an effectively higher temperature than $K = 5.0$ for same fixed bending stiffness \mathcal{K} , we conclude that the only effect of higher temperature in both these figures is the larger magnitude of the corresponding correlation function arising from stronger thermal fluctuation.

In order to understand these unusual features of the out-of-plane thermal fluctuations in the model (3.1), let us compare schematic typical configurations for this model with those of standard continuum models. Since wiggles exist in the rough phase of the continuum model on all length scales (smaller wiggles are part of the bigger ones which, in turn, are parts of even bigger ones,

CENTRAL LIBRARY
I. I. T., KANPUR

Inv. No. A125700

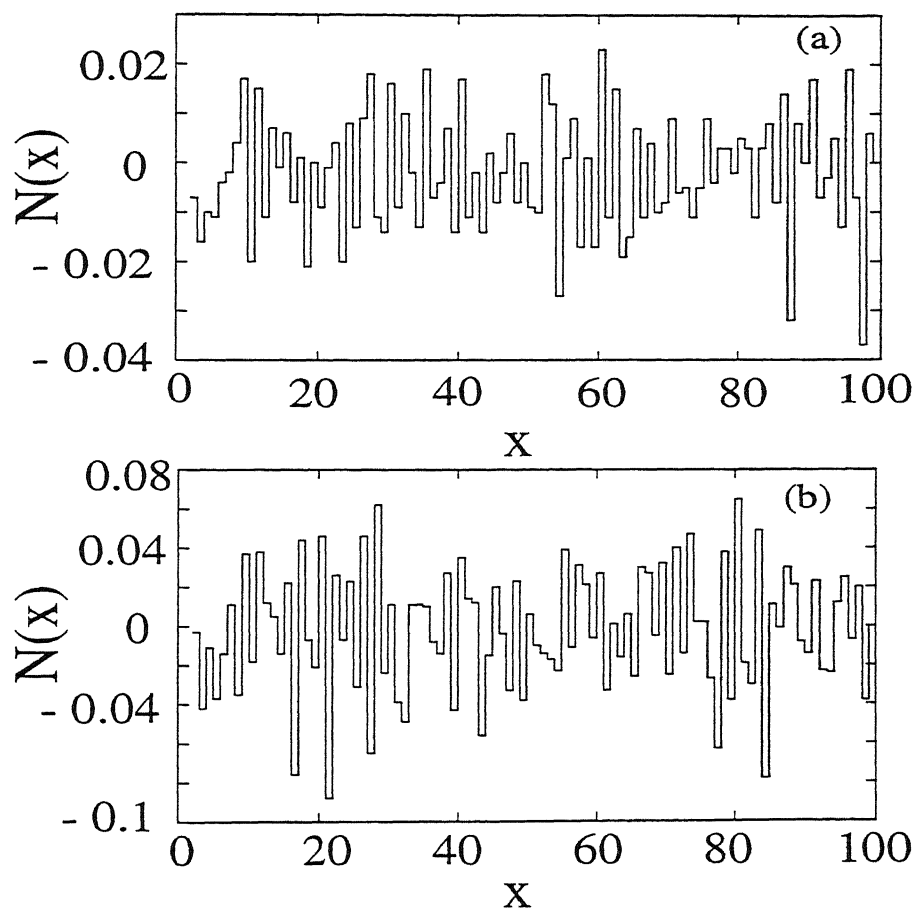


Figure 3.4: The normal-normal correlation function $N(x)$ for (a) $K = 5.0$, (b) $K = 1.0$.

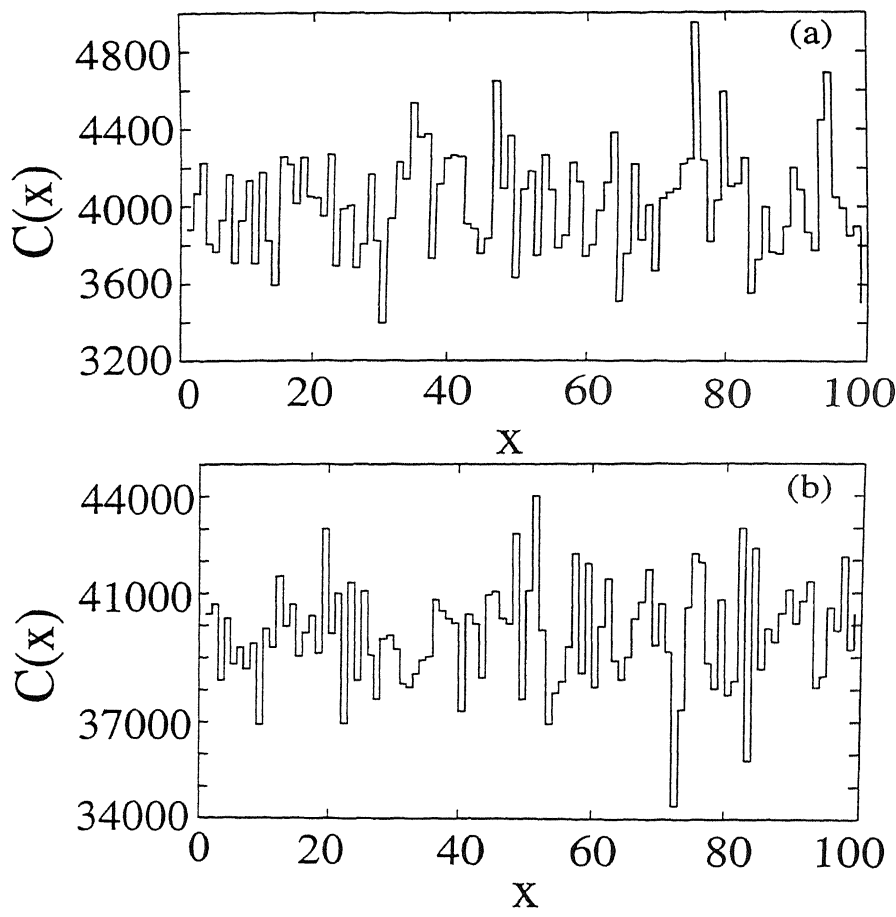


Figure 3.5: The height-height correlation function $C(x)$ for (a) $K = 5.0$, (b) $K = 1.0$.

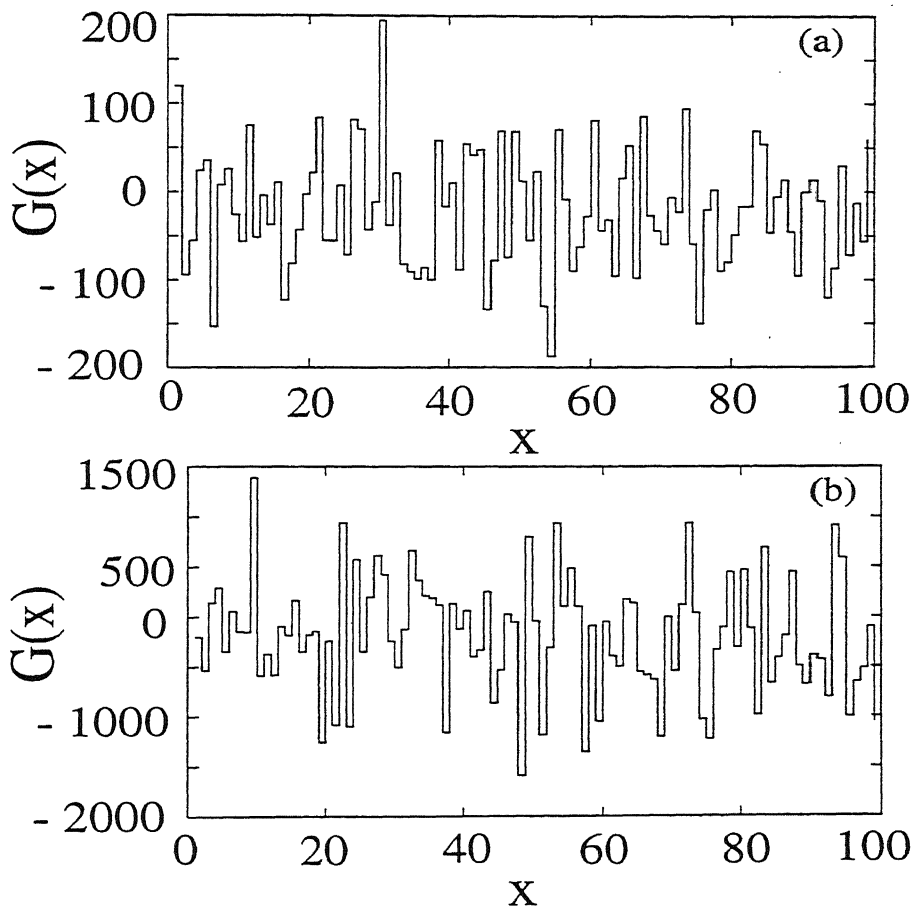


Figure 3.6: The correlation function $G(x)$ for (a) $K = 5.0$, (b) $K = 1.0$.

d so on) the width increases with increasing L . The absence of wiggles of all sizes leads to $\alpha = 0$ in our lattice SOS model. Moreover, it is obvious from these schematic representations of typical configurations why the normal-normal correlation exhibits a periodicity in our lattice SOS model. Note that the diverging area of the lattice membrane in equilibrium arises from the diverging area (length in $d = 1$) of the vertical regions of the membrane.

Next, we have computed the width of the interface as a function of L for the more general case $K \neq 0$, $J \neq 0$ simultaneously. In order to test the effect of non-vanishing K on the roughness of the SOS interface we chose the same value of J , namely, $J = 1.5$, as before, while K was chosen to be 1.0. It is clear from fig.3.2, that the non-vanishing bending rigidity tends to suppress the out-of-plane thermal fluctuations thereby reducing the width of the interface but the roughening exponent remains the same as in the special case $K = 0$. In other words, in the general case, when both J and K have non-vanishing values, the interface is rough but not crumpled.

We shall now explain why "switching on" of the bending stiffness \mathcal{K} does not lead to any change in the value of the roughening exponent of the standard UDSOS model with $\mathcal{J} \neq 0$, $\mathcal{K} = 0$. Consider, for simplicity, $d = 1$. Then, \mathcal{J} has the dimension of $[Energy]/[Length]$ whereas \mathcal{K} has the dimension of $[Energy]$. Therefore, there exists a crossover length $\ell_c^{(1)} = \mathcal{K}/\mathcal{J}$ such that the equilibrium structure of the interface on length scales $L \gg \ell_c^{(1)}$ is governed by \mathcal{J} . However, in the special case $\mathcal{J} = 0$, the equilibrium is governed solely by \mathcal{K} . It is straightforward to see [16] that if $\mathcal{J} = 0$ the interfacial width in equilibrium diverges. On the other hand, in the presence of non-vanishing \mathcal{J} , the interface must have a finite width; for a given \mathcal{K} , the larger is \mathcal{J} the smaller is the equilibrium width of the interface. Moreover, a larger value of \mathcal{K} , for

fixed $\mathcal{J}(> 0)$, leads to stronger suppression of the interfacial fluctuations. Nevertheless, if $\mathcal{J} \neq 0$ there is a very short early time regime where $W(L, t) \propto t^{1/2}$; the larger is the magnitude of \mathcal{J} the quicker is the onset of the deviation from this law. These arguments can be easily generalized to $d > 1$.

Now we study the dynamics of the UDSOS model interface analytically [118] in the special limit $J = 0$, but $K \neq 0$ by using a standard Master equation approach which is similar to that for the kinetic Ising models [120].

For simplicity, we consider only $d = 1$.

$$\begin{aligned} \frac{d}{dt}P(h_1 \dots h_L; t) = & - \sum_{i=1}^L \sum_{\{h'_i\}} [W(h_i \rightarrow h'_i)P(h_1 \dots h_i \dots h_L; t) \\ & - W(h'_i \rightarrow h_i)P(h_1 \dots h'_i \dots h_L; t)] \end{aligned} \quad (3.6)$$

where $P(h_1 \dots h_L; t)$ is the probability of having the system in a state (h_1, \dots, h_L) at time t . $W(h_i \rightarrow h'_i)$ is the transition probability, i.e., the probability of changing the state by changing the height variable at the i -th site from a value h_i to a value $h'_i = h_i \pm \delta$. The first sum on the right hand side goes over all sites and the second sum goes over all the allowed values of h'_i . Expectation values of quantities $A(\{h_i\})$ which depend on the height variables $\{h_i\}$ are defined by

$$\langle A(\{h_i\}) \rangle = \sum_{\{h_i\}} A(\{h_i\})P(\{h_i\}, t) \quad (3.7)$$

Therefore, we can write the equation of motion for the average value of $\langle A(\{h_i\}) \rangle$ as [121]

$$\frac{d}{dt} \langle A(h_i) \rangle = - \langle \sum_{\{h'_i\}} [A(h_i) - A(h'_i)]W(h_i \rightarrow h'_i) \rangle \quad (3.8)$$

To derive equation (3.8) from equation (3.7) we have used principle of detailed balance namely

$$W(h_i \rightarrow h'_i)P(h_1 \dots h_i \dots h_L; t) = W(h'_i \rightarrow h_i)P(h_1 \dots h'_i \dots h_L; t) \quad (3.9)$$

Since the transition probabilities $W(h_i \rightarrow h'_i)$ depend on the neighbouring height variables h_{i+1} and h_{i-1} only we choose the probabilities $W(h_i \rightarrow h'_i)$ to be of the following form [120]

$$W(h_i \rightarrow h'_i) = [1 - \gamma(\delta_{h_i, h_{i+1}} + \delta_{h_i, h_{i-1}} - \delta_{h'_i, h_{i+1}} - \delta_{h'_i, h_{i-1}})] \quad (3.10)$$

where $\gamma = \tanh(\beta \Delta E(h_i, h'_i)/2)$ with $\Delta E(h_i, h'_i)$ being the energy change of the system for $h_i \rightarrow h'_i$. For the case $J = 0$ and $K \neq 0$ we have

$$\Delta E(h_i, h'_i) = K(\delta_{h_i, h_{i+1}} + \delta_{h_i, h_{i-1}} - \delta_{h'_i, h_{i+1}} - \delta_{h'_i, h_{i-1}}) \quad (3.11)$$

For simplicity, from now onwards, we shall consider only transitions between neighbouring states $h_i \rightarrow h_i \pm 1$. Some of the possible transition probabilities for different neighbouring height variables have been tabulated in table 3.1. Associated changes in the energy also have been given in the table.

The equation of motion for the average value $\langle h_i(t) \rangle$ can now be written from equation (3.8) as

$$\begin{aligned} \frac{d}{dt} \langle h_i(t) \rangle &= - \langle [h_i - (h_i + 1)]W(h_i \rightarrow h_i + 1) \\ &\quad + [h_i - (h_i - 1)]W(h_i \rightarrow h_i - 1) \rangle \\ &= - \langle W(h_i \rightarrow h_i - 1) - W(h_i \rightarrow h_i + 1) \rangle \\ &= \sum_{\{h_i\}} P(h_1 \dots h_i \dots h_L; t) [W(h_i \rightarrow h_i - 1) - W(h_i \rightarrow h_i + 1)] \end{aligned} \quad (3.12)$$

From the table it is evident that for every possible transition there is a reverse transition. The initial configuration in one case is the initial configuration of the other case (see row 1 and row 12 in table 3.1) whose energy contribution is opposite in sign. The contributions coming from these


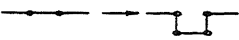



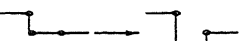
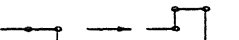

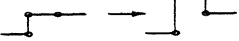
h_{i-1}	h_{i+1}	h'_i	configuration	ΔE	W
h_i	h_i	$h_i + 1$		$2K$	$1 - 2\gamma(2K)$
h_i	h_i	$h_i - 1$		$2K$	$1 - 2\gamma(2K)$
h_i	$h_i + 1$	$h_i + 1$		0	1
h_i	$h_i + 1$	$h_i - 1$		K	$1 - \gamma(K)$
$h_i + 1$	h_i	$h_i + 1$		0	1
$h_i + 1$	h_i	$h_i - 1$		K	$1 - \gamma(K)$
h_i	$h_i - 1$	$h_i + 1$		K	$1 - \gamma(K)$
h_i	$h_i - 1$	$h_i - 1$		0	1
$h_i - 1$	h_i	$h_i + 1$		K	$1 - \gamma(K)$

Table 3.1: Some of the possible transitions and the corresponding transition probabilities for UDSOS model in $d = 1$


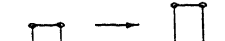
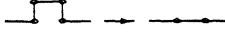
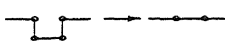
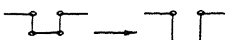
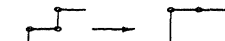
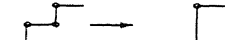
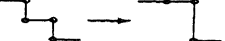
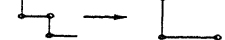
h_{i-1}	h_{i+1}	h'_i	configuration	ΔE	W
$h_i - 1$	h_i	$h_i - 1$		0	1
$h_i - 1$	$h_i - 1$	$h_i + 1$		0	1
$h_i - 1$	$h_i - 1$	$h_i - 1$		$-2K$	$1 - 2\gamma(2K)$
$h_i + 1$	$h_i + 1$	$h_i + 1$		$-2K$	$1 - 2\gamma(2K)$
$h_i + 1$	$h_i + 1$	$h_i + 1$		0	1
$h_i - 1$	$h_i + 1$	$h_i + 1$		$-K$	$1 - \gamma(-K)$
$h_i - 1$	$h_i + 1$	$h_i - 1$		$-K$	$1 - \gamma(-K)$
$h_i + 1$	$h_i - 1$	$h_i + 1$		$-K$	$1 - \gamma(-K)$
$h_i + 1$	$h_i - 1$	$h_i - 1$		$-K$	$1 - \gamma(-K)$

Table 3.1: Contd.

cancels each other in the above sum. Summing over all possible transition we get

$$\begin{aligned} \frac{d}{dt} \langle h_i(t) \rangle &= 0 \\ \text{i.e. } \langle h_i(t) \rangle &= \text{constant} \end{aligned} \quad (3.13)$$

Physically this means that as the system evolves with time the mean position remains fixed. This is in accordance with the results of our MC simulation reported earlier [116]. One can compare this result with the growth law of the standard SOS model with only interfacial tension [122] where $\langle h_i(t) \rangle \simeq t^{-p}$ with an exponent $p \geq 1/2$ for $d \leq 2$ and $\langle h_i(t) \rangle \simeq \exp(-\lambda(T)t)$, ($\lambda(T) > 0; T < \infty$) for $d > 2$.

The width of the interface is defined through

$$W(t) = \langle (h_i(t) - \langle h_i(t) \rangle)^2 \rangle = \langle h_i^2(t) \rangle - \langle h_i(t) \rangle^2$$

To compute the growth law for the interface width we calculate $\langle h_i^2(t) \rangle$. From equation (3.8) we can write the equation of motion for $\langle h_i^2(t) \rangle$ as

$$\begin{aligned} \frac{d}{dt} \langle h_i^2(t) \rangle &= \langle [W(h_i, h_i + 1) + W(h_i, h_i - 1)] \rangle \\ &+ 2 \langle h_i [W(h_i, h_i + 1) - W(h_i, h_i - 1)] \rangle \end{aligned} \quad (3.14)$$

Summing over all the possible transitions we find that the second term in the above equation vanishes and the first term gives a constant which is a function of temperature alone. So we have

$$\begin{aligned} \frac{d}{dt} \langle h_i^2(t) \rangle &= \text{constant} \\ \text{i.e. } \langle h_i^2(t) \rangle &\propto t \end{aligned} \quad (3.15)$$

So, the width of the interface $W(t) \propto \sqrt{t}$; the results of our MC simulation (fig 3.7) [116] are in

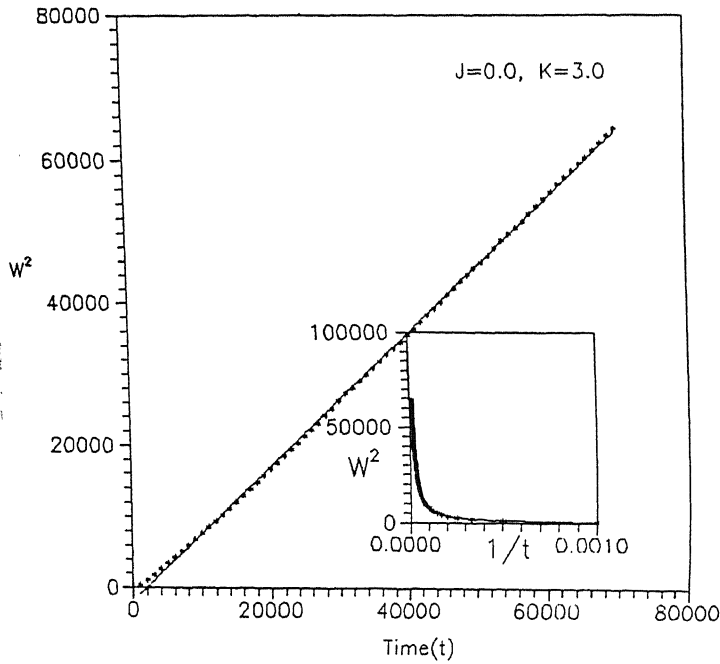


Figure 3.7: The square of the interfacial width plotted against time t for $J = 0.0, K = 3.0$. The inset shows the same data plotted against $1/t$ to emphasize the fact that, when $J = 0, K \neq 0$, the interfacial width diverges in the limit $t \rightarrow \infty$.

excellent agreement with this growth law. So for $d = 1$ we have $\beta \simeq 1/2$. Subsequently, we have also repeated the computation in $d = 2$ and have observed that $\beta \simeq 1/2$ also in $d = 2$ [119].

3.4 RDSOS Model

We now motivate the imposition of restrictions on the value of N and the purpose of introducing the RDSOS model. If the discrete SOS models with bending stiffness are to be interpreted as models of amphiphilic membranes then it is useful to examine the physical meaning

of the unusual crumpling exhibited by the UDSOS model. For a fluctuating amphiphilic membrane there are two independent extensive variables, namely, the *total area* A of the membrane and the area A_p of the projection of the membrane on a reference base plane; for incompressible membranes A can change only if the membrane exchanges amphiphiles with a reservoir maintained at a fixed chemical potential μ whereas A_p can be altered by applying appropriate tension τ . Thus, one can define four different ensembles [124] :

- (i) (A, A_p) -ensemble: the membrane is *isolated* and *framed*;
- (ii) (μ, A_p) -ensemble: the membrane is *open* and *framed*;
- (iii) (A, τ) -ensemble: the membrane is *isolated* and *unframed*;
- (iv) (μ, τ) -ensemble: the membrane is *open* and *unframed*.

All the models considered in this chapter describe *framed* membranes. Since the area A diverges in the UDSOS model with $\mathcal{J} = 0$ in the limit $t \rightarrow \infty$, irrespective of A_p , this corresponds, effectively, to an *open framed* membrane. On the other hand, in a realistic situation amount of amphiphiles available is likely to be finite and, therefore, it motivates us to impose restrictions on the allowed fluctuations of the membrane area A by restricting N to remain finite.

Next, we describe the MC results for the RDSOS model. We have monitored the width of the interface $W(L, t)$, for fixed L , as a function of time t in $d = 1$ and $d = 2$, starting from an initially flat configuration, following the algorithm of the MC simulation described earlier, and then repeated the computation with different values of L . We carried out these computations for several different sets of values of the parameters J , K and N , namely, (i) $J = 1, K = 0, N = 1$, (ii) $J = 0, K = 1, N = 1$, (iii) $J = 1, K = 0, N = 2$, (iv) $J = 0, K = 1, N = 2$.

The data for $W(L, t)$ in the case (i) is identical to that for the case (ii) as there is no

difference between the effects of J and K if $|\Delta h_i| = 0, 1$, as already explained above. Comparing the data for the case (iii) with those in the cases (i) and (ii) we find that, for any given t , $W(L, t)$ is certainly larger in the case (iii) as the height restrictions are less severe.

From the best fit to the curves $W(L, t)$ we find that the exponent β is *approximately* 0.25 not only in both the cases (i) and (ii) but also in the cases (iii)-(iv) thereby suggesting that $\beta \simeq 0.25$ is independent not only of N but also of J and K so long as N is finite unless both J and K vanish simultaneously. This estimate is to be contrasted with $\beta \simeq 0.5$ for UDSOS model.

We illustrate our method of analysis with the data for the parameter values $J = 0, K = 1, N = 2$. The width $W(L, t)$ of the RDSOS model for five different values of L are plotted in fig.3.8. The corresponding height-height correlation function $C(l)$ of the RDSOS model for the same values of the parameters, namely, $J = 0, K = 1, N = 2$ has been plotted in fig.3.9. From the best fits in figs.(3.8) and (3.9) we find $\beta \simeq 0.25$ and $\alpha \simeq 0.5$. In fig. 3.10 we have plotted $W(L, t)/L^\alpha$ vs t/L^z using the data of fig.3.8 and the values of the exponents α, β estimated above. We find that all the curves of fig. 3.8 collapse onto a single curve in fig.3.10, thus supporting the Family-Vicsek scaling relation [123]

$$W(L, t) \equiv L^\alpha f\left(\frac{t}{L^z}\right) \quad (3.16)$$

where $z = \alpha/\beta$. Thus, we conclude, the exponent β change its value from $\beta = 0.5$ to $\beta = 0.25$ when constraints are imposed restricting the maximum allowed height difference Δh_i to finite N .

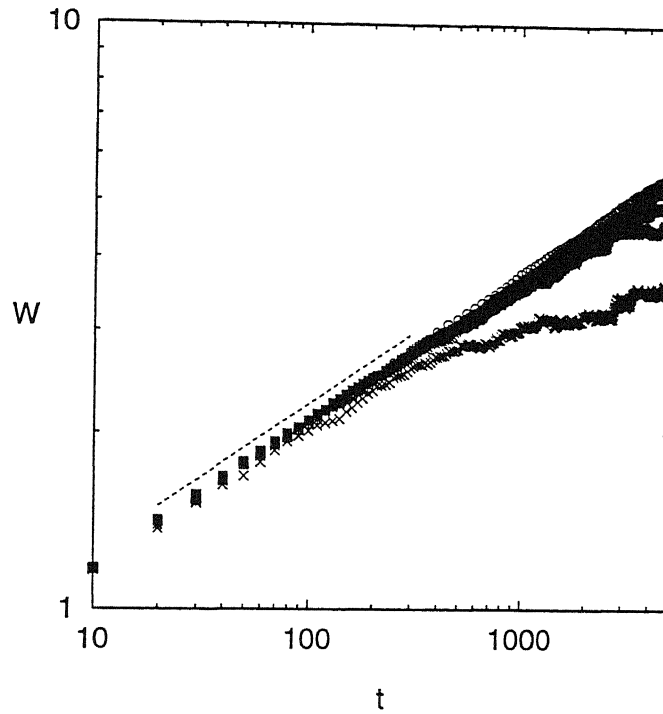


Figure 3.8: The time evolution of the width W of the interface in the RDSOS model in $d = 1$ for $N = 2$ (i.e., $|\Delta h_i| = 0, 1$ and 2). The different symbols correspond to different system sizes L : $L = 100(\times)$, $L = 200(*)$, $L = 400(\square)$, $L = 800(\blacksquare)$ and $L = 10000(\circ)$. The dashed line has slope $\beta = 0.25$. The parameter values are $J = 0$, and $K = 1$.

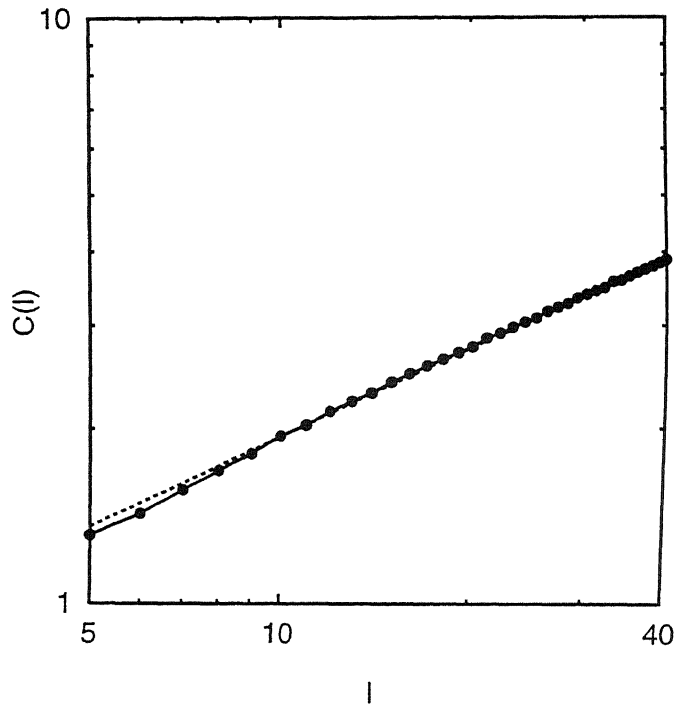


Figure 3.9: Height-height correlation function $c(l)$ for $J = 0, K = 1, N = 2$. The dashed line is the best fitted curve.

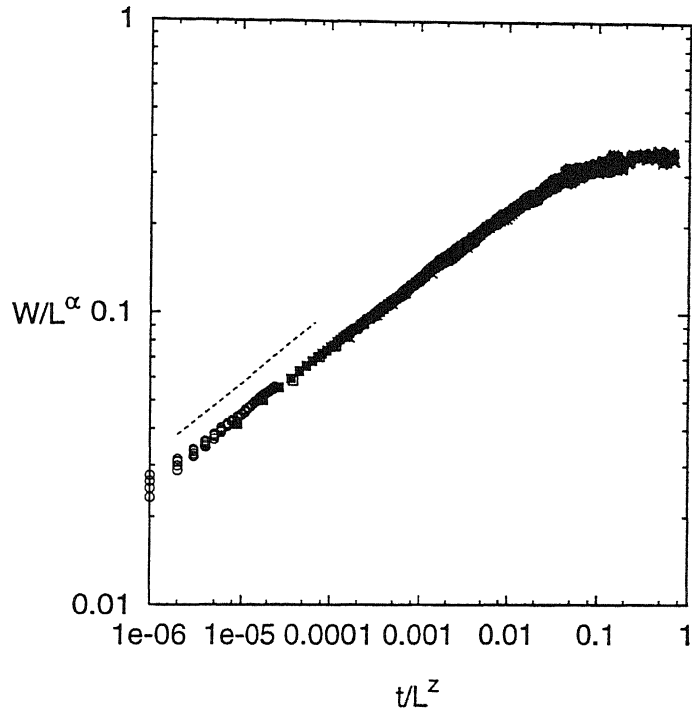


Figure 3.10: The data of figure 3.9 rescaled according to equation (3.16). The different symbols correspond to different system sizes L : $L = 100(\times)$, $L = 200(*)$, $L = 400(\square)$, $L = 800(\blacksquare)$ and $L = 10000(\circ)$. The slope of the dashed line is $\beta = 0.25$.

3.5 Comparison with Other Models

We can now compare our UDSOS model with the model of Kahng et al [99]. Kahng et al considered the following SOS hamiltonian that is equivalent to Eq. (1.1)

$$H_{SOS} = (J + 4M) \sum_{(r,r')}^{NN} |h_r - h_{r'}| + 2M \sum_{(r,r')}^{DNN} |h_r - h_{r'}| + M \sum_{(r,r')}^{LNNN} |h_r - h_{r'}| \quad (3.17)$$

while the RSOS Hamiltonian is given by

$$H_{RSOS} = J \sum_{(r,r')}^{NN} |h_r - h_{r'}| + 2M \sum_{(r,r')}^{DNN} |h_r - h_{r'}| + M \sum_{(r,r')}^{LNNN} |h_r - h_{r'}|, \quad (3.18)$$

where NN , DNN , and $LNNN$ mean nearest-neighbor columns, diagonal-nearest-neighbor, and linearly next-nearest-neighbor columns respectively. For both these models they calculated the moments of density gradient and the surface density as defined in chapter 2. The special SOS models considered by Kahng et al. do *not* include any bending energy of the type included in our model. Thus, interactions in their SOS models are similar to the first term on the right hand side of our equation (3.1). But, in addition to the interaction between the nearest-neighbour columns, they also allow interactions between farther-neighbour pairs of columns; the latter was motivated by the similar farther-neighbour interactions between the spin-pairs in the Widom model [35] The roughening of the interface in the Widom model has been described in chapter 2.

One common feature of our SOS model and the Widom model [35] is that there are bending energies associated with bendings over one lattice spacing. Another lattice model, which associates bending energies over bendings of the interface over single lattice spacings, has been found to mimic reliably the energies associated with bendings of interfaces over truly molecular dimensions [128]. However, the reliability of such bending energies in mimicing the energies associated

with bendings over longer length scales remains to be explored in detail.

We now compare the dynamics of evolution in our UDSOS and RDSOS models, from flat initial configurations, with some surface growth models. The crucial difference between our SOS models and the surface growth models is that the former describe relaxation to the thermal equilibrium while the latter are never in equilibrium. Therefore, the exponent α describes equilibrium roughening of the UDSOS and RDSOS models studied here whereas it describes kinetic roughening in the case of the surface growth models. The process $h_i \rightarrow h_i + 1$ in the SOS models studied here is the analogue of *deposition* of a particle on the column of particles rooted at the i -th site whereas the reverse process $h_i \rightarrow h_i - 1$ in our SOS models may be interpreted as *evaporation* of a particle from the existing column at the same site.

In the UDSOS model, except for an initial transient period starting from the flat conformation, there are large number of sites where the increase of height does not cost any extra energy if $\mathcal{J} = 0$, $\mathcal{K} \neq 0$. However, in the UDSOS model, there is a fraction of sites where energy change is possible when height is increased even if $\mathcal{J} = 0$. Therefore, although the process $h_i \rightarrow h_i + 1$ in our SOS models may be interpreted as random deposition of particles the deposition probability is not independent of the site. Moreover, no evaporation of particles is allowed in random deposition model of surface growth [123] In spite of these differences, the exponents α and β for our UDSOS model have the same values as the corresponding ones for the random deposition model of surface growth; for both $\beta = 0.5$, $\alpha = \infty$ [116, 123] .

The exponents α and β for the RDSOS model are different from the corresponding values for the restricted SOS model of surface growth [125] but are identical to the corresponding

exponents for the random deposition model with surface relaxation [125, 127] which is known to belong to the same universality class as that of the Edwards-Wilkinson model [123]. Mapping the restricted solid-on-solid model to a spin model and using the Master equation treatment for the spin systems, Plischke et al. [127] obtained $\beta = 0.25$. This is identical to the value of β in our RDSOS model in spite of $\mathcal{K} = 0$ in ref. [127] because of the fact that \mathcal{K} does not affect the exponent β of the RDSOS model when N is finite.

3.6 Conclusion

In this chapter we have proposed a discrete model of an interface with a specific form of the bending energy; this bending energy is associated with bending of the interface over as short a length scale as the size of a molecule. In the case of UDSOS model when the out-of-plane thermal fluctuations of this interface are controlled only by this bending stiffness it is crumpled but the nature of the crumpling is very different from that observed in the continuum models. We have shown that although the conformation of the interface in this case satisfies one particular definition of a crumpled manifold, it does not satisfy two other widely used definitions of crumpling although all these three definitions are known to be mutually consistent when applied to the continuum models. We have studied some dynamical properties of a UDSOS model in the special case $\mathcal{J} = 0, \mathcal{K} \neq 0$ in $d = 1$ by using a Master equation approach and the width of the interface W is found to vary with time t as $W \equiv \sqrt{t}$. By identifying an appropriate crossover length, we have also explained why the roughening exponent α of the UDSOS model in the presence of non-zero \mathcal{J} is independent of whether or not it has non-vanishing bending stiffness \mathcal{K} .

Introduction of a new RDSOS model is motivated through the examination of four different ensembles. By carrying out MC simulation of this RDSOS model, we compute an exponent β which characterizes the time-dependence of its width during the *very early stages* of its dynamical evolution from a flat initial configuration.

Finally, we point out some analogies between the relaxation from flat initial configuration to thermally roughened equilibrium conformation of these SOS models and the nonequilibrium growth of some kinetically roughened model surfaces.

Chapter 4

Oil - Water Interface in the 2-dimensional Larson type of model¹

4.1 Introduction

In all the models discussed so far in this thesis bending energy of the amphiphilic monolayer is introduced as a parameter. In real amphiphilic systems bending should arise from the microscopic interaction between different molecules and the conformational degrees of freedom of the amphiphilic molecules. Larson model discussed in chapter 1 explicitly takes into account the conformational degrees of freedom of the amphiphilic chain molecules and captures several essential features of these complex systems [3]. Here the system is modelled as a simple cubic lattice of size $L_x \times L_y \times L_z$. Each of the molecules of water and oil can occupy a single lattice site. A *single-chain* amphiphile can be described by the symbol $\mathcal{T}_m\mathcal{N}_p\mathcal{H}_q$ where \mathcal{T} denotes *tail*,

¹A paper based on this chapter has already been published by us (Prabal K. Maiti, Phys. Lett. A, **230**, 369 (1997))

\mathcal{H} denotes *head* and \mathcal{N} denotes the '*liaison*' or neutral part of the amphiphiles. m , p and q are integers denoting the lengths of the tail, neutral region and head, respectively, in the units of lattice sites. Thus, each amphiphile is a self-avoiding chain of non-overlapping sites of length $\ell = (m + p + q)$. We refer to each unit of an amphiphile, regardless of whether it is a part of the head, tail or liaison, as a *monomer*.

Jan, Stauffer and collaborators [45–47] reformulated the Larson model in terms of Ising-like variables, in the same spirit in which a large number of simpler lattice models had been formulated earlier for the convenience of calculations. The "water-loving" head group in this lattice model is assumed to be "water-like" and, similarly, the "oil-loving" tail group is assumed to be "oil-like". In this model an Ising spin variable S is assigned to each lattice site; $S_i = 1$ (-1) if the i -th lattice site is occupied by a water (oil) molecule. An amphiphile occupies several lattice sites each successive pairs of which are connected by rigid nearest-neighbour bond. If the j -th site is occupied by a monomer belonging to an amphiphile then $S_j = 1, -1, 0$ depending on whether the monomer at the j th site belongs to head, tail or neutral part. This version of the model takes into account *more* realistic features such as variation in the strength of the interactions between units, neutral parts of the chain, conformational interactions and repulsion between 'ionic' head groups [47].

The inter-molecular as well as intra-molecular inter-monomer interactions are taken into account through the interaction between the corresponding pair of Ising spins. Two spins interact provided the spins are located on the nearest- neighbour sites on the lattice. Thus, the Hamiltonian for the system is given by the standard form for an Ising spin system with only

nearest-neighbour interaction:

$$H = -J \sum_{\langle ij \rangle} S_i S_j. \quad (4.1)$$

We measure the temperature of the system in the units in which the monomer-monomer interaction $J = 1.0$ and the Boltzmann constant $k_B = 1.0$. The models were *simpler* than that developed by Larson in that only nearest neighbour interactions were allowed.

The moves allowed for the amphiphiles in the model are as follows: (i) *reptation*, (ii) *Kink movement*, (iii) *spontaneous chain-buckling*: a portion in the middle of the chain is allowed to buckle spontaneously (figure 4.1(a)). (iv) *pull*: an amphiphile which is not fully extended because of the existence of a buckle is allowed to be pulled out so as to wash out the buckle (figure 4.1(b)). (v) *wag*: the end of the tail of the amphiphile are allowed to 'wag' in a manner shown in figure 4.1(c), where the new position of the end monomer is chosen randomly from among the nearest-neighbour sites, which is occupied by oil/water. The moves allowed for the amphiphilic molecules in the algorithm are related to similar moves introduced earlier in the context of polymers [138, 139]; the "kink" move in our algorithm is identical to the "normal-bead motion" in ref [138]. Moreover, the "spontaneous chain-buckling" in our model not only generates new "buckles" or enhances the hump of existing buckles but also leads to the "crankshaft motion" [138] of existing buckles

Standard "Metropolis algorithm" is implemented. Each amphiphile is allowed to try each of the above mentioned moves once during each MC step. Time is measured in the units of the MC steps per molecule.

With the above model Stauffer, Jan and Pandey [45] studied the interfacial energy of an

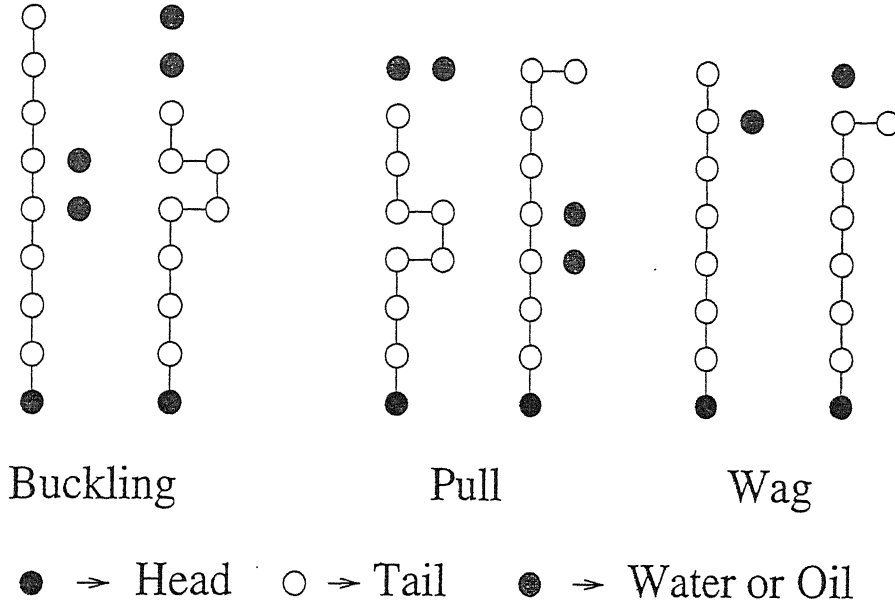


Figure 4.1: New moves introduced in reformulated version of Larson model

oil-water interface as a function of amphiphile concentration. They used amphiphiles of structure $\mathcal{H}_1\mathcal{N}_4\mathcal{T}_1$ with the spin of the head $S = +1$ and the tail $S = -1$ and looked at both two and three dimensional interfaces. Glauber Kinetics and only the reptation movement for the amphiphile was used. The interfacial energy was found to decrease as the concentration of surfactant was increased and was close to zero at a concentration of $\phi_a = 20\%$. It was also observed that the spontaneous magnetization $\sum_i S_i$, at a fixed temperature below the critical temperature $T_c = 4.51J$ of the pure Ising model, was destroyed by the presence of amphiphile showing that the amphiphiles made oil and water miscible *below* their normal miscibility temperature, explicitly demonstrating three-phase co-existence. With the above reformulation of the Larson model a lattice model of double-chain amphiphiles and gemini surfactants can be developed which has been described in chapters 6-7.

In this chapter we study the roughening properties of the interface in the above formulation

of the Larson model. We also investigate the physical origin of the lowering of oil-water interfacial tension by the single-chain surfactants in the reformulated Larson model. For these purpose we have computed the interfacial width in this model for different system sizes, temperatures and amphiphile concentrations by carrying out Monte Carlo simulation.

4.2 The Model

The system is modelled as a 2-dimensional square lattice of size $L_x \times L_y$. Each lattice site is occupied by one of the three molecular species, namely, either oil or water or a monomer belonging to an amphiphile. For simplicity we take the amphiphiles to be $\mathcal{H}_1\mathcal{T}_1$ i.e. amphiphiles molecule consist of a single head unit and a single tail unit. This model is similar to the model proposed by Kawakatsu and Kawasaki [129] for the study of phase separation process in immiscible binary mixture with a surfactant. A somewhat more realistic spin model of this type has been used to study the equilibrium properties of microemulsions by Chen et al [50].

The initial states are always constructed in such a way that water occupied the upper part while oil occupied the lower part of the lattice. The amphiphiles are put randomly at the interface. Periodic boundary condition is applied in the X -direction whereas a fixed boundary condition is applied in the Y -direction. The molecules in the two uppermost layers remain water while those in the two lowermost layers remain oil throughout the simulation. This initial condition helps us creating an interface in equilibrium. Liverpool and Bernardes [57], in their study of the behaviour of membranes with surfactants of type $\mathcal{H}_2\mathcal{N}_1\mathcal{T}_3$ and $\mathcal{H}_3\mathcal{T}_3$ without head-head repulsion, also found that a monolayer at the oil water interface could be stabilized by confining walls. During

the updating of the states of the system in our MC simulation we used Glauber dynamics (flip dynamics) for water and oil and the moves mentioned in section 4.1 for the amphiphiles. We measure the temperature of the system in the unit of J and the Boltzmann constant $k_B = 1.0$. We follow the standard Metropolis algorithm, explained chapter 1.

The interface profile was determined at each selected time as a density profile $\rho(y)$ - which is the fraction of water (oil) molecules in a particular lattice plane (i.e. fixed y). The width of the interface was determined through [115, 130, 101]

$$W^2 = \int y^2 w(y) dy - \left(\int y w(y) dy \right)^2 \quad (4.2)$$

with the statistical weight given by the density gradient

$$w(y) = -\left(\frac{d\rho}{dy}\right)/(\rho_1 - \rho_2) \quad (4.3)$$

Here ρ_1 and ρ_2 are the densities in the up (water rich) and down (oil rich) phase far away from the interface and the buffer planes at the ends of the lattice. All these integrals run from the bottom to the top of the lattice. In our discrete lattice, the integrals are of course replaced by sums.

Once the equilibrium is achieved, after every 1000 MC steps per site width of the interface is calculated and then averaged over 15 such runs to get the thickness W .

4.3 Results

First we have calculated the the width of the interface when there is no amphiphiles present in the system. This corresponds to the case of two dimensional Ising model. Width has been

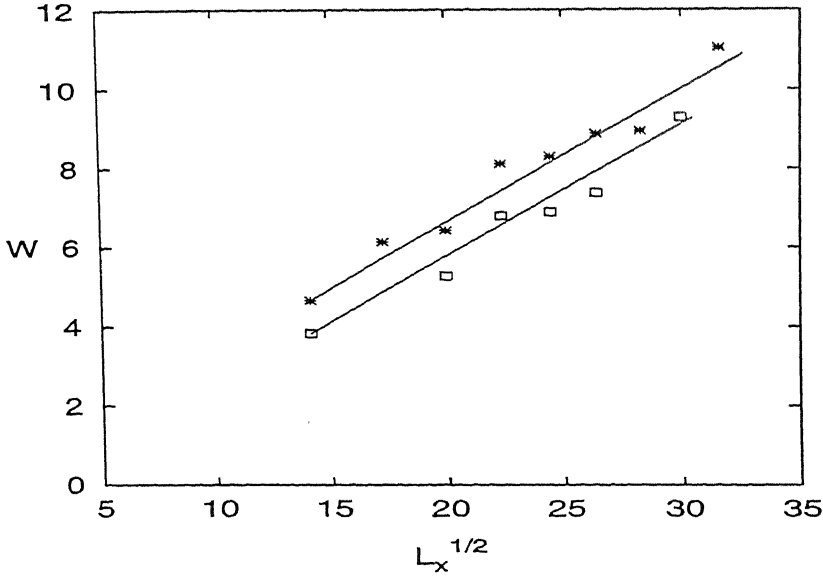


Figure 4.2: The width of the interface of the two dimensional Ising model is plotted against $\sqrt{L_x}$ for two different values of J : $J = 1.5$ (*) and $J = 1.8$ (□).

calculated for two different temperatures $J = 1.5$ and $J = 1.8$. We show in figure 4.2 that our data are indeed consistent with the known result that the width (W) of the interface of the two dimensional Ising model is proportional to $\sqrt{L_x}$. Moreover note that for the same value of L_x , the smaller the value of J , the larger the width of the interface as small J corresponds to higher temperature.

Next in Figure 4.3. we plot the width of the interface as a function of $\sqrt{L_x}$ for the same values of J as in Figure 4.2. but now for different non-zero concentration of amphiphiles (ϕ_a). Clearly the interface is still rough in the presence of amphiphiles. Moreover note that for a given L_x and J , the interface is wider for higher concentration of amphiphiles ($\phi_a = 80\%$) compared

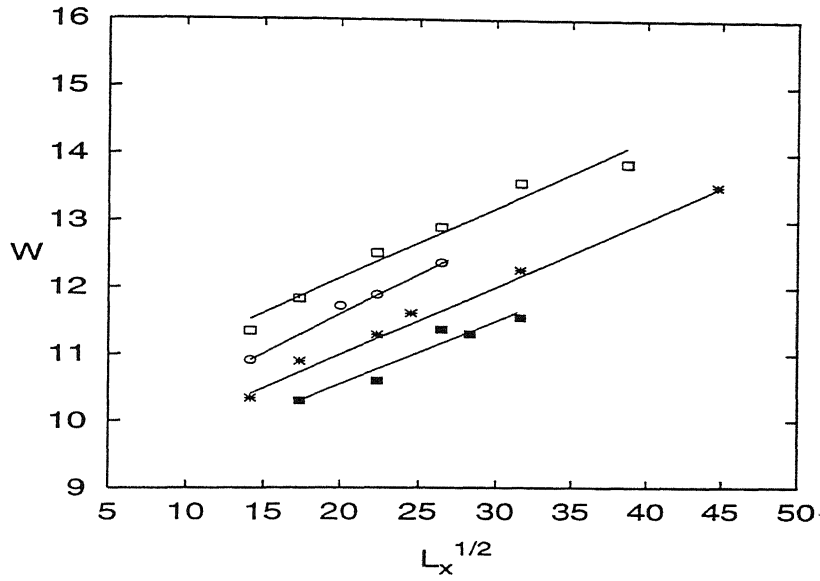


Figure 4.3: The width of the interface of the Larson model for different concentration (ϕ_a) of amphiphiles for different values of J is plotted against $\sqrt{L_x}$: $J = 1.5$ and $\phi_a = 50\%$ (*), $J = 1.5$ and $\phi_a = 80\%$ (\square), $J = 1.8$ and $\phi_a = 50\%$ (\blacksquare) and $J = 1.8$ and $\phi_a = 80\%$ (\circ).

COL		$\rho(y)$
4	a a a a a a a a a	+1.0
3	a a a a a a a a a	+1.0
2	-1.0
1	-1.0

Fig. 4.4(a)

COL		$\rho(y)$
4	a a a a a a a a a	+1.0
3	a a a a . a a a a	+0.8
2	-1.0
1	-1.0

Fig. 4.4(b)

Figure 4.4: (a) Picture of the interface when no amphiphiles are present. (b) interface after a single spin flip. a denotes water molecule and . denotes oil molecule.

to the interface width for lower concentration of amphiphiles $\phi_a = 50\%$.

The increase of interface width with increasing concentration of amphiphiles is a consequence of the lowering of the oil-water interfacial tension by the amphiphiles. This reduction in surface tension has also been observed by Stauffer et. al [45] in a ternary mixture of oil, water and amphiphiles. In their simulation they used amphiphiles of chain length 6. However, as is evident from our simulation, this lowering of interfacial tension and consequent widening of the interface width can be captured with amphiphiles of shortest possible length, namely, two monomers. Therefore it is the amphiphilicity of the surfactant which is essential for the reduction of interfacial tension.

We shall now argue that the lowering of the interfacial tension by the amphiphiles in the model studied here is of entropic origin.

Consider Figure 4.4(a) and Figure 4.4(b). In Figure 4.4(a) we have created an interface without any amphiphiles. Figure 4.4(b) gives the picture of the interface after a single spin flip

COL	$\rho(y)$
4	a a a a a a a a +1.0
3	a a a a A a a a +1.0
2 - -1.0
1 -1.0

Fig. 4.5(a)

COL	$\rho(y)$
4	a a a a A a a a +1.0
3	a a a a - a a a a +0.8
2 a -0.8
1 -1.0

Fig. 4.5(b)

Figure 4.5: (a) Picture of the interface when one single amphiphile is present. (b) interface after the amphiphile has made a reptation movement. a denotes water molecule and . denotes oil molecule. A and - are the head and tail of the amphiphile molecule respectively.

and also the value of $\rho(y)$. The weight factor (Equation 4.3) in discrete form can be written as

$$w(y) = \frac{\rho(y-1) - \rho(y+1)}{2(\rho_1 - \rho_2)}. \quad (4.4)$$

Here $\rho_1 = 1$ and $\rho_2 = -1$. The width of the interface given by Equation. 4.1 can be written for the discrete case as follows

$$W^2 = \sum_{m=1}^{COL} (y_m - y_{boundary})^2 w(y_m) - \left(\sum_{m=1}^{COL} (y_m - y_{boundary}) w(y_m) \right)^2. \quad (4.5)$$

where $y_{boundary}$ gives the position of the interface and is given by $COL/2$. Here $y_{boundary} = 2$. Substituting the values of $w(y_m)$ (using Equation 4.4) in Equation 4.5 we find width of the interface to be 0.1 Now consider Figure 4.5(a) and Figure 4.5(b). In Figure 4.5(a) we have created an interface with a single amphiphile. Figure 4.5(b) gives the picture of the interface after the amphiphile has made reptation movement in one of the possible directions and also the value of $\rho(y)$. Reptation movement in two other possible directions also give the same value of $\rho(y)$ Substituting the values of $w(y_m)$ (using Equation 4.4) in Equation 4.5 we find width of the interface to be 0.2. So we see that the width of the interface has increased when there is

amphiphile movement. Amphiphile movement gives rise to larger variation in $\rho(y)$ as compared to the single spin flip. This is equivalent to the statement that the the presence of amphiphiles reduces the tensions of the oil-water interface and the decrease in interfacial tension allows a larger width of the interface. This reduction in the tension is due to the fact that as the interfacial area is increased the translational entropy of the amphiphile molecule is increased (for a fixed number of amphiphile molecules). This increase in entropy lowers the system free energy and thus reduces surface tension from its bare value [142].

4.4 Conclusion

In summary we have shown that the width of the oil-water interface in the Larson model varies as $\sqrt{L_x}$. Moreover, the wider interface in the presence of amphiphiles in this model is a consequence of the lowering of the oil-water interfacial tension by the surfactants; we have argued that this reduction of surface tension in this model is of entropic origin.

Chapter 5

Out-of-plane phase segregation and in-plane clustering in a binary mixture of amphiphiles at air-water interface¹

5.1 Introduction

After studying the properties of the amphiphilic monolayer at the oil-water interface in chapters 2,3 and 4 we now investigate the air-water interface in the presence of single chain amphiphiles. The spatio-temporal organization of amphiphiles in a system where water is separated

¹A paper based on this chapter has already been published by us (Debashish Chowdhury, Prabal K. Maiti, S. Sabhapandit and P. Taneja, Phys. Rev. E, in press

from air above it by the air-water interface has been studied by Chowdhury [131]. This is different from the oil-water interface in a microemulsion, because, unlike oil and water in a microemulsion, here the air and water are not allowed to get dispersed in each other. Consequently it is sometimes referred to as a pseudo-ternary system.

The Hamiltonian is the same as Equation 4.1 though air was represented by $S_i = -1$. Systems of sizes $L_x \times L_y \times L_z$ were studied. The system consisted of L_{air} layers of air, lying on top of $L_z - L_{air}$ layers of water, with the amphiphiles initially distributed at the interface. The amphiphiles were of the type $\mathcal{H}_2\mathcal{T}_n$ where $n = 5$ or 15 . The moves of the molecules of water, air and amphiphiles are slightly modified so as to reflect the fact that air and water were not allowed to exchange position as dispersions of air and water inside each other is not possible.

In addition to the three movements described earlier, an extra movement of lateral diffusion of chains along the interface was allowed. Chowdhury studied the behaviour of a small concentration of chains placed at the air-water interface. The largest system size studied was $30 \times 30 \times 100$. At low temperatures, they all remained at the interface but as the temperature was increased more and more of the amphiphiles moved to the bulk signifying an increase in the solubility with temperature. There was a dramatic increase in solubility over a narrow range of temperature. This trend is consistent with the earlier experimental observations. It was also observed that at any given temperature, the solubility was lower for amphiphiles with longer hydrophobic chains than for those with shorter hydrophobic chains, also in agreement with experiment.

Chowdhury et al. [86] also studied the case where the polar heads of amphiphiles are either *grafted* or *adsorbed* on a solid substrate. When they are grafted, they are fixed to a particular point on the surface and can only move by chain conformational rearrangements. If the chains

are adsorbed, they cannot move away from the substrate, but they can diffuse laterally on the surface. Experimentally this has been extensively studied in the context of Langmuir-Blodgett films [85].

Chowdhury et al. studied several properties such as the number of monomers at depth z , the average vertical extent of amphiphiles, information on the average orientation of the amphiphilic molecules and that of the bonds connecting the monomers. Chowdhury et al. [86] observed, for *grafted* and *adsorbed* amphiphiles, that the orientational order increased with surface density in agreement with experiment [85], theory [87] and Molecular dynamics simulation [88].

In this chapter we are interested in binary mixtures of single chain amphiphiles in water and at air-water interface. We introduce a microscopic lattice model of a binary mixture of amphiphilic molecules, of two different lengths, in a system where water is separated from the air above it by a sharp well defined interface. We demonstrate an entropy-driven phase segregation in a direction perpendicular to the air-water interface when the initial total surface density of the amphiphiles is sufficiently high. We also investigate (a) the conformations of the amphiphiles, (b) the distribution of the sizes of the clusters of monomers belonging to the long amphiphiles as well as of those belonging to the short amphiphiles in planes parallel to the interface, (c) the effects of varying the lengths, total concentration and the ratio of the numbers of the two types of the amphiphilic molecules, the strength of the inter-monomer interactions and temperatures.

We shall compare the phenomena observed in our computer simulation with some similar phenomena in grafted polymers and compare the underlying physical mechanisms in the two cases.

The chapter is organized as follows: The model and the characteristic quantities of interest

are defined in the sections 5.2 and 5.3, respectively. The concentration profiles of chemically identical amphiphiles of two different lengths are presented in section 5.4. The in-plane clustering of the amphiphile monomers are studied in section 5.5. Conformations of the amphiphiles are investigated in section 5.6. Results for chemically different amphiphiles are summarized in section 5.7. In section 5.8, we compare our results with laboratory experiments and binary mixture of grafted polymers. Finally, in section 5.9, we present a summary of our results.

5.2 The Model

The model developed is based on the reformulated Larson model of microemulsions discussed in chapter 4. The system is modelled as a simple cubic lattice of size $L_x \times L_y \times L_z$ where the horizontal air-water interface is parallel to the XY -plane and the *vertically downward* direction is chosen as the $+Z$ -axis.

Since we are studying a binary mixture of the amphiphiles, let us represent them by the two symbols $\mathcal{H}_{q_\ell} \mathcal{T}_{m_\ell}$ and $\mathcal{H}_{q_s} \mathcal{T}_{m_s}$ for the long and short amphiphiles, respectively, so that the lengths of the long amphiphiles is $L_\ell = q_\ell + m_\ell$ and that of the short amphiphiles is $L_s = q_s + m_s$. All our investigations have been carried out for a fixed value of $q_\ell = q_s = 2$.

Notice that the monomers of the same chain as well as different chains are not allowed to occupy the same lattice site; this represents a hard-core intra-chain as well as inter-chain repulsion for chain separations smaller than one lattice spacing. Moreover, at any non-vanishing temperature, during the out-of-line thermal fluctuations of the chains, the hard-core repulsion leads to steric repulsion between the chains. Furthermore, in the present formulation, there are

no potential energies associated with the torsion of isolated amphiphiles in water.

Since both types of amphiphiles are represented by the Ising spin variables the amphiphiles may be regarded as *chemically* identical if the strength of the interaction J is also assumed to be identical for both types of amphiphiles. However, chemically different types of amphiphiles can be modelled by taking different values of the interactions J_{LL} , J_{SS} and J_{LS} , where J_{LL} is the interaction between two monomers both belonging to the long amphiphiles, J_{SS} is that between two monomers both belonging to short amphiphiles while J_{LS} is that between two monomers one of which belongs to a long amphiphile and the other to a short amphiphile.

In our model here, chemically different amphiphiles can be described by first associating a "strength" C_i with the i -th site ($i = 1, 2, \dots, N$). If the i -th site is occupied by water or air then $C_i = 1$ whereas $C_i = C_\ell(> 0)$ if the i -th site is occupied by a monomer belonging to a long amphiphile while $C_i = C_s(> 0)$ if the i -th site is occupied by a monomer belonging to a short amphiphile. In this case, the Hamiltonian for the system is given by

$$H = -J \sum_{\langle ij \rangle} C_i C_j S_i S_j \quad (5.1)$$

Here we study the binary mixtures of chemically identical as well different amphiphiles.

In each of the computer experiments, the initial state is constructed in such a way that air occupies the upper part while water occupies the lower part of the lattice. We begin with a mixture of N_ℓ long amphiphiles and N_s short amphiphiles; the heads of all the amphiphiles were initially put randomly on the sites in a horizontal lattice plane immediately below the air-water interface in a lattice of size $L_x \times L_y \times L_z$ and each of the amphiphiles was fully extended in the vertical direction. The system is then equilibrated at temperature T using the following dynamics:

during the updating of the states of the system in our MC simulation, air and water molecules were not allowed to exchange position as dispersion of air and water inside each other is not possible in our model.

The moves allowed for the amphiphiles in our model are as follows : (i) *reptation* (ii) *spontaneous chain-buckling*, (iii) *Kink movement* and (iv) *Lateral diffusion at the interface*: those amphiphiles whose heads are located no deeper than the molecular layer at the interface are allowed to move laterally where one of the four possible directions is chosen randomly and each of the units of the amphiphile is moved in that direction by one lattice constant. Each of these moves is possible only if the new positions are not occupied by any other amphiphile.

We follow the standard "Metropolis algorithm": each of the above mentioned moves takes place certainly if $\Delta E < 0$ and with a probability proportional to $\exp(-\Delta E/T)$ if $\Delta E \geq 0$, where ΔE is the change in energy that would be caused by the proposed move of the amphiphile under consideration. Each amphiphile is allowed to try each of the above mentioned moves once during each MC step. Time is measured in the units of the MC steps per molecule.

The largest systems simulated were $60 \times 60 \times 100$. However, the data for smaller systems, e.g., $30 \times 30 \times 100$ do not differ significantly from those for these large systems. Therefore, most of the production runs were made for $30 \times 30 \times 100$ systems. The data were averaged over sufficient number of different initial configurations; typically ten configurations were found to be adequate.

5.3 Definitions of characteristics quantities of interest

Now we define all the quantities we intend to compute for these models through MC simulation. We compute all these characteristic quantities for the long amphiphiles and the short amphiphiles separately.

The gross features of the spatial organization of the constituent molecules can be expressed through the equilibrium profiles of concentrations of the amphiphiles in the Z -direction, i.e., in the direction perpendicular to the air-water interface. So far as the concentration profiles of the amphiphiles are concerned, one can calculate two different quantities: at each layer one can count the number of monomers or one can count just the number of hydrophilic *heads* in that layer.

It is straightforward to see that at any non-vanishing temperature, the amphiphiles cannot remain fully extended. One of the quantities that characterize the average size of the amphiphiles is their average radius of gyration (R_g) which is defined by

$$R_g = \left[\frac{1}{N_a L_a} \sum_{j=1}^{N_a} \sum_{i=1}^{L_a} \{R_i(j) - R_{cm}(j)\}^2 \right]^{1/2} \quad (5.2)$$

$$R_{cm} = \frac{1}{L_a} \sum_{i=1}^{L_a} R_i$$

where $R_i(j)$ is the position of i -th monomer of the j -th amphiphile and R_{cm} is the corresponding center of mass of a single amphiphile. The symbol [...] shows the ensemble averaging over different configurations. The symbols L_a and N_a denote, respectively, the length and the number of the amphiphiles of the particular species under consideration; for the computation of the radius of gyration of the long amphiphiles we take $L_a = L_\ell$, $N_a = N_\ell$ and for that of the short amphiphiles we take $L_a = L_s$, $N_a = N_s$.

Next, we introduce a measure of the average projection of the amphiphiles on the Z -axis at a given instant of time t as follows: we calculate $\Delta Z(t)$, the difference of the instantaneous values of the z -coordinates of the highest and the lowest monomers (i.e., the monomers with the largest and the smallest values of z -coordinates), on each amphiphile and average it over all the amphiphiles of the same species present in the system thereby getting $\langle \Delta Z(t) \rangle$. The data are, then, averaged over a sufficiently large number of runs thereby getting the configurationally-averaged value $[\langle \Delta Z(t) \rangle]$. In order to get a more detailed information on the distribution of vertical extent of the amphiphiles we simultaneously also calculate $P(\Delta Z)$, the fraction of the amphiphiles with vertical extent ΔZ at equilibrium.

Another related quantity of interest is $[\langle R_z(t) \rangle]$, the average instantaneous projection of the vector $\vec{R}(t)$ on the Z -axis where $\vec{R}(t)$ for a given amphiphile is the vector *from* the first monomer on its head *to* the last monomer on its tail. Note that, in equilibrium, the first monomer on the head and the last monomer on the tail of an amphiphile do not necessarily have the largest and smallest z -coordinates. Therefore, in general, $[\langle R_z \rangle]$ is smaller than $[\langle \Delta Z \rangle]$. Moreover, ΔZ is always positive whereas, in general, for amphiphiles in water, [131], $R_z(t)$ can be both positive and negative. Therefore, at every temperature T the equilibrium value of $[\langle R_z(t) \rangle]$ has been used as the order parameter for measuring the *average orientational order* (Ψ) exhibited by the "head-to-tail" vectors at the temperature T .

A detailed information on the orientation of the individual *bonds* between the monomers of the amphiphiles is contained in the so-called "bond orientational order parameter", defined as

$$\Phi(p) = (1/N_a) \sum_{i=1}^{N_a} (3 \langle (z_{i,p+1} - z_{i,p})^2 \rangle - 1) / 2 \quad (p = 1, \dots, L_a - 1) \quad (5.3)$$

where $i = 1, 2, \dots, N_a$ ($N_a = N_\ell$ for the long amphiphiles and $N_a = N_s$ for the short amphiphiles) refer to the amphiphiles and $z_{i,p}$ refers to the z -coordinate of the p -th monomer on the i -th amphiphile. Thus, $z_{i,p+1} - z_{i,p}$ is the difference in the heights of the two end points of the p -th bond connecting the p -th and $p + 1$ -th monomers of the i -th amphiphile. For example, $\Phi(p) = -0.5$ describes a situation where the p -th bond, on the average, lies in a plane parallel to the air-water interface whereas $\Phi(p) = 1$ corresponds to a vertical p -th bond. The factors 3 in the numerator and 2 in the denominator in equation (4) have been chosen so that $\Phi(p) = 0$ in case of complete randomness in the orientation of the corresponding bond. In this chapter we shall study the effects of varying the parameters $L_\ell - L_s$, $R_d = N_\ell/N_s$, T , C_i and C_j etc.

5.4 Concentration profiles for chemically identical amphiphiles of different lengths

We begin with a mixture of 405 long amphiphiles and 405 short amphiphiles, i.e., $N_\ell = 405 = N_s$ and the size of the lattice is $30 \times 30 \times 100$. The system was equilibrated at a temperature $T = 2.5$ using the dynamics described in section 2. The concentration profile of the hydrophilic heads of the long as well as the short amphiphiles are shown in fig.5.1. The two profiles are clearly shifted with respect to each other thereby establishing a vertical phase segregation of the long and the short amphiphiles. We shall refer to this computer experiment as the *first* experiment.

Next we carry out further experiments to establish the physical reason for this phase segregation. We reduce the concentrations of both types of the amphiphiles by a factor of 9, but keeping the relative concentration ratio of the two types 1 : 1, as before, without changing the

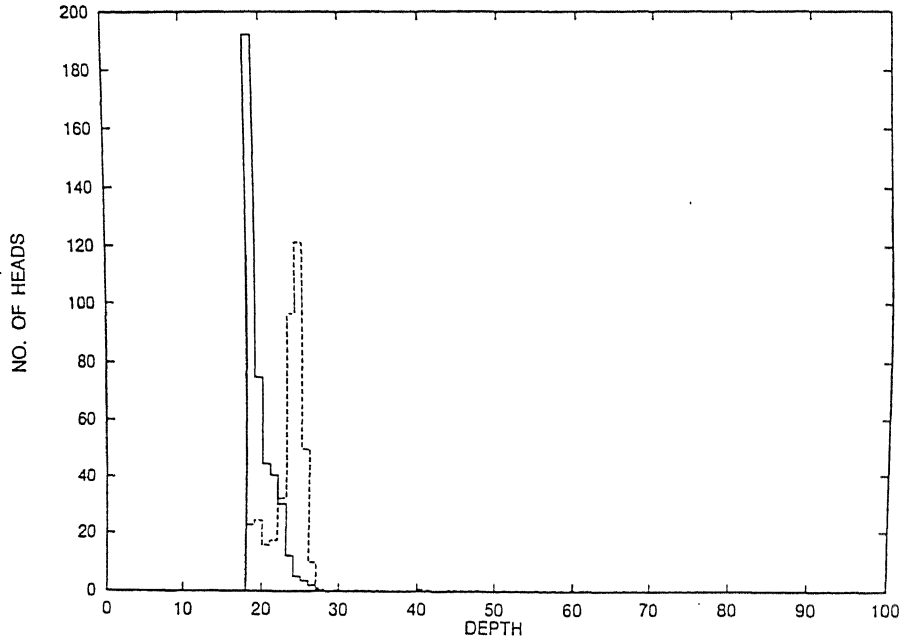


Figure 5.1: The equilibrium concentration profile of the hydrophilic heads perpendicular to the air-water interface. The system consists of $30 \times 30 \times 100$ lattice sites and contains a mixture of 405 long amphiphiles of length 17 and 405 short amphiphiles of length 7 equilibrated at temperature $T = 2.5$. The solid lines correspond to the long amphiphiles whereas the dashed lines correspond to the short amphiphiles.

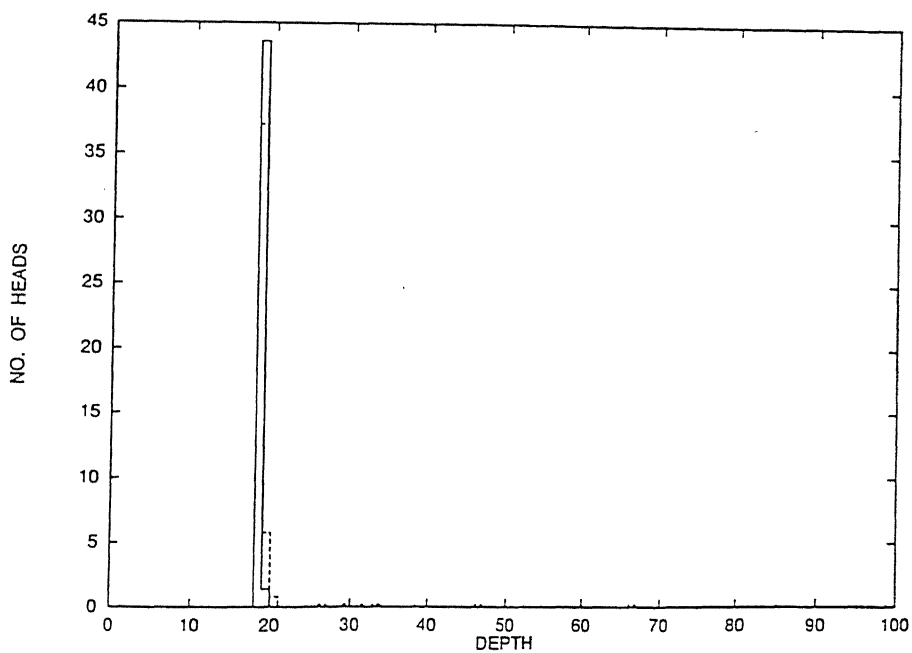


Figure 5.2: Same as in fig.5.1 except that there are 45 amphiphiles of each type, instead of 405.

size of the system. In other words, we now repeat the first experiment with 45 long amphiphiles and 45 short amphiphiles in a system of size $30 \times 30 \times 100$ at $T = 2.5$. Interestingly, unlike fig.5.1, no vertical phase segregation is now observed in the equilibrium profiles plotted in fig.5.2. We refer to this experiment as the *second* experiment.

Note that the crucial difference between the first and the second experiments lies in the different initial surface densities of the amphiphiles; the total number of amphiphiles in the first experiment is 810 whereas that in the second experiment is 90 although the total number of sites available in the plane immediately below the air-water interface is 900 in both the experiments. In other words, the initial surface density of the amphiphiles in the first experiment is 90% whereas that in the second experiment is only 10%. Does it imply that the vertical phase segregation observed in the first experiment occurs only if the surface-density of the amphiphiles is sufficiently high. In order to check this possibility we carry out our *third* experiment.

In the third experiment we keep the numbers of amphiphiles of both varieties fixed at 45 but the lattice size is taken to be $10 \times 10 \times 100$. Thus, the numbers of amphiphiles of both types in this experiment are identical to those in the second experiment while the initial surface density of the amphiphiles in this experiment is identical to that in the first experiment. In the third experiment we observe a vertical phase segregation (see fig.5.3) which is very similar to that observed earlier in the first experiment! Thus, we conclude that the vertical phase segregation takes place only if the initial *surface density* of the amphiphiles is sufficiently high.

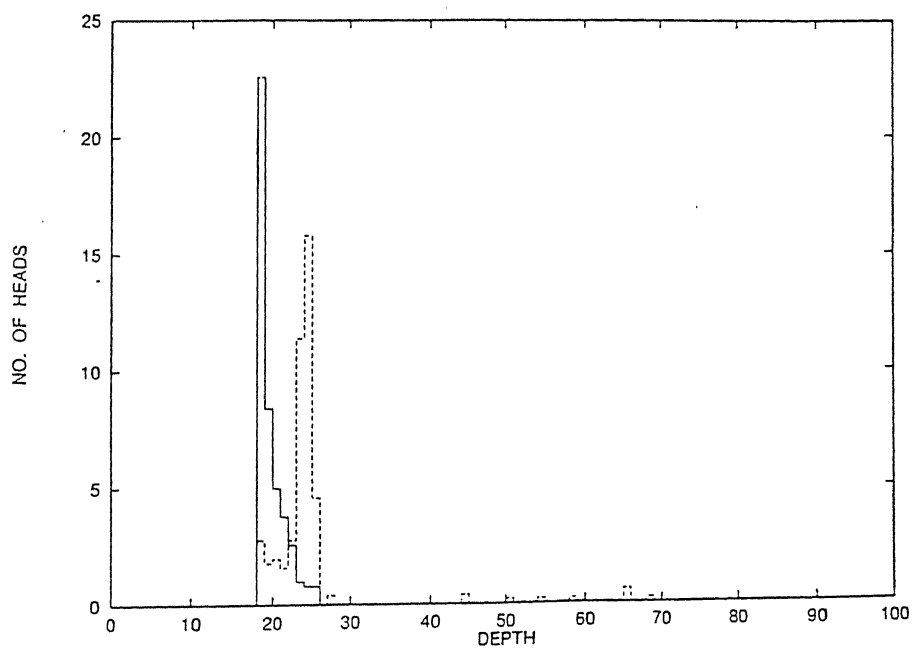


Figure 5.3: Same as in fig.5.2 except that the size of the lattice is $10 \times 10 \times 100$.

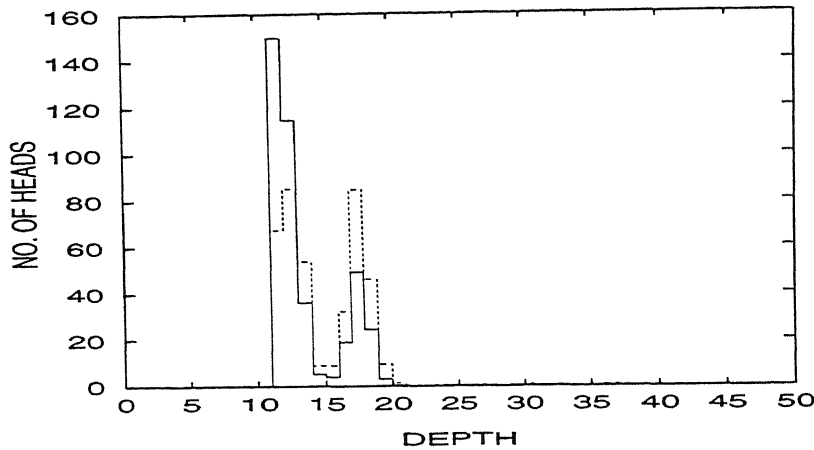


Figure 5.4: Same as in fig.5.1 except that the lengths of the long and the short amphiphiles are 17 and 13, respectively.

5.4.1 Dependence on the lengths of the hydrophobic tails

In this subsection we shall examine the effects of varying the lengths n_ℓ and n_s of the hydrophobic tails by keeping the size of the heads of both types of amphiphiles fixed at $m_\ell = m_s = 2$ in a binary mixture of equal numbers of the two types of the amphiphiles.

We have repeated the *first* experiment with amphiphiles of lengths 17 and 13, instead of 17 and 7. The vertical phase segregation observed in this experiment (see fig.5.4) is qualitatively very similar to that observed in the first experiment. However, the phase segregation is not as complete as it was in fig.5.1. Similarly, again repeating the first experiment with amphiphiles of lengths 10 and 7 we observed vertical phase segregation of the long and short amphiphiles, as before (fig.5.5). Thus, in a binary mixture of equal numbers of chemically identical amphiphiles of two different lengths, the phase segregation is more complete when the longer amphiphiles are

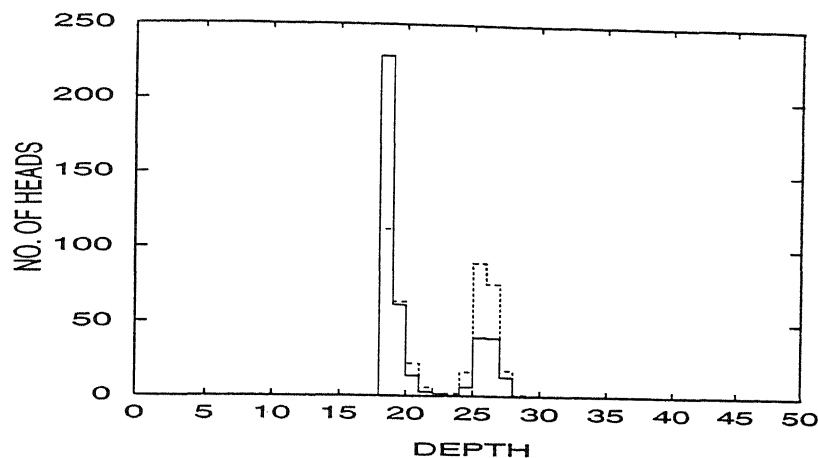


Figure 5.5: Same as in fig.5.1 except that the lengths of the long and the short amphiphiles are 10 and 7, respectively.

very long and the shorter amphiphiles are very short.

Since in this section we are considering chemically identical amphiphiles, a binary mixture of 405 long amphiphiles and 405 short amphiphiles reduces to a system of 810 effectively identical amphiphiles in the limit of vanishing length difference. Even in such a situation, a fraction of the amphiphiles are forced out of the monolayer in the equilibrium state provided the amphiphiles are sufficiently long (fig.5.6).

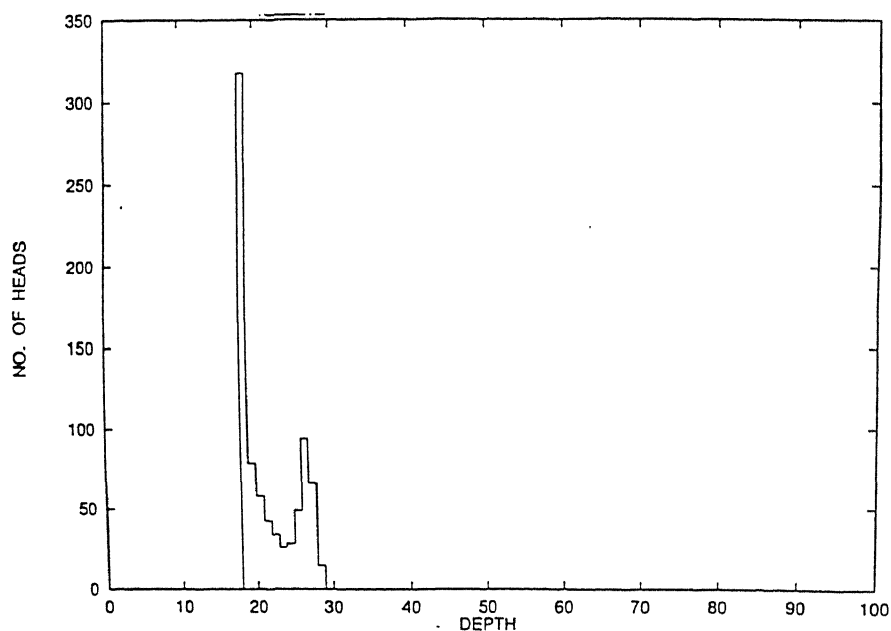


Figure 5.6: The equilibrium concentration profile of the hydrophilic heads perpendicular to the air-water interface. The system consists of $30 \times 30 \times 100$ lattice sites and contains 810 amphiphiles each of length 17. The system has been equilibrated at temperature $T = 2.5$.

5.4.2 Dependence on the ratio of the initial surface densities of the two components

So far, we have taken equal initial surface densities of the long and short amphiphiles. In this subsection we study the effects of varying the ratio of the initial surface densities of the two types of amphiphiles. Since in all our earlier computer experiments we did not find any significant difference in the results (when appropriately normalized) for lattices of cross-section 30×30 and 20×20 , all the experiments to be discussed in this subsection have been carried out for $20 \times 20 \times 100$ lattices. Moreover, since the extent of unmixing is largest for the amphiphiles of lengths 17 and 7, the computer experiments in this subsection have been carried out with the lengths 17 and 7 of the long and the short amphiphiles, respectively.

The concentration profiles of the hydrophilic heads of both the long and short amphiphiles are shown in figs.5.7(a)-(d) for four different ratios of the initial surface-densities of the two types of the amphiphiles. If the ratio $R_d = N_\ell/N_s$ is small (figs.5.7(b) and 5.7(d)) very few of the longer amphiphiles require to be sterically expelled from the long-rich layers. With the increase of the ratio R_d not only the population of shorter amphiphiles in the long-rich layers decrease, but an increasingly larger number of the longer amphiphiles are sterically expelled.

5.4.3 Dependence on the temperature

The values of the parameters in figs.5.8(a)-(d) are identical to those in figs.5.7(a)-(d) except that the temperature in fig.5.8 is $T = 1.0$ in contrast to $T = 2.5$ in fig.5.7. No vertical

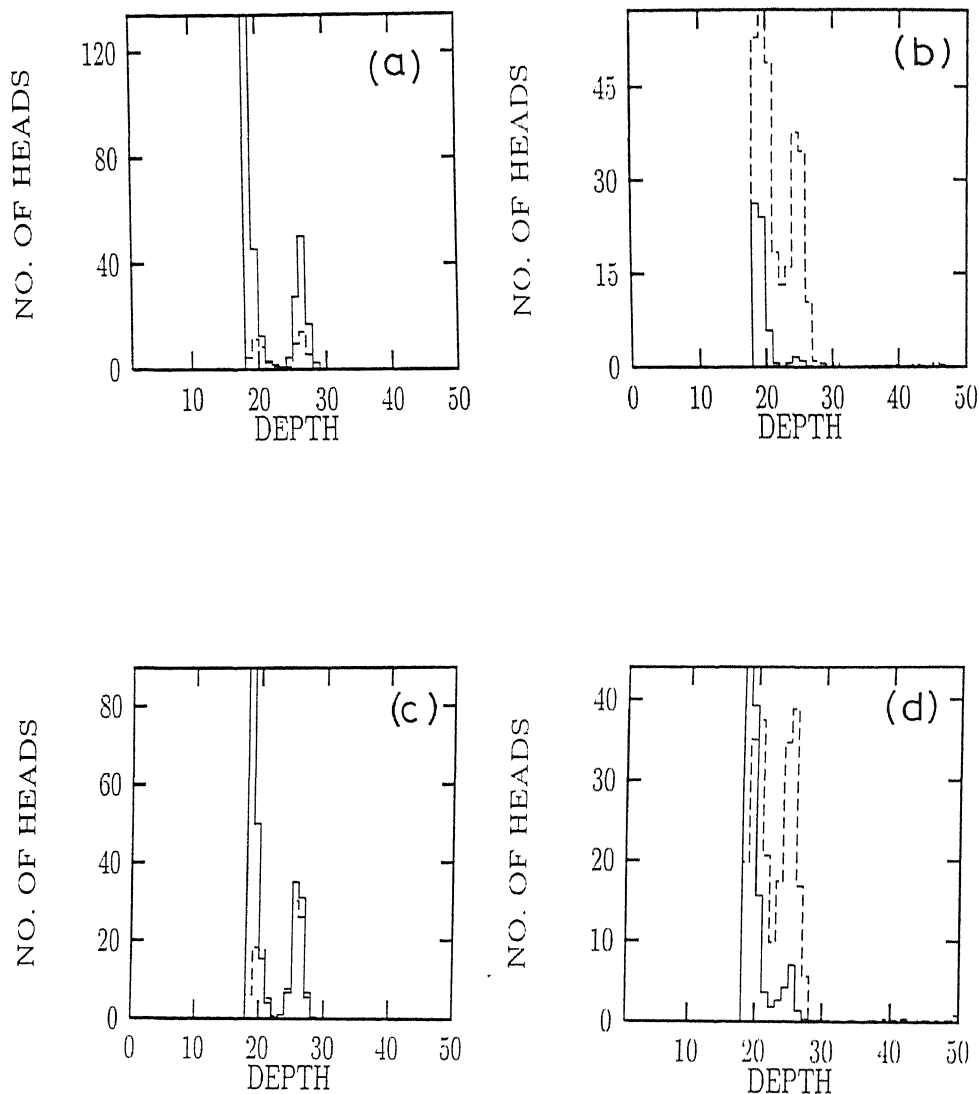


Figure 5.7: The equilibrium concentration profile of the hydrophilic heads at $T = 2.5$ perpendicular to the air-water interface in a system consisting of $20 \times 20 \times 100$ lattice sites. The numbers of long and short amphiphiles are, respectively, 300 and 60 in (a), 60 and 300 in (b), 240 and 120 in (c), 120 and 240 in (d); the continuous line corresponds to the long amphiphiles and the dashed line corresponds to the short amphiphiles.

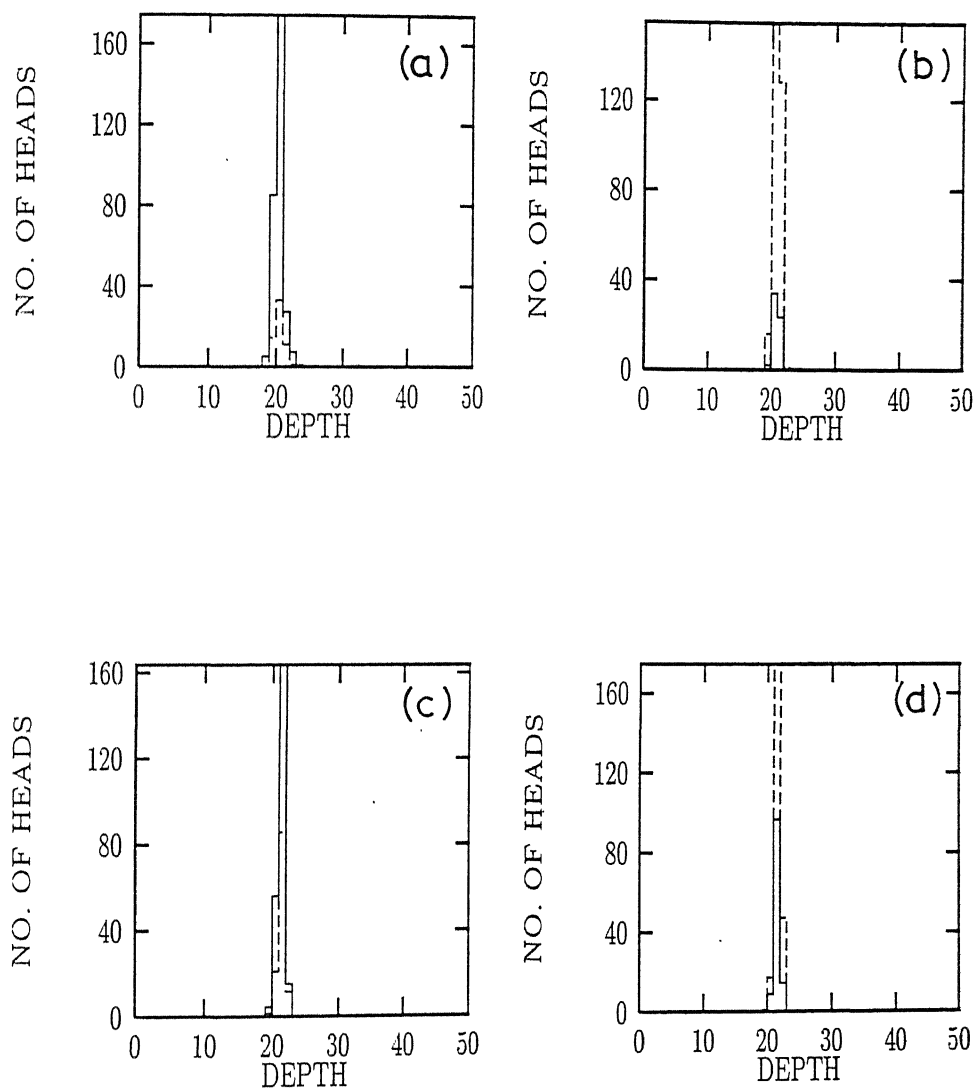


Figure 5.8: Same as in fig.5.7, except that the temperature of the system is $T = 1.0$.

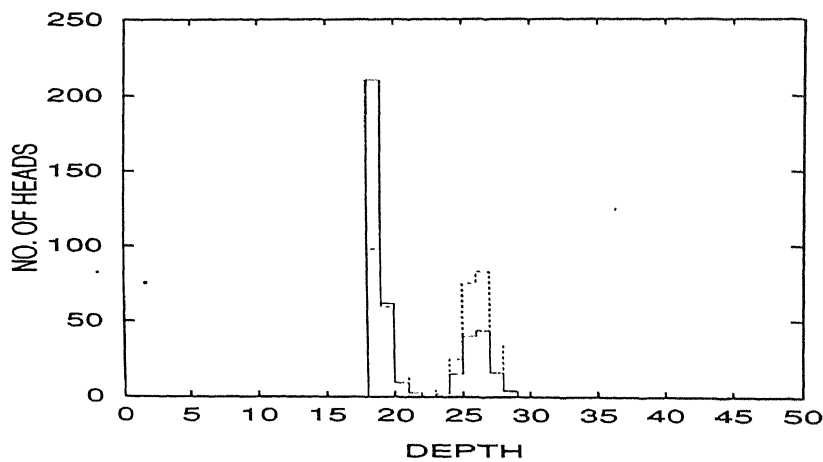


Figure 5.9: Same as in fig. 5.4, except that the bending stiffness of each of the amphiphiles is $K = 2$ in contrast to $K = 0$ in fig.5.4.

phase segregation takes place at the lower of the two temperatures. Clearly, temperature plays a crucial role in driving the out-of-plane phase segregation phenomenon. This is consistent with our interpretation that the phase segregation of the long and the short amphiphiles is *entropy*-driven; at low temperatures the likelihood of spontaneous buckling of the chains is very small and, hence, the steric interaction is suppressed.

5.4.4 Effect of bending stiffness of the amphiphiles

Because of the discreteness of the lattice only bends by 90° of an amphiphile at a lattice site is possible. Every bend of an amphiphile is assumed to cost an energy K . This is the bending stiffness of the individual amphiphiles, in contrast to the bending stiffness of the amphiphilic

membranes considered in chapters 2 and 3. In fig.5.9 we show the equilibrium concentration profile for a mixture of 405 amphiphiles of length 17 and an equal number of amphiphiles of length 13 in a $30 \times 30 \times 100$ system, where each bending of the amphiphiles of either variety costs an energy of $K = 2$ in the units of J . Clearly, there is no significant difference between the profile in fig.5.9 and the corresponding profile for $K = 0$ shown in fig.5.4. Thus, bending stiffness of the amphiphiles do not have significant effect on this phase segregation phenomenon unless K is very large; in the limit of $K \rightarrow \infty$ a total of $L_x \times L_y$ number of amphiphiles can be accommodated in the monolayer at the air-water interface irrespective of the lengths of each of the individual amphiphiles because each amphiphile remains straight and fully extended in this limit. In other words, the extent of unmixing keeps decreasing as the value of K keeps increasing far beyond J .

5.5 In-plane clustering of the amphiphiles

So far we have focussed our attention on the concentration profiles of the amphiphiles in a direction perpendicular to the air-water interface. How are the monomers belonging to the long and short amphiphiles arranged in each of the planes parallel to the interface? In order to answer this question we have computed the distributions of the sizes of the clusters formed by the monomers belonging to the long and short amphiphiles in each of the lattice planes. A Hosen-Kopelman cluster counting algorithm [72] calculates the cluster size distribution. A cluster of monomers belonging to long (short) amphiphiles in a given plane is defined as the

set of those nearest-neighbour lattice sites which are occupied by monomers belonging to long (short) amphiphiles only [132].

We have analyzed the equilibrium state of a $30 \times 30 \times 100$ lattice containing 405 long and 405 short amphiphiles. Let $N(S)$ be the number of clusters of size S in a given lattice plane. The quantity $N(S) \times S$ is plotted against S in each of the figures 5.10(a)-(d); the continuous lines correspond to the long amphiphiles whereas the dashed lines correspond to the short amphiphiles. Clearly, as we move from the top of the system across long-rich layers to short-rich layers (and eventually deeper inside water), the nature of the clustering changes. In the 20th layer (fig.5.10a) the monomers belonging to long amphiphiles form a single large cluster coexisting with a distribution of smaller clusters of monomers belonging to short amphiphiles. The size of the largest cluster formed by the monomers belonging to short amphiphiles in layer 21 is larger than the largest cluster formed by the monomers belonging to the long amphiphiles (fig.5.10b). As we move to the layer 22 we find that the clusters of the monomers of long amphiphiles are much smaller than in the preceding layer (fig.5.10c). Beyond this layer even the size of the clusters of monomers of short amphiphiles rapidly decreases as we move deeper into water (fig.5.10d).

This behaviour is in sharp contrast with the corresponding cluster size distributions when the initial surface density of the amphiphiles is small. We have repeated the computation with 90 long and 90 short amphiphiles keeping all the other parameters identical to those in fig.5.10. Since no phase segregation takes place in this case, almost all the monomers are confined to layers at and above the air-water interface. $N(S) \times S$ in the layers 14 to 17 are shown, respectively, in the figs. 5.11(a),(b), (c) and (d); the largest cluster in each of these layers consists of monomers

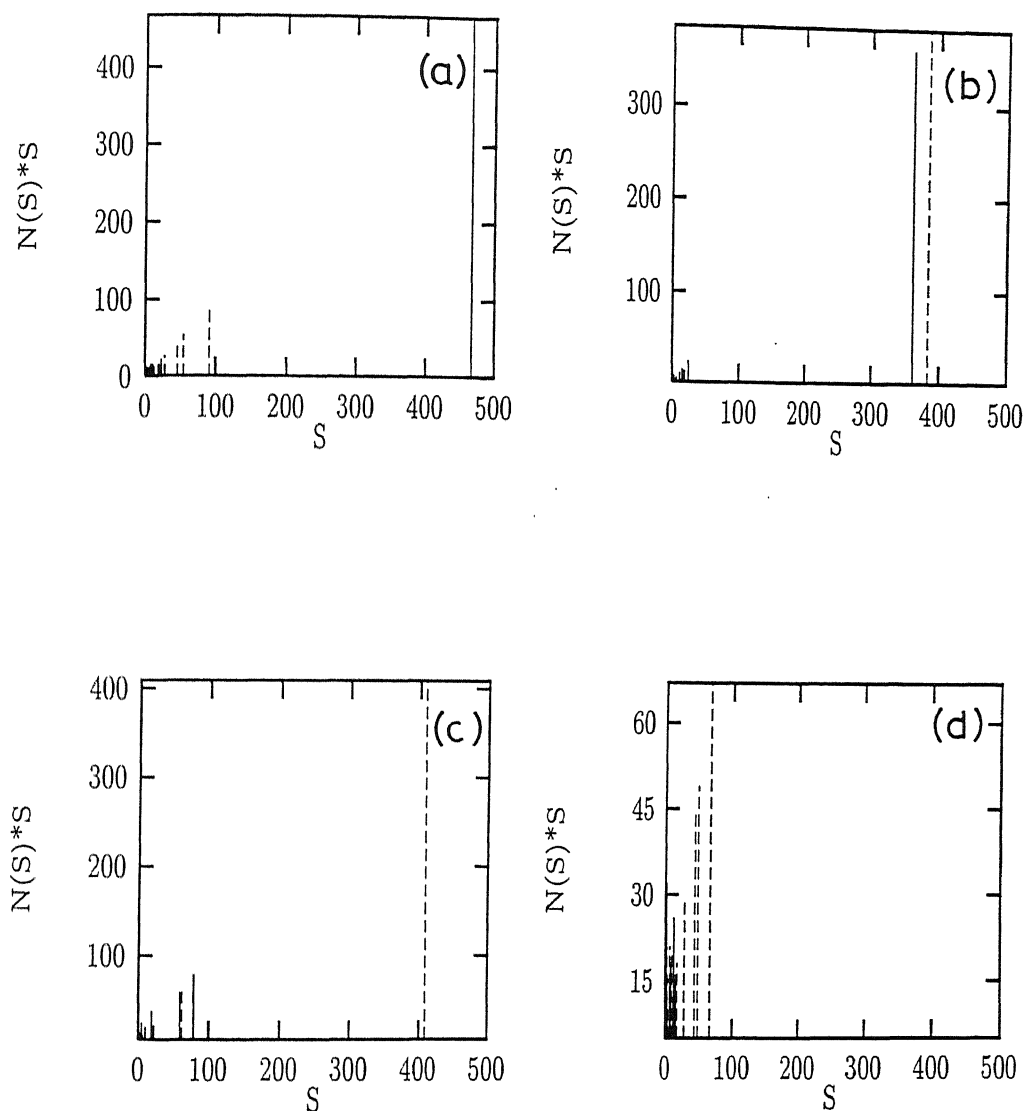


Figure 5.10: The distribution of the sizes of the clusters formed by the monomers belonging to the long and the short amphiphiles in the layers (a) 20, (b) 21, (c) 22 and (d) 23, respectively. The values of all the parameters are identical to those in fig.5.1. The continuous and the dashed lines correspond to the long and short amphiphiles, respectively.

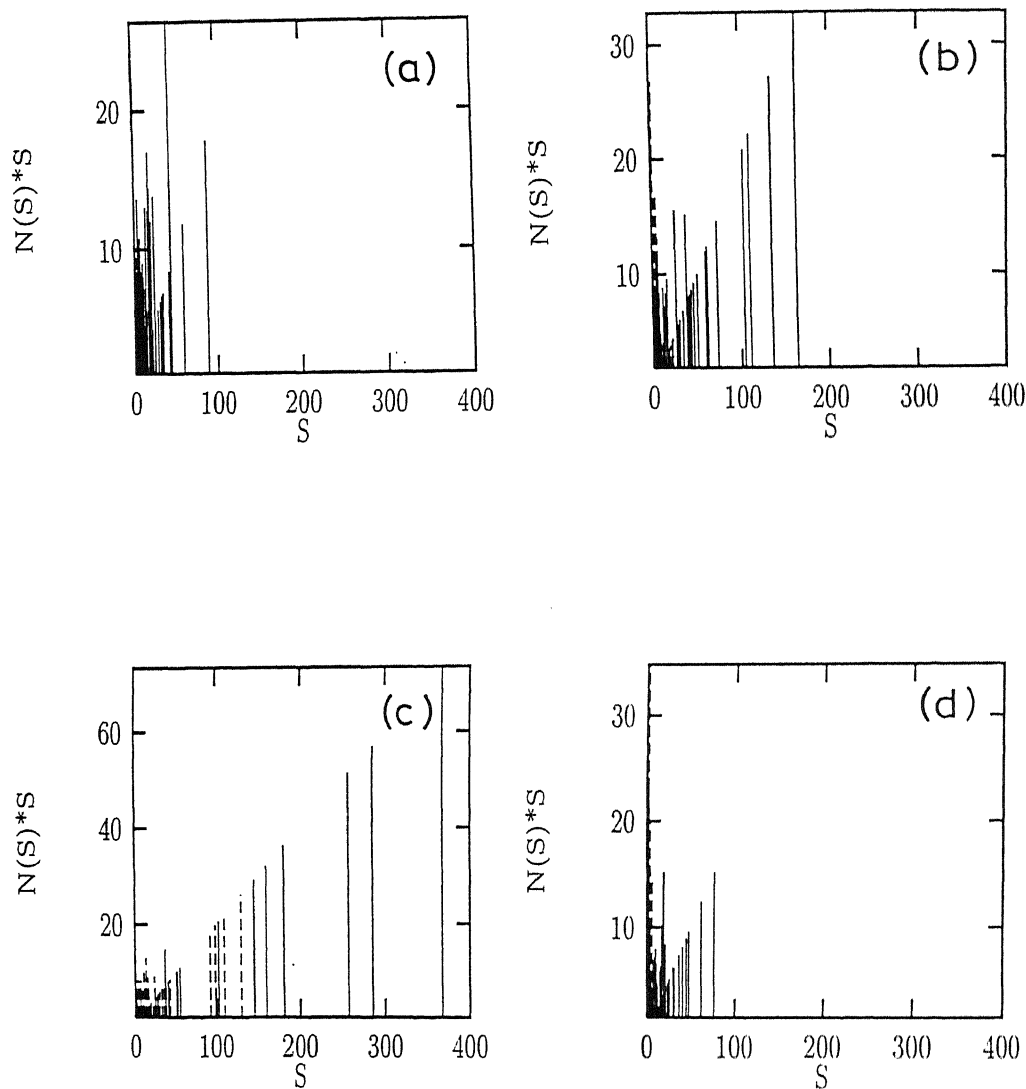


Figure 5.11: Same as in fig.5.10, except that the number of both the long and short amphiphiles is 90 and figures (a), (b), (c), (d) correspond to the layers 14, 15, 16 and 17, respectively.

belonging to the longer amphiphiles.

Liverpool and Bernardes [58] investigated the in-plane clustering of amphiphiles at the oil-water interface in a lattice model based on a Larson-type prescription for modelling the ternary system. An oil-water interface was constructed in the initial configuration where the lower half of the system was occupied by water (just as in our model) whereas the upper half was occupied by oil (instead of air) and the amphiphiles were uniformly distributed over the entire system. As the system began evolving with time, the amphiphiles moved quickly to the interface forming clusters. However, since the molecules of oil and water were allowed to exchange positions, the planar interface itself was subsequently destroyed spontaneously. On the other hand, the air-water interface in our model is stable as air and water are not allowed to exchange their positions.

5.6 Conformation of amphiphiles

Variations of the Z -components of the position of the center of mass, Z_{cm} , of the amphiphiles with time (Monte carlo steps per molecule) are shown in fig. 5.12; the positions are measured from a reference plane in the air. The corresponding radius of gyration of the amphiphiles are plotted in fig.5.13. The figures (a) and (c) in both correspond to a high density for which vertical phase segregation was observed (see figs 5.1 and 5.3). On the other hand, the figures (b) and (d) in both correspond to a low density for which no vertical phase segregation was exhibited (see fig 5.2).

In all the four figures (a)-(d), the center of mass of the long amphiphiles lie at a higher level,

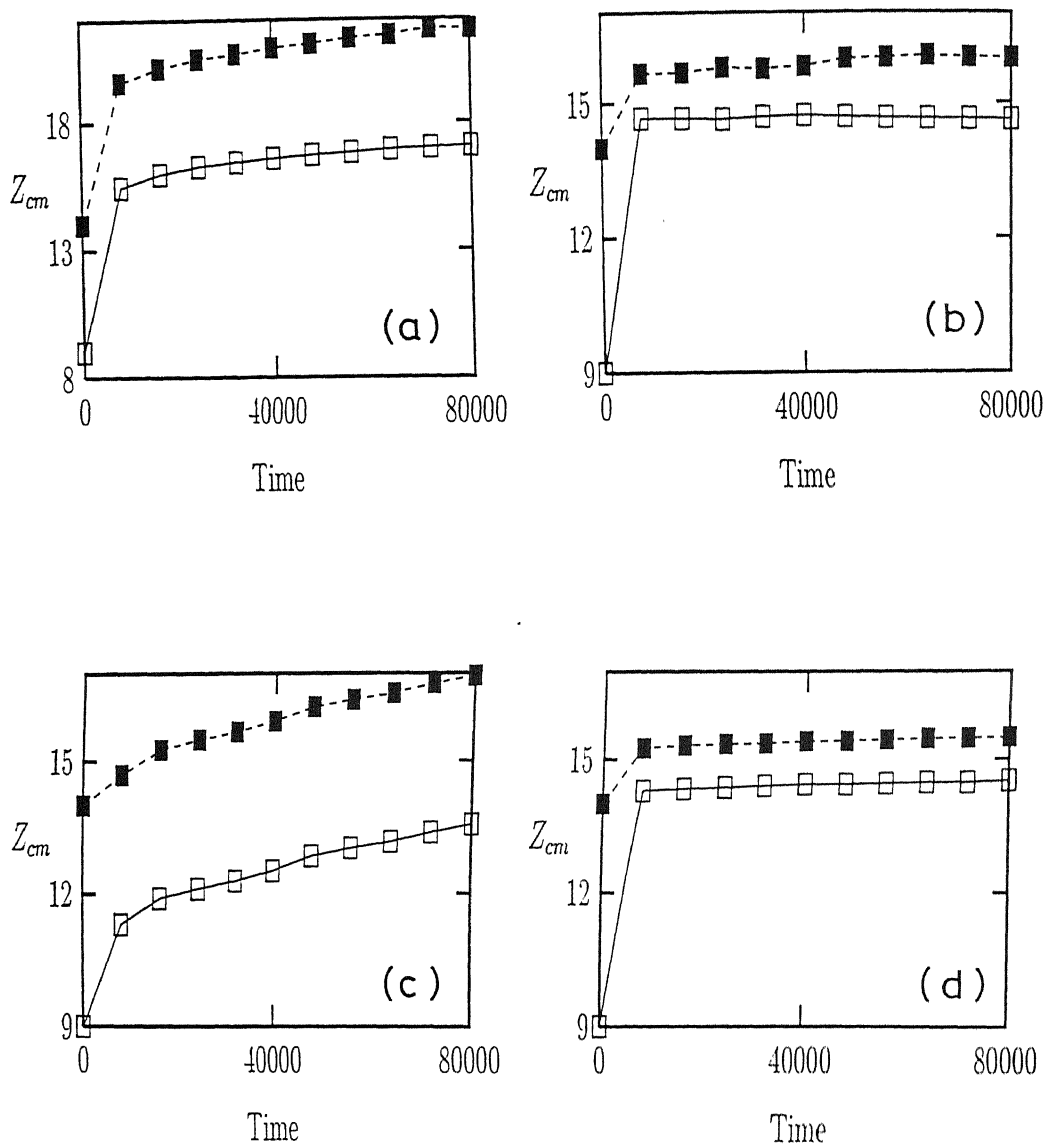


Figure 5.12: The Z component of center of mass (Z_{cm}) of the amphiphiles averaged over all the amphiphiles is plotted against MC steps; (a) $N_\ell = N_s = 405$ and $T = 2.5$, (b) $N_\ell = N_s = 45$ and $T = 2.5$, (c) $N_\ell = N_s = 405$ and $T = 1.0$, (d) $N_\ell = N_s = 45$ and $T = 1.0$. The continuous line and white square correspond to the long amphiphiles and the dashed line and black square correspond to the short amphiphiles.

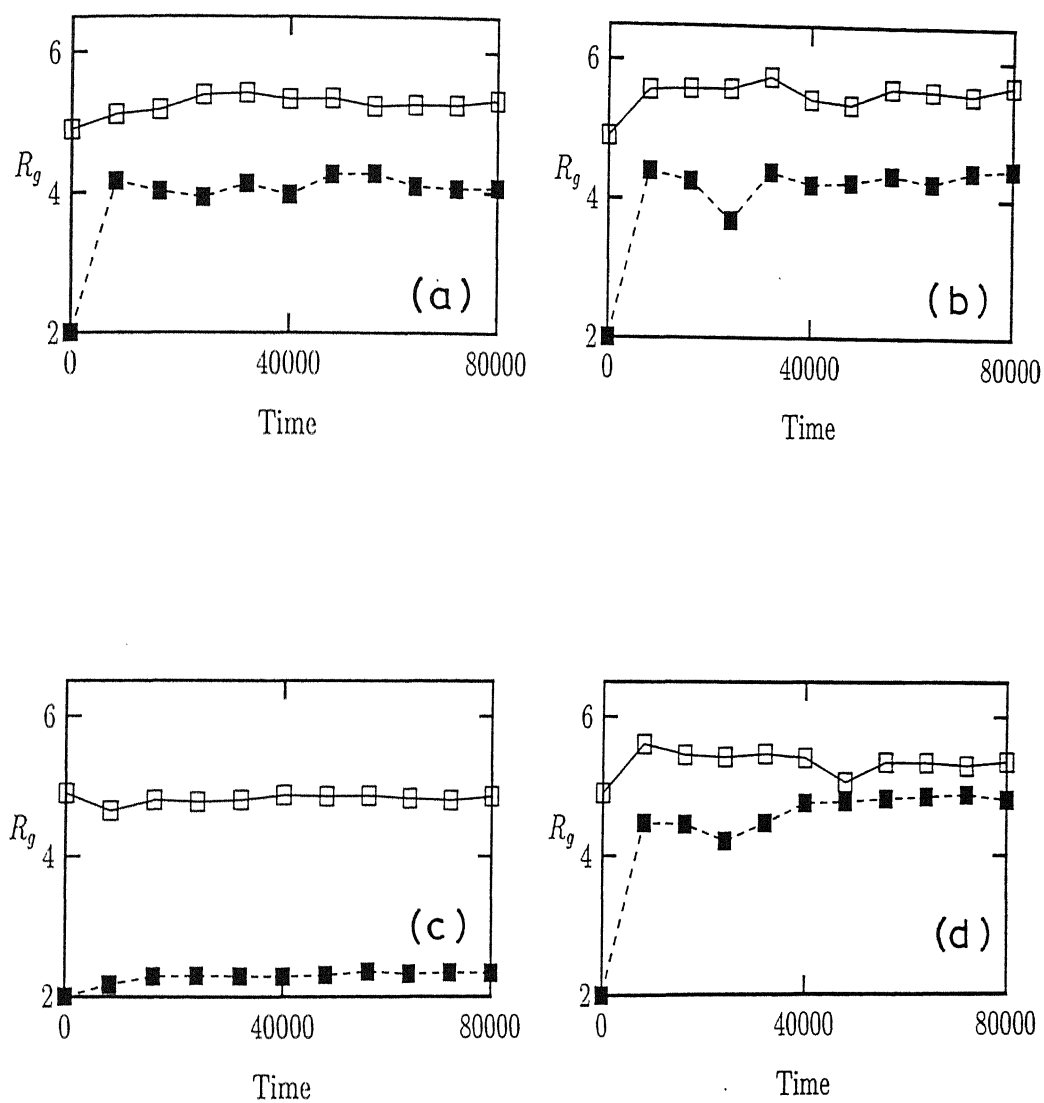


Figure 5.13: The averaged radius of gyration (R_g) of the amphiphiles plotted against MC steps; and the parameters and notations for figs.(a), (b), (c) and (d) correspond to those in fig. 5.12.

as expected. Moreover, comparing the figure 5.12(a) with 12(c) and 12(b) with 12(d) we find that at higher temperatures the equilibration is much quicker. Furthermore, at higher temperatures, the center of mass of the long amphiphiles lies at a significantly lower level compared to that at lower temperatures; this is a consequence of the "crumpling" of the amphiphiles caused by the increase of temperature. Most interesting observation is that there is significantly larger lowering of the center of mass of the short amphiphiles in fig.5.12(a) as compared to that in fig.5.12(c); thermal crumpling alone is inadequate to explain such large lowering of the center of mass. This is consistent with our earlier observation of the vertical phase segregation and the interpretation in terms of entropically- induced steric repulsion.

Since, at low densities, both the long and short amphiphiles get enough space to access all possible conformations, no significant "swelling" takes place by increasing the temperature from $T = 1.0$ to $T = 2.5$. In contrast, at high densities, the radius of gyration of the short amphiphiles at $T = 2.5$ is almost double of that at $T = 1.0$ (see fig.5.13).

In fig. 5.14 we plot the average vertical extension $[< \Delta Z >]$ of the amphiphiles as a function of time for different temperature and for different surface densities of amphiphiles. The corresponding distribution of the *vertical extensions* $P(\Delta Z)$ of the amphiphiles for different values of surface densities and temperatures are shown in Fig. 5.15. At low densities, there is practically no change in $[< \Delta Z >]$ (see figs.5.14(b) and (d)) as well as in $P(\Delta Z)$ of amphiphiles of both types when the temperature is increased from $T = 1.0$ to $T = 2.5$. At high densities, the data for $[< \Delta Z >]$ of the amphiphiles at $T = 2.5$ are almost identical to those observed at low densities. In contrast, both the long and short amphiphiles remain much more extended (i.e., $[< \Delta Z >]$ is much larger) at the same high density when the temperature is $T = 1.0$.

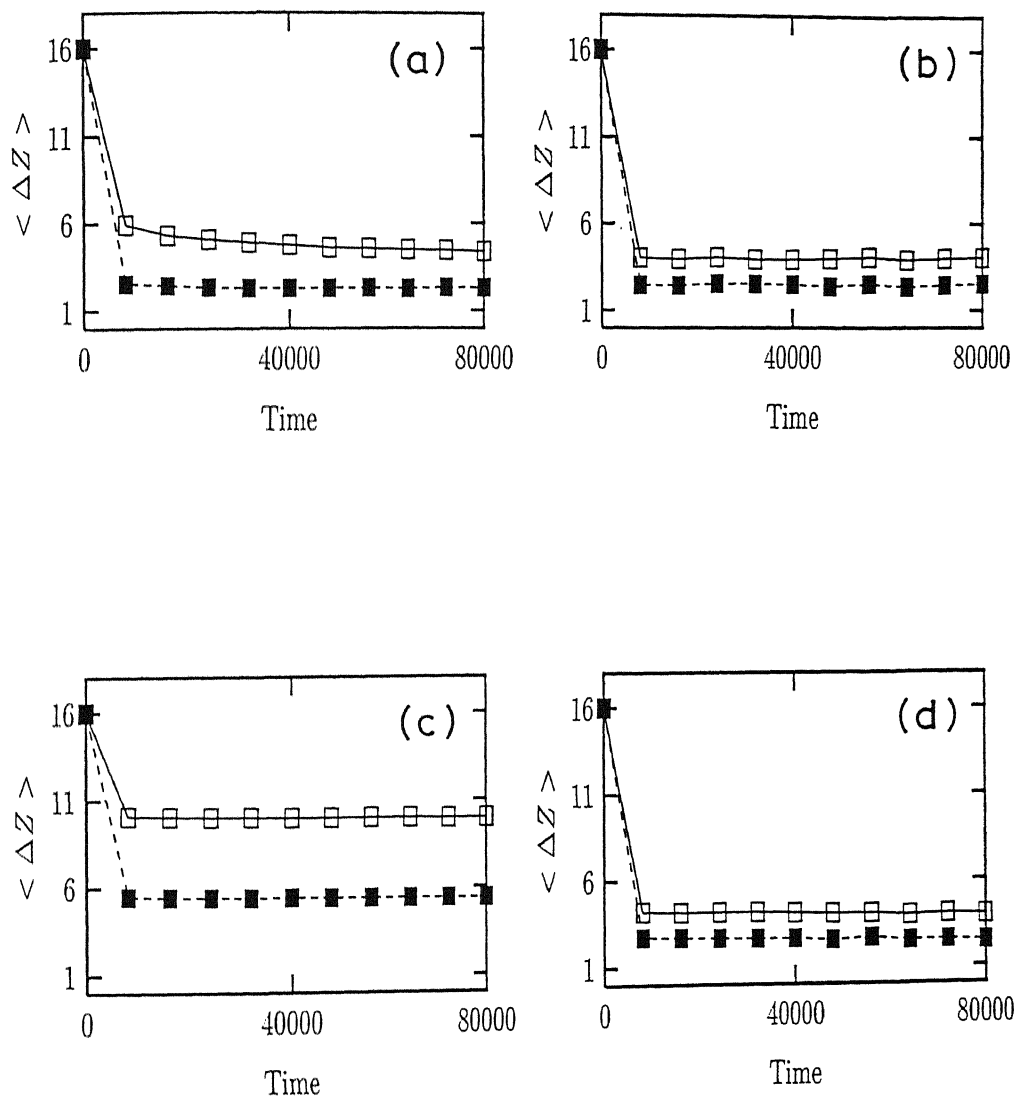


Figure 5.14: The average vertical extension $\langle \Delta Z \rangle$ plotted against MC steps and the parameters and notations for figs (a), (b), (c), (d) correspond to those in fig.5.12.

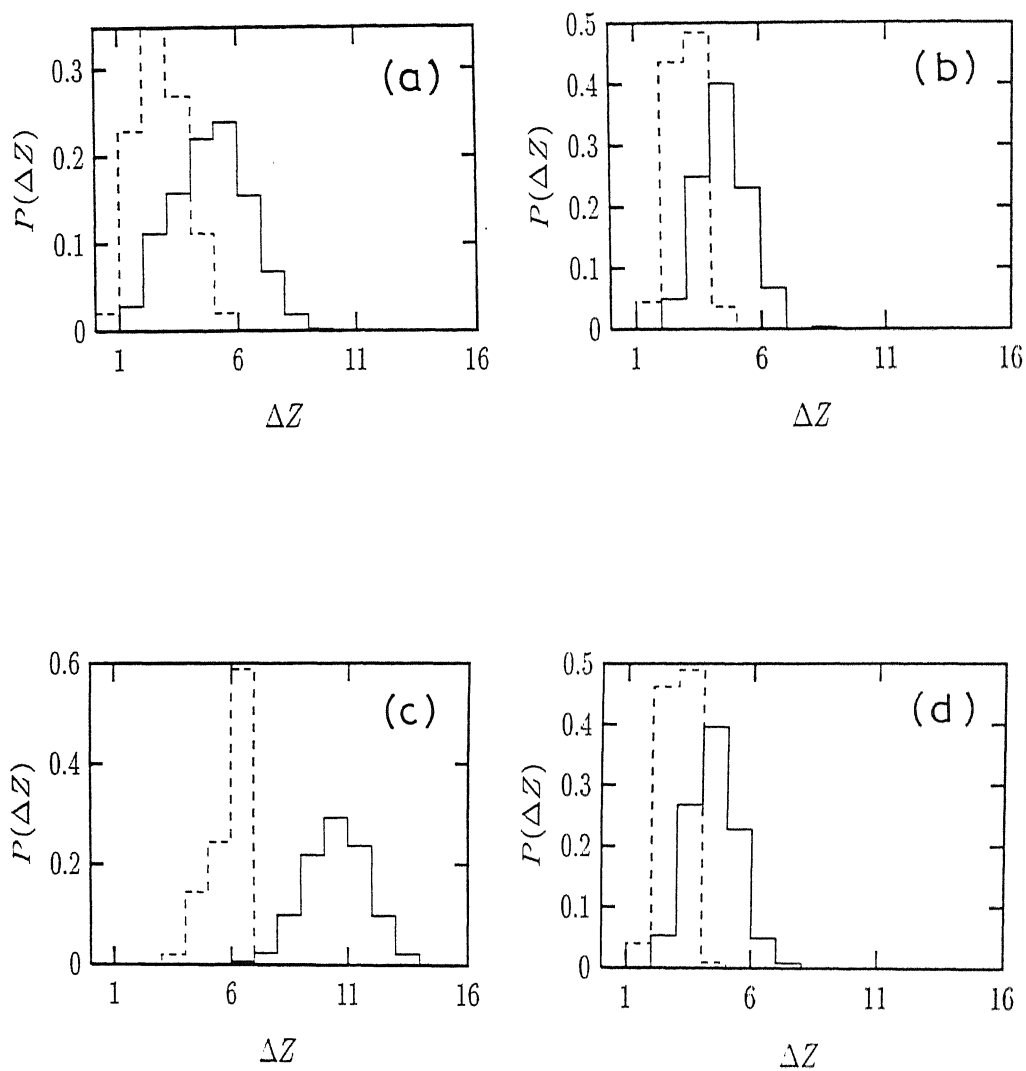


Figure 5.15: The probability distribution of the vertical extensions $P(\Delta Z)$. The parameter values and the notations for figs. (a), (b), (c), (d) are same as in fig.5.12.

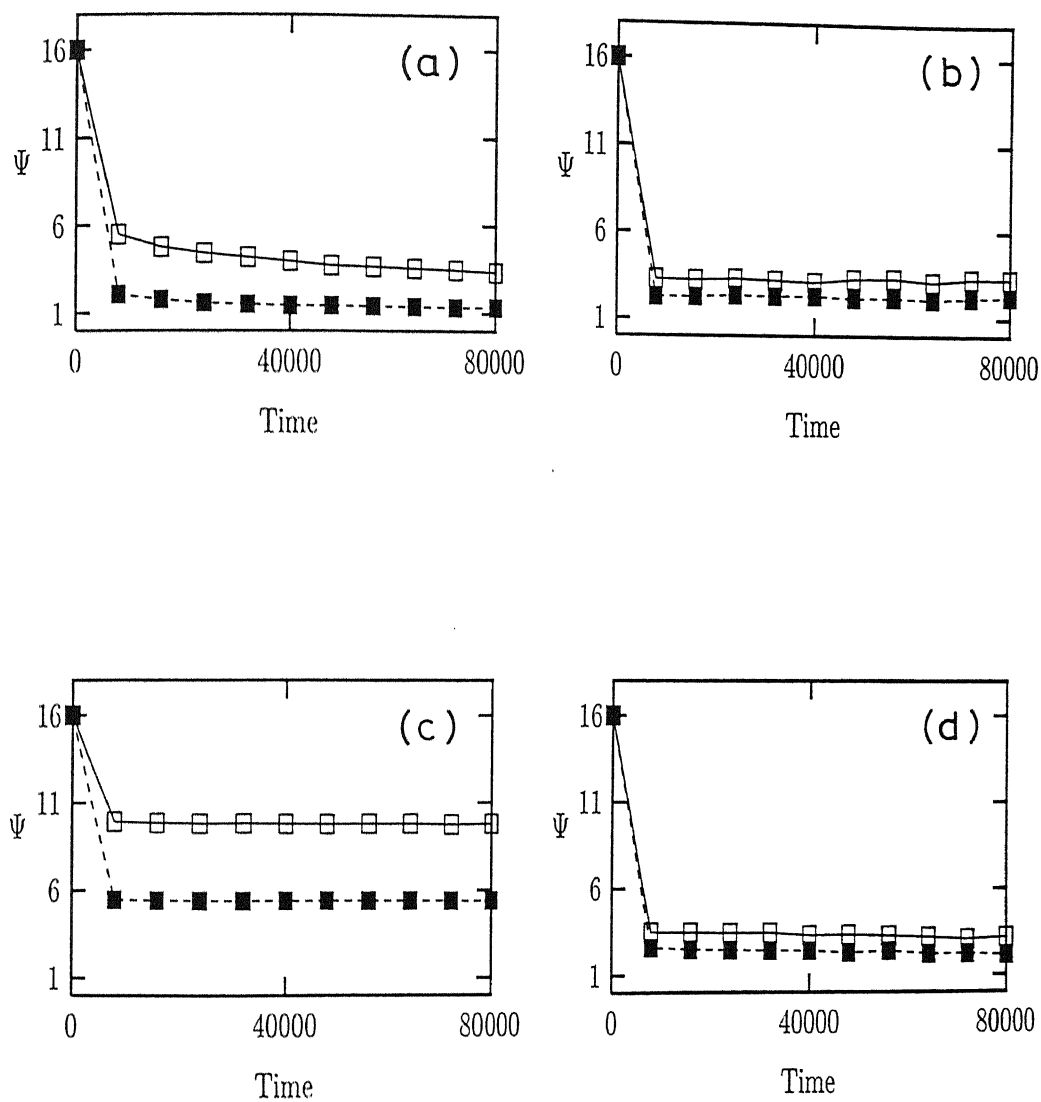


Figure 5.16: Average orientational order parameter Ψ for different temperatures and surface densities of amphiphiles. The parameter values and notations for figures (a), (b), (c), (d) are same as in fig.5.12.

Fig. 5.16 shows the variation of the average orientational order parameter Ψ with concentration and temperature. At low densities, there is practically no variation in Ψ by decreasing the temperature from $T = 2.5$ to $T = 1.0$. On the other hand, at higher concentrations, significant increase in the orientational ordering takes place by decreasing the temperature. A higher value of Ψ indicates a higher position of the hydrophilic head compared to the location of the tip of the hydrophobic tail.

The bond-orientational order parameters ϕ_p of the amphiphiles are plotted against the bond number p in fig. 5.17, where p is counted from the head. It demonstrates that, when the concentration is high, the bonds near the hydrophilic head are more likely to be oriented vertically than in any other direction; the closer is this bond to the head the stronger is this tendency. Even for high densities at low temperatures (fig.5.17(c)) the last bond is equally likely to be oriented in any of the six allowed directions.

5.7 Chemically different amphiphiles

The strengths of the inter-monomer interactions were varied by varying C_ℓ and C_s . When $C_\ell = 10 = C_s$ both the long and short amphiphiles spontaneously entered into water (see fig.5.18a). However, when $C_\ell = 10$ and $C_s = 1$ the longer amphiphiles move deeper into water although both the varieties move into water (fig.5.18b). On the other hand, when $C_s = 10$ and $C_\ell = 1$ it is the shorter amphiphiles which move deeper into the water (fig.5.18c).

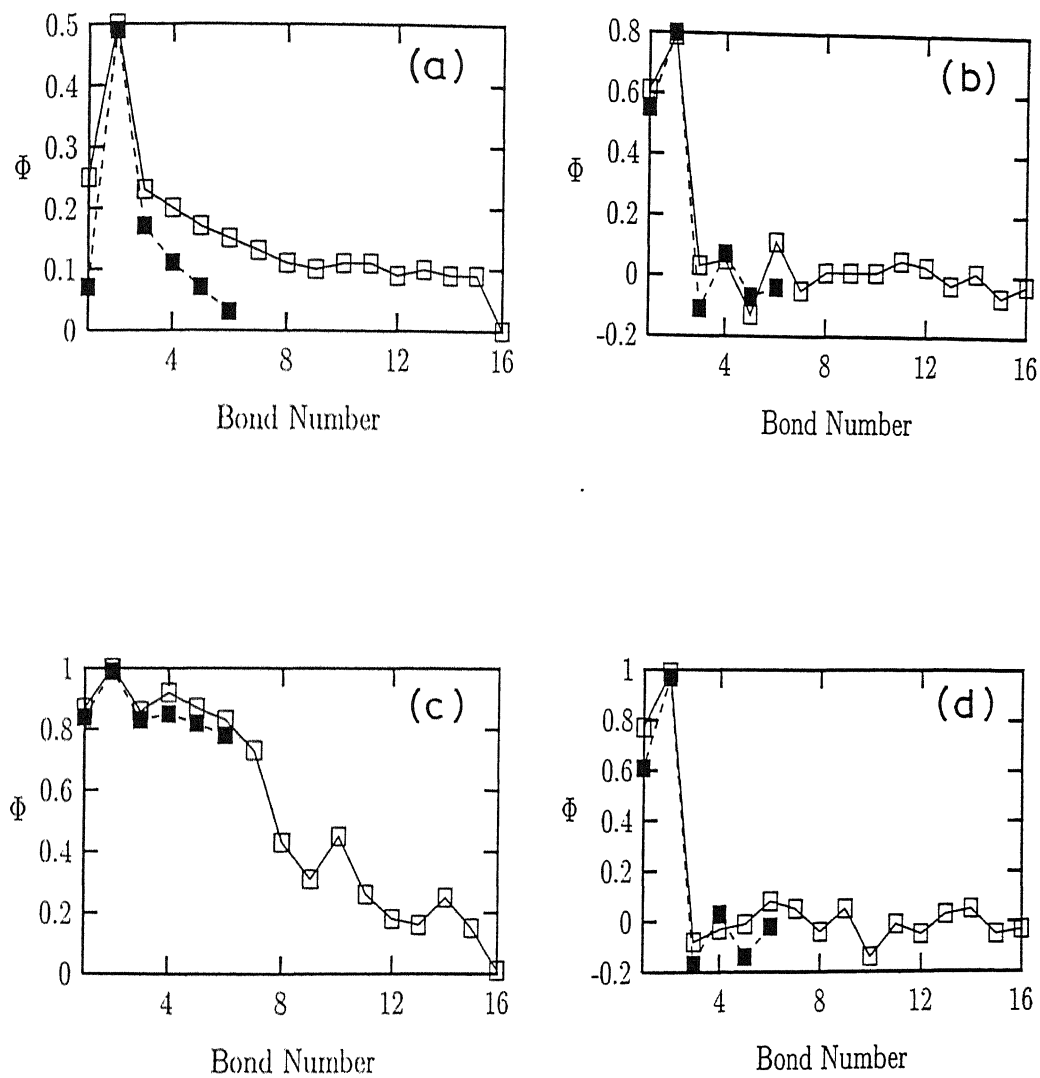


Figure 5.17: Average bond order parameter Φ as a function of bond number. The parameter values and the notations for figures (a), (b), (c), (d) are same as in fig.5.12.

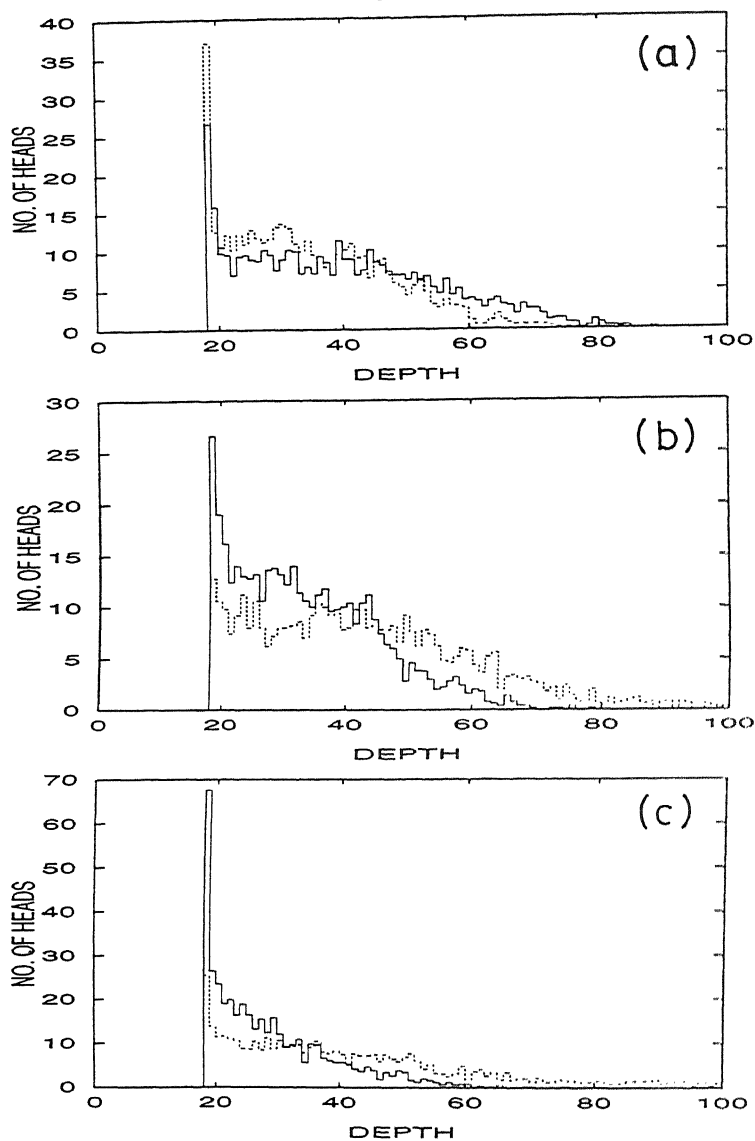


Figure 5.18: The equilibrium concentration profile of the hydrophilic heads at $T' = 2.5$ perpendicular to the air-water interface in a system consisting of $30 \times 30 \times 100$ lattice sites. The numbers of both long and short amphiphiles are 405; (a) $C_\ell = C_s = 10$, (b) $C_\ell = 10$ and $C_s = 1$, (c) $C_\ell = 1$ and $C_s = 10$. The continuous line corresponds to the long amphiphiles and the dashed line corresponds to the short amphiphiles.

5.8 Physical mechanism, Comparison with experiments and similar phenomena in other systems

Why is the majority of the short amphiphiles in the binary mixture so selectively pushed out of the original monolayer? The answer to this question is very closely related to the physical mechanism that leads to the phenomenon of vertical phase separation. If the surface density is high, the tails of the amphiphiles encounter stronger steric repulsion. If the short chains move down by a few molecular layers, that leaves more empty space for the unconstrained movement of the tails of the neighbouring long amphiphiles. The same would not be possible if the long amphiphiles, instead of the short ones, were selectively pushed into water by the same amount. It has been argued earlier in a different context [133] that the short amphiphiles, by placing themselves in between long amphiphiles, create more space for the movement of the long amphiphiles. Entropy-driven phase separation has been observed recently in a wide variety of systems [136], [137]. Very recently it has been demonstrated through computer simulations [135] that entropy-driven phase separation is possible in polymer blends characterized by vanishing Flory χ where $\chi \propto 2\epsilon_{12} - \epsilon_{11} - \epsilon_{22}$, ϵ_{ij} being the energy of interaction between two nearest-neighbour segments of type i and j .

The system studied in this chapter have some similarities with binary mixtures of polymer chains grafted on solid surfaces [140, 141]. A direct comparison of such polymer brushes with our results would require a study of mixture of grafted polymers of two drastically different lengths when the surface coverage is very high and temperature is not too low.

5.9 Summary and conclusion

In this chapter we have investigated the out-of-plane phase segregation of the amphiphiles in a binary mixture at the air-water interface. We have also studied the nature of the in-plane clustering of the monomers belonging to the long and the short amphiphiles. The entropy-driven phase segregation can be observed in laboratory experiments with chemically identical amphiphiles of two different lengths. For complete unmixing of the two components the long amphiphiles should be as long as possible and the difference in the lengths of the two types of the amphiphiles should also be large.

Chapter 6

Self assemblies of single chain and double chain amphiphiles

6.1 Introduction

All the previous chapters deal almost exclusively with the interfacial properties except in chapter 5 where we have studied both the interfacial as well as bulk properties. In the remaining part of the thesis we will study the bulk properties of the self assembling amphiphilic systems. In chapters 4 and 5 only single-chain amphiphiles have been considered although the general conclusions drawn from our MC studies are valid also for double-chain amphiphiles. In this chapter we shall study the bulk properties of the single chain as well as double chain amphiphiles. This chapter bridges the gap between chapter 7 where we shall develop a model for gemini surfactants which are double chain amphiphiles and chapters 4 and 5 where we have considered only single chain amphiphiles.

In this chapter we compare and contrast the self-assemblies of single-chain and double-chain amphiphiles, respectively, in water. We have studied binary mixture of amphiphiles at the air-water interface in chapter 5. Here we study the self-assemblies of binary mixtures of single-chain and double-chain amphiphiles and compare these with those formed by the corresponding single species of amphiphiles

6.2 Micelle formation

For single chain amphiphiles *micellar* aggregates form at low concentration of amphiphiles, i.e. at concentration just above CMC. Stauffer, Jan and Pandey [45], using type $\mathcal{H}_1\mathcal{N}_4\mathcal{T}_4$, studied the behaviour of amphiphiles in water beginning from a disordered distribution of chains and found that they always formed clusters (which they called micelles) whose average size, denoted by a peak in the size distribution, increased with time. Stauffer et al. [46] performed a more detailed study of the properties of the model for structure $\mathcal{H}_1\mathcal{N}_4\mathcal{T}_4$. The length of the chains and the strength of the hydrophilic and hydrophobic interaction were varied. They used Glauber Kinetics and only the reptation movement. Simulations were performed on lattices of sizes up to $173 \times 173 \times 173$. For the same type amphiphile as that studied in [45] at a concentration of $\phi_a = 0.1$, they observed that between temperature of $t = 2.1$ and $t = 4.1$, a distribution of micelles with a stable mean size (weight average) was formed. Below $t = 2.1$, the micelles grow indefinitely and above $t = 4.1$ a mixed phase was observed. A simulation of the $\mathcal{H}_1\mathcal{N}_5$ with the spin of the head $S = +2$ showed the growth of the mean cluster size to be slowed down, while one of $\mathcal{H}_1\mathcal{N}_4\mathcal{T}_1$ with head $S = +2$ and tail $S = -2$ gave similar behaviour as the $\mathcal{H}_1\mathcal{N}_4\mathcal{T}_1$ with

head $S = +1$ and tail $S = -1$.

Jan, Stauffer and collaborators [46, 47] extended the model further to describe single-chain surfactants with ionic heads. According to their formulation, the monomers belonging to the ionic heads have Ising spin $+2$ to mimic the presence of electric charge. The repulsive interaction between a pair of ionic heads is taken into account through an (antiferromagnetic) interaction $J = -1$ between pairs of nearest neighbour sites, both of which carry spins $+2$; however, the interaction between all other pairs of nearest-neighbour spins is assumed to be $J = 1$. By restricting the range of the repulsive (antiferromagnetic) interaction between the "charged" heads to only one lattice spacing one is effectively assuming very strong screening of the Coulomb repulsion between ionic heads by the counterions.

When head-head repulsion was included, the mean micelle size remained constant more or less independent of temperature. The repulsion was thus conjectured to be important for the stability of micelles [46]. Jan and Stauffer [47] also studied surfactants $\mathcal{H}_2\mathcal{N}_1\mathcal{T}_3$ with structure $+2, +1, 0, -1, -1, -1$ also with head-head repulsion and found stable micelles. However, in any of the above mentioned work the morphology of the micellar aggregates was not studied. Smit et al. [60] showed the formation of spherical micelles with Molecular dynamics simulation. Here we report the formation of stable spherical micelles by looking at the actual morphology of the aggregates formed during Monte Carlo simulation; to my knowledge, this is the first direct evidence of the formation of spherical micelles in the Larson model of single-chain surfactants.

We have performed simulations for much longer amphiphiles $\mathcal{H}_1\mathcal{N}_1\mathcal{T}_4$ in water. We allowed all the moves for amphiphiles described in chapter 4 : (i) *reptation*, (ii) *kink*, (iii) *spontaneous buckling* and (iv) *pull*. The simulations were performed on lattice of size $100 \times 100 \times 100$ at

in amphiphile concentration $\varphi_a = 0.009$ and temperature $t = 2.2$. Starting with amphiphiles uniformly distributed in the cubic lattice, spherical micelles formed at the end of the simulation (see figure 6.1).

Simulation with amphiphiles $\mathcal{H}_2\mathcal{N}_1\mathcal{T}_9$ also gives spherical micelles; figure 6.2 shows the snapshot of the 3-dimensional micelles.

Next we performed simulation for a binary mixture of single chain amphiphiles in water. Since we are studying a binary mixture of the amphiphiles, let us represent them by the two symbols $\mathcal{H}_{q_\ell}\mathcal{N}_1\mathcal{T}_{m_\ell}$ and $\mathcal{H}_{q_s}\mathcal{N}_1\mathcal{T}_{m_s}$ for the long and short amphiphiles, respectively, so that the lengths of the long amphiphiles is $L_\ell = q_\ell + m_\ell + 1$, and that of the short amphiphiles is $L_s = q_s + m_s + 1$. All our investigations have been carried out for a fixed value of $q_\ell = q_s = 2$, $L_\ell = 12$ and $L_s = 6$. The ratio of the volume fraction of the long and short amphiphils was kept at 7 : 3. In this case also we get a distribution of spherical micelles. Figure 6.3 shows one snapshot of such micellar aggregates.

6.3 Vesicle formation

In water, amphiphiles can form "bilayers" which consist of two monolayers of oppositely oriented amphiphiles such that the hydrophobic tails of amphiphiles in the two monolayers are hidden inside thereby minimizing contact with water. A bilayer can close itself to avoid contact between the hydrocarbon tails and water at the edges of the membrane and form what is called *vesicles*. Thus *vesicles* separates an inner region of an aqueous fluid from another aqueous fluid in its exterior. In recent years there has been an increasing interest in vesicles mainly because of

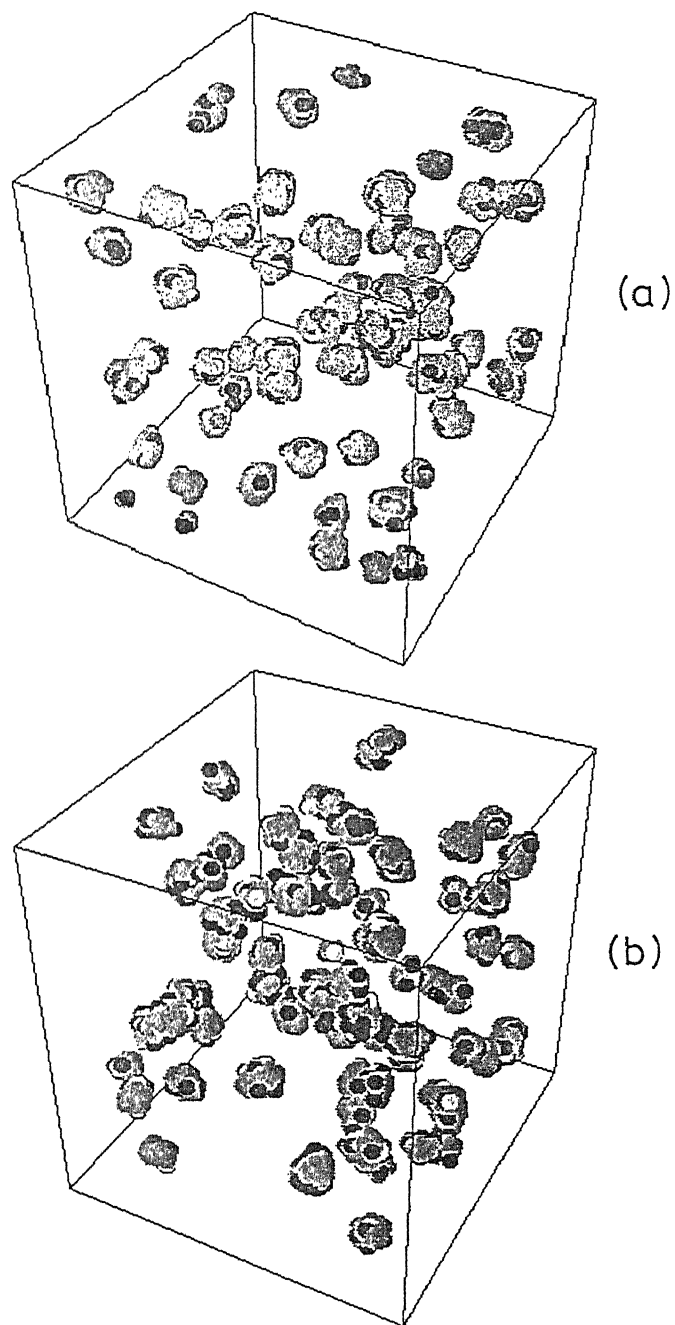


Figure 6.1: Snapshots of micellar aggregates formed by single-chain (a) nonionic surfactants (b) ionic surfactants with $m = 14$ and the density 0.01. The symbols black spheres and grey spheres represent monomers belonging to head and tail, respectively.

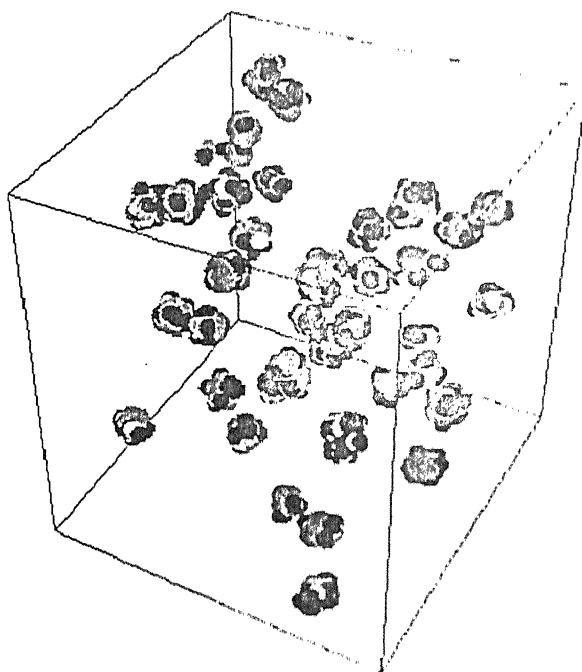


Figure 6.2: Same as in figure 6.1(a) except that now $m = 9$

their wide application in biology and medicine as model cell membranes, as well as their strong potential as drug carriers and others encapsulating agents of industrial relevance [143]. However, whereas the vesicles are widespread and form spontaneously in nature, the artificial formation of vesicles requires the input of some form of energy, for example sonification. Safran et al.[142] have shown that mixture of two surfactants can lead to spontaneous vesicles formation. In contrast to the situation for single amphiphiles, where large vesicles are usually not energetically stable in comparison with flat bilayers, vesicles composed of two species of amphiphiles can have lower curvature energies than flat bilayers and hence more stable. Vesicles have been found to form spontaneously in some aqueous surfactant systems, including solutions containing (i) mixtures of lecithin and lysolecithin [144], (ii) mixtures of long and short chain lecithins [145], (iii) mixtures of cationic and anionic surfactants [90].

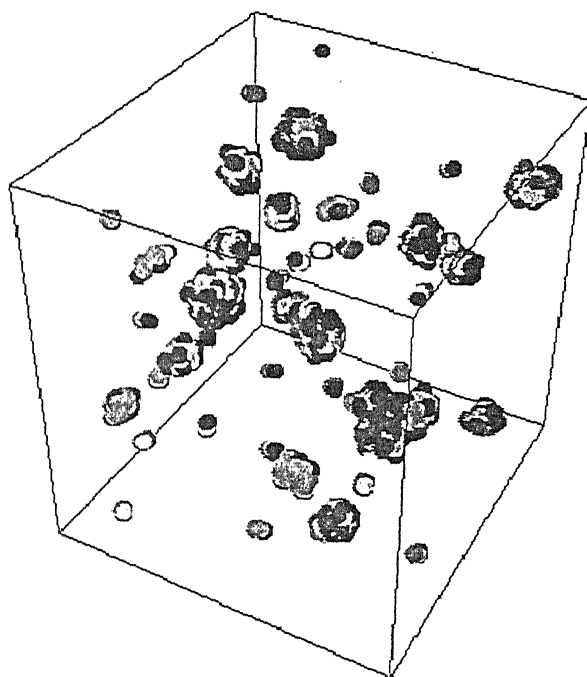


Figure 6.3: Snapshots of the micellar aggregates formed by the binary mixture of single chain amphiphiles. Black sphere represent head and grey sphere represent tail.

Recently a microscopic lattice model of double-chain amphiphiles with a single head was developed by Bernardes by extending the Larson model of single-chain amphiphiles in ternary microemulsions and its later generalizations. A lattice model of double-chain amphiphiles with a single hydrophilic head can be described by the symbol $\mathcal{T}_m \mathcal{N}_p \mathcal{H}_q \mathcal{N}_p \mathcal{T}_m$. m , p and q are integers denoting the lengths of the tail, neutral region, and head, respectively, in the units of lattice sites. Extensive MC simulation showed the spontaneous formation of vesicles. The simulations were performed on amphiphile $\mathcal{T}_4 \mathcal{N}_1 \mathcal{H}_2 \mathcal{N}_1 \mathcal{T}_4$ of length $\ell = 12$ in a binary solution. These correspond to double chain amphiphiles which have been conjectured to be more suited to forming bilayer membranes [33]. Simulations were performed on a $40 \times 40 \times 50$ system at a temperature of $t = 2.2$ with 533 amphiphiles for up to 4×10^7 MC steps. Beginning with a uniform distribution of amphiphiles throughout the whole lattice, a large vesicle is formed at the end of the simulation. It should be noted that at this temperature the system is below its condensation transition temperature and consequently all the amphiphiles tend to aggregate in one large cluster. Simulation with shorter double chain amphiphiles $\ell = 10$ has also been performed yielding vesicle formation.

We extend Bernardes model to include binary mixture of double chain amphiphiles and report the spontaneous formation of vesicles of different sizes. The simulations were performed on a mixture of long amphiphiles $\mathcal{T}_4 \mathcal{N}_1 \mathcal{H}_2 \mathcal{N}_1 \mathcal{T}_4$ of length $L_\ell = 12$ and short amphiphiles $\mathcal{T}_1 \mathcal{N}_1 \mathcal{H}_2 \mathcal{N}_1 \mathcal{T}_1$ of length $L_s = 6$. The ratio of the long and short amphiphiles was 7 : 3. Initially both types of amphiphiles were uniformly distributed in the cubic lattice of size $L \times L \times L_z$. Periodic boundary conditions were adopted in the x and y directions. Fixed boundary conditions were applied in the z direction where the states of the two uppermost and two lowermost planes were kept "frozen"

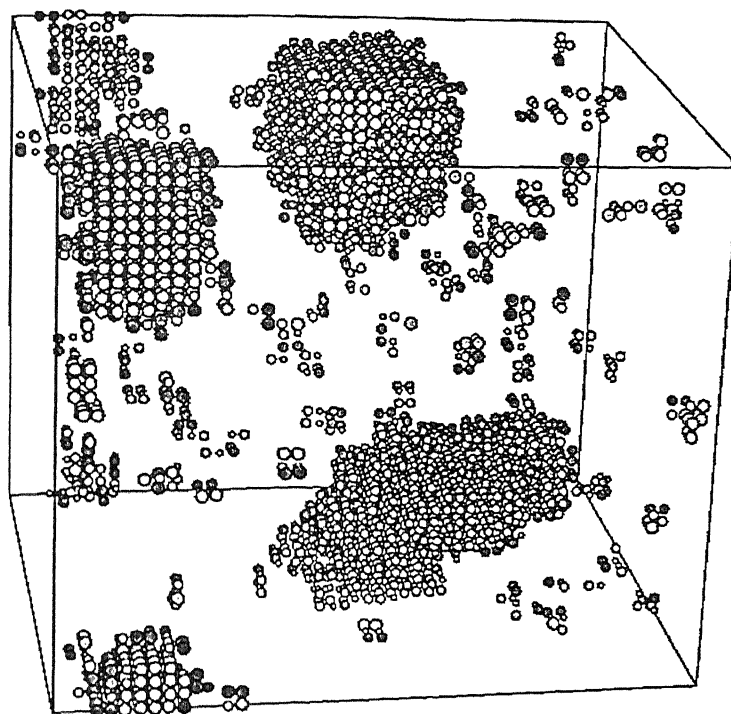


Figure 6.4: (a) Snapshots of the vesicles formed by the binary mixture of double chain amphiphiles. Black sphere represent head and grey sphere represent tail.

in the corresponding initial states, and no movement of the amphiphiles through these planes was allowed. Amphiphiles can move in the lattice changing position with water molecules through different types of movements discussed in chapter 4; namely reptation, kink and buckling. After 10^7 MC steps we get vesicles of different sizes. Figure 6.4(a) shows different sizes of the vesicles formed in our simulation. For comparison, the vesicles formed by the single component double chain amphiphiles has been shown in Figure 6.4(b).

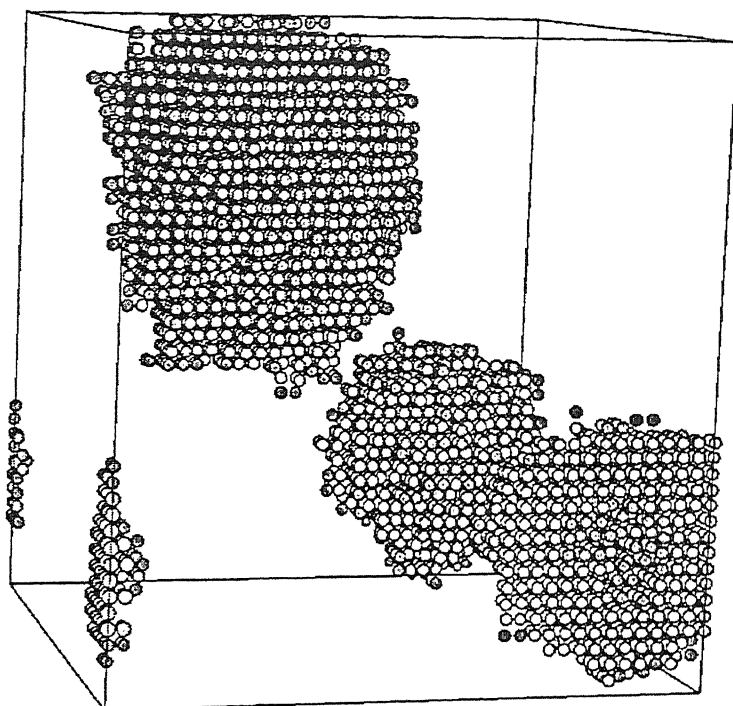


Figure 6.4: (b) Snapshots of the vesicles formed by the single component double chain amphiphiles. Black sphere represent head and grey sphere represent tail.

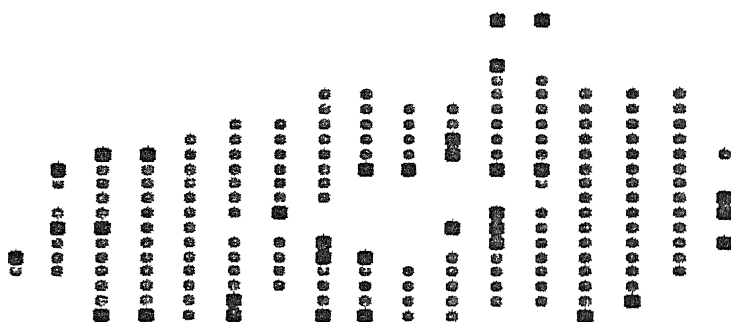


Figure 6.4: (c) A typical cross-section of the vesicle Black sphere represent head and grey sphere represent tail.

6.4 Conclusion

In this chapter we have compared and contrasted the self assemblies of single chain and double chain amphiphiles. In binary mixture of water and single chain amphiphiles, when the concentration and temperature is sufficiently low, we get spherical micelle-like aggregates. For a mixture of long and short single chain amphiphiles in water also we get spherical micelles. For double-chain amphiphiles when only one species are present in water, we get one large single vesicle. On the other hand, the amphiphiles form simultaneously more than one vesicle (of relatively smaller sizes) when a fraction of the long amphiphiles are replaced by shorter double-chain amphiphiles.

Chapter 7

A Microscopic Model of Gemini Surfactants: Self-assemblies in Water and at Air-Water Interface¹

7.1 Introduction

It is well known that micelles are formed when the concentration of the surfactants in water exceeds what is known as critical micellar concentration (CMC) [10]. In reality, CMC is not a single concentration but a very narrow range of concentration (it is more appropriate to call it characteristic micellar concentration [46, 47]). Experimentally, for example, the CMC is found to (i) increase with the increase in the ionic strength of the heads in case of ionic surfactants,

¹The following papers are based on this chapter:
P. K. Maiti, D. Chowdhury, cond-mat/9706052, submitted for publication, P. K. Maiti and D. Chowdhury, in preparation.

(ii) decrease with increasing tail length [1], (iii) decrease with decreasing temperature [22]. (iv) increase with the increase in the size of head in case of non-ionic surfactants [54]. The CMC calculated from computer simulation with the Larson-type models excellently agree with the above experimental results [46, 47, 54, 52].

In this chapter we develop a microscopic model of *gemini* surfactants and, carrying out Monte Carlo (MC) computer simulations, investigate how the shapes and sizes of these molecules as well as their mutual interactions and their interactions with the molecules of water give rise to some unusual aggregation phenomena. We simulate *gemini* surfactants with (a) hydrophobic spacers and also those with (b) hydrophilic spacers. For each of these two types of *gemini* surfactants we consider both ionic and non-ionic (but polar) hydrophilic heads. Another aim of this chapter is to report the results of a complimentary MC study of the spatial organization of these model *gemini* surfactants (particularly, their tails and spacers) at the air-water interface in order to answer some of the fundamental questions raised on this point and speculations made in the literature [146]. A microscopic model for single-chain surfactants at the air-water interface was developed in chapter 5. In this chapter we replace the single-chain surfactants by the model *gemini* surfactants developed here, thereby getting the desired microscopic model of *gemini* surfactants at the air-water interface.

In contrast, two unusual features of the CMC of *gemini* surfactants with *ionic heads* and *hydrophobic spacer* are:

(i) for a given fixed length of each of the two tails, the CMC *increases* with the length of the spacer till it reaches a maximum beyond which CMC *decreases* with further increase of the spacer length [15, 152–154];

i) for a given length of the spacer, the CMC *increases* with increasing tail length [12, 13].

Moreover, the micellar aggregates formed by the gemini surfactants with short spacers even at low concentrations just above the CMC are "long, thread-like and entangled" [16, 155], in contrast to the spherical shapes of the micelles formed by single-chain surfactants at such low concentrations. Furthermore, the CMC of gemini surfactants with *ionic heads* and *hydrophilic spacer* decrease monotonically with the increase of the length of the spacer [156]. Our aim is to understand the physical origin of these unusual properties of gemini surfactants. We also make some new predictions on the morphology of the micellar aggregates of gemini surfactants with long tails and long spacer.

Synthesis of gemini surfactants with non-ionic (polar) heads in laboratory experiments remains one of the challenging open problems. But, our computer experiments on model gemini surfactants with non-ionic heads enable us to predict their morphologies and the variation of their CMC with the lengths of tails and spacers.

In the presence of the air-water interface, where do the tails and the spacer of an isolated gemini surfactant find themselves- do they lie inside water or outside (i.e., in the air), do they get crowded close to the interface or do they spread out as far away from the interface as possible? How does the effective area of cross-section of an isolated gemini surfactant at the air-water interface vary with the increase of the length of the spacer when the spacer is (a) hydrophobic, (b) hydrophilic? How do the conformations of the gemini surfactants and spatial organizations of their tails and spacers vary with the increase of the density which gives rise to unavoidable interactions (both direct and entropic) among the surfactants? We try to answer these fundamental questions by carrying out computer experiments on a microscopic model that

we propose here.

The model and the characteristic quantities of interest are defined in section 2. The results on the micellar aggregates, in bulk water, formed by the gemini surfactants with hydrophobic and hydrophilic spacers are reported in two subsections of section 3. The results of the investigations on the spatial organization of the gemini surfactants with hydrophobic and hydrophilic spacers at the air-water interface are given in section 4. Finally, a summary of the main results and the conclusions drawn from these are given in section 5.

7.2 The Model and The Characteristic Quantities of Interest

7.2.1 General aspects

Now we propose a microscopic lattice model of gemini surfactants. In terms of the symbols used earlier to denote the primary "structure" of the microscopic lattice model of single-chain surfactants, Bernardes' lattice model of double-chain surfactants, with a single hydrophilic head, can be described by the symbol $\mathcal{T}_m \mathcal{N}_p \mathcal{H}_q \mathcal{N}_p \mathcal{T}_m$. In terms of the same symbols, the microscopic lattice model of a gemini surfactant, which we propose here, can be represented by the symbol $\mathcal{T}_m \mathcal{N}_p \mathcal{H}_q \mathcal{S}_n \mathcal{H}_q \mathcal{N}_p \mathcal{T}_m$ where n is the number of lattice sites constituting the spacer represented by the symbol \mathcal{S} (see fig.7.1).

In our model, an Ising spin variable S is assigned to each lattice site; $S_i = 1$ (-1) if the i -th lattice site is occupied by a water (oil) molecule. If the j -th site is occupied by a monomer

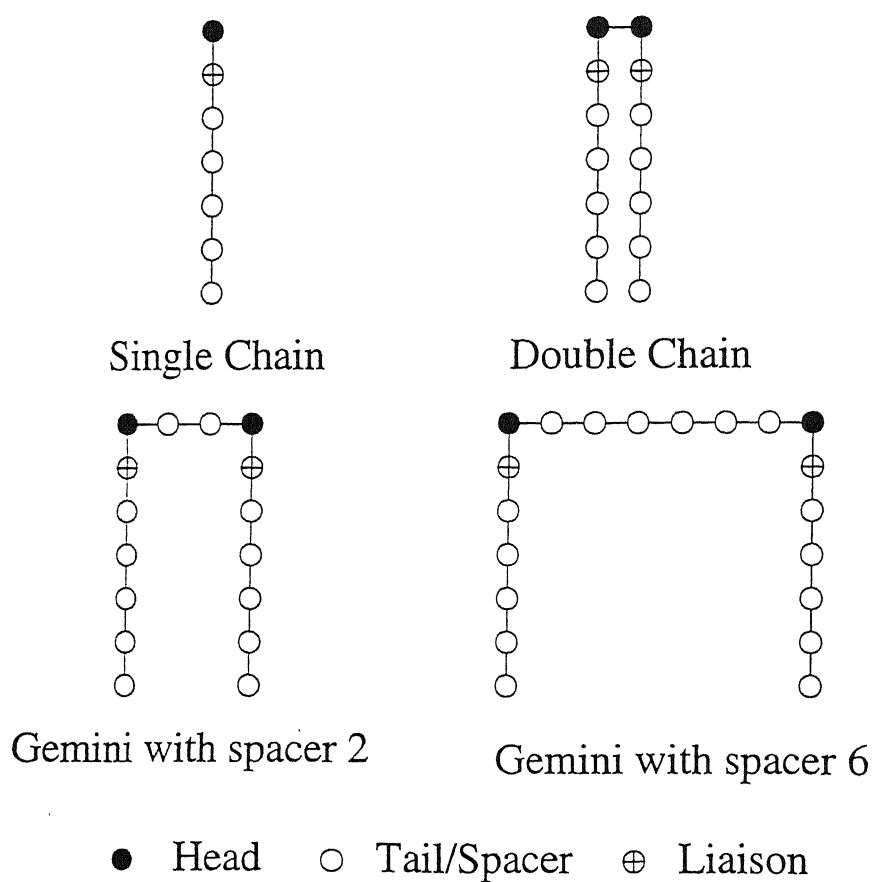


Figure 7.1: Larson-type models of single-chain, double-chain and gemini surfactants.

belonging to a surfactant then $S_j = 1, -1, 0$ depending on whether the monomer at the j th site belongs to head, tail or neutral part. A monomer belonging the spacer is assigned a spin value -1 if the spacer is hydrophobic and $+1$ if the spacer is hydrophilic. The monomer-monomer interactions are taken into account through the interaction between the corresponding pair of Ising spins which is assumed to be non-zero provided the spins are located on the nearest-neighbour sites on the lattice. Thus, the Hamiltonian for the system is given by the standard form

$$H = -J \sum_{\langle ij \rangle} S_i S_j. \quad (7.1)$$

where attractive interaction (analogue of the ferromagnetic interaction in Ising magnets) corresponds to $J > 0$ and repulsive interaction (analogue of antiferromagnetic interaction) corresponds to $J < 0$ [46, 47]. The temperature T of the system is measured in the units of J/k_B where k_B is the Boltzmann constant.

To our knowledge, all the gemini surfactants synthesized so far have ionic heads. Therefore, we incorporate the effects of the ionic heads following the same way as has been described in chapter 6. The monomers belonging to the ionic heads have Ising spin $+2$ to mimic the presence of electric charge. The repulsive interaction between a pair of ionic heads is taken into account through an (antiferromagnetic) interaction ($J = -1$).

In order to predict the properties of gemini surfactants with non-ionic (polar) heads and to investigate which of the aggregation phenomena exhibited by the ionic gemini surfactants arise from the electric charge on their ionic heads, we have also considered a model of gemini surfactants with non-ionic polar heads which is obtained from the model of ionic gemini surfactants by replacing all the $+2$ Ising spin variables by Ising spin $+1$ (and, accordingly, the interactions

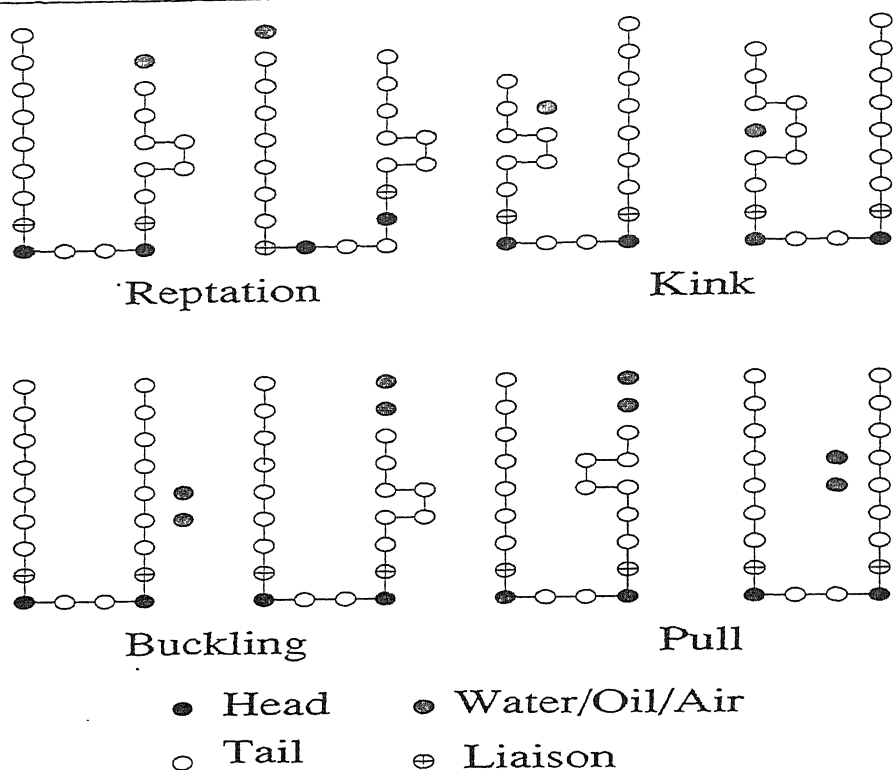


Figure 7.2: Schematic representation of the moves attempted by every surfactant at every MC step.

−1 between the heads on nearest-neighbour sites are replaced by +1). Moreover, in order to investigate the role of the chain stiffness we have used a chain bending energy [81]; every bend of a tail or a spacer, by a right angle at a lattice site, is assumed to cost an extra amount of energy $K(> 0)$.

Starting from an initial state (which will be described in the subsections 7.2.2 and 7.2.3), the system is allowed to evolve following the standard Metropolis algorithm: each of the attempts to move a surfactant takes place certainly if $\Delta E < 0$ and with a probability proportional to $\exp(-\Delta E/T)$ if $\Delta E \geq 0$, where ΔE is the change in energy that would be caused by the proposed move of the surfactant under consideration.

Next, we specify the allowed moves of the surfactants for the appropriate sampling of the states of the system in a MC simulation. We have generalized the moves for single chain surfactants (discussed in chapter 4) appropriately for the gemini surfactants and schematic representation of these moves are shown in fig.7.2; although the moves are illustrated using one of two tails, each of the moves (except reptation, which involves the entire surfactant) in our algorithm is equally likely to be applied on the two tails as well as the spacer. The moves allowed for the surfactants in our model are as follows:

(i) *reptation*: this is identical to the reptation move for single-chain surfactants described earlier; (ii) *spontaneous chain buckling*: a portion in the middle of one of the two tails or the spacer is randomly picked up and allowed to buckle with the probability mentioned above; (iii) *kink movement*: a kink formed by the buckling or reptation is allowed to move to a new position with the appropriate probability calculated according to the prescription mentioned above; (iv) *pull move*: this is the reverse of spontaneous chain buckling; a buckled part of one of the two tails or the spacer is pulled so as to make it more extended. In addition to these moves, each of the surfactants is allowed to move laterally in one of the six possible directions, which is chosen randomly with probability $1/6$ and each monomer of the surfactant is moved in that direction by one lattice spacing. Each of these moves is possible only if the new positions of all the monomers are not occupied simultaneously by monomers belonging to other surfactants. Each surfactant is allowed to try each of the above mentioned moves once during each MC step. The moves of the molecules of water and air are described in the subsections 7.2.2 and 7.2.3 below.

In principle, one can study the aggregation of gemini surfactants deep inside bulk water and their spatial organization close to air-water interface by MC simulation of a single system

ere the lower part of the lattice representing water is sufficiently large and the density of surfactants is also sufficiently high so that a large fraction of these can be found deep inside water in the form of micellar aggregates. However, for the convenience of computation, we study these two aspects of the problem separately; in the first part we investigate only the phenomenon of aggregation of gemini surfactants in bulk water and in the second part we investigate only the spatial organization of the tails and spacers of the gemini surfactants at (and near) the air-water interface when the total volume fraction occupied by the surfactants is quite small. Both these parts of our computations are based on the general model described above and the specific differences involved in these two are explained separately in the next two subsections.

2.2.2 Model of Gemini Surfactants in Bulk Water

In order to investigate the spontaneous formation of micellar aggregates and their morphology, model gemini surfactants are initially dispersed randomly in a $L_x \times L_y \times L_z$ system which contains only water and surfactants. Periodic boundary condition is applied in all the three directions thereby mimicking bulk water which is infinite in all the directions. So far as the moves of the molecules of water are concerned, each molecule of water is allowed to exchange position with a monomer belonging to a surfactant, provided that is necessary for the implementation of an attempted move of a surfactant.

7.2.3 Model of Gemini Surfactants at Air-Water Interface

Just as in the preceding subsection, the system under investigation is modeled as a simple cubic lattice of size $L_x \times L_y \times L_z$. However, in contrast to simulating a bulk of water, which is infinite in all directions, we now simulate a semi-infinite vertical column of air separated from a semi-infinite vertical column of water below by a sharp horizontal air-water interface. In the Cartesian coordinate system the horizontal air-water interface is parallel to the XY -plane and the *vertically downward* direction is chosen as the $+Z$ -axis. Each of the molecules of water and air can occupy a single lattice site. A classical Ising spin variable S is assigned to each lattice site; $S_i = 1$ (-1) if the i -th lattice site is occupied by a water molecule (air molecule or empty). Our prescription for assigning the Ising spin variables to the sites occupied by the monomers of the amphiphiles is identical to that given in the preceding subsection. Periodic boundary conditions are applied along the X and Y directions. The lattice sites in the uppermost and the lowermost layers are occupied by "down" and "up" spins respectively, which were not updated during the computer simulation. These boundary conditions mimic the physical situation mentioned above which we intend to simulate.

In the initial state the surfactants are so arranged that their spacers lie flat, and fully extended, horizontally in the first layer of water immediately below the air-water interface and their tails are fully extended vertically into air. The system is then allowed to evolve towards equilibrium following the Metropolis algorithm explained earlier. So far as the moves of the individual molecules are concerned, air and water are not allowed to exchange positions, as dispersion of air and water inside each other is not possible in our model. However, if some monomers of a

When a surfactant comes out of water, the vacant sites are occupied by inserting water molecules; this is consistent with our assumption that the water column is semi-infinite in the Z -direction. Moreover, we impose an additional constraint that none of the heads of the surfactant molecules can come out of water.

2.4 Characteristic Quantities of Interest

The most direct approach to investigate the morphology of the micellar aggregates and the spatial organization of the different parts of individual surfactants is to look at the snapshots of the system after equilibration. For studying the variations of CMC with the lengths of the tails and the spacers one has to use a well-defined prescription for computing the CMC; this is a subtle point as the CMC is not a unique single concentration, as mentioned before. We follow the prescription proposed, and used successfully in the case of single-chain surfactants [46, 47]; we identify CMC as the amphiphile concentration where half of the surfactants are in the form of solvated chains and the other half in the form of clusters consisting of more than one neighbouring amphiphile.

We have introduced a quantitative measure of the effective cross-sectional area A of the Gemini surfactants projected onto the air-water interface. We compute $|\Delta x|_m$ and $|\Delta y|_m$ which are the maximum differences in the X - and Y -coordinates, respectively, of the monomers and define A as

$$A = [(|\Delta x|_m)^2 + (|\Delta y|_m)^2]^{1/2} \quad (7.2)$$

The vertical extension $\langle Z \rangle$ is defined as the difference in the Z -coordinates of the

highest and lowest monomers (i.e. monomers with highest and lowest value of Z -coordinates) of a single surfactant. A quantitative measure of the gross features of the spatial organization of the tails and spacers of the gemini surfactants at the air-water interface is the equilibrium profiles of the concentrations of the corresponding monomers in the Z -direction, i.e., in the direction perpendicular to the air-water interface. More precisely, at each molecular layer, we count separately the *number* of monomers belonging to the tails and the spacers (and also the heads and neutral parts) in that particular layer and average the data over sufficiently large number of configurations after equilibration of the system.

We have carried out MC simulations of the model $\mathcal{T}_m \mathcal{N}_p \mathcal{H}_q \mathcal{S}_n \mathcal{H}_q \mathcal{N}_p \mathcal{T}_m$ of gemini surfactants for $p = q = 1$ and for three different values of the tail length, namely, $m = 5, 15$ and 25 . In our simulation of the surfactants at the air-water interface we do not find any observable difference in the concentration profiles obtained in single runs for $100 \times 100 \times 100$ systems and for larger systems containing identical surface-density of surfactants, all the profiles reported in this chapter have been generated for system sizes $L_x = L_y = L_z = L = 100$ by averaging over sufficiently large (10-25) number of runs. The same size of the system was also found to be large enough to avoid severe finite-size effects on the CMC data; each of the data points for the CMC is obtained by averaging over typically 10 runs. For a given m we have computed the CMC for spacer lengths $2 \leq n \leq 20$.

3 Micellar Aggregates of Gemini Surfactants

3.1 Aggregates of Gemini Surfactants: Results for Hydrophobic Spacers

The CMC of *ionic* gemini surfactants with *hydrophobic* spacers are plotted against the spacer length for two different lengths of the tail, namely, $m = 5$ and $m = 15$, in figs. 7.3(a) and 7.3(b), respectively. The *non-monotonic* variation of CMC with the spacer length, in figs. 7.3(a) and 7.3(b), is in qualitative agreement with the experimental observations [152–155]. However, this is in sharp contrast to the monotonic decrease of the CMC with the length of the hydrophobic tail of single-chain model surfactants of the type $\mathcal{T}_m\mathcal{N}_p\mathcal{H}_q$ [46, 47, 54]. Moreover, for a given length of the hydrophobic spacer, the CMC of this type of gemini surfactants *increases* when the bending stiffness K of the hydrophobic chains is switched on (see figs. 7.3(a) and (b)). Furthermore, we observe that, for a given length of the hydrophobic spacer, the CMC of ionic gemini surfactants *increase* with the increase of the tail length (see fig.7.4); this trend of variation is also consistent with the corresponding experimental observations [12, 13].

For a given tail length (see fig.7.5 for $m = 5$ and $m = 15$), the CMC of model gemini surfactants with *hydrophobic* spacers decreases *monotonically* with the increase in the spacer length when the polar head group is *non-ionic*. This is in sharp contrast to the non-monotonic variation observed for ionic gemini surfactants. However, for a given spacer length, the trend of the variation of CMC of non-ionic gemini surfactants with the tail length is similar to that observed for ionic gemini surfactants, i.e., CMC increases with the increase of the length of the

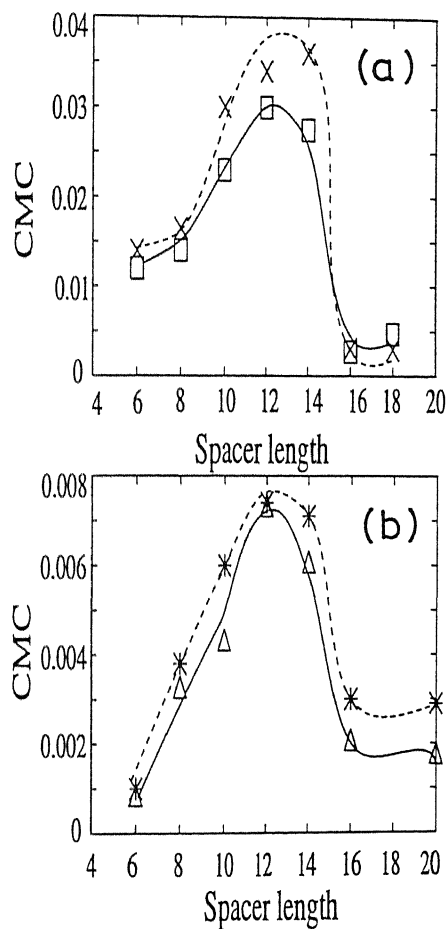


Figure 7.3: (a) Variation of CMC of ionic geminis with hydrophobic spacer length; $m = 15$, $T = 2.2$. The symbols \square and \times correspond to $K = 0$ and $K = 2$, respectively. (b) Same as (a), except that $m = 5$. The symbols \triangle and $*$ correspond to $K = 0$ and $K = 2$, respectively. The continuous curves are merely guides to the eye.

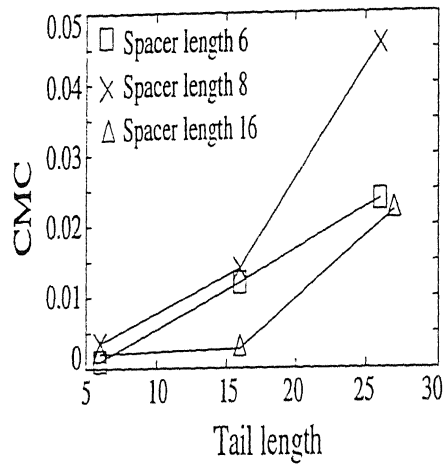


Figure 7.4: Variation of CMC of ionic geminis with tail length at $T = 2.2$ for three different lengths of the hydrophobic spacer, namely, $n = 6, 8, 16$. The straight lines connecting the successive data points are merely guides to the eye.

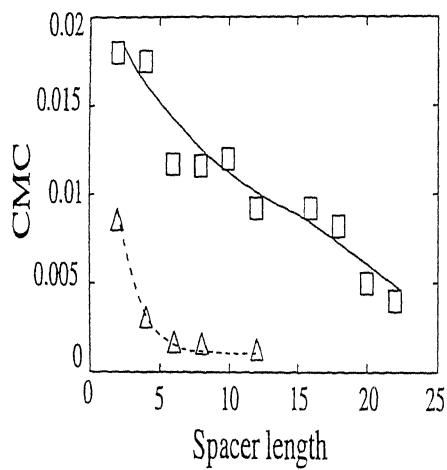


Figure 7.5: Variation of CMC of non-ionic geminis with the length of the hydrophobic spacer; $m = 15$ (\square) and $m = 5$ (\triangle) both with $K = 0$ and at $T = 2.2$. The continuous curves are merely guides to the eye.

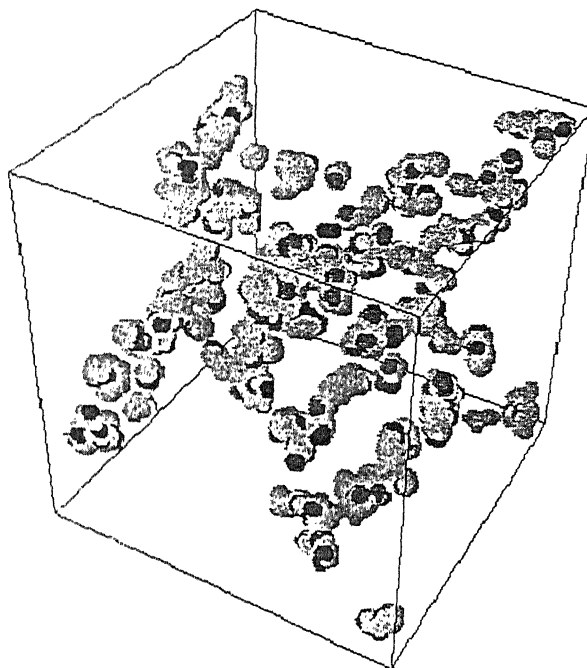


Figure 7.6: Snapshots of the micellar aggregates formed by ionic geminis with hydrophobic spacer; $m = 15$, $n = 2$ and $K = 0$ at $T = 2.2$ when the surfactant density is 0.007. The symbols black spheres, dark grey spheres and light grey spheres represent monomers belonging to head, tail and spacer, respectively.

tail.

Instantaneous snapshots of the micellar aggregates formed by *long tailed* ($m = 15$) gemini surfactants with *ionic heads* and *hydrophobic spacer* are shown for spacer lengths $n = 2$ (fig. 7.6) and $n = 16$ (fig.7.7). The morphology of the aggregates in fig.7.6 are similar to the "long, thread-like and entangled" micelles observed in laboratory experiments [16] and in MD simulations [148] on gemini surfactants with short hydrophobic spacers. Moreover, our data in fig.7.7 suggest that rod-like ("columnar") micelles are formed by gemini surfactants with *ionic head* and *long tail* ($m = 15$) when the length of the *hydrophobic spacer* is also long ($n = 16$).

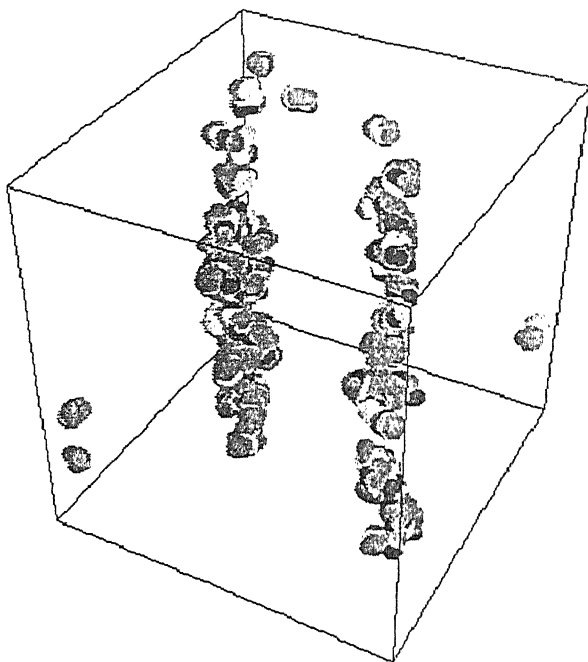


Figure 7.7: Same as in fig.6, except that $n = 16$ and the density is 0.005.

The morphologies of the aggregates in fig.7.6 and 7.7 are in sharp contrast with the spherical shape of the micelles (see fig.7.8) formed by single-chain ionic surfactants of comparable tail size even at concentrations somewhat higher than those in the figures 7.6 and 7.7.

There is no significant difference between the morphologies of the micellar aggregates of ionic and non-ionic single-chain model surfactants represented by the symbol $\mathcal{T}_m\mathcal{N}_p\mathcal{H}_q$ [98]. Similarly, we do not observe any significant difference also in the shapes of the aggregates of ionic surfactants (figs.7.6 and 7.7) and those of non-ionic gemini surfactants (see figs.7.9 and 7.10) with hydrophobic spacers, for given values of m , n and comparable concentration, in spite of qualitatively different trends of variation of their CMCs with spacer lengths.

Note that the rod-like micelles, shown in fig.7.7, are formed when the length of the hydrophobic spacer and the combined length of the tail and the neutral part of the gemini surfactants are

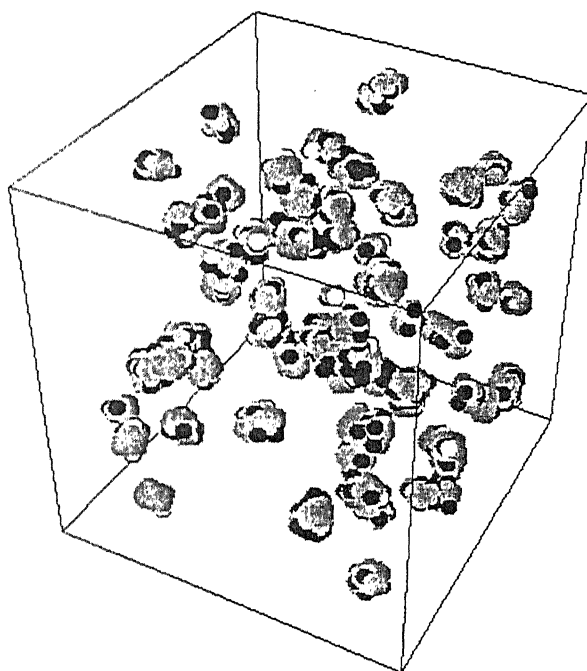


Figure 7.8: Snapshots of micellar aggregates formed by single-chain ionic surfactants with $m = 14$ and the density 0.01. The symbols black spheres and grey spheres represent monomers belonging to head and tail, respectively.

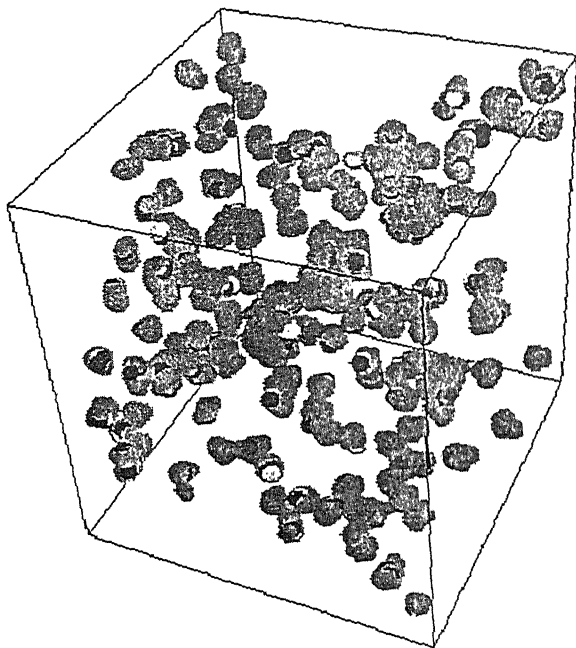


Figure 7.9: Same as in fig.7.6, except that the geminis are non-ionic.

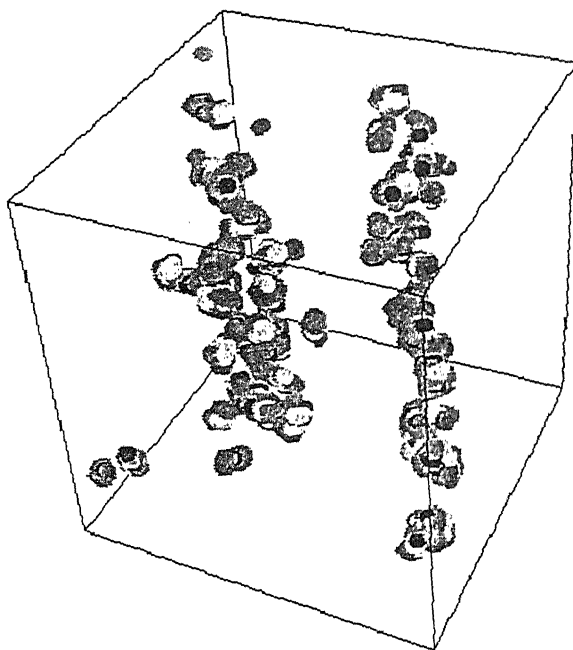


Figure 7.10: Same as in fig.7.7, except that the geminis are non-ionic.

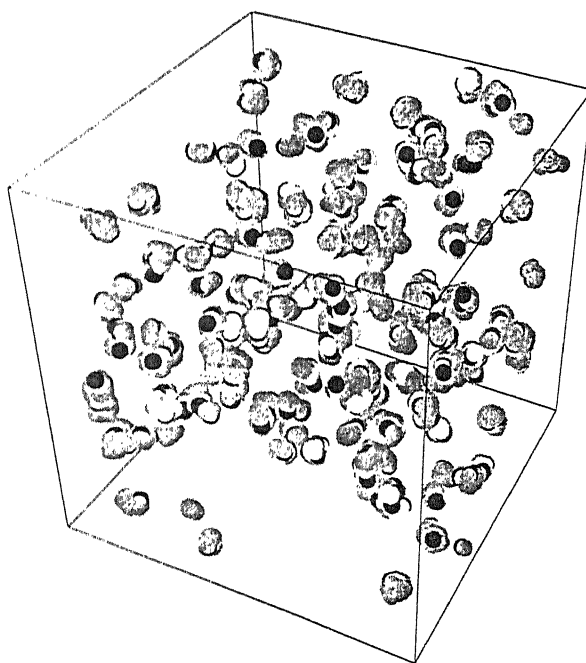


Figure 7.11: Snapshots of micellar aggregates formed by ionic gemini surfactants with hydrophobic spacer; $m = 5$, $n = 6$ and $K = 0$ at $T = 2.2$ when the surfactant density is 0.005.

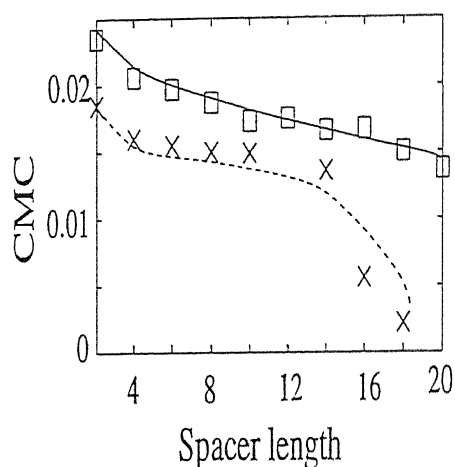


Figure 7.12: Variation of CMC of ionic geminis with hydrophilic spacer length; $m = 15$, $\Gamma = 2.2$. The symbols \square and \times correspond to $K = 0$ and $K = 2$, respectively.

both equal to 16. Does this imply that rod-like micelles are formed whenever the hydrophobic spacer and the tail are equal (or comparable) in length? In order to answer this question we have also looked at the snapshots of the micellar aggregates of similar gemini surfactants with shorter tails and spacers; a typical example, shown in fig.7.11, corresponds to $m = 5$, $n = 6$. The fact that these micelles are also "long, thread-like and entangled", like those in fig.7.6, in contrast to the rod-like micelles of fig.7.7, suggests that the morphology of the ionic gemini surfactants with hydrophobic spacers is dominantly determined by the length of the spacer; long, thread-like micelles are formed if the spacer is short and rod-like micelles are formed if the spacer is long.

7.3.2 Aggregates of Gemini Surfactants; Results for Hydrophilic Spacers:

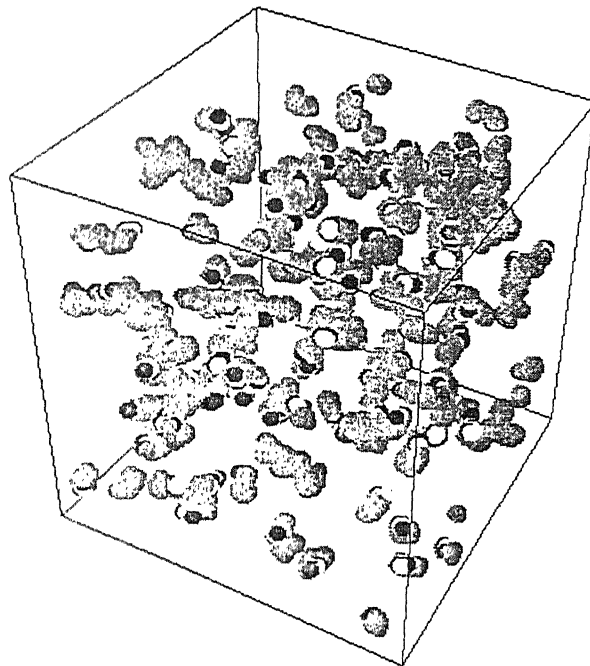


Figure 7.13: Same as fig. 7.6 except that the spacer is hydrophilic.

In fig.7.12 we plot the CMC against the length of the *hydrophilic* spacer for gemini surfactants with *ionic* head and tail length $m = 15$ (the qualitative features of the corresponding curve for $m = 5$ are very similar and, therefore, not shown). In contrast to the non-monotonic variation of CMC observed earlier with the variation of the length of hydrophobic spacers, now we find a *monotonic* decrease of CMC with the increase of the length of the hydrophilic spacer. This trend of variation is in qualitative agreement with the corresponding experimental observation [156]. Moreover, for given lengths of the hydrophobic spacer and the tail, n and m , the CMC for the bending energy $K = 2$ is lower than that for $K = 0$ (see fig.7.12); this trend of variation is exactly opposite to the corresponding trend observed earlier in the case of gemini surfactants with hydrophobic spacers.

The snapshots of the micellar aggregates formed by the gemini surfactants with *ionic heads*

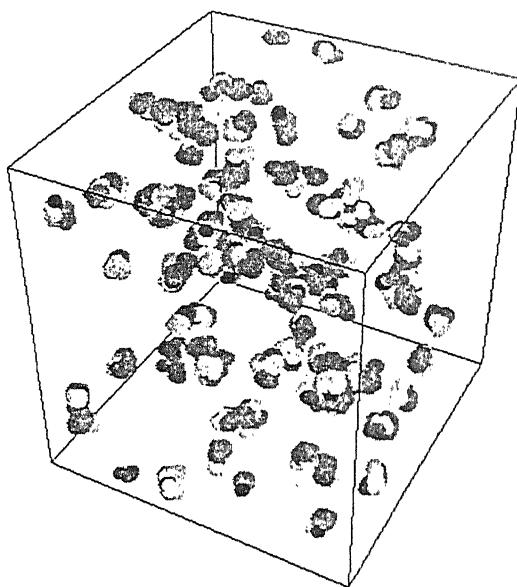


Figure 7.14: Same as fig. 7.7 except that the spacer is hydrophilic.

and *hydrophilic spacer* are shown for spacer lengths $n = 2$ (fig. 7.13) and for $n = 16$ (fig.7.14) for densities which are identical to those in the figs.7.6 and 7.7, respectively. Comparing the morphologies of the aggregates in fig.7.6 and fig.7.13 we find that the gemini surfactants with hydrophobic spacers form coarser (albeit fewer in number) aggregates compared to the corresponding geminis with hydrophilic spacers; this is also consistent with the fact that the CMC of the gemini surfactants with spacer length $n = 2$ are higher when the spacers are hydrophilic as compared to that for hydrophobic spacers.

The difference in the morphologies of ionic geminis with hydrophobic and hydrophilic spacers is much more striking when the spacer is longer ($n = 16$) (compare the fig.7.7 with fig.7.14)-the micelles are more or less spherical when the spacers are hydrophilic!

An important difference between the micellar aggregates of gemini surfactants with hydrophobic spacers and those with hydrophilic spacers is that more spacer monomers are found on

the outer surface of the aggregate (i.e., in contact with water) when the spacer is hydrophilic. This is consistent with one's intuitive expectation because the hydrophilic spacers like to be in contact with water.

The snapshots of the micellar aggregates of non-ionic gemini surfactants with hydrophilic spacers are very similar to those for the corresponding ionic gemini surfactants (and, therefore, not shown in any figure).

Hydrophilic spacers gain energy by remaining surrounded by water. On the other hand, hydrophobic spacers as well as tails try to avoid contact with water by hiding inside micellar aggregates. That is why in the snapshots of micellar aggregates we see that a larger number of monomers belonging to the spacers are in contact with water, when the spacers are hydrophilic, than those when the spacers are hydrophobic. And this is prominent particularly for long spacers.

7.4 Spatial Organization of Gemini Surfactants at Air-Water Interface: Results for Hydrophobic and Hydrophilic Spacers

7.4.1 Dilute regime

First let us consider the dilute regime where the concentration of the surfactants is so low that not only all of them remain, almost certainly, at the air-water interface but every surfactant may be regarded as, effectively, isolated from each other. In this limit the cross-sectional area A

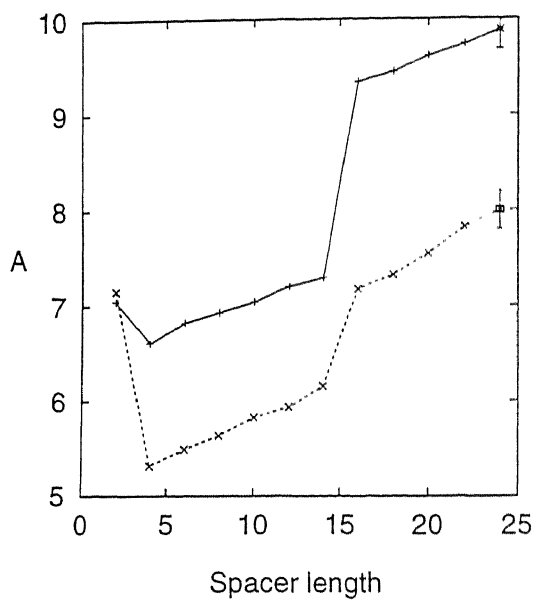


Figure 7.15: Variation of cross-sectional area of isolated individual gemini surfactant with spacer length. The solid line for hydrophobic spacer and broken line for hydrophilic spacer. To give an indication of the accuracy of the data points the error bar of only one point has been shown.

of the molecules is determined by only intra-molecular interactions, which is dominated by the steric (entropic) interactions among the tails and the spacer. We plot the cross-sectional area A of isolated individual gemini surfactants as a function of the length of the spacer in fig.7.15, in both the cases of (a) hydrophobic and (b) hydrophilic spacers. The spacer is very stiff when its length is $n = 2$ as no wiggle can form. The area A for $n = 4$ is smaller than that for $n = 2$ irrespective of the nature of the spacer (i.e., hydrophobic or hydrophilic); this is caused by the formation of wiggle on the spacer which brings the two heads closer. Further increase of the spacer length gives rise to a linear increase of the area A . However, a sharper increase in A takes place when the length of the spacer becomes equal to that of the tails; on both sides of this regime of sharp rise, the rate of increase of A with n is practically identical.

Because of its stiffness against wiggle formation, the spacer of length $n = 2$ can buckle neither towards air nor towards water and remains parallel (like a rigid rod) to the air-water interface. Therefore, if $n = 2$, the cross-sectional area A of isolated gemini surfactants with hydrophilic spacers is practically identical to that of gemini surfactants with hydrophobic spacers. However, for all larger values of n , A is smaller if the spacer is hydrophilic; a hydrophilic spacer buckles into water thereby leaving most of the space in the air above the heads available for occupation by the tails. On the other hand, the hydrophobic tails take up a substantial amount of available space in a cap-like volume in the air just above the heads thereby forcing the tails to spread out radially outward and, hence, increasing the effective area A .

Evidence in support of this scenario emerges also from the plots of vertical extension $\langle Z \rangle$ of the isolated gemini surfactants against the length of the spacer (see fig.7.16); a larger $\langle Z \rangle$ of gemini surfactants with hydrophilic spacer, as compared to those of gemini surfactants with

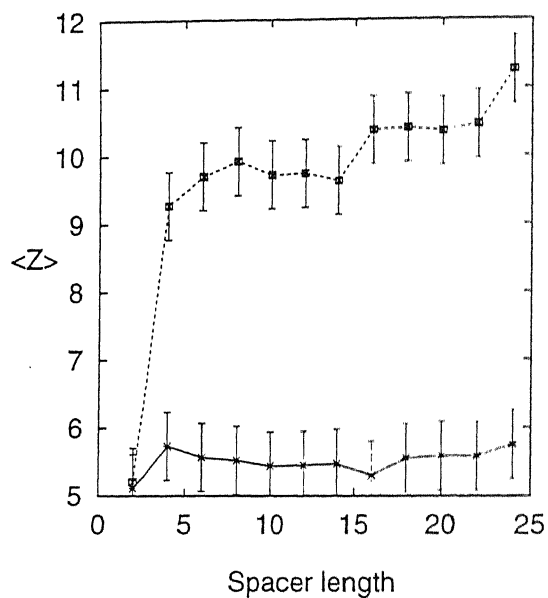


Figure 7.16: Variation of vertical extension of individual gemini surfactant with spacer length.

The solid line for hydrophobic spacer and broken line for hydrophilic spacer.

hydrophobic spacer of identical length, arises from the fact that the hydrophilic spacers buckle into water while their tails remain outside water.

7.4.2 High Surface density regime

The concentration profiles of the tails of the gemini surfactants with hydrophobic spacers are shown in fig.7.17(a) and the corresponding concentration profiles for gemini surfactants with hydrophilic spacers are shown in fig.7.17(b). In the case of gemini surfactants with hydrophobic spacer, the spacers minimize contact with water by arranging themselves just outside the water, but do not venture out too far from the interface. On the other hand, the hydrophilic spacers gain energy by moving inside water thereby leaving more space just outside water which become available for occupation by the tails; consequently, one would have naively expected, the tails of the gemini surfactants with hydrophilic spacers are likely to be found closer to the interface than those of the gemini surfactants with hydrophobic spacers. However, what we observe in reality in fig.7.17(b) is much more dramatic- a significantly large fraction of the monomers belonging to the tails are pulled into water along with the heads (see fig.7.18) to which they are attached! The loss of energy due to the increase in the area of contact between the hydrophobic tails and water is compensated by the gain of energy from the increase of contact between hydrophilic spacers and water as well as the gain of conformational entropy of the system arising from the larger amount of space available to those chains which remain at the interface. This interpretation is supported by our observation that this effect is more prominent at higher densities of surfactants. Some other manifestations of the entropic effect have been observed earlier [80–82].

The conclusions drawn from averaged concentration profiles are supported by the instan-

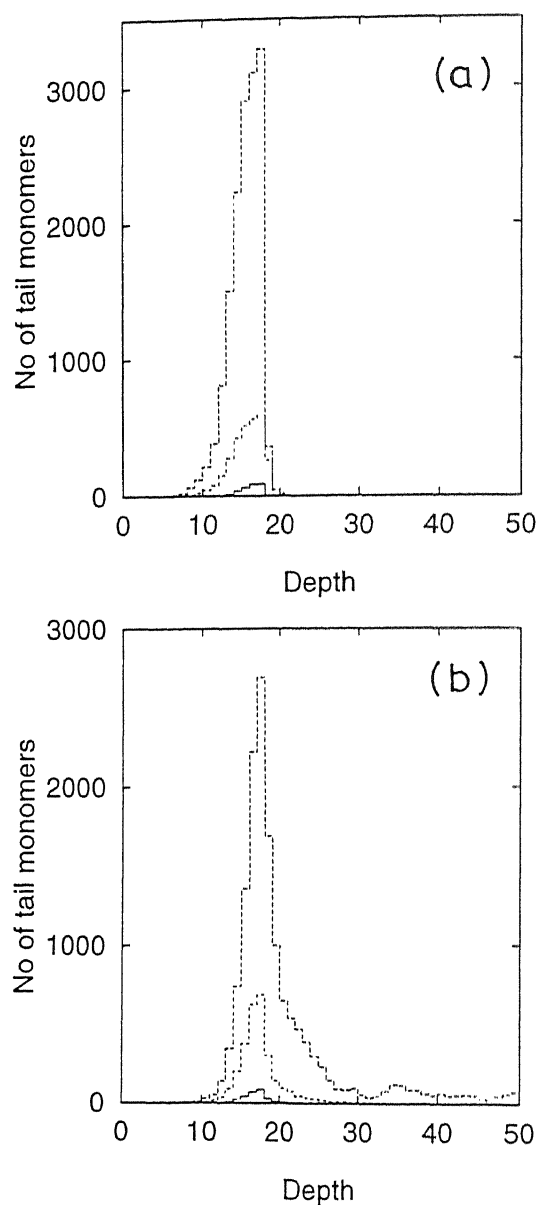


Figure 7.17: Concentration profiles for tail monomers for three different cases when the number of amphiphiles present in the systems are (i) 500 (solid line), (ii) 100 (broken line) and (iii) 10 (dashed line). (a) hydrophobic spacer (b) hydrophilic spacer.

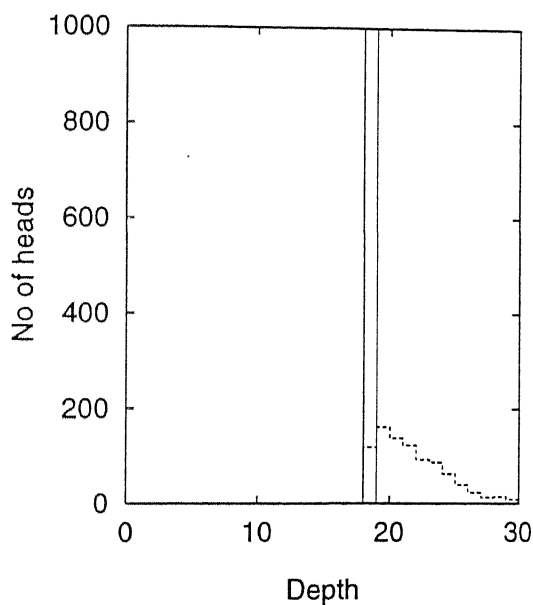


Figure 7.18: Concentration profiles for heads when the number of amphiphiles is 500. Solid line is for hydrophobic spacer and broken line for hydrophilic spacer.

taneous snapshots of the surfactants. Figure 7.19(a) 7.20(a) gives the snapshot of the gemini surfactants with hydrophobic spacer at the interface. For clarity we have shown only heads and spacers in fig. 7.19(a) and heads, tails and liaisons in fig. 7.20(a). This can be contrasted with the snapshots for hydrophilic spacer (fig 7.19(b) and 7.20(b)). In fig. 7.19(b) we have shown only heads and spacers and in fig. 7.20(b) we have shown heads, tails and liaisons. For hydrophilic spacer we find that the spacers and heads prefer to go inside water leaving space for tails at the interface.

7.5 Summary and Conclusion

In this chapter we have developed models of both ionic and non-ionic gemini surfactants with hydrophobic spacers as well as those with hydrophilic spacers. We have investigated the morphologies of the micellar aggregates of these gemini surfactants and computed the corresponding CMCs by carrying out MC simulations.

The main features of the aggregation of gemini surfactants with *hydrophobic* spacers can be summarized as follows: (i) the micelles are far from spherical- for short spacers these are long "thread-like" and for long spacers these are "rod-like"; (ii) the CMC varies non-monotonically with increasing spacer length; (iii) the CMC increases with the increase of the bending stiffness of the tails and spacers.

The main features of the aggregation of gemini surfactants with *hydrophilic* spacers can be summarized as follows: (i) the micelles are more or less spherical; (ii) the CMC decreases monotonically with increasing spacer length; (iii) the CMC decreases with the increase of the

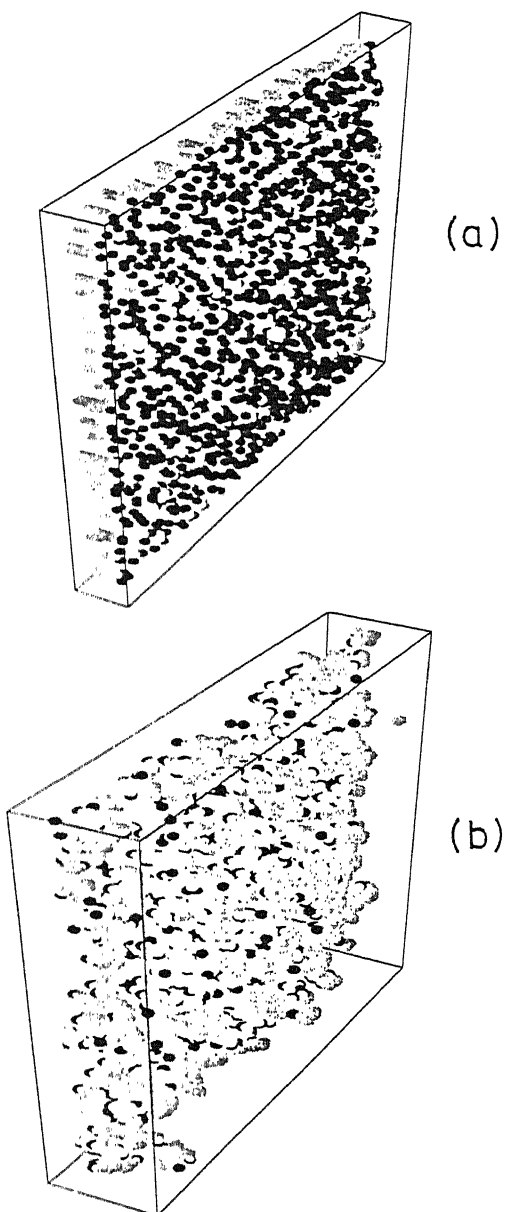


Figure 7.19: Snapshots of the gemini surfactants at the interface (a) with hydrophobic spacer and (b) with hydrophilic spacer. The black sphere represent monomers belonging to heads and grey sphere represent monomers belonging to spacers.

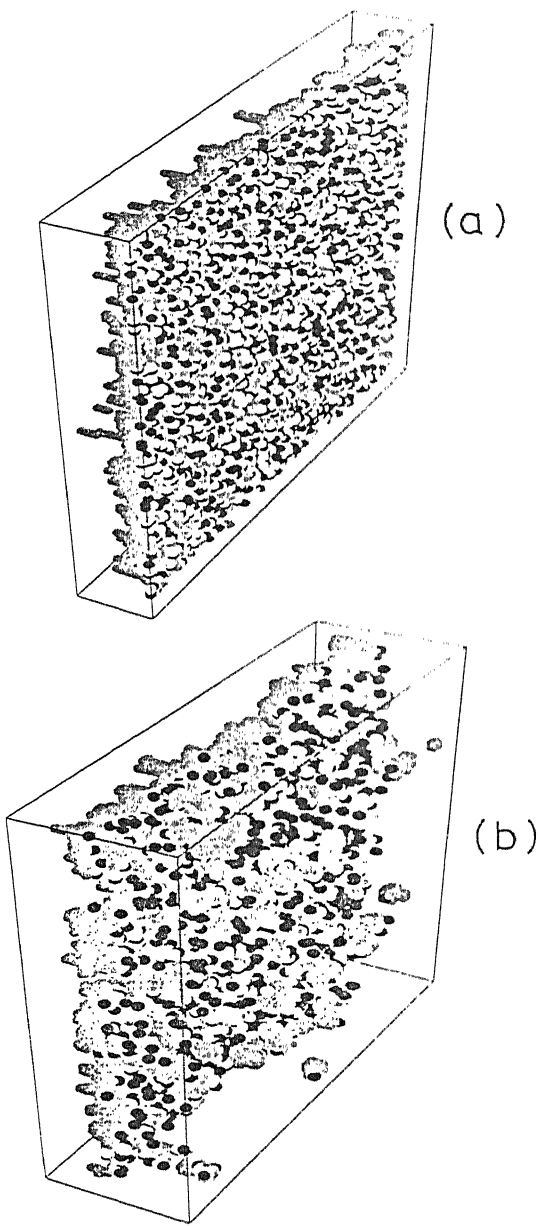


Figure 7.20: Same as in figure 7.19 except that now the black sphere represents monomers belonging to heads, grey sphere represent monomers belonging to tails and white sphere represent monomers belonging to liaisons.

bending stiffness of the tails and spacers.

In contrast to the case of single chain surfactants the CMC increases with the hydrocarbon tail length for both the ionic and non-ionic gemini surfactants irrespective of whether the spacer is hydrophobic or hydrophilic. However like the case of single chain surfactants the morphologies of the ionic gemini surfactants are identical to that of the corresponding non-ionic gemini surfactants both for hydrophobic as well as hydrophilic spacer.

Therefore, we conclude that (i) the shapes of aggregates are dominantly determined by the geometric shape and size of the molecules and whether the spacer is hydrophobic or hydrophilic, whereas (ii) the variation of CMC with spacer length is strongly influenced by the ionic charge and, again, whether the spacer is hydrophobic or hydrophilic.

In the case gemini surfactants at the air-water interface for dilute regime, the cross-sectional area for single isolated gemini surfactant increases with the spacer length both for hydrophobic and hydrophilic spacer. However beyond a certain length of the spacer the cross-sectional area is larger for the hydrophobic spacer as compared to that for hydrophilic spacer. These trends are consistent with the variation of vertical extension $\langle Z \rangle$ with spacer length; a larger value of $\langle Z \rangle$ for hydrophilic spacer as compared to the hydrophobic spacer of identical length is observed in our simulations.

For extremely high surface density of surfactants at the air-water interface we have demonstrated qualitatively the spatial organization of the gemini surfactants for both the case of hydrophobic and hydrophilic spacers.

In view of the above observations, it seems that the main effects of introducing the spacer is to impose an additional geometrical constraint on the packing of surfactant molecules and,

therefore, to influence their aggregate shape and other properties.

Molecular dynamics (MD) simulations of a similar molecular model of gemini surfactants has been carried out by Karaborni et al. [148]. In their model, particles of water interact mutually via a truncated Lennard-Jones (LJ) potential with sufficiently long cut-off to incorporate both the short-range repulsion and long-range attraction. The mutual interactions between the pairs of particles belonging to the tail were also similar. But, the cut-off range of the tail-water and head-head interactions were so short that no attraction was possible. However, the chains and spacers simulated by Karaborni et al. were much smaller than those investigated here. Besides, Karaborni et al. neither investigated the CMC and its variations with lengths of the tails and spacer nor considered any model of gemini surfactants with hydrophilic spacers. One should also try to develop more efficient MD algorithms to repeat our computations with more realistic interaction potentials on a continuum to check if any of the morphologies observed in this chapter have been influenced significantly by the discrete lattice.

It would be interesting to investigate the effects of weakening of the screening (i.e., increasing the range) of the repulsive Coulomb interaction between the ionic heads on the results reported here; but, such a MC study will require much larger computational resources.

Chapter 8

Monte Carlo simulation of amphiphiles in complex fluids confined in porous medium

8.1 Introduction

Effects of confining surfaces on simple fluids have been investigated for several years, particularly in the context of fluids in porous media [158]. However, the statistical mechanics of confined complex fluids has received very little attention so far. Investigations of these systems will not only contribute to the basic understanding of phase ordering in confined systems, but may also find application in oil extraction technology [160], because oil, brine (a solution of inorganic salts in water) and surfactants in earth's crust form a complex fluid like microemulsions.

Chowdhury et al.[159] have studied the structure of ternary microemulsions confined in model

pores through Monte Carlo (MC) simulation of Widom model. However, they have considered only single 'pores' in the form of 'slits'. The real porous materials are known to consist of an interconnected network of pores of different shapes and sizes. Moreover the model they consider, the Widom model, has many drawbacks in describing the phase diagram of ternary mixture. Recently Liverpool and Bernardes [58] have studied the aggregation of amphiphiles in ternary mixtures confined by walls (which can be considered as single pore). They have used reformulated Larson model discussed in chapter 4. The main result of their study is that at low temperature almost all the amphiphiles form a spanning cluster. However at high temperature, the cluster breaks up into small clusters. In this chapter we propose a methodology for studying the equilibrium structure of ternary microemulsions confined in a porous medium (such as Vycor glass). We illustrate the use of our proposed method by applying it to Larson model of ternary microemulsions confined in a model porous medium with neutral confining walls.

The chapter is organized as follows: in section 2 we describe our model, and in section 3 we describe how a model vycor glass (which is a porous medium) is prepared in a computer experiment. In the subsequent sections we illustrate the methods we propose here for the computer simulation of microemulsions in porous media.

3.2 The Model

Our model is based on the Larson model of microemulsions [41, 42, 44] and its later generalizations discussed in chapters 1 and 4 [46, 47].

A detailed analysis of the distribution of the sizes of clusters of amphiphiles can be performed

using techniques developed for the analysis of cluster statistics in percolation theory [132]. An amphiphile belongs to a cluster if any of its monomers is a nearest-neighbour of any of the monomers of amphiphiles already counted as part of the cluster. A Hoshen-Kopelman cluster counting algorithm [72] calculates the cluster size distribution $n(s)$ of clusters with s monomers (units).

8.3 Preparation of the Model porous medium

The model porous medium used in our simulation is constructed by first allowing a binary mixture to phase segregate using the cell dynamics scheme (CDS) [162] and, then, etching out one of the two components. This method was suggested by Chakrabarti [161] for modelling Vycor-like porous media. The porosity of the medium, which is defined as the volume fraction occupied by the pores, was kept $50(\pm 1)\%$. In the following we outline the cell dynamics scheme [162] for generating the model porous media. The single cell dynamics is described by

$$\psi(t+1, n) = f(\psi(t, n)) \quad (8.1)$$

where $\psi(t, n)$ is the value of the order parameter in the cell n at time t . For the nonconserved order parameter, the CDS model gives

$$\begin{aligned} \psi(t+1, n) &= f(\psi(t, n)) + D[\langle\langle \psi(t, n) \rangle\rangle - \psi(t, n)] \\ &\equiv \mathcal{F}[\psi(t, n)] \end{aligned} \quad (8.2)$$

where D is a positive constant proportional to the phenomenological diffusion constant; $\langle\langle * \rangle\rangle - *$ is isotropized discrete Laplacian. We use the following definition of $\langle\langle * \rangle\rangle$ on the

three dimensional cubic lattice

$$\begin{aligned} \langle\langle \psi(t, n) \rangle\rangle &= \frac{6}{80} \sum (\psi \text{ in the nearest - neighbour cells}) \\ &+ \frac{3}{80} \sum (\psi \text{ in the next - nearest - neighbour cells}) \\ &+ \frac{1}{80} \sum (\psi \text{ in the 3rd nearest - neighbour cells}) \end{aligned} \quad (8.3)$$

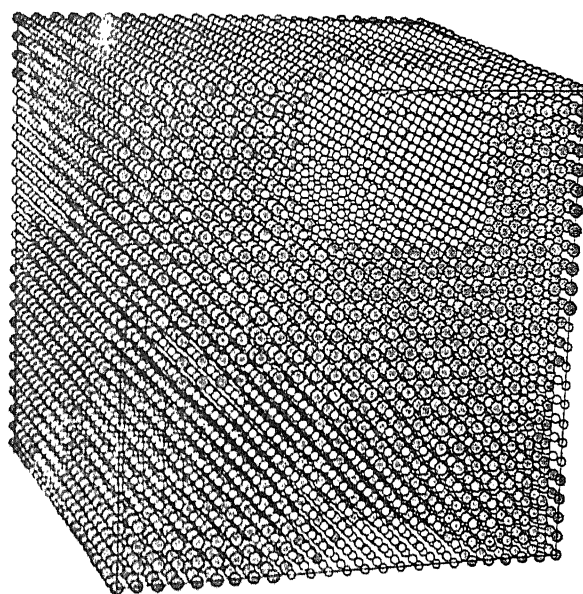
Since the choice of the injection function f does not affect the result, we choose the following form for the function f for our simulation

$$f(x) = A \tanh x \quad (8.4)$$

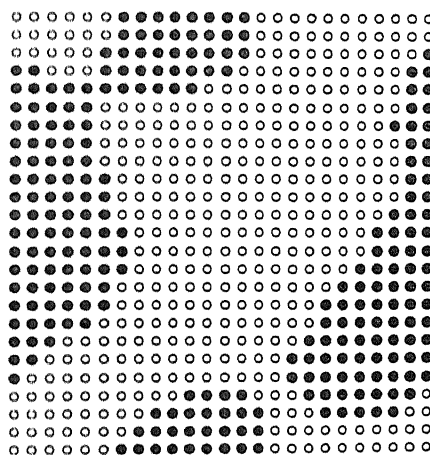
where A is a parameter which is greater than 1. In our simulation we start from a $L_x \times L_y \times L_z$ cubic lattice consisting of a 50% – 50% random mixture of two components. We use periodic boundary condition for the simulation. The values of the parameter A and D were chosen to be 1.3 and 0.5. The system was then allowed to evolve according to the cell dynamics equation (8.3). A porous medium of desired pore thickness can be created by stopping the phase separation process after an appropriate number of iteration steps and etching out one of the two phases. A model porous media has been shown in fig 8.1(a). Figure 8.1(b) shows a cross section of this model porous medium. The porosity, which is defined as the fraction of the vacancies on the lattice, of the model porous medium is about 50%.

8.4 Results and Discussion

Once the model porous medium is created, oil, water and amphiphiles molecules were put inside the pore following Larson-like prescription, as explained before. If a site is occupied by the



(a)



(b)

Figure 8.1: (a) A model porous medium (b) A typical cross section, Dark grey represent rocks and light grey represents pores.

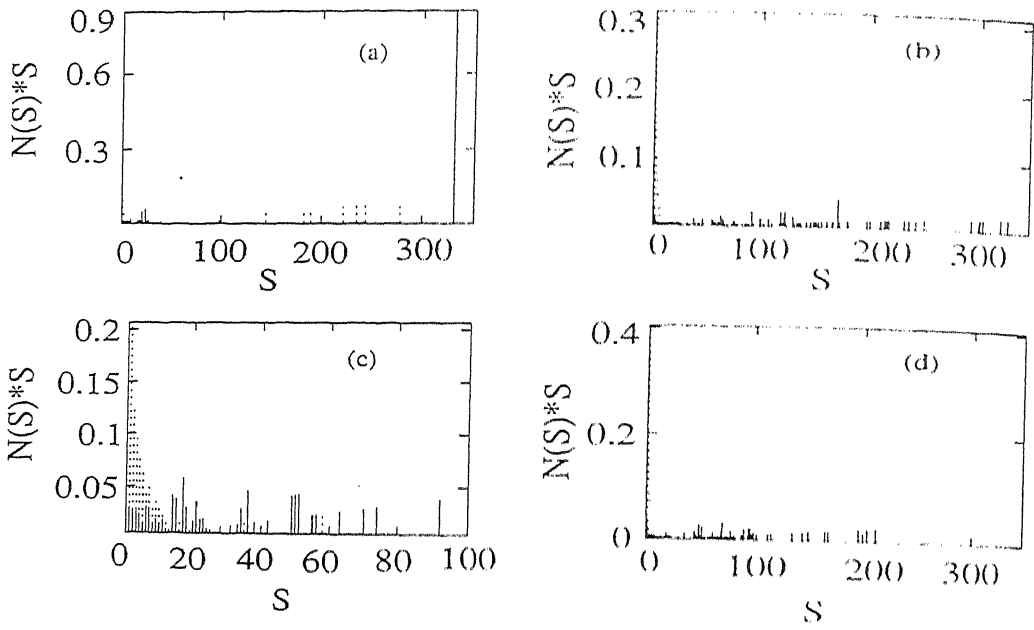


Figure 8.2: Cluster size distribution amphiphiles inside (a) single pore (c) vycor glass. Cluster size distribution for oil inside (b) single pore and (d) vycor glass. The solid line is for temperature 1 and dashed line is for temperature 4.

rock it is represented by $S_i = 0$ (for non interacting rocks). If the rocks are interacting then depending on the nature of interaction we put $S_i = 1$ if the rocks are "water-loving" and $S_i = -1$ if it is "oil-loving". The amphiphiles were of the type $\mathcal{H}_2\mathcal{N}_1\mathcal{T}_3$. First we simulated the system when oil-water-amphiphiles are confined by walls from the above and below (this corresponds to single pore). We have studied the cluster size distribution of the amphiphiles for 25^3 lattice where the total volume fraction occupied by the amphiphiles is 15% (number of amphiphiles is 390). The ratio of oil and water was kept at 50% – 50%. At low temperatures (e.g., $T = 1.0$) almost all the amphiphiles (331) form a huge cluster (figure 8.2(a)) [58]. At high enough temperatures (e.g., $T = 4.0$) the large cluster breaks into smaller clusters fig 8.2(a). When the simple confining walls are replaced by the interconnected tortuous porous structure (vycor glass) the amphiphiles



Figure 8.3: (a) A cross section of bicontinuous microemulsion inside single pore. w denotes water molecule, o denotes oil molecule and H and T denote head and tail of the amphiphile molecule.

cannot form a large cluster since the movements of the amphiphiles are now constrained by the presence of rocks (Fig. 8.2(c)). For low concentration (10%) of oil (water) droplets of oil in water (water in oil) are formed. Figures 8.2(b) and 8.2(d) give the cluster size distribution of oil in single pore and vycor glass respectively.

When the concentration of oil and water are comparable we get bicontinuous structure for both single pore and vycor like porous medium. Figures 8.3(a) and 8.3(b) show the bicontinuous microemulsions inside single pore and porous medium respectively.

For low concentration (say 10%) of either oil or water, micelles are formed at sufficiently low temperatures. Cross section of the micellar aggregates have been shown in figures 8.4(a) and

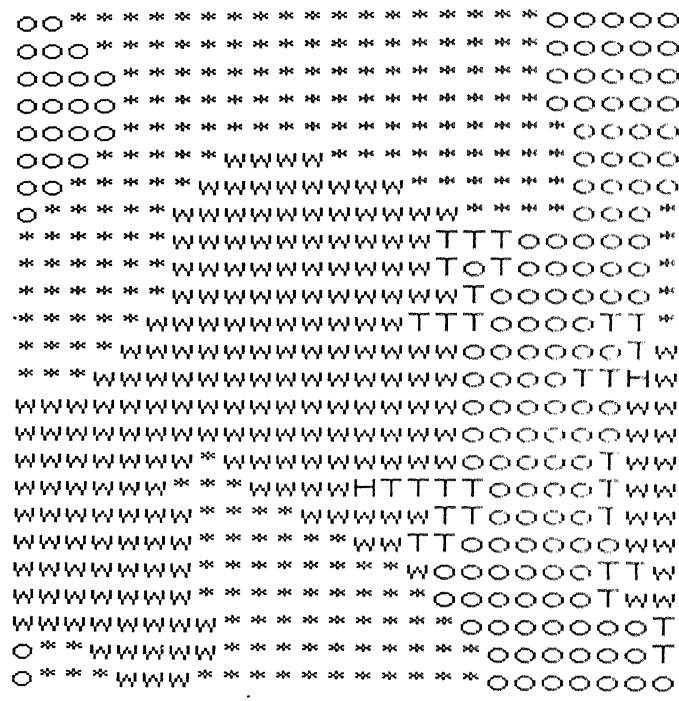


Figure 8.3: (b) A cross section of bicontinuous microemulsion inside porous medium. * denotes rocks.



Figure 8.4: (a) Micellar aggregates (oil droplet) inside single pore.

8.4(b).

8.5 Summary and conclusion

In this chapter we have proposed a method of computer simulation of the ternary microemulsion confined in porous medium (such as vycor glass). The emphasis was on the methodology and not on the results. To illustrate the method we have calculated the cluster size distribution of amphiphiles and oil inside the porous medium at two different temperatures. We have also looked at the structure of the microemulsion for different concentration ratios of oil and water.

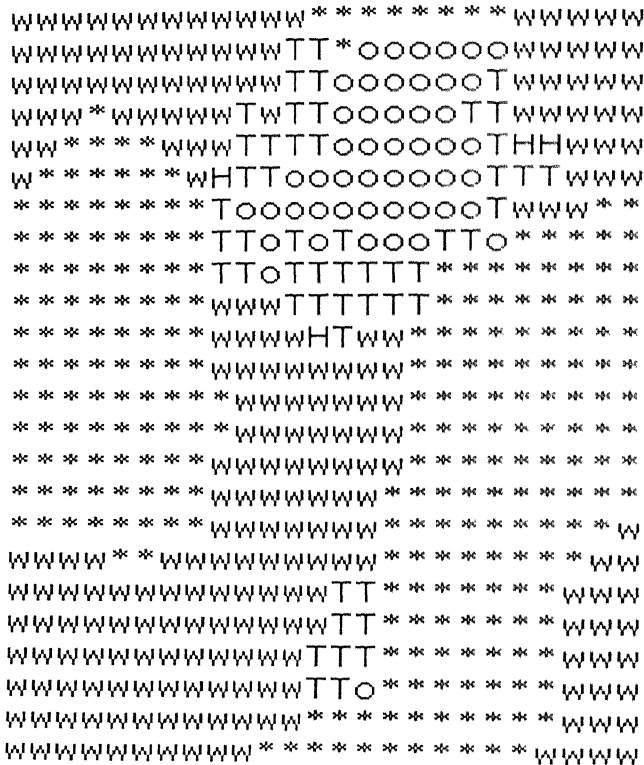


Figure 8.4: (b) Micellar aggregates (oil droplet) inside porous medium.

Chapter 9

Conclusion

In this thesis we have studied the bulk as well as interfacial behaviour of the amphiphilic systems from the microscopic point of view using statistical mechanical approaches, particularly, the techniques of MC simulation. We have considered two different approaches to study the amphiphilic systems, namely, interface/membrane model and microscopic lattice model. However, so far as the membrane approach is concerned, we have studied only the out-of-plane thermal fluctuations of some model membrane. We have not studied any self-assemblies and bulk properties using membrane model approach. We have investigated the self-assemblies exclusively through MC simulation of microscopic lattice models.

In chapter 2 of the thesis we have studied the nature of the amphiphilic monolayer membrane at the oil-water interface in the Widom model which is the simplest microscopic lattice model of ternary microemulsions. The Widom model is a classical Ising spin model with nearest-neighbour as well as farther-neighbour interactions on an appropriate lattice. The nearest-neighbour interactions gives rise to interfacial tension and the farther-neighbour interactions contribute to the

bending stiffness of the amphiphilic monolayer; these farther-neighbour interactions give rise to a richer bulk phase diagram of the Widom model, as compared to that of the nearest-neighbour Ising model. We have found that these farther-neighbour interactions do not affect the interface roughening exponent i.e. the membrane is rough but not crumpled. Nevertheless, the oil-water interface in the Widom model is wider than that in the Ising model with only nearest-neighbour interactions.

The absence of the crumpling transition in the Widom model is attributed to the fact that in the Widom model we can not switch off the interfacial tension and study the effect of bending stiffness only. On the other hand liquid-like amphiphilic membranes whose out-of-plane thermal fluctuations are governed by the bending stiffness alone are known to be crumpled. To make a clear distinction between the interfacial tension and bending stiffness and to get a possible crumpling transition we have proposed a discrete model of an interface (both unrestricted discrete SOS (UDSOS) and restricted discrete SOS (RDSOS)) with a specific form of the bending energy; this bending energy is associated with bending of the interface at right angles. These have been discussed in chapter 3. When the out-of-plane thermal fluctuations of the interface in the UDSOS model are controlled only by this bending stiffness it is crumpled but the nature of the crumpling is very different from that observed in the continuum models. We have shown that although the conformation of the interface in this case satisfies one particular definition of a crumpled manifold, it does not satisfy two other widely used definitions of crumpling although all these three definitions are known to be mutually consistent when applied to the continuum models. We have studied some dynamical properties of a UDSOS model in $d = 1$ in the special case of vanishing interfacial tension but non-zero bending stiffness by using a Master equation approach

and the width of the interface W is found to vary with time as \sqrt{t} . By identifying an appropriate crossover length, we have also explained why the roughening exponent α of the UDSOS model in the presence of non-zero interfacial tension is independent of whether or not it has non-vanishing bending stiffness.

Introduction of a new RDSOS model is motivated through the examination of four different ensembles. By carrying out MC simulation of this RDSOS model, we compute an exponent β which characterizes the time-dependence of its width during the *very early stages* of its dynamical evolution from a flat initial configuration.

So far the bending rigidity has been introduced as a parameter in all the models of membranes. In real amphiphilic systems this arises naturally from the microscopic interaction among the constituent molecules and from their conformational degrees of freedom. So it is natural to consider a more realistic model where the conformational degrees of freedom of the amphiphilic molecules are taken into account. In chapter 4 we have studied the roughening properties of the amphiphilic membrane at the oil-water interface in the Larson model which explicitly incorporates the conformational degrees of freedom of the amphiphilic molecules. We have shown that the width of the interface varies as $\sqrt{L_x}$, and hence the oil-water interface in the Larson model is rough but not crumpled. Moreover, the wider interface in the presence of amphiphiles in this model is a consequence of the lowering of the oil-water interfacial tension by the surfactants; we have argued that this reduction of surface tension in this model is of entropic origin. After studying the nature of amphiphilic monolayer at the oil-water interface we shift our emphasis towards air-water interface and, then, study some of the bulk properties the amphiphilic systems.

In chapter 5 we have investigated the out-of-plane phase segregation of the amphiphiles in

a binary mixture, of two species which are chemically identical but has different lengths, at the air-water interface. We have demonstrated an entropy-driven phase segregation in a direction perpendicular to the air-water interface when the initial total surface density of the amphiphiles is sufficiently high. The steric repulsion between the tails of the longer amphiphiles is argued to be the driving force behind this phase segregation phenomena. In other words, this phase segregation is driven by the gain of conformational entropy, contrary to the phenomenon of energy-driven phase segregations, e.g., in a binary alloy. We have also studied the nature of the in-plane clustering of the monomers belonging to the long and the short amphiphiles.

So far we have studied only the interfacial properties of the systems containing only single chain amphiphiles although in chapter 5 we have studied some of the bulk properties. In the subsequent chapters we have focussed attention on both the interfacial as well as bulk properties. In chapter 6 we have looked at the morphologies of the aggregates formed by single chain and double chain amphiphiles. Our computer simulations have shown the formation of stable spherical micelles for single chain amphiphiles both for single species as well as for binary mixture of single chain amphiphiles. On the other hand double chain amphiphiles have been found to aggregate forming vesicles.

Gemini surfactants which are complex double chain amphiphiles are thought to be the next generation surfactants for their unusual characteristics, such as very low critical micellar concentration (CMC) and a high efficiency in reducing the oil-water interfacial tensions in comparison with the conventional single chain surfactants. We have proposed a microscopic lattice model of these gemini surfactants in chapter 7. By extensive MC simulation we have studied the aggregation behaviour of these gemini surfactants in water and the spatial organization of these

gemini surfactants in a system where water is separated from the air above it by a sharp well defined interface. We have also calculated the critical micellar concentration (CMC) by varying different parameters. The results of our numerical investigations are summarized as follows: (i) For *hydrophobic* spacer these model geminis form long, thread-like and entangled micellar aggregates even at low concentrations, where single-chain model surfactants form spherical micelles, provided the spacer is not too long. On the other hand, rod-like micellar aggregates form when the hydrophobic spacer is sufficiently long. When the spacer is *hydrophilic* we get more or less spherical micelles. There is no qualitative difference between the morphologies of the aggregates formed by ionic gemini surfactants and those formed by the corresponding nonionic gemini surfactants, irrespective of whether the spacer is hydrophobic or hydrophilic.

(ii) For ionic gemini surfactants with *hydrophobic* spacer the CMC varies non-monotonically with the increase in spacer length, whereas it decreases monotonically with spacer length for non-ionic gemini surfactants. On the other hand, when the spacer is *hydrophilic* the CMC decreases monotonically with spacer length both for ionic as well as non-ionic gemini. (iii) The CMC is found to *increase* with the increase of the bending stiffness of the tails and spacers if the spacer is *hydrophobic*. In contrast, the CMC *decreases* with the increase of the bending stiffness of the tails and spacers when the spacer is *hydrophilic*. (iv) In contrast to the single chain surfactants the CMC of gemini surfactants increases with the tail length (both for ionic and non-ionic) irrespective of whether the spacer is hydrophobic or hydrophilic. (v) In case of the gemini surfactants at the air-water interface for extremely dilute regime the cross-sectional area of the isolated individual gemini surfactants increases with the spacer length for both hydrophobic as well as hydrophilic spacer. We also find the similar trend of variation for the vertical extension. However when the

spacer is long, for a given value of spacer length, the cross-sectional area is smaller if the spacer is hydrophilic, whereas the vertical extension is larger for the hydrophilic spacer as compared to the case when the spacer is hydrophobic. For the case of high surface density regime we have shown the spatial organization of the gemini surfactants qualitatively for both the case when the spacer is hydrophobic as well as for the case when the spacer is hydrophilic. Some of the trends of variation are counter-intuitive but are in excellent agreement with the available experimental results.

From the observations in chapter 7 we infer that (i) the shapes of aggregates are dominantly determined by the geometric shape and size of the molecules and whether the spacer is hydrophobic or hydrophilic, whereas (ii) the variation of CMC with spacer length is strongly influenced by the ionic charge and, again, whether the spacer is hydrophobic or hydrophilic.

In chapter 8 we have presented a numerical scheme for computer simulation of ternary microemulsion inside porous medium, e.g., vycor glass.

9.1 Future direction of research

It is important to calculate the gain in conformational entropy over the energy loss quantitatively and to show that it is the driving force behind the phase segregation phenomena described in chapter 5. Future research also should try to explain quantitatively (i) the non-monotonic variation of CMC with spacer length and (ii) increase of CMC with the increase of hydrophobic tail length for gemini surfactants. To explain the unusual morphologies of the aggregates formed by the gemini surfactants, both in water and at air-water interface, is another

challenging problem.

The $A-B$ block copolymer serves as a surfactant in a A/B homopolymer blend. A binary polymer blend containing an amphiphilic block copolymer shows similar phase separated structures like microemulsions [163]. It would be interesting to apply our methodology of modelling to such ternary polymer mixtures and study the phase behaviour and to see whether any interesting new phenomena can arise. Recently there has been lot of interest on 'living polymers'. There is substantial experimental evidence that for low surfactant concentration certain surfactant solutions contain large one dimensional aggregates which can be considered as 'living polymer'[164]. So it would be interesting to study the structure and dynamics of the "living polymers" using the lattice models of the same type as studied extensively in this thesis.

References

- [1] D. F. Evans and H. Wennerstrom, *The colloidal domain where physics, chemistry, biology and technology meet*, VCH, New York (1994).
- [2] G. Gompper and M. Schick *Phase Transitions and Critical Phenomena*, Vol. 16, ed. C. Domb and J. Lebowitz, (Academic Press, London 1994)
- [3] T. B. Liverpool, in *Annual Reviews of Computational Physics*, vol. IV, edited by D. Stauffer, (World Scientific, Singapore 1996)
- [4] D. Chowdhury, *J. Phys: Cond. Matt.*, **6**, 2435 (1994);

T. Kawakatsu, K. Kawasaki, M. Furusaka, H. Okabayashi and T. Kanaya *J. Phys.: Cond. Matt.*, **6**, 6385 (1994);

M. Laradji, H. Guo, M. Grant and M.J. Zuckermann *Adv. Chem. Phys.*, **89**, 159 (1995).
- [5] R. Lipowsky *Nature*, **349**, 475 (1991).
- [6] J. N. Israelachvili *Intermolecular and Surface Forces* (Academic, New York 1991).
- [7] G. Cevc ed. *Phospholipid Handbook*, (Dekker, New York 1993).

- [8] L. Peliti in *Fluctuating Geometries in Statistical Mechanics and Field Theory* ed. F. David and P. Ginsparg, (North-Holland, Amsterdam 1996).
- [9] V. Degiorgo and M. Corti *Physics of Amphiphiles: Micelles, Vesicles and Microemulsions*, (North-Holland, Amsterdam 1985).
- [10] C. Tanford *The Hydrophobic Effect: Formation of Micelles and Biological Membranes*, (Wiley, New York 1980).
- [11] Y.F. Deinega, Z.R. Ulberg, L.G. Marochko, V.P. Rudi and V.P. Deisenko, *Kolloidn Zh.*, **36**, 649 (1974).
- [12] F. M. Menger and C. A. Littau, *J. Am. Chem. Soc.*, **113**, 1451 (1991).
- [13] F. M. Menger and C. A. Littau, *J. Am. Chem. Soc.*, **115**, 10083 (1993).
- [14] M. Rosen, *Chemtech*, **23**, 30 (1993).
- [15] R. Zana, M. Benrraou and R. Rueff, *Langmuir*, **7**, 1072 (1991).
- [16] R. Zana and Y. Talmon, *Nature*, **362**, 228 (1993).
- [17] L.D. Song and M.J. Rosen, *Langmuir*, **12**, 1149 (1996).
- [18] L. E. Scriven *Nature*, **263**, 123 (1976); L. E. Scriven in *Micellization, Solubilization and Microemulsions* ed. K.L. Mittal, (Plenum, New York 1977).
- [19] G. Gompper and J. Goos, in *Annual Reviews of Computational Physics*, vol. II, edited by D. Stauffer, (World Scientific, Singapore 1995).

- [20] M. Kahlweit, R. Strey, M. Aratono, G. Busse, J. Jen and K.V. Schubert *J. Chem. Phys.*, **95**, 2842 (1991).
- [21] A. Pouchelon, J. Meunier, D. Langevin, D. Chatenay and A.M. Cazabat *Chem. Phys. Lett.*, **76**, 277 (1980).
- [22] E.D. Goddard and G.C. Bensen *Can. J. Chem.*, **35**, 1936 (1957); N.M. van Os, G.J. Daane and T.A.B.M. Nolsman *J. Coll. Int. Sci.*, **115**, 402 (1987).
- [23] M. Abu Hamdiyyah and K. Kumar *J. Phys. Chem.*, **94**, 6445 (1990).
- [24] B. Lindman and H. Wennerstrom *Topics Current Chem.*, **87**, 1 (1984).
- [25] P. Guering and B. Lindmann *Langmuir*, **1**, 464 (1985).
- [26] P. G. de Gennes and C. Taupin, *J. Phys. Chem.*, **88**, 2294 (1982).
- [27] P.G. de Gennes and J. Prost *The Physics of Liquid Crystals*, (Clarendon, Oxford 1993).
- [28] M. Kahlweit, M. Strey and P. Firman *J. Phys. Chem.*, **90**, 671 (1986).
- [29] R. Strey *Ber. Bunsenges. Phys. Chem.*, **97**, 742 (1993).
- [30] H. Hoffmann *Adv. Coll. Int. Sci.*, **32**, 123 (1990).
- [31] R. Strey, R. Schomäcker, D. Roux, F. Frederic and U. Olsson, *J. Chem. Soc. Faraday Trans.*, **86**, 2253 (1990).
- [32] D. Roux, C. Coulon and M.E. Cates *J. Phys. Chem.*, **96**, 4174 (1992).
- [33] G. Cevc and D. Marsh *Phospholipid Bilayers*, (Wiley, New York 1987).

- [34] O. Abillon, L. Lee, D. Langevin and K. Wong *Physica (Amsterdam)*, **A172**, 209 (1991).
- [35] J. Wheeler and B. Widom *J. Am. Chem. Soc.*, **90**, 3064 (1968); B. Widom *J. Chem. Phys.*, **81**, 1030 (1984); *ibid*, **84**, 6943 (1986).
- [36] M. Blume, V. Emery and R.B. Griffiths *Phys. Rev. A*, **4**, 1071 (1971).
- [37] G. Gommper and M. Schick, *Phys. Rev. Lett.*, **62**, 1647 (1989). *Phys. Rev. B*, **41**, 9148 (1990).
- [38] M. Laradji, H. Guo, and M. J Zuckermann, *J. Phys. Cond. Matter*, **6**, 2799 (1994).
- [39] M. Schick and W.-H. Shih *Phys. Rev. Lett.*, **59**, 1205 (1987).
- [40] S. Alexander *J. Physique Lett.*, **39**, L1 (1978).
- [41] R.G. Larson, L.E. Scriven and H.T. Davis *J. Chem. Phys.*, **83**, 2411 (1985).
- [42] R.G. Larson *J. Chem. Phys.*, **89**, 1642 (1988):
- [43] R.G. Larson *J. Chem. Phys.*, **91**, 2479 (1989).
- [44] R.G. Larson *J. Chem. Phys.*, **96**, 7904 (1992).
- [45] D. Stauffer, N. Jan and R.B. Pandey *Physica (Amsterdam)*, **198A**, 401 (1993).
- [46] D. Stauffer, N. Jan, Y. He, R.B. Pandey, D.G. Marangoni and T. Smith-Palmer *J. Chem. Phys.*, **100**, 6934 (1994).
- [47] N. Jan and D. Stauffer *J. Phys. II (France)*, **4**, 345 (1994).

- [48] F. H. Stillinger *J. Chem. Phys.*, **78**, 4654 (1983).
- [49] M. W. Deem and D. Chandler, *Phy. Rev. E*, **49**, 4268 (1994); M. W. Deem and D. Chandler, *Phy. Rev. E*, **49**, 4276 (1994).
- [50] K. Chen, C. Ebner, C. Jayaprakash and R. Pandit, *J. Phys.*, **C38** L361 (1987); *Phy. Rev. A*, **38** 6240 (1988).
- [51] T. P. Stockfisch and J. C. Wheeler, *J. Phys. Chem.* **92**, 3292 (1988).
- [52] A.T. Bernardes, V.B. Henriques and P.M. Bisch *J. Chem. Phys.*, **101**, 645 (1994).
- [53] R.G. Larson *Chem. Eng. Sci.*, **49**, 2833 (1994).
- [54] D. Stauffer and D. Woermann *J. Phys. II (France)*, **5**, 1 (1995).
- [55] S. Boyden, N. Jan and T. Ray *Nuovo Cimento*, **16D**, 1439 (1994).
- [56] M. Sahimi and P. Nowroozi *Phys. Rev. Lett.*, **73**, 1182 (1994).
- [57] T. B. Liverpool and A.T. Bernardes *J. Phys. II (France)*, **5**, 1003 (1995).
- [58] T. B. Liverpool and A.T. Bernardes *J. Phys. II (France)*, **5**, 1457 (1995).
- [59] A.T. Bernardes *J. Phys. II (France)*, **6**, 169 (1996); *unpublished*, (1996).
- [60] B. Smit, P.A.J. Hilbers, K. Esselink, L.A.M. Rupert, N.M. van Os and A.G. Schlijper *Nature*, **348**, 624 (1990); B. Smit, P.A.J. Hilbers, K. Esselink, L.A.M. Rupert, N.M. van Os and A.G. Schlijper *J. Phys. Chem.*, **95**, 6361 (1991); B. Smit, K. Esselink, P.A.J. Hilbers, N.M. van Os, L.A.M. Rupert and I. Szleifer *Langmuir*, **9**, 9 (1993).

- [61] K. Binder and D.W. Heermann *Monte Carlo Simulation in Statistical Physics*, (Springer-Verlag, Berlin 1988).
- [62] N. Metropolis, A.W. Rosenbluth, M.N. Rosenbluth, A.H. Teller and E. Teller *J. Chem. Phys.*, **21**, 1087 (1953).
- [63] K. Binder in *Computational Modelling of Polymers*, ed. J. Bicerano, (Marcel Dekker, New York 1992).
- [64] M.W. Matsen and D.E. Sullivan *Phys. Rev. A*, **41**, 2021 (1990); M.W. Matsen, M. Schick and D.E. Sullivan *J. Chem. Phys.*, **98**, 2341 (1993).
- [65] G. Gompper and M. Schick, *Phys. Rev. Lett.* **65**, 1116, (1990).
- [66] M. Laradji, H. Guo, M. Grant and M.J. Zuckermann *J. Phys. A: Math. Gen.*, **24**, L629 (1991); *em J. Phys.: Cond. Mat.*, **4**, 6715 (1992).
- [67] M. Teubner and R. Strey, *J. Chem. Phys.* **87**, 3195 (1987).
- [68] K. Kawasaki and T. Kawakatsu, *Physica A* **164**, 549, (1990); G. Gompper and S. Klein, *J. Phys. II France* **2**, 1725 (1992).
- [69] K. Chen, C. Jayaprakash, R. Pandit and W. Wenzel, *Phys. Rev. Lett.* **65**, 2736 (1990).
- [70] A. Hansen, M. Schick and D. Stauffer *Phys. Rev. A*, **44**, 3686 (1991).
- [71] D. Stauffer and A. Aharony *Introduction to Percolation Theory*, (Taylor and Francis, London 1994);
M. Sahimi *Applications of Percolation Theory*, (Taylor and Francis, London 1994).

- [72] J. Hoshen and R. Kopelman *Phys. Rev. B*, **14**, 3438 (1976).
- [73] M. Almgren and S. Swarup *J. Phys. Chem.*, **86**, 4212 (1982); *ibid*, **87**, 876 (1983).
- [74] R. Aschauer and D. Beysens *Phys. Rev. E*, **47**, 1850 (1993); *J. Chem. Phys.*, **98**, 8194 (1993).
- [75] P. Honorat, D. Roux and A.M. Bellocq *J. Phys. Lett.*, **45**, L691 (1984).
- [76] J.S. Wang *Physica (Amsterdam)*, **166A**, 173 (1990); H.-O. Heuer *J. Phys. A.*, **26**, L333 (1993); I.O. Mayer *J. Phys. A.*, **22**, 2815 (1989).
- [77] H. Rieger and A.P. Young *J. Phys. A.*, **26**, 5279 (1993);
- [78] T. Kunitake, R. Ando and Y. Ishikawa *Mem. Kyushu University*, **46**, 221 (1986).
- [79] H. Rehage and A. Burger *Physica (Amsterdam)* **A194**, 424 (1993); A. Burger and H. Rehage *Die Ang. Makrom. Chem.*, **202/203**, 31 (1992); H. Rehage, E. Schnabel and M. Veyssié *Makrom. Chem.*, **189**, 2395 (1988).
- [80] D. Chowdhury *J. Phys. II (France)*, **5**, 1469 (1995).
- [81] D. Chowdhury, *Langmuir*, **12**, 1098 (1996).
- [82] Chowdhury D., Maiti P.K., Sabhapandit S. and Taneja P., *Phys. Rev.E*, June (1997).
- [83] F.E. Runge and H. Yu *Langmuir*, **9**, 3191 (1993); J.Y. Fang and R.A. Uphaus *Langmuir*, **10**, 1005 (1994).
- [84] Y. Moroi *Prog. Surf. Coll. Sci.*, **77**, 55 (1988).

- [85] G.G. Robert *Adv. Phys.*, **34**, 475 (1985).
- [86] D. Chowdhury, A.T. Bernardes and D. Stauffer *in press*
- [87] M. Milik, A. Kolinski and J.J. Skolnik *J. Chem. Phys.*, **93**, 4440 (1990).
- [88] M. Murat and G. S. Grest, *Macromolecules*, **22**, 4054 (1989); **24**, 704 (1991);
Phys. Rev. Lett. **63**, 1074 (1989);
G. S. Grest, *Macromolecules*, **27**, 418 (1994) .
- [89] B.P. Gaber, J.M. Schnur and D. Chapman *Biotechnological Applications of Lipid Microstructures*, (Plenum, New York 1988).
- [90] E.W. Kaler, A. Kamalakara Murthy and B.E. Rodriguez and J.A.N. Zasadzinski *Science*, **245**, 1371 (1989); E.W. Kaler, K.L. Herrington and A. Kamalakara Murthy *J. Chem. Phys.*, **96**, 6698 (1992).
- [91] A.J. Bray *Adv. Phys.*, **43**, 357 (1994).
- [92] J.D. Gunton, M. San Miguel and P.S. Sahni in *Phase Transitions and Critical Phenomena*, Vol. 8, ed. C. Domb and J. Lebowitz, (Academic Press, London 1983)
- [93] F. Mallamace, N. Micali, S. Trusso and S.H. Chen *Phys. Rev. E*, **51**, 5818 (1995).
- [94] A.T. Bernardes and T.B. Liverpool *in preparation*.
- [95] K. Watanbe, M. Ferrario, and M. Klein, *J. Phys. Chem.*, **92**, 819 (1988)

-
- [96] S H Chen and R Rajagopalan (eds) *Micellar solutions and microemulsions*, (Springer, Berlin, 1990)
- [97] G. Gompper and M. Schick, in *Modern Ideas and problems in amphiphile science*, eds W. Gelbert, D. Roux and A. Ben-Shaul (Springer 1993)
- [98] P.K. Maiti and D. Chowdhury, *J. Phys. I France* **5**, 671 (1995).
- [99] B. Kahng, A. Berera and K. A. Dawson, *Phys. Rev. A*, **42**, 6093 (1990)
- [100] D. Morawietz, D. Chowdhury, S. Vollmar and D. Stauffer, *Physica A*, **187**, 126 (1992)
- [101] N. Jan and D. Stauffer, *J. Phys. France* **49**, 623 (1988)
- [102] K. A. Dawson, *Phy. Rev. A*, **36**, 3383 (1987).
- [103] K. A. Dawson, M. D. Lipkin and B. Widom, *J. Chem. Phys.* **88**, 5149 (1988)
- [104] K. A. Dawson, B. L. Walker and A. Berera, *Physica A*, **165**, 320 (1990)
- [105] A. Hansen, M. Schick and D. Stauffer, *Phys. Rev. A*, **44**, 3686 (1991)
- [106] A. G. Petorv and I. Bivas, *Prog. Surf. Sci.*, **16**, 389 (1984)
- [107] D. Nelson, T. Piran and S. Weinberg (eds) *Statistical Mechanics of Membranes and Surfaces*, (World Scientific, Singapore, 1988)
- [108] W. Helfrich, in: *Liquids at Interfaces*, eds J. Charvolin, J. F. Joanny and J. Zinn-Justin (Elsevier, 1990)

- [109] R. Lipowski, in : *Fundamental Problems in Statistical Mechanics VII*, ed. H. Van Beijeren (Elsevier, 1990)
- [110] M. D. Mitov, J. F. Faueon, P. Meleard and P. Bothorel, *Adv. in Supramolec. Chemistry*, **2**, 93 (1992).
- [111] W. Helfrich, *Z. Naturforsch.*, **28c**, 693 (1973).
- [112] J.D. Weeks, in: *Ordering in Strongly Fluctuating Condensed Matter Systems*, ed. T. Riste (Plenum), 6093 (1990).
- [113] D. A. Huse, W van Saarloos and J. D. Weeks, *Phy. Rev. B*, **32**, 233 (1985).
- [114] H. van Beijeren and I. Nolden, in: *Topics in Current Physics, Volume 43: Structure and Dynamics of Surfaces II, Phenomena, Models, and Methods*, ed. W. Schommers and P. von Blanckenhagen (Springer -Verlag, Berlin, 1987.
- [115] R. H. Swendsen, *Phy. Rev. B*, **15**, 5421 (1977).
- [116] P. K. Maiti, D Chowdhury and J. K. Bhattacharjee, *Phy. Rev. E*, **54**, 2670 (1996).
- [117] H. Muller-Krumbhaar, in: *MC' methods in Statistical Physics*, ed. K. Binder (Springer, 1986); see also Y. Saito and H. Muller- Krumbhaar, in: *Applications of MC Methods in Statistical Physics*, 2nd edn., ed. K. Binder (Springer, 1987)
- [118] P.K. Maiti and D. Chowdhury, submitted to PRE.
- [119] P.K. Maiti and D. Chowdhury, unpublished.

- [120] R. J. Glauber, *J. Math. Phys.*, **4**, 294 (1963).
- [121] L. E. Reichl, *An Introduction to modern statistical physics*, (University of Texas, Austin, press, 1980).
- [122] H. Muller Krumbhaar, *Z. Phys.B*, **25**, 287 (1976) .
- [123] A. -L. Barabasi and H. E. Stanley, *Fractal concepts in surface growth*, (Cambridge University Press, 1995)
- T. Halpin-Healey and Y.C. Zhang, *Phys.Rep.* , **254**, 215 (1995).
- [124] F. David and S. Leibler, *J. de Phys.II*, **1**, 959 (1991).
- [125] J.M. Kim and J.M. Kosterlitz, *Phys. Rev. Lett.* **62**, 2289 (1989);
- T. Ala-Nissila and O. Venalainen, *J. Stat. Phys.*, **76**, 1083 (1994).
- [126] P. Meakin, P. Ramanlal, L.M. Sander and R.C. Ball, *Phys.Rev.A* , **34**, 5091 (1986).
- [127] M. Plischke, Z. Racz and D. Liu, *Phys. Rev. B*, **35**, 3485 (1987).
- [128] D. Chowdhury and D. Stauffer, *Physica A*, **189**, 70 (1992).
- [129] T. Kawakatsu and K. Kawasaki, *J. Colloid. Interface. Sc.*, **148**, 23 (1992).
- [130] Z. Burkner and D. Stauffer, *Z. Phys. B*, **53**, 241 (1983).
- [131] D. Chowdhury, *J. de. Phys II*, **5**, 1469 (1995).
- [132] D. Stauffer and A. Aharony, *Introduction to Percolation Theory*, (Taylor and Francis, London 1994).

- [133] I. Szleifer, D. Kramer, A. Ben-Shaul, W.M. Gelbart and S.A. Safran, *J. Chem. Phys.*, **92**, 6800 (1990).
- [134] V. Rosilio, G. Albrecht, Y. Okumura, J. Sunamoto and A. Baszkin, *Langmuir*, **12**, 2544 (1996).
- [135] S. K. Kumar and J. D. Weinhold, *Phys. Rev. Lett.* **77**, 1512 (1996).
- [136] T. Biben and J. P. Hansen, *Phys. Rev. Lett.*, **66**, 2215 (1991).
- [137] D. Frenkel, *J. Phys. Condensed Matt.*, **6**, A71 (1994) and references therein
- [138] M. T. Gurler, C. C. Crabb, D. M. Dahlin and J. Kovac, *Macromolecules*, **16**, 398 (1983).
- [139] K. Kremer and K. Binder, *Comp. Phys. Rep.*, **7**, 259 (1988).
- [140] P. Y. Lai and E. B. Zhulina, *Macromolecules*, **25**, 5201 (1992).
- [141] P. Y. Lai, *J. Chem. Phys.*, **100**, 3351 (1994).
- [142] S. A. Safran, *Statistical mechanics of surfaces, interfaces and membranes*, Frontier in Physics Vol 92, Addison - Wesley (1994)
- [143] J. H. Fendler, *Membrane Mimetic Chemistry*, Wiely, New York, 1982.
- [144] H. Hauser, *Chem. Phys. Lipids*, **43**, 283, 1987.
- [145] N. E. Gabriel, M. F. Roberts, *Biochemistry*, **23**, 4011, 1984.
- [146] H. Diamant and D. Andelman, *Langmuir*, **10**, 2910 (1994);
Langmuir, **11**, 3605 (1995).

- [147] S. De, V. K. Aswal, P. S. Goyal and S. Bhattacharya, *J. Phys. Chem.*, **100**, 11664 (1996).
- [148] S. Karaboni, K. Esselink, P. A. J. Hilbers, B. Smit, J. Karthaus, N. M. van Os and R. Zana, *Science*, **266**, 254 (1994).
- [149] R. J. Hunter, *Foundations of Colloid Science* (Clarendon, Oxford, 1986) (reprint 1993), Vol. I, p. 576.
- [150] P. Mukherjee and K. J. Mysels, *CMC of Aqueous Surfactant Systems*, Natl. Stand. Ref. Data. Ser., Natl. Bur. Stand. No.36 (U.S. GPO, Washington, DC, 1971)
- [151] W. Gelbert, A. Ben Shaul and D. Roux (eds.) *Micelles, Membranes. Microemulsions and Monolayers* (Springer, Berlin, 1994)
- [152] E. Alami, G. Beinert, P. Marie and R. Zana, *Langmuir*, **9**, 1465 (1993).
- [153] Frindi M., Michels B., Levy H. and Zana R., *Langmuir*, **10**, 1140 (1994).
- [154] S. De, V. K. Aswal, P. S. Goyal and S. Bhattacharya, *J. Phys. Chem.*, **100**, 11664 (1996).
- [155] H. Hirata, N. Hattori, M. Ishida, H. Okabayashi, M. Frusaka and R. Zana, *J. Phys. Chem.*, **99**, 17778 (1995).
- [156] Y.P. Zhu, A. Masuyama, Y. Kobata, Y. Nakatsuji, M. Okahara and M.J. Rosen, *J. Coll. and Interf. Sci.* **158**, 40 (1993).
- [157] A. T. Bernardes, *J. Phys. II France*, **6**, 169 (1996);
Langmuir, **12**, 5763 (1996).

- [158] R. D. Evans, *J. phys. Cond. Matter* **2**, 8989, 1990.
- [159] D. Chowdhury and D. Stauffer, *J. Chem. Phys.*, **95**, 7664 (1991).
- [160] D. O. Shah and R. S. Schechter, *Improved oil recovery by Surfactant and polymer flooding*, (Academic, New York 1977).
- [161] Chakrabarti A, *Phy. Rev. Lett.* **69**, 1548 (1992).
- [162] Oono Y and Puri S, *Phy. Rev. Lett.*, **58**, 863 (1987).
- [163] F. Bates and G. H. Fredrickson, *Annu. Rev. Phys. Chem.*, **41**, 525 (1990);
F. Bates, *Science*, **251**, 898 (1991).
- [164] M. E. Cates and S. J. Candau, *J. Phys.: Condens. Matter*, **2**, 6869 (1990).

List of Publications

1. *Spin rotationally symmetric path integral formulation of N -orbital Hubbard model* : Prabal K Maiti, Avinas Singh, *Phys. Rev. B*, **49**, 6078 (1994).
2. *Improved performance of the Hopfield and Little neural network models with time delayed dynamics* : Prabal K. Maiti, Prabir K. Dasgupta and Bikas K. Chakrabarti , *Int. J. Mod. Phys. B*, **9**, 3025 (1995).
3. *Oil-Water Interface in the Widom model: Is it smooth, rough or crumpled?* : Prabal K. Maiti, Debashish Chowdhury, *J. Phys. I France*, **5**, 671 (1995).
4. *Discrete solid-on-solid model of interface with bending rigidity: Roughening versus crumpling* : Prabal K. Maiti, Debashish Chowdhury and Jayanta K. Bhattacharjee, *Phys. Rev. E*, **54**, 2670 (1996).
5. *Spin glass theory in neural network* : Prabal K. Maiti in *Modelling of complex systems*, ed. J. K. Bhattacharjee and A. K. Mallik, (Narosa, New Delhi, 1997) p 329-404.
6. *Oil-Water interface in the 2-dimensional Larson type of model* : Prabal K. Maiti, *Phys. Lett. A*, **230**, 369 (1997).

7. *Out-of plane phase segregation and in plane clustering in a binary mixture of amphiphiles at air water interface* : Debashish Chowdhury, Prabal K. Maiti, S. Shabapandit and P. Taneja, *Phys. Rev. E* June, 1997.
8. *Solid-on-solid model of interface with bending rigidity II: restricted and unrestricted step sizes* : Prabal K Maiti, Debashish Chowdhury, submitted for publication.
9. *Micellar Aggregates of Gemini Surfactants: Monte Carlo Simulation of a Microscopic Model*: Prabal K Maiti, Debashish Chowdhury, cond-mat/9706052 submitted for publication.
10. *A Microscopic Model of Gemini Surfactants: Self-assemblies in Water and at Air-Water Interface*, Prabal K Maiti, Debashish Chowdhury, to be published.

Other Publications of
Prabal Kumar Maiti
During 1992-1997

Modelling of Complex Systems

EDITORS

J.K. Bhattacharjee

A.K. Mallik



Narosa Publishing House

New Delhi Madras Bombay Calcutta London

Contents

<i>Preface</i>	v
Overview	1
1. Dynamical Systems <i>J.K. Bhattacharjee</i>	5
2. Nonlinear Mechanical Vibrations <i>A.K. Mallik and B. Ravindra</i>	71
3. Hydrodynamic Instabilities <i>J.K. Bhattacharjee</i>	127
4. Chemical Systems <i>N. Sathyamurthy</i>	169
5. Nonlinear Time Series Analysis <i>A. Kumar and S.K. Mullick</i>	201
6. Complex Seismic Behaviour of Buildings <i>C.V.R. Murty</i>	241
7. Pattern Formation in Complex Fluids <i>D. Chowdhury</i>	303
8. Spin Glass Theory in Neural Networks <i>P.K. Mairiy</i>	329
9. Monte-Carlo Computation for Complex Systems <i>V.A. Singh and G.C. John</i>	405
INDEX	435

SPIN GLASS THEORY IN NEURAL NETWORKS

8.1 Introduction

8.1.1 Generalities

Biological computers - the brain and the nervous system have existed for millions of years and they are marvellously effective in processing sensory information and controlling the interactions of the living systems with their environment. Seeing something, recognizing a face or recalling from memories takes an enormous amount of computation. For example, to "see" something, first the images received in our eyes are coded by our nervous system in fantastic richness of details, then processed and restored in our consciousness, corrected for changes of illumination, mood and any other circumstances. The fact that biological computation is so effective suggests that it may be possible to attain similar capabilities in artificial devices or at least it is possible to model the brain where the peculiarities of its performances emerge naturally.

Although our brain functions as an information processing computer, the basic principle on which its functioning is based is quite different from that of a conventional computer. A conventional computer stores informations by assigning addresses, which identify the physical locations where the data will be stored in the hardware. When the central processor requires a piece of data, it issues an instruction to read the data at a particular

Spin-rotationally-symmetric path-integral formulation of a generalized \mathcal{N} -orbital Hubbard model

Prabal K. Maiti and Avinash Singh

Department of Physics, Indian Institute of Technology, Kanpur 208016, India

(Received 28 June 1993; revised manuscript received 22 October 1993)

A spin-rotationally-symmetric path-integral formulation with a vector order parameter is presented for a generalized \mathcal{N} -orbital Hubbard model which yields the correct Hartree-Fock result in the saddle-point approximation, and also the spin-wave mode representing transverse Gaussian fluctuations. A systematic expansion of the action in powers of inverse \mathcal{N} , wherein spin-rotational symmetry and hence the Goldstone mode are preserved order by order, is developed, and the first order $O(1/\mathcal{N})$ quantum corrections to the ground-state energy and sublattice magnetization obtained. Setting $\mathcal{N} = 1$ yields a quantitatively correct description of the antiferromagnetic state of the one-orbital Hubbard model at half-filling.

I. INTRODUCTION

Recently there has been interest in developing a spin-rotationally-symmetric path-integral formulation of the Hubbard model.^{1,2} Up until recently the situation has been that the process of taking the saddle-point approximation has led to inconsistencies in the resulting theory.³ Thus if the Hubbard interaction term is decomposed in terms of charge-density and spin-density terms, $n_{i\uparrow}n_{i\downarrow} = \frac{1}{4}[(n_{i\uparrow} + n_{i\downarrow})^2 - (n_{i\uparrow} - n_{i\downarrow})^2]$, the resulting theory yields correct HF energies, however, the presence of a scalar magnetic order parameter $(n_{i\uparrow} - n_{i\downarrow})$ in the theory leads to the absence of Goldstone modes. On the other hand, the $-\frac{2}{3}\mathbf{S}_i \cdot \mathbf{S}_i$ representation introduces a vector order parameter $\langle \mathbf{S}_i \rangle$, and hence Goldstone modes in the theory, however, because of the $\frac{2}{3}$ factor, the single-particle spectrum obtained at the Hartree-Fock level is incorrect.

In the present paper we show that, using a generalized \mathcal{N} -orbital Hubbard model,^{4,5} it is possible to develop a path-integral formulation wherein the effective action is both spin-rotationally invariant and exhibits a correct Hartree-Fock result at the saddle point. For the Hubbard model there is no formal expansion parameter in the problem to control the perturbative expansion, whereas in a perturbative treatment it is important to ensure that all conservation laws and symmetries are obeyed systematically. In particular the Goldstone mode which follows from spin-rotational symmetry must be preserved in perturbation theory. In the path-integral formulation of the generalized \mathcal{N} -orbital Hubbard model $\frac{1}{\mathcal{N}}$ acts as an expansion parameter and spin-rotational symmetry is guaranteed order by order in the expansion because the perturbative piece of the Hamiltonian is manifestly rotationally symmetric. In the saddle-point approximation, which yields the classical action of $O(1)$, we recover the correct HF result, and this is also exact in the limit $\mathcal{N} \rightarrow \infty$. The quantum fluctuation effects appear

at higher orders and we consider Gaussian fluctuation around the saddle point yielding an $O(1/\mathcal{N})$ correction to the action, from which we discuss evaluation of the quantum corrections to the ground-state energy and sublattice magnetization.

We consider the following Hamiltonian for a generalized \mathcal{N} orbital Hubbard model with \mathcal{N} orbitals per site:^{4,5}

$$\mathcal{H} = -t \sum_{\langle ij \rangle \sigma \alpha} (a_{i\sigma\alpha}^\dagger a_{j\sigma\alpha} - \text{H.c.}) + \frac{U}{\mathcal{N}} \sum_{i\alpha\beta} (a_{i\uparrow\alpha}^\dagger a_{i\uparrow\alpha} a_{i\downarrow\beta}^\dagger a_{i\downarrow\beta} + a_{i\uparrow\alpha}^\dagger a_{i\downarrow\alpha} a_{i\downarrow\beta}^\dagger a_{i\uparrow\beta})$$

Here α, β are orbital indices. The factor $\frac{1}{\mathcal{N}}$ is in the interaction term to render energy density in the $\mathcal{N} \rightarrow \infty$ limit. The two interaction terms are density and exchange type with respect to orbital and together can be expressed as⁵

$$\sum_{\alpha\beta} (a_{i\uparrow\alpha}^\dagger a_{i\uparrow\alpha} a_{i\downarrow\beta}^\dagger a_{i\downarrow\beta} + a_{i\uparrow\alpha}^\dagger a_{i\downarrow\alpha} a_{i\downarrow\beta}^\dagger a_{i\uparrow\beta}) = -\mathbf{S}_i \cdot \mathbf{S}_i$$

where $\Psi_{i\alpha}^\dagger \equiv (a_{i\uparrow\alpha}^\dagger, a_{i\downarrow\alpha}^\dagger)$, $\mathbf{S}_i = \sum_{\alpha} \Psi_{i\alpha}^\dagger \frac{\boldsymbol{\sigma}}{2} \Psi_{i\alpha}$ is the spin-density operator, and $n_i = \sum_{\alpha} \Psi_{i\alpha}^\dagger \frac{1}{2} \Psi_{i\alpha}$ is the averaged charge-density operator at site i . The interaction term, expressed as above with the expansion parameter $\frac{1}{\mathcal{N}}$ in front, is manifestly spin-rotationally symmetric and hence the Goldstone mode is preserved order by order in a systematic $\frac{1}{\mathcal{N}}$ expansion.

II. PATH-INTEGRAL FORMULATION

To set up the path-integral formulation of the model we go to the Grassmann-variable representation

antisymmetry of the many-body fermion

$$(\bar{\Psi}_{i\alpha}\Psi_{j\alpha} + \text{H.c.}) + \frac{U}{N} \sum_i \left(\sum_{\alpha} \bar{\Psi}_{i\alpha} \frac{\sigma}{2} \Psi_{i\alpha} \right)^2. \quad (3)$$

and $\Psi_{i\alpha}$ are column vectors containing Grassmanns for the two spins, corresponding to the operators $\Psi_{i\alpha}^\dagger$ and $\Psi_{i\alpha}$. Here we have dropped which simply shifts the position of the Fermi now the partition function $\mathcal{Z} = \text{Tr} e^{iHt}$, in the limit at zero temperature, can be expressed in the path integral formalism as a functional integral over variables:

$$\mathcal{D}\bar{\Psi}\mathcal{D}\Psi e^{i \int \mathcal{L} dt}, \quad (4)$$

the Lagrangian density is given by

$$i(\partial_t)\bar{\Psi}_{i\alpha} + t \sum_{(ij)\alpha} (\bar{\Psi}_{i\alpha}\Psi_{j\alpha} + \text{H.c.}) - \frac{U}{N} \sum_i \left(\sum_{\alpha} \bar{\Psi}_{i\alpha} \frac{\sigma}{2} \Psi_{i\alpha} \right)^2. \quad (5)$$

With the quartic interaction term, we make use of the Hubbard-Stratonovich transformation, and introduce a vector field $\phi_i(t) = \sum_{\alpha} \phi_{i\alpha}(t)$ at each point in time.

$$\Psi_{i\alpha}^2 = \text{const} \int d\phi e^{-\frac{U}{N}(\phi_i^2 - \phi_i \cdot \sum_{\alpha} \Psi_{i\alpha} \sigma \Psi_{i\alpha})}. \quad (6)$$

$\phi_i(t)$ couples with the total spin at site i (over all orbitals). The interaction term is now quadratic and it is now possible to integrate out the Grassmann field to get an effective action in terms of $\phi(t)$. Integrating over the Grassmann variables for the partition function,⁶

$$\mathcal{D}\phi e^{iS_{\text{eff}}(\phi)}, \quad (7)$$

the effective action is given by

$$= \int dt \left[-\frac{U}{N} \sum_i \phi_i^2(t) - i \sum_{\alpha} \text{Tr} \ln [i\partial_t - H_{\alpha}(\phi)] \right]. \quad (8)$$

The operator $H_{\alpha}(\phi)$ is the effective one-particle Hamiltonian for orbital α and in the two-spin basis is

$$= \delta_{i,i'} \left[-t \sum_{(ij)} (|i\rangle\langle j| + \text{H.c.}) \mathbb{1} \pm \sum_i \frac{U}{N} \phi_i \cdot \sigma |i\rangle\langle i| \right]. \quad (9)$$

Now to get the HF result we obtain the action in the saddle-point approximation, wherein the action is minimized with respect to variations in the field, i.e., $\frac{\delta S_{\text{eff}}}{\delta \phi_{i\alpha}^{\mu}(t)} = 0$, where $\mu = (x, y, z)$. At the saddle point we obtain

$$\phi_{i\alpha}^{\mu}(t) = \pm i \text{Tr}_{\sigma} \left(G_{\alpha}(i, t; i, t) \frac{\sigma^{\mu}}{2} \right), \quad (10)$$

where we have defined the single-particle Green's function in the two-spin basis as

$$G_{\alpha}(i, t; j, t') = \left\langle i, t \left| \frac{1}{i\partial_t - H_{\alpha}} \right| j, t' \right\rangle. \quad (11)$$

We define the local magnetic moment due to an electron in orbital α by

$$\langle S_{i\alpha}(t) \rangle = i \text{Tr}_{\sigma} \left(G_{\alpha}(i, t; i, t) \frac{\sigma}{2} \right) \quad (12)$$

and hence at the saddle point the vector field $\phi_{i\alpha}$ is nothing but the local magnetization

$$\phi_{i\alpha}(t) = \pm \langle S_{i\alpha}(t) \rangle. \quad (13)$$

III. HARTREE-FOCK RESULT

Now we show that within the saddle-point approximation we get the correct HF result for the half-filled system. For half-filling we expect an antiferromagnetic ground state, which is characterized by an ordering wherein the local magnetization has equal magnitude but opposite direction on sites of the two sublattices. We choose the z direction as the direction of ordering without any loss of generality. Thus, we have $\phi_{i\alpha}^x = \phi_{i\alpha}^y = 0$, and

$$\phi_{i\alpha}^z = \frac{1}{2} m (-1)^i, \quad (14)$$

where $m = |n_{i\alpha}^\uparrow - n_{i\alpha}^\downarrow|$, the staggered or sublattice magnetization is the order parameter in the AF state. The sum over orbitals in the total field ϕ_i^z in Eq. (9) yields a factor N , and therefore, at the saddle point, the effective one-particle Hamiltonian may be written, again in the two-spin basis, as

$$H_{\alpha} = -t \sum_{(ij)} (|i\rangle\langle j| + \text{H.c.}) \mathbb{1} + \sum_i (-1)^i \Delta \sigma^z, \quad (15)$$

where $\Delta = \frac{1}{2} (Nm) U / N = Um/2$ is the gap parameter. The corresponding Hamiltonian in momentum space, and now expressed in the two-sublattice basis, can be written, for spin- σ electrons, as⁷

$$H_{k\sigma} = \begin{bmatrix} -\sigma\Delta & \epsilon_k \\ \epsilon_k & \sigma\Delta \end{bmatrix}, \quad (16)$$

where $\epsilon_k = -2t \sum_{\mu} \cos(k_{\mu}a)$ is the free-particle energy on the lattice. The eigenvalues yield the quasiparticle energies, $E_k = \pm \sqrt{\Delta^2 + \epsilon_k^2}$, and electronic amplitudes on sites of the two sublattices are obtained from the eigenvectors $(a_{k\sigma} \ b_{k\sigma})$. The sublattice magnetization, which is the absolute difference in electronic densities on sites

of the two sublattices, is given by

$$m = \frac{2}{N} \sum_k' (a_{k\uparrow}^2 - b_{k\uparrow}^2) = \frac{2}{N} \sum_k' \frac{\Delta}{\sqrt{\Delta^2 + \epsilon_k^2}}. \quad (17)$$

Here the sum is over all occupied states lying in the lower Hubbard band, and N is the number of lattice sites. With $2\Delta = mU$, this leads to the self-consistency condition

$$\frac{1}{U} = \frac{1}{N} \sum_k' \frac{1}{\sqrt{\Delta^2 + \epsilon_k^2}} \quad (18)$$

from which the (HF) sublattice magnetization may be determined as a function of the interaction strength U .⁷

IV. SPIN WAVES

We now study the spin-wave modes, which are low-lying, collective excitations in the antiferromagnet, representing transverse fluctuations around the broken-symmetry direction. We do this by allowing for small transverse fluctuations in the vector field $\phi_{i\alpha}(t)$, around the saddle-point value, $\phi_i^{(0)}$:

$$\phi_{i\alpha} = \phi_i^{(0)} + \delta\phi_{i\alpha}. \quad (19)$$

Since $\phi_i = \sum_{\alpha} \phi_{i\alpha}$, summed over all orbitals, we have, for substitution in Eq. (8),

$$\phi_i^2 = \mathcal{N}^2(\phi_i^{(0)})^2 + 2\phi_i^{(0)} \cdot \sum_{\alpha} \delta\phi_{i\alpha} + \sum_{\alpha\beta} \delta\phi_{i\alpha} \cdot \delta\phi_{i\beta}. \quad (20)$$

Correspondingly $H_{\alpha}(\phi)$ being linear in ϕ can be written as

$$H_{\alpha}(\phi) = H^{(0)} + \delta H_{\alpha}, \quad (21)$$

where $H^{(0)}$ represents the effective one-particle Hamiltonian [Eq. (15)] at the saddle point, and in the two-spin basis, δH_{α} is given by

$$\delta H_{\alpha} = \frac{U}{N} \sum_{i\beta} \delta\phi_{i\beta} \cdot \sigma_i \langle i |.$$

By making the above substitution in Eq. (8) and expanding in powers of δH_{α} , we obtain an expansion for the effective action $S_{\text{eff}}(\phi)$ around the saddle point values of $\phi_i(t)$. Within the Gaussian approximation keeping terms only up to second order, we have

$$S_{\text{eff}}(\phi) = S^{(0)} + \delta S^{(2)},$$

where $S^{(0)}$ is the (classical) action evaluated at the point:

$$S^{(0)} = \int dt \left[-\frac{U}{N} \sum_i \mathcal{N}^2(\phi_i^{(0)})^2 - i \sum_{\alpha} \text{Tr} \ln[i\partial_t - H^{(0)}] \right],$$

which is \mathcal{N} times the classical action for the one-orbital model, and in terms of $G^{(0)}$, the Green's function [11] at the saddle point, we have

$$\delta S^{(2)} = \int dt \left[-\frac{U}{N} \sum_{i\alpha\beta} \delta\phi_{i\alpha}(t) \cdot \delta\phi_{i\beta}(t) + \frac{i}{2} \sum_{\gamma=1}^N \text{Tr} [G^{(0)} \delta H_{\gamma} G^{(0)} \delta H_{\gamma}] \right].$$

Since we are interested in spin waves, we consider only transverse fluctuations, i.e., $\delta\phi_i^z = 0$. It is convenient to work with $\delta\phi^{\pm}$ which are defined as $(\delta\phi^x \pm i\delta\phi^y)/\sqrt{2}$ and $\sigma^{\pm} = (\sigma^x \pm i\sigma^y)/2$, instead of x and y components. The $\delta\phi \cdot \sigma$ term in δH is then expressed as $\sqrt{2}(\delta\phi^{+}\sigma^{-} + \delta\phi^{-}\sigma^{+})$. Substituting for δH from Eq. (22) and performing the sum over the internal space and time coordinates coming from the trace in the second term, we can write this as

$$\delta S^{(2)} = -\frac{U}{N} \int dt \int dt' \sum_{ij} \sum_{\alpha\beta} \sum_s [\delta\phi_{i\alpha}^s(t) D^{s\bar{s}}(it, jt') \delta\phi_{j\beta}^{\bar{s}}(t')],$$

where the superscripts s and \bar{s} refer to the two signs, $s = -\bar{s} = \pm$, and the matrix elements of D^{--} are given by D^{--} being given analogously,

$$\begin{aligned} D^{--}(it, jt') &= \delta_{ij} \delta(t - t') - i \frac{U}{N} \sum_{\gamma=1}^N \text{Tr}_{\sigma} [G^{(0)}(it, jt') \sigma^{+} G^{(0)}(jt', it) \sigma^{-}] \\ &= \delta_{ij} \delta(t - t') - i U G_{\uparrow}^{(0)}(it, jt') G_{\downarrow}^{(0)}(jt', it). \end{aligned}$$

Fourier transformation to frequency space and momentum space (the latter within a two-sublattice basis as translational symmetry is present only within this basis) yields the following expression for the quantum correction to action:

$$\delta S^{(2)} = -\frac{U}{N} \sum_{\alpha\beta} \sum_s \sum_Q \int \frac{d\Omega}{2\pi} \text{Tr} [\delta\phi_{\alpha}^s(Q, \Omega) D^{s\bar{s}}(Q, \Omega) \delta\phi_{\beta}^{\bar{s}}(Q, \Omega)],$$

trace is over the two-sublattice elements, and

$$\chi^0(Q, \Omega) = 1 - U \chi^0(Q, \Omega) = D^{+-}(Q, -\Omega). \quad (29)$$

$\chi^0(Q, \Omega)$ is the zeroth-order, antiparallel-spin

$$\chi^0(Q, \Omega) = i \sum_k \int \frac{d\omega}{2\pi} G^{(0)}_+(k, \omega) G^{(0)}_-(k - Q, \omega - \Omega). \quad (30)$$

$D^{+-}(Q, \Omega)$ is now rendered in a form familiar from random-phase approximation (RPA) expression for the inverse spin susceptibility. Poles of $D^{+-}(Q, \Omega)$ are spin-wave energies at the RPA level.⁷

To discuss the order of $\delta S^{(2)}$ relative to that of the classical action $S^{(0)}$. Assuming no correlation between fluctuations in different orbitals, i.e., $\langle \delta \phi_{\alpha}^+ \delta \phi_{\beta}^- \rangle = \delta_{\alpha\beta}$, we see that the sums over α, β contribute a factor of N , which cancels the N in the denominator, leaving a contribution which is $O(1/N)$ relative

to the classical action. In fact, generalizing to the n th-order term in the expansion for the action, with n being even for the averaging over fluctuations to survive, we have n factors of N in the denominator, coming from the explicit factor of $1/N$ in δH , and n sums over orbitals. Again, the absence of correlation between fluctuations in different orbitals requires the $n = 2m$ orbitals to be paired off into m pairs, leaving m independent sums over orbitals, yielding a factor of N^m . The net order of the n th-order term is therefore $(1/N)^{n/2}$, so that the expansion of the action, into quadratic, quartic, etc., terms, is formally seen as a perturbative expansion in powers of $1/N$:

$$S = N \left[S^{(0)} + \frac{1}{N} \delta S^{(2)} + \frac{1}{N^2} \delta S^{(4)} + \dots \right]. \quad (31)$$

Therefore, up to the (Gaussian) level of small transverse fluctuations around the saddle point, we have for the partition function

$$Z = \int \mathcal{D}(\delta \phi^+) \mathcal{D}(\delta \phi^-) \exp \left[-iU \sum_Q \sum_{s=\pm} \int \frac{d\Omega}{2\pi} [\delta \phi^s(Q, \Omega) D^{ss}(Q, \Omega) \delta \phi^s(Q, \Omega)] \right]. \quad (32)$$

Integrating over the bosonic fluctuations, we obtain,

$$Z = \int \mathcal{D}(\delta \phi^+) \mathcal{D}(\delta \phi^-) \exp \left[iN \left(S^{(0)} + \frac{i}{N} \sum_Q \int \frac{d\Omega}{2\pi} \text{Tr} [\ln D^{+-}(Q, \Omega) + \ln D^{-+}(Q, \Omega)] \right) \right], \quad (33)$$

where the trace is over the two-sublattice elements within

GROUND-STATE ENERGY AND SUBLATTICE MAGNETIZATION

The quantum correction to the action leads to the following correction to the ground-state energy:

$$E = \frac{1}{N} \sum_Q \int \frac{d\Omega}{2\pi} \text{Im} \text{Tr} \ln [1 - U \chi^0(Q, \Omega)]. \quad (34)$$

$\chi^0(Q, \Omega)$ (quantum) correction to ground-state energy due to transverse Gaussian fluctuations around the saddle point is, in a diagrammatic language, nothing but the correction due to transverse spin fluctuations at the saddle point. This correction has been evaluated in the tractable strong-coupling limit.⁸ Up to this order, the fluctuations lower the ground-state energy relative to the HF value due to mixing between the HF and the spin-wave states. Up to the $O(1/N)$ level the ground-state energy per site is³

$$-J \left[1 + \frac{1}{N} \sum_Q \left(1 - \sqrt{1 - \gamma_Q^2} \right) \right]. \quad (35)$$

where $\gamma_Q = \frac{1}{D} \sum_{\mu} \cos Q_{\mu}$. The first-order quantum correction to the ground-state energy is about 16% for the square-lattice case.

We now consider the quantum correction to the sublattice magnetization due to the Gaussian fluctuations around the saddle point. Now, the ground-state energy correction discussed above corresponds, in a diagrammatic language, to the ladder diagram consisting of ladders of interaction lines between fermion loops of opposite spin. Cutting fermion lines of both spins at the same ladder step yields the ladder-sum (RPA) contribution to the transverse spin susceptibility, and cutting just the \downarrow -spin (say) line yields the RPA spin-fluctuation correction to the \uparrow -spin fermion propagator. The correction to sublattice magnetization due to this (RPA) spin-fluctuation correction has been evaluated again in the strong-coupling limit.⁸ At the $O(1/N)$ level there is a 40% reduction for the square-lattice case, yielding a sublattice magnetization of 0.6. Due to an exact cancellation of the $O(1/N)^2$ contribution, this result actually holds to the two-loop level.⁵

These $O(1/N)$ corrections yield results which are identical to the $O(1/2S)$ corrections obtained within the spin-wave theory for the spin-1/2 quantum Heisenberg AF.⁹ This is not surprising as in the strong-coupling limit the N -orbital Hubbard model is equivalent to the spin

$S = \mathcal{N}/2$ Heisenberg AF. The systematic expansion in powers of $1/\mathcal{N}$ is perfectly equivalent, order by order, to the $1/2S$ expansion.

In conclusion, we have presented a spin-rotationally-symmetric path-integral formulation with a vector order parameter for a generalized \mathcal{N} -orbital Hubbard model. This procedure yields the correct Hartree-Fock result in the saddle-point approximation, and also the correct spectrum of spin-wave modes. A systematic expansion in powers of inverse \mathcal{N} is developed, and the first-order quantum corrections to ground-state energy and sublattice magnetization are obtained. As mentioned in the Introduction, the $1/\mathcal{N}$ expansion serves to systematize the fluctuation corrections about the HF state, and setting $\mathcal{N} = 1$ yields a quantitatively correct description of the AF state of the one-orbital Hubbard model at half-

filling.

In view of the above observation it is natural to enquire whether the ground state of the doped system in the large- \mathcal{N} limit might also describe the $\mathcal{N} = 1$ case, whether there are features associated with the one-orbital model which are missing from the large- \mathcal{N} model. Our analysis of the doped system in the large- \mathcal{N} limit is presented elsewhere.¹⁰ We simply note here that the behavior of holes in the ground state of the large- \mathcal{N} model is quite different from that in the $\mathcal{N} = 1$ case. In particular, the sequence of hopping events initiated by added holes, leaving strings of upturned spins behind, is absent in the large- \mathcal{N} model. The inhomogeneous magnetic ground states like the commensurate domain-wall states^{11,12} are therefore not ground states of the doped large- \mathcal{N} model.

¹H. J. Schulz, Phys. Rev. Lett. **65**, 2462 (1990).

²Z. Y. Weng, C. S. Ting, and T. K. Lee, Phys. Rev. B **43**, 3790 (1991).

³A. A. Gomes and P. Lederer, J. Phys. (Paris) **38**, 16 (1977).

⁴A. Singh and E. Fradkin, Phys. Rev. B **35**, 6894 (1987); a spinless version was used by M. Ma and E. Fradkin, *ibid.* **28**, 2990 (1984).

⁵A. Singh, Phys. Rev. B **43**, 3617 (1991).

⁶E. Fradkin, *Field Theories and Condensed Matter Systems*,

Frontiers in Physics Lecture Notes Series Vol. 82 (A. Wesley, Reading, MA, 1991).

⁷A. Singh and Z. Teseanović, Phys. Rev. B **41**, 611 (1990).

⁸A. Singh and Z. Teseanović, Phys. Rev. B **41**, 11457 (1990).

⁹T. Oguchi, Phys. Rev. **117**, 117 (1960).

¹⁰A. Singh (unpublished).

¹¹H. J. Schulz, J. Phys. (Paris) **50**, 2833 (1989).

¹²D. Poilblanc and T. M. Rice, Phys. Rev. B **39**, 9749 (1989).

IMPROVED PERFORMANCE OF THE HOPFIELD AND LITTLE NEURAL NETWORK MODELS WITH TIME DELAYED DYNAMICS

PRABAL K MAITI*, PRABIR K DASGUPTA and BIKAS K CHAKRABARTI†

*Saha Institute of Nuclear Physics
 1/AF Bidhannagar, Calcutta-700064, India*

Revised 8 September 1994

Revised 22 December 1994

We report the results of simulation of neural network models with the synaptic connections constructed using the Hebb's rule and the dynamics determined by the internal field, which has a weighted contribution from the time delayed signals. We consider both the asynchronous (or Glauber; Hopfield) and synchronous (Little) dynamics. Our numerical results and the finite size variation study (for sizes N within the range $250 \leq N \leq 4000$) support the previous indication [Sen and Chakrabarti, *Phys. Lett. A* **162**, 327 (1992)] of improved performance in the recall and overlap properties in the thermodynamic limit. It is identified that the time delayed term in the dynamics allows the network to come out of the spurious valleys in the "energy landscape" (defined without the delay term; Hopfield model). In an approximate analytical study of such models in the extreme dilution limit, the role of the time delayed term to suppress the (spin glass-like) noise is also indicated.

1. Introduction

The properties of associative memory models like the Hopfield and the Little models are now well studied.^{1–3} In such models, each two state (McCullough and Pitts) neuron is represented by the Ising spin variables $\sigma_i = \pm 1$; $i = 1, 2, \dots, N$. The symmetric synaptic interactions between the neurons are constructed following the Hebb's rule of learning, which says that for p number of patterns the synaptic strength J_{ij} for the pair of neurons i and j is

$$J_{ij} = J_{ji} = 1/N \sum_{\mu=1}^p \zeta_i^\mu \zeta_j^\mu, \quad (1)$$

where $\{\zeta_i^\mu\}$, $i = 1, 2, \dots, N$ represents the μ th pattern to be learned by the network. Each $\{\zeta_i^\mu\}$ can take values ± 1 . N is the total number of neurons, each

PACS Nos.: 87.10+e & 0.5.50+q

*Present Address: Dept. of Physics IIT, Kanpur 208016, India

†E-mail: bikas@sahaernet.in

connected to all other neurons, and $p = \alpha N$ denotes the total number of patterns to be learned. Any arbitrary pattern $\{S_i\}$ representing the state of the neurons at time t then evolves following the dynamics

$$S_i(t+1) = \text{sgn}(h_i(t)), \quad (2)$$

where h_i is the internal field on the neuron i due to all other neurons and is given by

$$h_i(t) = \sum_j J_{ij} S_j(t). \quad (3)$$

The “associative learning” of ($p = \alpha N$) number of random patterns (represented by $\{\zeta_i^\mu\}$ $\mu = 1, 2, \dots, p$) corresponds to the creation of that many attractors or fixed points (may also be limit cycles in the Little model) of the dynamics. In the case of sequential updating in (2), or the zero temperature Glauber dynamics as in the case of Hopfield model, one can define an energy-like function^{1,2}

$$\mathcal{H}(t) = - \sum_{i>j}^N J_{ij} S_i(t) S_j(t). \quad (4)$$

This energy function can be shown to decrease monotonically with time t , guaranteeing a fixed point of the dynamics such that after a finite number of iterations (t^*), the network dynamics stabilizes for all i and the fixed point equation is given by

$$S_i(t^* + 1) = S_i(t^*). \quad (5)$$

For parallel updating in (2), as in the case of the Little model, we can define a Lyapunov function²

$$\mathcal{L}(t) = - \sum_{i>j}^N J_{ij} S_i(t) S_j(t-1), \quad (6)$$

which can be shown to decrease monotonically with time t , guaranteeing a limit cycle or fixed point of the dynamics such that after a finite number of iterations (t^*) the network settles to the state

$$S_i(t^* + 1) = S_i(t^* - 1) \quad (7)$$

for all i .

Because of the possibility of defining the energy function for the Hopfield model with sequential or Glauber dynamics, the static properties of the model are well known and well understood from statistical physics.^{1,2} In particular, the memory loading capacity α_c (with significant overlap m_f^μ of the fixed point states $S_i(t^*)$ with the learned patterns ζ_i^μ , starting from any distorted pattern with initial overlap $m_i^\mu < 1$ within the domain of attraction) shows a discontinuous transition at $\alpha_c \simeq 0.138$ ($m_f^\mu \geq 0.97$ for $\alpha \leq \alpha_c$ and $m_f^\mu = 0$ for $\alpha > \alpha_c$ for any μ). The dynamics shows

an unusual critical slowing down near α_c .^{3,4} In particular, the average relaxation or recall time τ (average of t^* over various patterns, for a fixed amount of initial distortion) shows an unusual form of growth near $\alpha = \alpha_c$, although there is no real (static) phase transition (the recall or overlap states are metastable for $\alpha > 0.05$, where the minimum energy are the spin glass or spurious and the metastable overlap states disappear after $\alpha \simeq 0.14$).^{3,4} Although no analytic theory could be developed (for finite α), the static and dynamic properties of the fixed points (recall states) of the Little model are almost identical to that of the Hopfield model.^{2,3}

In the recent literature, there has been a number of indications^{5,6} that dynamically defined networks, with asymmetric synaptic connections J_{ij} may have better recall performance because of the suppression of spin glass-like states. The exactly solvable model of Derrida *et al.*⁶ indeed uses the same Hebb's rule for connection strength J_{ij} but with extreme dilution (inducing asymmetry). This gives better recall properties. There were also indications^{7,8} that addition of some local memory of each neuron, in the sense that the internal field $h_i(t)$ in (3) is determined by the cumulative effect of all the previous states of the neighboring $\sigma_j(t - \eta)$, $\eta = 1, 2, \dots, t$ (as indeed is biologically plausible; Peretto²), gives better recall dynamics in some analog network models. In all these cases, no effective energy function can be defined (because of the asymmetry of J_{ij} or of the local memory effects in h_i) and the use of statistical physics of spin glass-like systems is not possible. All the networks are thus defined dynamically. In a recent simulation study^{3,9} it has been shown that a dynamics with a single time step delay with some tunable weight λ .

$$S_i(t+1) = \text{sgn} \left[\sum_j J_{ij} (S_j(t) + \lambda S_j(t-1)) \right], \quad (8)$$

instead of (2), improves the performance of the Hopfield-like model (with sequential updating) enormously. Here the same synaptic connections J_{ij} in Eq. (1), obtained by using Hebb's rule, are employed. In particular, for a network with $N = 500$, the simulations indicated⁹ that the discontinuous transition for the overlap function at $\alpha_c (\simeq 0.14)$ disappears and becomes continuous. Accepting recall with final overlap $m_f \geq 0.9$, the effective threshold loading capacity α_c increases from 0.14 for $\lambda = 0$ to about 0.25 for $\lambda \simeq 1$. It was also found that average recall time or relaxation time⁴ τ (defined before) becomes minimum around $\lambda \simeq 1$ at any particular loading capacity α .

The above interesting and somewhat surprising results for this single step time delayed dynamics^{3,9} are from simulations of a rather small size ($N = 500$) of the network. Here we present the results of a detailed numerical study of this dynamics, both with asynchronous (sequential as well as random; Hopfield-like) and synchronous (Little-like) updating (Sec. 2). We check our numerical results for a bigger network (for $250 \leq N \leq 4000$) and study if there is any significant finite size effect. We find that the fixed point memory capacity improves considerably with λ , both with Hopfield and Little dynamics (asynchronous and synchronous,

respectively) and that the performance saturates after $\lambda = 1$. With 90% final overlap ($m_f \geq 0.90$) with the learned patterns, the loading capacity increases to almost $\alpha_c \simeq 0.25$ for $\lambda \geq 1$. The relaxation or average recall time τ , for any fixed loading capacity α (≤ 0.25), is also minimum at $\lambda = 1$. We could not detect any significant finite size effect (for $250 \leq N \leq 4000$) and we believe that this result is true in the thermodynamic limit. We also observe that for $\lambda = 1$, both the Little dynamics and Hopfield dynamics give identical results (all the limit cycles of the Little model disappear to give fixed points). The performance of the network for memory storage in limit cycles for negative λ has also been studied for Hopfield and Little dynamics. Here, the negative λ term provides a damping¹⁰ and limit cycles become frequent but the overlap properties deteriorate significantly. We have also studied the performance of such dynamics for randomly diluted networks. In Sec. 3 we give some approximate analytical formulation. In particular, in the extreme dilute limit,⁶ the better performance of the network is indicated by analyzing the evolution equation of the overlap function for the overlap states, by using local field analysis technique. In Sec. 4, we discuss the significance of these results.

2. Numerical Simulation and Results

We consider a network of N neurons (spins). The synaptic interactions J_{ij} between neurons i and j are found using the Hebb's rule (1) for a set of p -random Monte Carlo generated patterns $\{\zeta_i^\mu\}$, $\mu = 1, 2, \dots, p$; $i = 1, 2, \dots, N$. After this 'learning' stage, each pattern is corrupted randomly by a fixed amount (typically 10% of the neuron states are changed randomly; with initial overlap $m_i^\mu = 0.90$ for any pattern μ) and the dynamics (updating process) following (8) starts with these corrupted patterns. Both sequential (Hopfield) and parallel (Little) updating are employed. Since our updating process requires two initial patterns (at $(t-1)$ and $(t-2)$), we start with two randomly distorted patterns with the same value of distortion (for each μ). We study the overlap of the network state with the pattern μ during the updating process and the final overlap m_f^μ of the fixed points (checked for two successive time steps) or limit cycle patterns are noted. The averages over all p patterns (and over 2 to 5 sets of random number seed for the entire run) are taken (m_f = average of m_f^μ over all p). The number of iterations (t^*) required to reach the fixed points (or limit cycles) are also noted and their average (over the patterns) give the average recall or relaxation time (τ). Our typical results for the Hopfield model (dynamics) are for $N = 1000$ and those for the Little model are for $N = 500$. We consider mostly positive λ values. Negative λ values do not improve the performance and have been studied just for some typical investigations.

In Fig. 1, we give the variation of the final average overlap m_f (of any pattern) for the fixed point (checked over two successive time steps) with the redefined λ [$\lambda_R \equiv (1 - \lambda)/(1 + \lambda)$] at fixed loading capacity $\alpha \equiv p/N \simeq 0.25$ for sequential as well as random (Glauber) updating. It may be noted that for the Hopfield dynamics ($\lambda = 0$) the final overlap $m_f \leq 0.30$ for $\alpha = 0.25$. Strictly speaking, this

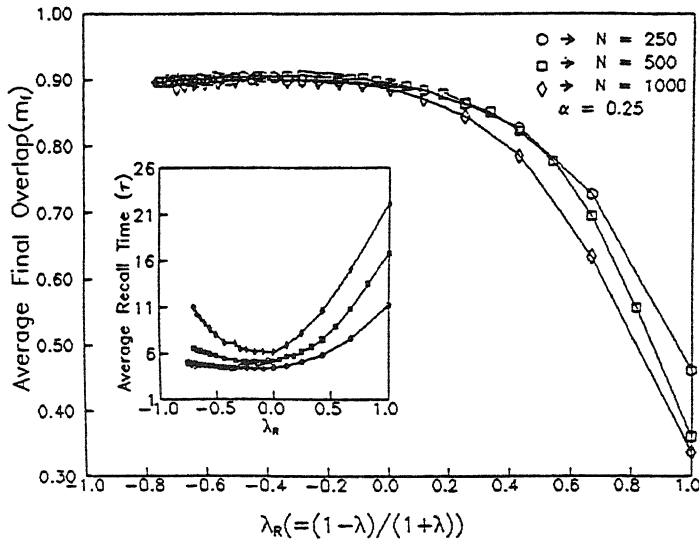


Fig. 1. The variation of the average final overlap m_f (for the fixed point obtained) with $\lambda_R (= (1 - \lambda)/(1 + \lambda)$, positive λ) at a fixed loading capacity $\alpha = 0.25$, with sequential dynamics for networks with $N = 250, 500$ and 1000 . The inset shows the variation of average recall or relaxation time τ against λ_R for different N .

value should be zero in the thermodynamic limit. The results shown in Fig. 1 are for $N = 250, 500$ and 1000 , and the nonvanishing value of m_f for $\lambda = 0$ ($\lambda_R = 1$) at $\alpha = 0.25$ is precisely due to this finite size effect as can be easily checked (decreases considerably as N becomes large). It is seen that the final overlap m_f gradually improves with increasing λ and it saturates beyond $\lambda = 1$ ($\lambda_R = 0$) to $m_f \simeq 0.90$ (for $\alpha = 0.25$). The inset figure shows that the average recall time (or relaxation time) τ also decreases as λ increases from $\lambda = 0$ and finally attains an optimal value (dependent on the network size N and loading capacity α) at $\lambda = 1$ ($\lambda_R = 0$), beyond which it increases again. The above results for τ are for sequential updating. For random updating, the qualitative behavior is again the same (although the magnitude of τ is somewhat larger).

In Fig. 2, we again plot the final average overlap m_f (for the fixed points) with λ_R for parallel (Little-like) updating. The results for the sequential (Hopfield-like) updating are also given here for comparison. The results for the fixed points are qualitatively and quantitatively same in both the Hopfield case and the Little case. The results are for $N = 500$. In particular, we find $m_f \simeq 0.90$ at $\alpha = 0.25$ for $\lambda \geq 1$ ($\lambda_R \leq 0$). The inset shows the variation of average recall time τ and the fraction of limit cycles with λ . Recall time τ again shows a minimum at $\lambda = 1$ ($\lambda_R = 0$), as in the Glauber (Hopfield) case. An interesting observation is that at $\lambda = 1$ the limit cycles of the Little model (parallel dynamics) disappear and all reach to fixed points with identical overlap properties as in the case of the Hopfield model.

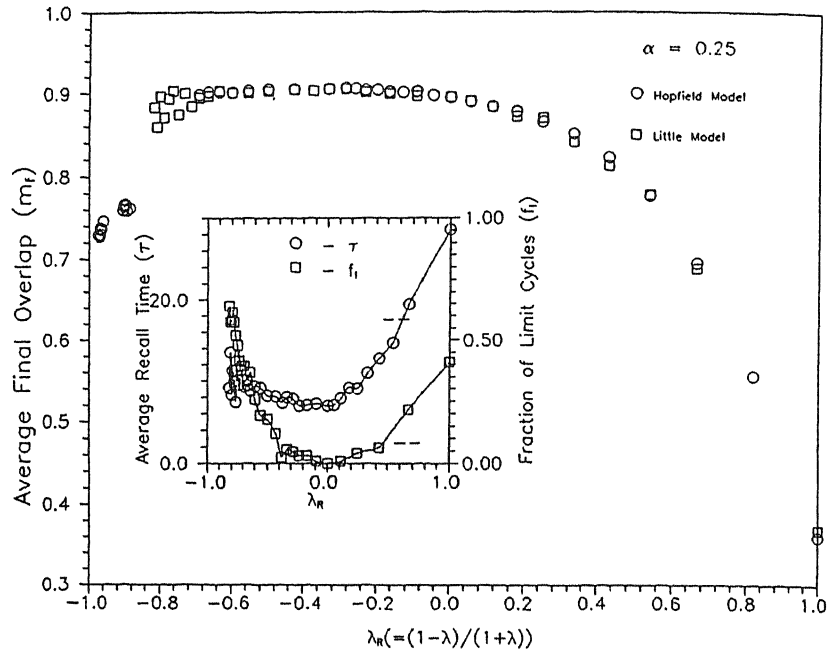


Fig. 2. Average final overlap m_f (for the fixed point obtained) at a fixed loading capacity $\lambda = 0.25$, for a network with $N = 500$ against $\lambda_R (= (1 - \lambda)/(1 + \lambda))$, positive λ . The results are for parallel updating (Little model); overlap results for the Glauber dynamics (Hopfield model) are also indicated. The inset shows the variation of average recall time τ and the fraction of limit cycles f_l against λ_R .

For sequential updating, the variation of the average final overlap m_f with the loading capacity α , for some typical positive values of λ , are shown in Fig. 3. The results are for $N = 1000$. The inset here shows variation of average recall time (τ) with α for different λ . For negative values of λ , even for sequential updating, one gets limit cycles (e.g. the fraction of limit cycles $\simeq 0.48$, for $\lambda = -0.8$ at $\alpha = 0.25$) and the fixed point fraction decreases further for parallel (Little) dynamics.¹⁰ However, the overlap with the learned patterns decreases considerably and we do not see any significant memory capability (for storage in limit cycles) for negative values of λ (typically $m_f \simeq 0.42$ for $\lambda = 0.8$ at $\alpha = 0.25$, using sequential updating).

In order to investigate the finite size effect in the improved performance of the network for positive λ values (for sequential dynamics), we studied the variation of average final overlap m_f with $1/N$ at fixed loading capacity $\alpha (= 0.20$ and $0.25)$ and fixed $\lambda (= 1)$. These results, for $250 \leq N \leq 4000$, are shown in Fig. 4. The inset there shows the same variation of m_f with $1/N$ at fixed $\alpha (= 0.25)$ for $\lambda = 0$. One can clearly compare the finite size effects observed: for $\lambda = 1$, no significant variation of m_f with $1/N$ is observed for both $\alpha = 0.20$ and 0.25 ($m_f \simeq 0.94$ for $\alpha = 0.20$, and $m_f \simeq 0.89$ for $\alpha = 0.25$ at $\lambda = 1$ as $N \rightarrow \infty$). For $\lambda = 0$, however there is significant finite size effect. From the extrapolation we find the extrapolated result for m_f (for large N) to be around 0.29 here at this $\alpha (= 0.25)$; see the inset.

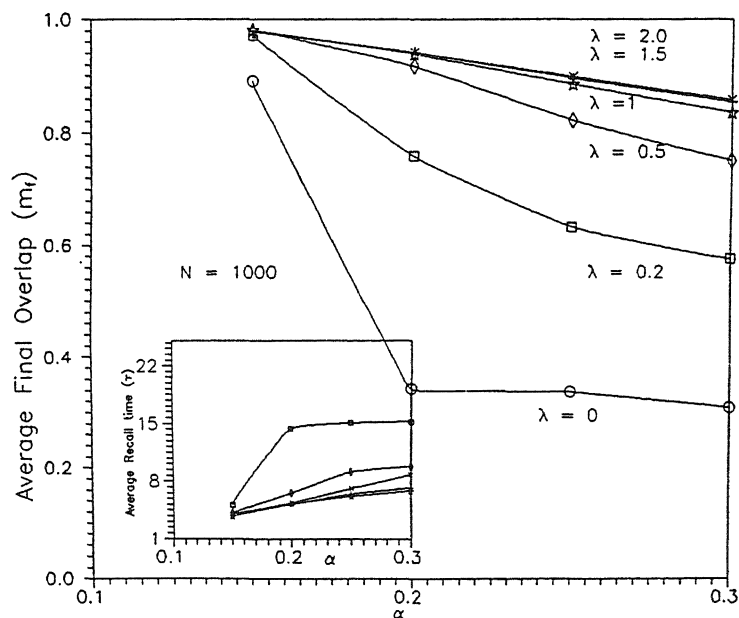


Fig. 3. Variation of average final overlap m_f against loading capacity for some typical values of λ , with sequential dynamics for $N = 1000$. The inset shows the variation of the recall time τ against α for the same values of λ .

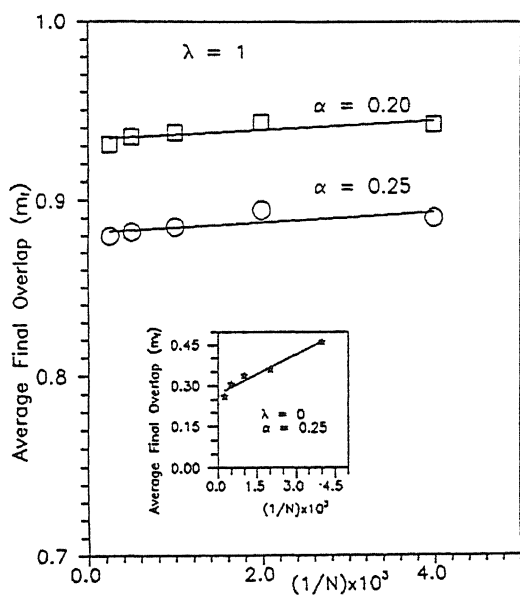


Fig. 4. Variation of average final overlap m_f against $1/N$ for fixed loading capacity $\alpha = 0.20$ and $\alpha = 0.25$ for $\lambda = 1$. The inset shows the same for $\alpha = 0.25$ at $\lambda = 0$. The results are for $250 \leq N \leq 4000$.

It is to be noted that for positive λ , the overlap and other properties saturate beyond $\lambda = 1$ ($\lambda_R = 0$) for any α . This is true even for very large values of λ , in the updating (8). This is somewhat tricky in the sense that apparently one time step is almost skipped in every updating; practically $\{S_i(t-2)\}$ (together with only a small fraction of $S_i(t-1)$) determines $\{S_i(t)\}$ through (8) and is kept in a 'buffer' for latter use and $\{S_i(t-1)\}$ from the 'buffer' is used to determine $\{S_i(t+1)\}$. We have checked independently the performance of such an updating ($S_i(t+1) = \text{sgn}[\sum_j J_{ij}(\lambda' S_j(t) + \lambda S_j(t-1))]$, instead of (8), with $\lambda' \rightarrow 0$). We find for $\lambda' = 0$, the Hopfield model result is recovered. In fact this can be seen from Fig. 2, where the overlap m_f decreases rapidly for very large values of λ in (8) ($\lambda \geq 10$). It may be noted, however, that the effective size of the domain of attraction of the fixed points depends very much on the ratio λ/λ' . This can be seen easily in the limit $\lambda \rightarrow 0$ but λ' finite (or $\lambda' \rightarrow 0$ but λ finite), where the change in energy of the network per updating step depends on the value of λ' (or λ), which determines the effective shape of the energy landscape seen by the dynamics.

As can be easily seen, for nonzero λ , the updating dynamics in (8) does not minimize the 'energy' function $E(t)$ defined as $E(t) = -\sum_{j>i} J_{ij} S_i(t) S_j(t)$, as the delay term contributes in the internal field. Some typical variations in $E(t)$

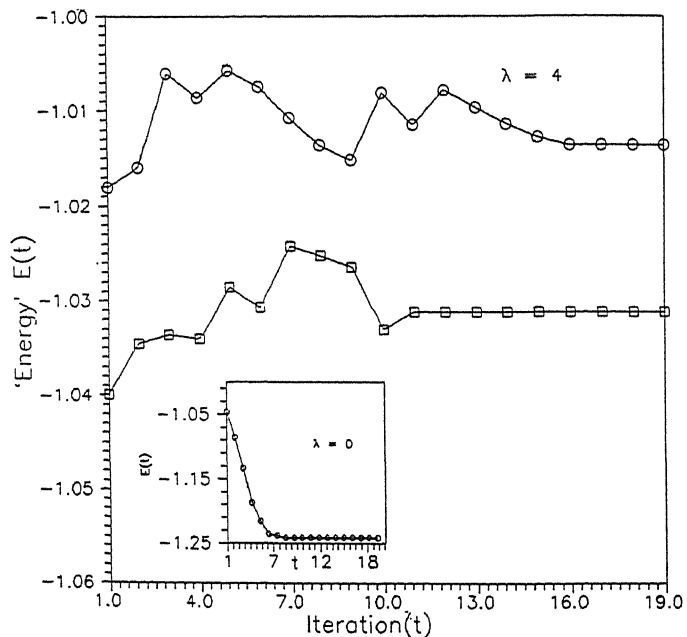


Fig. 5. The variation of the configurational "energy" $E(t)$ with time (updating iteration) t , for the sequential updating with $\lambda = 4$ for two typical cases (arbitrarily distorted patterns) before and after reaching the fixed points. The inset shows the same for a distorted pattern with $\lambda = 0$ dynamics.

with iterations (updating) are shown in Fig. 5 for $\alpha = 0.5$ and $\lambda = 4$. (The large values of α and λ are chosen here to ensure larger τ , so that the effect can be displayed over longer time range). The results clearly show the contribution of the λ term in escaping over the spurious valleys, in the “energy” landscape. The inset in Figure 5 shows the same variation for $E(t)$ in the $\lambda = 0$ (Hopfield) case. Here of course, it clearly decreases monotonically with time.

We have also studied the performance of this dynamics for diluted network (with sequential dynamics; $N = 500$), where a random fraction c of the synaptic connections J_{ij} removed. We show in Fig. 6, some results for overlap (m_f) against λ at a fixed loading capacity $\alpha = 0.20$ for some typical values of dilution concentration c . The inset shows the variation of m_f against α at a fixed $\lambda (= 1)$ for some typical values of c .

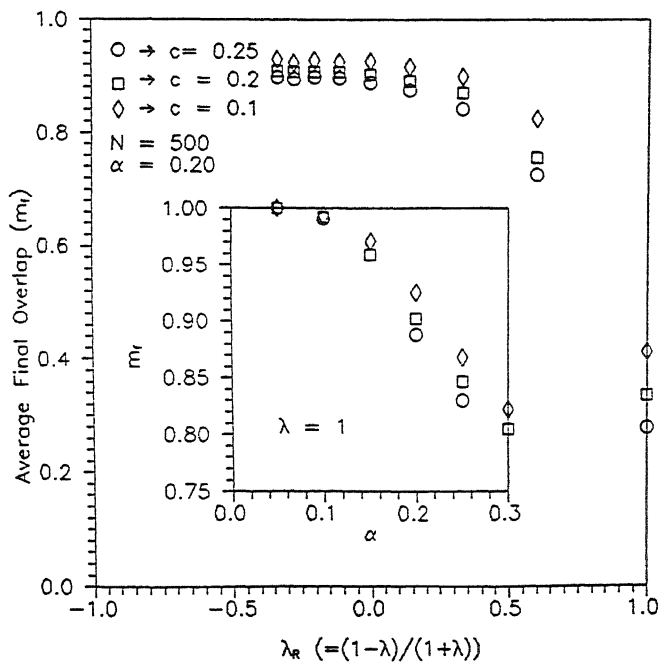


Fig. 6. The variation of average final overlap m_f with $\lambda_R (= (1 - \lambda)/(1 + \lambda))$, positive λ) at a fixed capacity $\alpha = 0.20$ with sequential dynamics for $N = 500$ at some typical values of c ($= 0.10, 0.20$ and 0.25). The inset shows the variation of m_f with α at $\lambda = 1$, for the same values of c .

3. Approximate Analytical Solution in Case of Strong Dilution

In this section we present an approximate analytical solution of the asymmetrically diluted version of the model described in the preceding section. In the limit of strong dilution, where only an infinitesimal fraction of the original number of synaptic connections remain, this model can be solved exactly (for $\lambda = 0$ in (8)) by using the method developed by Derrida *et al.*⁶ Following Derrida *et al.* we define the diluted

version of the J_{ij} as

$$J_{ij} = \frac{C_{ij}}{K} \sum_{\mu} \zeta_i^{\mu} \zeta_j^{\mu} \quad (9)$$

where C_{ij} and C_{ji} are independent random variables and hence J_{ij} is no longer symmetric. We have chosen the normalization $1/K$ rather than $1/N$ so as to give sensible results; as K is the number of remaining connections. The probability distribution for C_{ij} is assumed to have the form

$$P(C_{ij}) = \frac{K}{N} \delta(C_{ij} - 1) + \left(1 - \frac{K}{N}\right) \delta(C_{ij}). \quad (10)$$

With the above form of J_{ij} the local field at site i at any time t is given by

$$\begin{aligned} h_i(t) &= \sum_j J_{ij} [S_j(t) + \lambda S_j(t-1)] \\ &= \frac{1}{K} \sum_j C_{ij} \sum_{\mu} \zeta_i^{\mu} \zeta_j^{\mu} [S_j(t) + \lambda S_j(t-1)]. \end{aligned} \quad (11)$$

For any state $\{S_j\}$ of the network, we now break up the field $h_i(t)$ in Eq. (11) into a term coming from a particular pattern ν and a remaining crosstalk (noise) term:

$$h_i(t) = \frac{1}{K} \zeta_i^{\nu} \sum_j C_{ij} \zeta_j^{\nu} S_j(t) + \eta_i^{\nu}(t) + \frac{\lambda}{K} \zeta_i^{\nu} \sum_j C_{ij} \zeta_j^{\nu} S_j(t-1) + \eta_i^{\nu}(t-1), \quad (12)$$

where

$$\eta_i^{\nu}(t) = \frac{1}{K} \sum_{\mu \neq \nu} \zeta_i^{\mu} \sum_j C_{ij} \zeta_j^{\mu} S_j(t)$$

and

$$\eta_i^{\nu}(t-1) = \frac{\lambda}{K} \sum_{\mu \neq \nu} \zeta_i^{\mu} \sum_j C_{ij} \zeta_j^{\mu} S_j(t-1). \quad (13)$$

We see that the dynamics at zero temperature is governed by the update rule (for asynchronous as well as synchronous dynamics) $S_i(t-1) = \text{sgn}(h_i(t))$, where $h_i(t)$ is given by Eq.(12).

Like the fully connected network, in this case also we define the loading capacity $\alpha = p/K$, where p is the number of pattern to be stored in the network. In the very diluted case we can calculate critical loading capacity α_c (the maximum number of pattern we can store in the network with retrieval quality better than 90%). In order to calculate the critical loading capacity α_c we examine the stability of the patterns $\{\zeta_i^{\nu}\}$. To do that we find the overlap of an actual stable configuration $S_i = \text{sgn}(h_i)$ of the network with the pattern ζ_i^{ν} . We define the overlap m^{ν} as

$$m^{\nu} = \frac{1}{N} \sum_i \zeta_i^{\nu} S_i = \frac{1}{K} \sum_j C_{ij} \zeta_j^{\nu} S_j. \quad (14)$$

Both definitions of m^ν are equivalent (Hertz *et al.*²). Using the dynamics $S_i(t+1) = \text{sgn}(h_i(t))$ with $h_i(t)$ given by Eq.(12), we have a self-consistent equation for m^ν given by

$$\begin{aligned} m^\nu(t+1) &= \frac{1}{N} \sum_i \zeta_i^\nu \text{sgn}(h_i(t)) \\ &= \frac{1}{N} \sum_i \text{sgn}[m^\nu(t) + \lambda m^\nu(t-1) + \zeta_i^\nu(\eta_i^\nu(t) + \eta_i^\nu(t-1))]. \end{aligned} \quad (15)$$

Assuming independent fluctuations at (t) and $(t-1)$, the last term inside the third bracket of the above equation becomes a random variable whose mean is zero and whose variance is given by

$$\sigma^2 = \alpha[1 + \lambda^2 + 2\lambda m^\nu(t)m^\nu(t-1)], \quad (16)$$

and has a Gaussian distribution given by

$$P(\eta) = \frac{1}{\sqrt{2\pi\sigma^2}} \exp[-\eta^2/2\sigma^2]. \quad (17)$$

We now replace the summation in Eq.(15) by an integration over the random Gaussian variable η and we have the evolution equation for the overlap

$$\begin{aligned} m^\nu(t+1) &= \int d\eta P(\eta) \text{sgn}[m^\nu(t) + \lambda m^\nu(t-1) + \eta] \\ &= \text{erf} \left(\frac{m^\nu(t) + \lambda m^\nu(t-1)}{\sqrt{2\sigma^2}} \right). \end{aligned} \quad (18)$$

To replace the sum by the integral we had to assume the statistical independence of ζ_i^ν and η_i^ν 's, so that the symmetry $P(\eta) = P(-\eta)$ could be used. Moreover we are assuming that η_i^ν 's have the Gaussian distribution $P(\eta)$ given by (17), even though that was strictly valid only for $S_i = \zeta_i^\nu$. It can be shown that these assumptions are valid if (a) dilution is independent for ij and ji (which is indeed the case since C_{ij} and C_{ji} are assumed to be independent) and (b) we are in strongly diluted regime, $K \ll N$ (Hertz *et al.*²). At the steady state (i.e. when the fixed point has been reached) we have $m^\nu(t) = m^\nu(t-1) = m_f$ and the self-consistent equation for the overlap becomes

$$m_f = \text{erf} \left[\frac{m_f(1 + \lambda)}{(2\alpha(1 + \lambda^2 + 2\lambda m_f^2))} \right]. \quad (19)$$

The critical loading capacity α_c beyond which the only solution is $m_f = 0$ and below which there are solutions with $m_f \neq 0$, is given by¹⁰

$$\alpha_c = \frac{2(1 + \lambda)^2}{\pi(1 + \lambda^2)}. \quad (20)$$

This increased loading capacity owing to the suppression of fluctuation due to the λ term (see Eqs. (18) and (19)), can also be rationalized in a different way if one notes⁹ that the 'shadow' neurons $\sigma_i(t)$ ($\equiv S_i(t-1)$), representing the states of the neurons at the previous time steps, effectively increases the number of neurons from N to $2N$ (assuming there is no correlation between the states of the neurons and shadow neurons; away from fixed points). One can then rewrite the dynamical Eq. (8) in a single step updating form

$$\begin{pmatrix} S(t+1) \\ S(t+1) \end{pmatrix} = \text{sgn} \begin{pmatrix} J & \lambda J \\ 1 & 0 \end{pmatrix} \begin{pmatrix} S(t) \\ \sigma(t) \end{pmatrix}. \quad (21)$$

Such an asymmetric synaptic matrix might be argued (eg. Ref. 5) to be responsible for suppressing the spin glass noise, thereby increasing the loading capacity. In fact the largest eigenvalue of the synaptic matrix in (21) increases by a factor λ (in the $\lambda \rightarrow 0$ limit). This may be compared with that implied by (19), giving higher capacity due to suppression of noise.

4. Discussions

Our detailed numerical investigation clearly indicates that the recall time (τ) and the overlap properties (measured through the overlap function m_f) of a neural network with the synaptic connections formed using the Hebb's rule (1), are clearly improved with appropriately weighted ($\lambda \simeq 1$) time delayed dynamics (8) with sequential and parallel updating. These indeed support the observations reported in Refs. 3 and 9. Our simulation results for rather large network sizes were used for systematic extrapolations (see Fig. 4), which suggests the improved performance of the network (for $\lambda \geq 1$) to be valid in the thermodynamic limit. Approximate analytical consideration (see Sec. 3) also indicates the same.

It may be noted that with any finite λ , the dynamics (even for sequential updating) is not Glauber-like, since no energy function can be defined (as in the case of Hopfield model for $\lambda = 0$) which gets minimized during the updating process. Also, it may further be noted that although the λ term provides a momentum term, allowing the network to escape shallow spurious valleys (see the results for the time variation of the 'energy' function $E(t)$ in Sec. 2; Figure 5), the fixed point equations of the dynamics in (8) are the same as that of the Hopfield model: namely $S_i(t^* + 1) = \text{sgn}(h_i(t^*))$ with $h_i(t^*) = (1 + \lambda)[\sum_j J_{ij} S_j(t^*)]$. This indicates that the same J_{ij} , as defined in (1), contains more overlap states (with $m_f \geq 0.9$ for $\alpha \leq 0.25$ with $\lambda \simeq 1$ ^{3,9}) than those obtained using the Hopfield (Glauber) dynamics (which gives only the fixed point states with $m_f \geq 0.97$ for $\alpha \leq 0.14$ and $m_f = 0$ for $\alpha > 0.14$ $\lambda = 0$). The use of the dynamics given by Eq. (8) (which for finite λ does not necessarily minimize the energy in successive iterations) helps to access of these additional (over those for the Hopfield model) fixed points [already built-in with the synaptic connection given by Hebb's rule (Eq. (1))]. In fact, as already shown,⁹ see Sec. 3, the dynamics in (8) can be rewritten in a single time

step update form with redefined neuronal states, but then the synaptic interaction becomes asymmetric in an extended neuron state space (of size $2N$), which may be argued for the better performance. The essential role of the λ term (for positive λ) to suppress the spin glass-like noise has been indicated in an approximate noise calculation in the extreme dilute limit (in Sec. 3).

Acknowledgment

PKM is grateful to DST, India, for financial assistance and to SINP, Calcutta, for warm hospitality. BKC is grateful to A. C. C. Coolen and D. Sherrington for some useful comments and suggestions. We thank P. Sen for useful discussions.

References

1. D. J. Amit, H. Gutfreund and H. Sompolinsky, *Ann. Phys.* **173**, 30 (1987).
2. P. Peretto, *An Introduction to the Modelling of Neural Networks*, (Cambridge University Press, Cambridge, 1992); J. Hertz, A. Krogh and R. G. Palmer, *Introduction to the Theory of Neural Computation*, (Addison-Wesley, California, 1991); P. K. Maiti, in *Modeling and Prediction in Complex System*, ed. J. K. Bhattacharjee and A. K. Mallik (Norasa, Delhi, 1995) (in press).
3. B. K. Chakrabarti and P. K. Dasgupta, *Physica A* **186**, 33 (1992).
4. M. Ghosh, A. K. Sen, B. K. Chakrabarti and G. A. Kohring, *J. Stat. Phys.* **61**, 501 (1990); V. Banerjee and S. Puri, *Int. J. Mod. Phys. B* (1994) (in press).
5. G. Parisi, *J. Phys.* **A19**, L675 (1986).
6. B. Derrida, E. Gardener and A. Zippelius, *Europhys. Lett.* **4**, 167 (1987).
7. I. Kanter and H. Sompolinsky, *Phys. Rev.* **A35**, 380 (1987).
8. C. M. Marcus and R. M. Westerfield, *Phys. Rev.* **A42**, 2410 (1990).
9. P. Sen and B. K. Chakrabarti, *Phys. Lett.* **162**, 327 (1992).
10. V. Deshpande and C. Dasgupta, *J. Phys.* **A24**, 5015 (1991).